CENTRO DE INVESTIGACIÓN Y DE ESTUDIOS
AVANZADOS DEL INSTITUTO POLITÉCNICO NACIONAL

UNIDAD ZACATENCO

DEPARTAMENTO DE
INGENIERÍA ELÉCTRICA

SECCIÓN DE ELECTRÓNICA DEL ESTADO SÓLIDO

"SÍNTESIS, CARACTERIZACIÓN Y RESPUESTA FOTOCATALÍTICA DE ÓXIDOS SEMICONDUCTORES A BASE DE $NiTiO_3$"

T E S I S

Que presenta:

MARCO ALEJANDRO RUIZ PRECIADO

Para obtener el grado de:

DOCTOR EN CIENCIAS

Directores de la Tesis:

Dr. JOSÉ ARTURO MORALES ACEVEDO

Dr. ABDELHADI KASSIBA

Ciudad de México OCTUBRE, 2016

CENTRO DE INVESTIGACIÓN Y DE ESTUDIOS
AVANZADOS DEL INSTITUTO POLITÉCNICO NACIONAL

ZACATENCO UNIT

DEPARTMENT OF

ELECTRICAL ENGINEERING

SOLID STATE ELECTRONICS SECTION

"SYNTHESIS, CHARACTERIZATION AND PHOTOCATALYTIC RESPONSE OF $NiTiO_3$ BASED SEMICONDUCTIVE OXIDES"

T H E S I S

Presented by:

MARCO ALEJANDRO RUIZ PRECIADO

To obtain the degree of:

DOCTOR IN SCIENCE

Thesis directors:

Dr. JOSÉ ARTURO MORALES ACEVEDO

Dr. ABDELHADI KASSIBA

Mexico City OCTOBER, 2016

ACKNOWLEDGEMENTS

My deepest gratitude to CONACyT for providing a doctoral scholarship during the complete period of the PhD program and to Cinvestav for the financial support provided to attend to international congresses.

To the 3MPL doctoral school for their economic support that helped me cover the expenses of living in France and to the Caisse d'Allocations Familiales (CAF) for covering a percentage of the dormitory rent during my first stay there.

I am very grateful with my thesis directors Prof. Abdelhadi Kassiba and Prof. Arturo Morales Acevedo for their constant support in everything that was necessary to achieve the desired goals and to train me into becoming a better researcher. Without them, this work would not have been possible.

The quality of this work greatly improved thanks to the knowledge and experience that my advisors, Prof. Alain Gibaud and Prof. Makowska, shared with me. Prof. Alain Bulou made invaluable contributions on Raman spectroscopy. Prof. Arturo Manzo's advice on electrocatalysis made it possible for me to complete the related tasks.

The time spent by the evaluation committee members, referees and jury members in reviewing the work and contribute to it through their observations and recommendations, was of great help for developing the PhD project and it is very appreciated.

I would like to specially thank Dr. Gaspar Casados Cruz, Rosa María Nava, Matieu Edely, Yesenia Aguirre and all the engineers and faculty staff from Cinvestav and the University of Maine for the assistance provided during the development of the thesis work.

As always, my family and friends surrounded me with happy moments, constant encouragement and unconditional support along this path, which allowed me to take over the various difficulties found during the PhD program.

TABLE OF CONTENTS

LIST OF TABLES

LIST OF FIGURES

Fig. 7.1 Photocatalytic experimental setup.

Fig. 7.2 Optical absorption spectra of the MB charged solution during the photocatalytic process (left panel). Absolute MB concentration vs time (right panel). The dashed plot area shows the results in dark conditions and the white section displays the experimental measurements under illumination.

Fig. 7.3 Kinetics of the photocatalytic degradation of MB by visible light irradiated $NiTiO_3$. The graph reports the semi-logarithmic plot of the normalized concentration C/C_0 versus irradiation time.

Fig. 7.4 Cyclic Voltammetry of the ITO/Glass substrate (dashed line) and the P3-SG-A650C catalyst (solid line). NaOH 0.1 M was used supporting electrolyte. Scan rate of 20 mV/s.

Fig. 7.5 Cyclic Voltammetry of the P3-SG-A650C in the presence of Methanol. The activation in NaOH 0.1 M is showed as a reference. NaOH 0.1 M + Methanol 0.001 M, 0.01 M, 0.1 M and 1 M are displayed. The left-hand panel shows the reactions taking place. The right-hand panel allows to observe the change in intensity of the cathodic peak at 0.4 V with respect to methanol concentration. Scan rate 20 mV/s.

Fig. 7.6 Logarithm of peak current density (J_p) vs logarithm of methanol concentration (C) showing a linear behavior (left panel). Peak current density (J_p) vs methanol concentration (C) displaying the simulated behavior of peak current (right panel).

Fig. 8.1 UV-Vis absorption spectra obtained experimentally for the different $NiTiO_3$ powders (left) and the $NiTiO_3$ Thin Film deposited on quartz (right).

Fig. 8.2 UV-Vis absorption spectra calculated by the PM6 model for different clusters (left panel) and the experimental spectrum obtained for samples P1-SG-A1350C and P3-SG-A650C (right panel, black and red respectively).

Fig. 8.3 HOMO and LUMO orbitals calculated by the PM6 model for the $(NiTiO_3)_2$, $(NiTiO_3)_8$ and $(NiTiO_3)_{17}$ clusters. *(Larger version in Chapter II, Fig. 2.8)*

Fig. 8.4 Crystal structure of $NiTiO_3$ showing the NiO_6 (light gray) and TiO_6 (dark grey) octahedral.

Fig. 8.4 Tauc plots of P1-SG-A1000C (top left), P1-SG-A1350C (top right), P2-SSR-A1000C (middle left, P2-SSR-A1350C (middle right), P3-SG-A650C (bottom left) and Thin Film (bottom right).

Fig. 8.6 Experimental and simulation of the Raman spectrum of the representative $NiTiO_3$ thin film annealed at 1000 °C for 2 hours in air atmosphere.

Fig. 8.7 Raman spectra collected from a representative $NiTiO_3$ thin film annealed at 1000 °C for 2 hours in air atmosphere using: parallel polarization (top) and cross polarization (bottom).

Fig. 8.8 Raman spectra for the $(NiTiO_3)_{17}$ nanoparticles calculated by the parametrized PM6 method as well as experimental spectrum.

ABSTRACT

The thesis work is devoted to the synthesis of $NiTiO_3$-based semiconductive structures, *i.e.* powders and thin films, and the investigation of their related properties with the aim of their applications in photocatalysis. Theoretical approach and numerical simulations of the electronic, vibrational and optical properties of bulk and nanosized $NiTiO_3$ structures have been carried out in order to deepen the understanding of the experimental results. The synthesis of $NiTiO_3$ powders has been achieved by sol-gel and solid state reaction, while $NiTiO_3$ thin films have been grown by rf-sputtering. Characterizations on their structural, vibrational and optical properties confirm the stabilization of polycrystalline $NiTiO_3$ in its ilmenite phase in both powders and thin films as well. The determination of a band gap at 2.25 eV suggests the feasibility to implement the synthesized materials as visible-light-active photocatalysts. This feature has been tested in the degradation of methylene blue in aqueous solution using rf-sputtered $NiTiO_3$ thin films irradiated with visible light, achieving the degradation of 60% of the initial concentration of the colorant in 300 minutes. In addition, the electro-oxidation of methanol has been accomplished by applying an external voltage on an electrode containing $NiTiO_3$ powders in alkaline media. The Ni ions present in the catalyst have been identified as the active species with the oxidation of the organic molecules on the surface of Ni^{3+} sites. As a main achievement, $NiTiO_3$ has been synthesized as powders and thin films with suitable characteristics for efficient heterogeneous photocatalysis and the catalytic capabilities of $NiTiO_3$ have been demonstrated on the photodegradation of Methylene Blue and the electro-oxidation of methanol.

Key Words:

$NiTiO_3$, Semiconducting oxydes, Nanostructures, DFT, Sol-Gel, Solid state reaction, Rf-sputtering, Nanopowders, Thin Films, Photocatalysis, Electrocatalysis

RESÚMEN

El trabajo de tesis ha sido dedicado a la síntesis de estructuras semiconductoras basadas en $NiTiO_3$ y a la investigación de sus propiedades con el fin de utilizarlas como fotocatalizadores. Un estudio teórico de las propiedades electrónicas, vibracionales y ópticas para el $NiTiO_3$ volumétrico, así como nanométrico ha sido llevado a cabo buscando profundizar en el entendimiento de los resultados experimentales. La síntesis de polvos de $NiTiO_3$ ha sido lograda por sol-gel y reacción en estado sólido, mientras que películas delgadas de $NiTiO_3$ han sido crecidas por rf-sputtering. La caracterización de sus propiedades estructurales, vibracionales y ópticas confirman la obtención de $NiTiO_3$ policristalino en su fase ilmenita. La determinación de un ancho de banda prohibida de aproximadamente 2.25 eV sugiere la posibilidad de implementar los materiales sintetizados, como fotocatalizadores activos en el rango de luz visible. Esta característica ha sido probada en la degradación de Azul de Metileno en solución acuosa, usando películas de $NiTiO_3$ (obtenidas por rf-sputtering) irradiadas con luz visible, logrando la degradación del 60% de la concentración inicial del colorante en 300 minutos. Adicionalmente, la electro-oxidación de metanol ha sido lograda al aplicar un voltaje externo a un electrodo que contiene polvos de $NiTiO_3$ en un medio alcalino. Los iones de Ni presentes en el catalizador han sido identificados como las especies activas, y que la oxidación de las moléculas orgánicas ocurre en la superficie de los sitios de Ni^{3+}. En resumen, $NiTiO_3$ ha sido sintetizado en forma de polvos y de películas delgadas con características favorables para realizar fotocatálisis heterogénea eficientemente y las capacidades catalíticas del $NiTiO_3$ han sido demostradas mediante la fotodegradación de Azul de Metileno y la electro-oxidación de metanol.

Palabras clave:

$NiTiO_3$, Óxidos semiconductores, Nano-estructuras, DFT, Sol-Gel, Reacción en Estado Sólido, RF-sputtering, Nano-polvos, Películas delgadas, Fotocatálisis, Electrocatálisis.

RESÚMÉ

Le travail de thèse est consacré à la synthèse de structures semi-conductrices à base de $NiTiO_3$, et l'étude de leurs propriétés dans le but de les appliquer en photocatalyse. Une étude théorique et des simulations numériques ont été effectuées pour analyser les propriétés électroniques, vibrationnelles et optiques de $NiTiO_3$ massif ou sous forme de clusters nanométriques. Les poudres $NiTiO_3$ ont été synthétisées par sol-gel par réaction en phase solide, tandis que les films minces ont été obtenus par pulvérisation cathodique rf-magnétron. Les caractérisations de leurs propriétés physiques confirment l'obtention de $NiTiO_3$ polycristallin dans sa phase ilménite. La détermination du gap électronique à 2.25 eV suggère la faisabilité de mise en œuvre des matériaux synthétisés comme photocatalyseurs actifs sous irradiation en lumière visible. Cette fonctionnalité a été testée par la dégradation du bleu de méthylène en solution aqueuse en utilisant les couches minces de $NiTiO_3$ sous irradiation visible, atteignant la dégradation de 60% de la concentration initiale du colorant en 300 minutes. En outre, l'électro-oxydation du méthanol a été réalisée en appliquant une tension externe sur une électrode contenant des poudres $NiTiO_3$ dans des milieux alcalins. Les ions de Ni présents dans le catalyseur ont été identifiés comme des espèces actives et que l'oxydation des molécules organiques se produit sur la surface des sites de Ni^{3+}. En résumé, $NiTiO_3$ a été synthétisé sous forme de poudres et de films minces ayant des caractéristiques appropriées pour la photocatalyse hétérogène efficace et les capacités catalytiques de $NiTiO_3$ ont été démontrées sur la photodégradation du bleu de méthylène et l'électro-oxydation de méthanol.

Mots clés:

$NiTiO_3$, Oxydes semi-conducteurs, Nanostructures, DFT, Sol-Gel, Réaction en phase solide, pulvérisation cathodique rf-magnétron, Nanopoudres, Films minces, Photocatalyse, Electrocatalyse

CHAPTER I: INTRODUCTION

Heterogeneous photocatalysis using inorganic solid semiconductors consists in the process of a radiation mediated chemical reactions that occur at the interface between the semiconductor and an aqueous or gaseous medium.[1] The involved physico-chemical mechanism is based on redox reactions that must take place at the same time. The one involving oxidation from photogenerated holes occurs simultaneously with the reduction reaction induced by photogenerated electrons. During such a complex process, the photocatalyst must maintain the stability of its main physical features, such as crystalline structure, surface states and its electronic and optical behaviors.

The photocatalytic phenomena started attracting interest in the late 1960s after the discovery by Honda and Fujishima of the photoelectrolysis of water using titanium dioxide (TiO_2) as photocatalyst. From that time, a large scientific community developed exhaustive works on several classes of materials and on the improvement of the experimental processes with the aim of enhancing the photocatalytic efficiency. Nowadays, this research topic is critical due to the applications to important society challenges such as finding a new source of renewable energy and environment preservation. Indeed, by exploiting the solar radiation to produce hydrogen, new generations of engines may be used instead of the traditional engines that rely on fossil fuels. For the challenging goal of environmental care, photocatalytic degradation of organic and inorganic pollutants from water and atmosphere may be conducted based on semiconducting material with photoactivity under a defined spectral range of radiation. For these reasons, photocatalysis has been studied extensively developing a wide range of photocatalytic materials with competitive efficiencies. The process contributes efficiently to clean and renewable energy generation as well as offering a friendly solution for environmental care.

More specifically, in the energy generation area, photocatalysis has been of particular interest in the production of hydrogen from water electrolysis[2] and the conversion of CO_2 into hydrocarbon fuels[3,4] using solar energy as radiation source. On the other hand, photocatalysis has promising applications for environmental conservation and restoration, such as germicide and antimicrobial activity,[5–7] nitrogen fixation in agriculture,[8] removal of

NO_x/SO_x air pollutants,[9–11] degradation of organic compounds for water treatment[12] and purification of wastewaters from the textile industry.[13,14]

The most studied material for photocatalytic applications is titanium dioxide (TiO_2) in its anatase phase, because of its efficient photogeneration of excitonic states with high concentrations, long lifetimes and high oxidizing and reductive potentials.[15–17] However, titanium dioxide possesses a band gap greater than 3 eV making necessary the use of costly UV light sources or, alternatively, only a narrow spectral range of the solar radiation (4-6 %) can be exploited. Thus, the use of suitable doping agents to notably reduce its band gap,[18–21] or the association of TiO_2 with other semiconducting structures able to harvest visible-light,[22–25] remains an open task in order to achieve visible-light-driven photocatalysis and decrease the over-all cost of the process.

It is clear that finding alternative photoactive semiconducting structures with low electronic band gaps (less than 2.5 eV) and high oxidizing and/or reduction potentials constitute a challenge that could contribute significantly to the preservation of natural habitats and improve the life quality of millions of people.[26,27]

Research on new semiconducting photocalysts that meet the above-mentioned criteria is vast, and as an example, bismuth based semiconducting oxides such as $BiVO_4$ have demonstrated efficient activity on visible light photocatalysis.[28–30] This material is characterized by an electronic energy gap close to 2.5 eV, allowing the harvesting of a large spectral range of solar radiation, promoting then, efficient photocatalytic reactions.

In similar approaches, perovskite-type oxides like titanates have been studied as functional inorganic materials for a wide range of applications and photocalysis is considered among the most promising ones.[31–33] For this reason, titanate oxides such as $ATiO_3$ (A = Ni, Fe, Sr, Co, Mn, Cu, Zn, etc.) are subject of intensive research and some of them have demonstrated efficient photocatalytic activity.[34] As examples, $FeTiO_3$ and $SrTiO_3$ have shown very good photocatalytic activity.[35] Among the members of the titanates family, nickel titanate ($NiTiO_3$), holds tremendous promise for a wide range of applications, especially as semiconductor rectifier, high temperature superconductor, gas sensor, and photocatalyst.[36]

$NiTiO_3$ is typically an n-type semiconducting material that crystallizes in the ilmenite structure and presents antiferromagnetic behavior and its band gap value is around 2.2 eV, well adapted for visible-light-driven photocatalysis. [31–34,36,37]

CHAPTER I

1. STATE OF THE ART

a. Review on TiO_2 as a photocatalyst over time

Titanium dioxide (TiO_2) possesses properties that makes it the ideal photocatalyst. Actually, most of the understanding and advances in photocatalysis is directly linked to the investigations on TiO_2. This is why reviewing the history of TiO_2 as a photocatalyst will also give insight into photocatalysis as an active field of research.

In the late 1960s, Honda and Fujishima began investigating the photoelectrolysis of water, using a n-type single crystal of a TiO_2 (in its rutile phase) semiconducting electrode and accomplished to demonstrate the electrolysis of water for the first time by exposing the TiO_2 electrode to UV light while connected to a platinum counter electrode through an electrical load.[38]

When the surface of the rutile TiO_2 electrode was exposed to spectral radiations with energies greater than its band gap, photocurrent flowed from the platinum counter electrode to the TiO_2 electrode through the external circuit. The direction of the current revealed that the oxidation reaction (oxygen evolution) occurred at the TiO_2 electrode and the reduction reaction (hydrogen evolution) at the Pt electrode. This observation shows that water can be decomposed, using UV light, into oxygen and hydrogen without applying an external voltage.

Later on, during the decade of the 1980s, intensive researches were done on photocatlytic water splitting using suspensions of powdered TiO_2 (in the anatase phase) attached to Pt particles. The results of these studies were inconsistent and the reactions were inefficient. The reason for the low efficiency is that the production sites of H_2 and O_2 are very close to each other, making it very likely for the gases to recombine and form water again. To solve this problem, organic compounds were added to the aqueous suspension of platinized TiO_2. Thus, water was reduced producing H_2 at the Pt sites and the organic compounds are oxidized instead of water by photogenerated holes at the TiO_2 sites and the H_2 production proceeds efficiently.[39]

In general, anatase phase (E_g = 3.2 eV) has proven to be more efficient than rutile (E_g = 3.0 eV) for hydrogen production in photocatalysis. The main reason for the higher photocatalytic

efficiency observed in anatase, is the higher reduction potential of the photogenerated electrons. For this reason, anatase TiO_2 is the crystalline phase of choice when highly efficient photocatalysis is required, demonstrating to be superior to any other material tested to date. But even when TiO_2 photolysis reaction is very efficient, it can only absorb the UV spectral range contained in the solar spectrum, which is a small fraction. Due to the requirement of costly artificial sources of UV radiation, and therefore, from the point of view of H_2 production, TiO_2 photocatalyst is not very attractive for water splitting at industrial level. In this way, consequent efforts were no longer centered on the evolution of H_2 but rather on the oxidation power of TiO_2 for degrading hazardous pollutants present in water or air. In this novel approach, the reduction reactions taking place at the surface of the catalyst didn't need platinization as required for H_2 evolution, hence, TiO_2 powders can be employed under ambient conditions. It is important to notice that both reactions, reduction and oxidation, occur at the surface of the semiconductor and therefore, the experimental process is simplified. Further optimization of the experimental setup involves the immobilization of the TiO_2 particles on supports (as thin films) in order to handle the catalyst more easily. The use of TiO_2 as thin films allowed its implementation as self-cleaning coatings in relatively small areas for which the UV radiation coming from the sun is sufficient to induce the photocatalytic reactions.

Up to this day, the photocatalytic mechanism of TiO_2 is well understood and the experimental setup has been properly improved over time, but even after extensive trials, the industrialization of TiO_2 as a photocatalyst for wastewater treatment in large quantities has not been accomplished and it is mainly because of the limitation imposed by its wide band gap. For this reason, the investigation on decreasing titanium dioxide's band gap trough doping or other approaches became a trending topic nowadays. Unfortunately, doped TiO_2 (under visible radiation) have failed to match the efficiency of undoped TiO_2 (under UV radiation).

The evolution of the field has led contemporary research in photocatalysis to focus not only in the efficiency of the redox reactions but also in acknowledging the spectral range required to induce such reactions.

b. Review on visible-light active perovskites

The search of a semiconductor that presents similar characteristics to those of TiO_2, while having a smaller band gap, has led to the investigation of the perovskite-like family of materials. Perovskites are represented by the general formula ABO_3, and normally, in this crystal structure the A site is occupied by the larger cation, while the B site is occupied by the smaller one. Perovskites exhibit properties suitable for numerous technological applications.[40] The origin of such properties lie in the crystal structure of perovskites, having corner-connected BO_6 octahedra and 12 oxygen coordinated A cations located in between the eight BO_6 octahedra, this crystal structure is illustrated in Fig. 1.1.

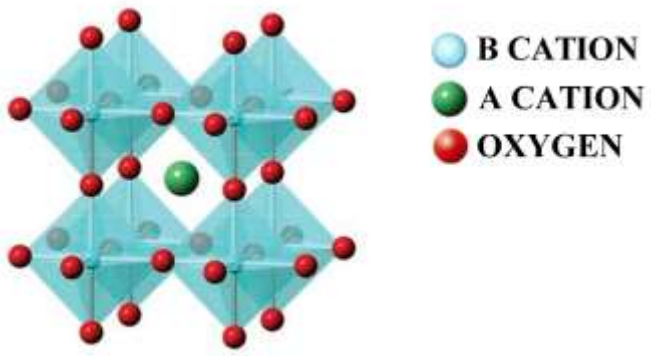

Fig. 1.1 *ABO_3 perovskite crystal structure.*

The perfect structure of the octahedral connection results in a cubic lattice, however, depending on the ionic radii and electronegativity of the A and B site cations, tilting of the octahedra takes place and gives rise to lower symmetry structures. As seen from the crystal structure, B site cations are strongly bonded with the oxygen, while A site cations have relatively weaker interactions with oxygen. Depending on the type of the cations occupying the lattice sites, these interactions could be altered to yield the different perovskite crystal geometries. For example, different degrees of tilting of the octahedra give rise to different electronic and optical properties. The degrees of tilting may affect the band structure, electron and hole transport properties, photoluminescence, and dielectric behavior.[41,42]

From the point of view of photocatalysis, perovskite structures may offer significant advantages over the binary oxides for several reasons. Perovskites may exhibit favorable

band edge positions which allow various photoinduced reactions. For example, as compared to the binary oxides, several perovskites have sufficiently cathodic conduction band (CB) energies for hydrogen evolution.[43] Also, A and B site cations in the lattice give a broader scope to design and alter the band structure as well as other photophysical properties. Moreover, another advantage compared to binary photocatalysts like TiO_2 and ZnO, whose electronic band gaps are above 3 eV (requiring UV light to be excited), is that some perovskite photocatalysts, like $NiTiO_3$, are photoactive under visible light.

The perovskite family is mainly divided into titanates ($ATiO_3$), tantalates ($ATaO_3$), vanadates (AVO_3), niobates ($ANbO_3$) and ferrites ($AFeO_3$). Among them, titanate perovskites, despite having mostly band gap energies greater than 3 eV, show excellent photocatalytic properties under UV radiation,[40] and as for TiO_2, doping is an approach commonly employed to expand the absorption of these materials into the visible range. One of the reasons for certain titanates to present good photocatalytic activity is that they have a conduction band minimum more negative than TiO_2 does, making them more suitable for hydrogen evolution. In addition to that, they also show good photostability and resistance to corrosion in aqueous solutions. Some of those titanates are $SrTiO_3$, $BaTiO_3$, $MgTiO_3$, $MnTiO_3$ and $FeTiO_3$ (see Fig. 1.2).

For instance, $SrTiO_3$ has been one of the most widely studied titanates because of its strong oxidizing and reducing capabilities, arising from the position of its valence and conduction band edges. Despite having a band gap around 3.25 eV, some works describe the doping or the combination of $SrTiO_3$ with different structures to improve the photocatalytic activity under visible light. For example, Rh-doped $SrTiO_3$ combined with O_2-evolving photocatalysts like $BiVO_4$ or $AgNbO_3$ has been tested for stoichiometric water splitting reactions, successfully establishing the feasibility of a "Z scheme" photocatalysis under visible light for this kind of materials.

Another wide-band-gap titanate $CaTiO_3$ (3.6 eV) has demonstrated visible light catalytic activity after being doped with Cu atoms.

These structures are useful for water splitting thanks to their CB potential. However, certain transition metal titanates do not possess the desired CB potential for water reduction (Fig. 1.2), though they have band gap values in the visible region, such as $CoTiO_3$ and $NiTiO_3$, and could be suitable for degradation of organics or other photo-oxidation reactions.

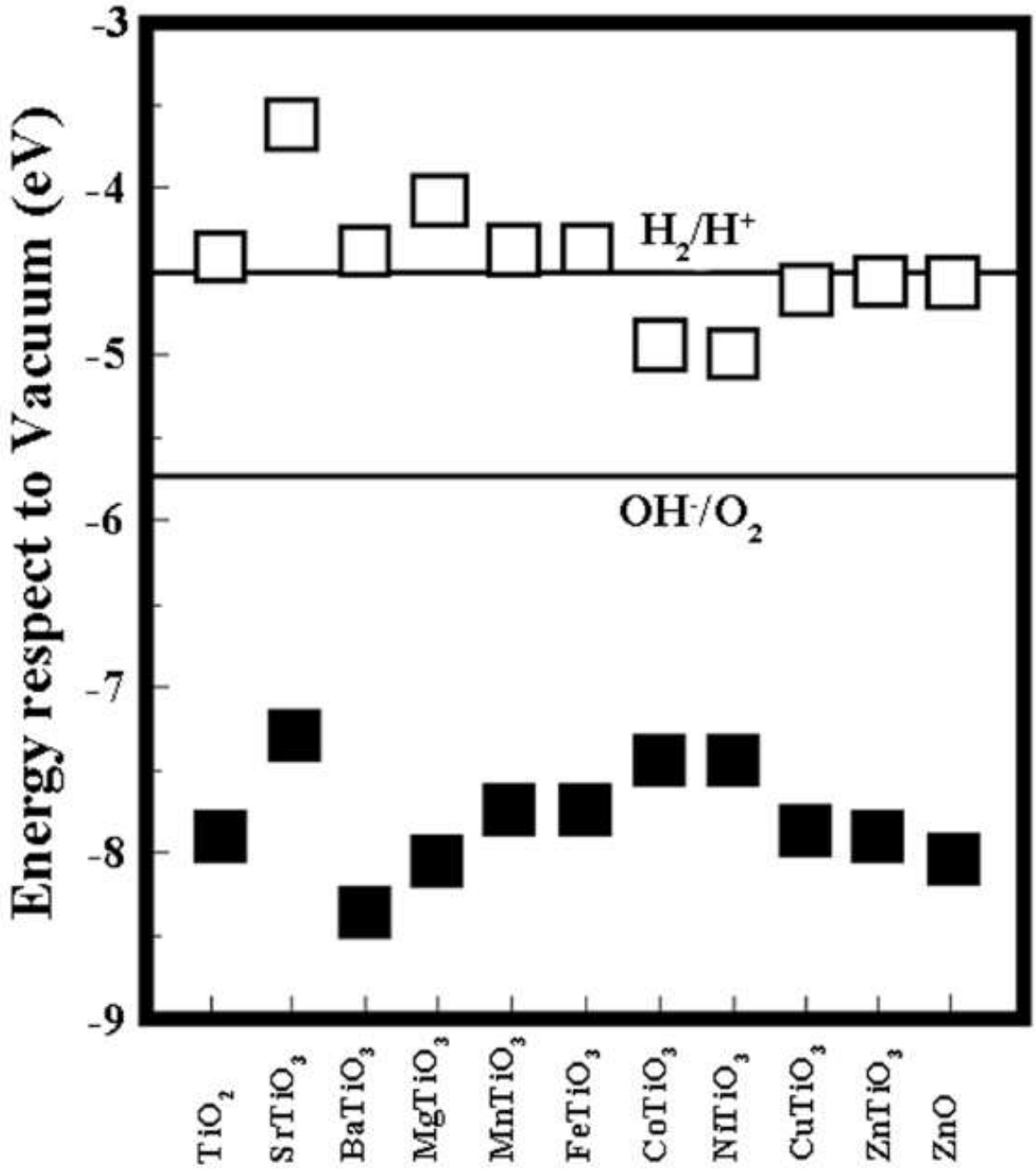

Fig. 1.2 *Energy positions of conduction band edges and valence band edges at pH 0 for selected metal oxide semiconductors. The bottom of the open squares represents conduction band edges, and the top of solid squares represent valence band edges. The solid lines indicate water stability limits. Image taken from American Mineralogist, 85, (2000).*[43]

c. Nickel titanate ($NiTiO_3$)

Nickel titanate ($NiTiO_3$) has been attracting much attention in recent years because it holds tremendous promise for a wide range of applications, for example as semiconductor rectifier, high temperature superconductor, gas sensors, and specifically as a photocatalyst.[36] $NiTiO_3$ is an n-type semiconducting material whose band gap energy value has been mostly reported to be between 2.2 and 2.3 eV, it also possesses high electrical resistivity and high permittivity. Additionally, survey on the reports of $NiTiO_3$ indicates that this material shows antiferromagnetic behavior.[37]

At ambient conditions, $NiTiO_3$ stabilizes in the ilmenite crystalline structure with space group $(R\bar{3})$ with both Ni and Ti possessing octahedral coordination and the alternating cation layers occupied by Ni^{2+} and Ti^{4+} alone, as illustrated in Fig. 1.3.[18]

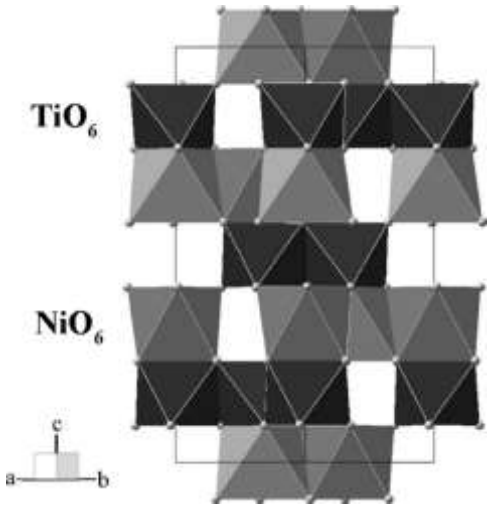

Fig. 1.3 *$NiTiO_3$ crystal structure. The NiO_6 (light gray) and TiO_6 (dark grey) octahedral are shown.*

The lattice parameters values for the ilmenite structure, according to the standard reference, are a=b=5.0326 Å, and c=13.796 Å and the values for $\alpha = \beta = 90°$, $\gamma = 120°$. [20–23]

$NiTiO_3$ nanoparticles and thin films have been commonly synthesized by different methodologies such as solution combustion, polymeric precursor, sol–gel spin coating, sol–gel, modified pechini, flux, stearic acid gel, co-precipitation and solid state methods. Depending on the method, the temperature at which the crystallization begins varies between

500 °C and 600 °C and temperatures as high as 1400 ºC may be necessary to obtain good crystalline characteristics.[20–23,25–27,31–33,36,44,45]

Above 1400 ºC, $NiTiO_3$ undergoes a second-order phase transition from the ilmenite structure with space group $R\bar{3}$ to the corundum structure with space group $R\bar{3}c$, which is due predominantly to a Ni-Ti order-disorder transition.[26] $NiTiO_3$ is the first ternary titanate with ilmenite structure for which a transition to a corundum structure with a random distribution of the cations could be proven. With increasing radius of the bivalent 3d metal ions the statistical structure becomes less favorable and should lead to a hypothetical transition above the melting point for $CoTiO_3$, $MnTiO_3$ or $FeTiO_3$. The observed variation of the order parameter with the temperature could be divided into a critical region and another one governed by the law of mass action for the exchange of Ni and Ti.[26]

In its ilmenite phase, the light absorption spectrum of $NiTiO_3$ presents a broad intense absorption band in the visible region from 600 to 800 nm leading to the light yellow color of $NiTiO_3$.[44] Regarding its band gap, some discrepancies among the reports indicate that the insight into its optical characteristics is necessary. In the literature, the band gap of $NiTiO_3$ is reported to be in a wide spectral range that goes from close to 2 eV up to 3.5 eV.[37,43,46–52] Nevertheless, most reports agree that the lower value of the electronic transitions is around 2.25 eV, which is enough to harvest visible light and high enough to ensure efficient photocatalysis.

As it has been explained before, photocatalytic processes are based on electron/hole pairs generated by means of optical absorption. The photogenerated charge carriers can give rise to redox reactions with species adsorbed at the surface of the catalysts. Different kinds of target contaminants have been used as probe molecules in order to measure the photocatalytic potential of a certain material, for example, methylene blue, rhodamine B, methyl orange, phenol and nitrobenzene are among the more commonly used probe molecules.[44]

d. The mechanism of heterogeneous photocatalysis in aqueous media

Heterogeneous photocatalysis is a versatile and low-cost alternative for water decontaminant treatment where pollutants of biological, organic or inorganic nature can be eliminated. The nature of the photocatalytic phenomenon requires the pollutant and the catalyst to be in close proximity with each other in the presence of light.

The basic process of a photocatalytic reaction starts with the absorption of light by the catalyst, which generates an electron-hole pair, followed by its separation and migration to the surface and finalizing with the redox reaction of an adsorbed molecule. This process is represented schematically in Fig. 1.4. As a result of irradiation, the semiconducting particle can behave either as an electron donor or acceptor for molecules in contact with it. Thermalization and recombination losses limit the overall efficiency of the catalytic reaction, but the excited electrons and holes that reach the surface can participate in redox reactions with different molecules, *e.g.* water; hydroxide ions (OH^-); organic compounds or oxygen, leading to the mineralization of the pollutant.

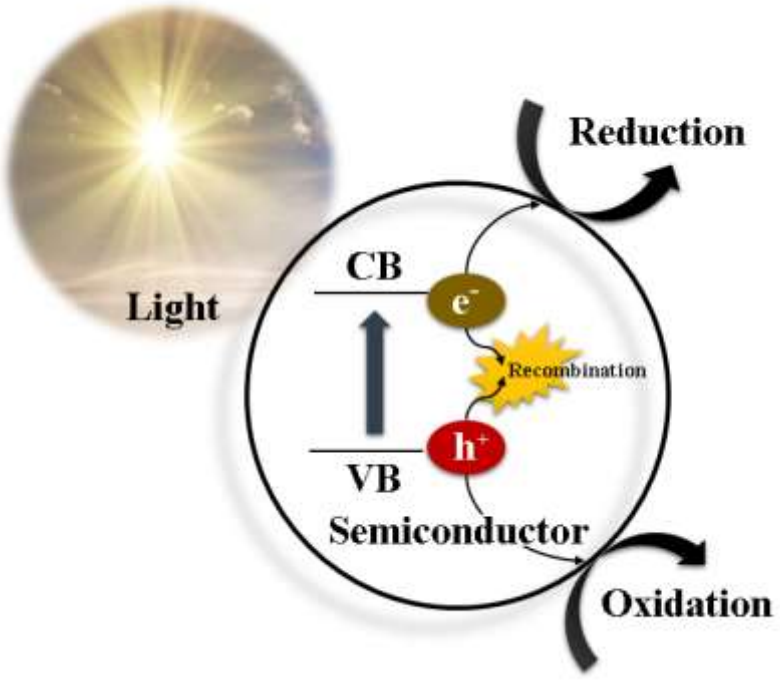

Fig. 1.4 *Schematics of the general photocatalytic process for a spherical semiconductive catalytic particle.*

Photogenerated charge carriers can react directly with adsorbed oxygen and pollutants, but reactions with water are predominant since water molecules are significantly more abundant than pollutant molecules.

Photocatalysts such as TiO_2 and $NiTiO_3$ show great oxidation potential due the position of their valence band edge. Oxidation of water or OH's by holes produces the hydroxyl radical, which is a powerful oxidant able to rapidly attack pollutants on the semiconductor surface. The position of the conduction band edge of TiO_2 allows the reduction of oxygen radicals that can also participate in degrading contaminants in the solution.

Since the redox reactions take place on the surface of the semiconductor by adsorbing molecules, it is important to understand how molecules are adsorbed. In this matter, the fundamental theory of adsorption that generally applies to photocatalysis is the Langmuir-Hinshelwood theory which postulates that adsorption is limited to a monolayer and that excess molecules are therefore "reflected" back. That is to say that adsorption at one photocatalyst site does not affect the adsorption at adjacent sites and that the rate of adsorption of the molecules at equilibrium is equal to the rate of desorption.

The variation of the pollutant concentration with respect to time according to Langmuir-Hinshelwood kinetics is described by equation (1.1).

$$r = -\frac{dC}{dt} = \frac{a \cdot K_{ads}^{LH} \cdot C}{1 + K_{ads}^{LH} \cdot C} = kC \tag{1.1}$$

Where K_{ads}^{LH} is the Langmuir-Hinshelwood adsorption equilibrium constant, a is the pseudo-first order rate constant, and k is an observable rate constant, defined by equation (1.2).

$$k = \frac{a \cdot K_{ads}^{LH}}{1 + K_{ads}^{LH} \cdot C} \tag{1.2}$$

If in a photocatalytic experiment, the initial concentration of a pollutant is known and the variation in concentration is being monitored, and then, by using equations (1.1) and (1.2), the reaction rate constant k can be determined.

e. Photocatalytic degradation of organic dyes

Originally, the motivation to study the photocatalytic degradation of organic dyes arises from the need to treat contaminated wastewater released mainly by the textile industry, claimed to be responsible for the release of as much as 15% of the total world production of dyes, and by other industries such as the paper industry, the beauty products industry and the food industry that are also responsible for the release of considerable amounts of dye charged wastewater.

When speaking of photocatalytic degradation of a certain organic dye mediated by a semiconductor catalyst, the degradation pathway of the organic dye can be schemed as depicted by equations (1.3) – (1.5):

$$Semiconductor + h\nu \rightarrow Semiconductor^{*} \tag{1.3}$$

$$Semiconductor^{*} + H_2O \rightarrow Semiconductor^{*} + H^{+} + OH \tag{1.4}$$

$$OH + Dye\ Molecule \rightarrow Intermedietes \rightarrow CO_2 + H_2O + Mineral\ Salts \tag{1.5}$$

In this stepped reaction, the semiconductor is first excited by light ($Semiconductor^{*}$) electrolyzing water molecules adsorbed on its surface, then the OH radicals produced will react with the dye molecules and will eventually lead to the formation of CO_2 and mineral salts. These mineral salts, as well as the intermediate byproducts, must be well identified and their formation should be carefully monitored and characterized in order to define the complete degradation process induced by a specific catalyst. Different catalyst may induce different degradation pathways resulting in different intermediates byproducts and mineral salts.

Nowadays, the degradation of organic dyes is not necessarily studied with the above-mentioned problematic in mind, but as a mean to demonstrate the photocatalytic capabilities (within limitations) of developing materials. In other words, the dyes no longer serve as the actual contaminants that have to be degraded in order to protect the environment from their toxicity, but rather as a tool for demonstrating the potential of a catalyst. In this frame, the

systematic study of intermediate products and mineralization is not of primary interest, since the first goal is to determine whether the new material is capable of accelerating redox reactions or not.

The evaluation of the photocatalytic response is commonly carried out by monitoring the kinetics of disappearance of the primary substance (*i.e.* the organic dye). This is typically done by measuring the change in the relative intensity of the absorption spectrum of the dye-charged solution over time. UV-Vis absorption spectrometry is the technique of choice to monitor the degradation of the dyes because it is non-expensive and easy to use. Additionally, studying the factors affecting the photocatalytic degradation rates is important. These factors include the initial dye concentration, the pH of the solution and the light intensity, among others.

The organic dyes that are more commonly used for evaluating photocatalytic responses are thiazine dyes (with a dominance of methylene blue) and xanthene dyes (with dominance of rhodamine B).

If the material in question happens to induce photocatalytic degradation on organic dyes, then further investigations must be performed in order to monitor intermediate products and mineralization processes, as well as testing different contaminants other than organic dyes.

f. Electro-oxidation of methanol in alkaline media and Direct Alkaline Methanol Fuel Cells (DAMFC)

Easy storage and handling, high-energy density and wide availability are features that make alcohols attractive as promising alternative power sources for transportation, portable electronics and stationary applications. Compared to the use of hydrogen in fuel cells, liquid alcohol fuels are easy to store and transport and the fact that the alcohol is being directly oxidized, also eliminates the heavy reformer needed to produce hydrogen from liquid or gaseous carbonaceous fuels. The device in which the direct oxidation of an alcohol is used as fuel are known as direct alcohol fuel cells in which the alcohol is oxidized at the anode in an acidic medium using a proton exchange membrane (PEM). However, it is known that for

many reactions, electrocatalysts perform better in alkaline electrolytes, and direct alkaline methanol fuel cells (DAMFC) take advantage of this fact. The selection of methanol as the alcohol to be oxidized is supported on the fact that methanol, with only one carbon in its molecule and no C-C bonds, is the simplest alcohol and this makes of the electro-oxidation of methanol relatively simple compared to the electro-oxidation of other alcohols.

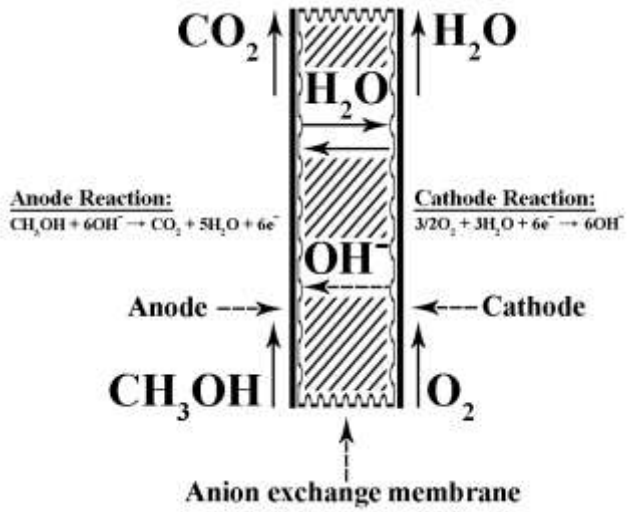

Fig. 1.5 *Schematic diagram of a direct alkaline fuel cell.*

Fig. 1.5 schematizes the principle of a direct methanol alkaline fuel cell, where on the anode, methanol is oxidized to carbon dioxide and electrons are produced, while on the cathode side, oxygen accepts electrons and is reduced to produce hydroxide ions. Hydroxide ions are then transferred through the electrolyte to the anode. The oxidation of methanol in the anode and the reduction of oxygen in the cathode are represented by equations (1.6) and (1.7), respectively.

$$CH_3OH + 6OH^- \rightarrow CO_2 + 5H_2O + 6e^- \quad (1.6)$$

$$(3/2)O_2 + 3H_2O + 6e^- \rightarrow 6OH^- \quad (1.7)$$

Equations (1.6) and (1.7) summarize in a very simple way the redox processes occurring in a direct alkaline methanol fuel cell, in which both reactions are necessary to maintain equilibrium. At the same time, a stable catalyst is crucial for the redox reaction to happen efficiently during long periods of time.

2. PROBLEM STATEMENT

As mentioned before, anatase TiO_2 fulfills all the requirements for an efficient photocatalyst. The minimum of its conduction band (E_{BC}) is sufficiently negative in the electrochemical scale for the photogenerated electrons to produce the reduction of the adsorbed species, and the maximum of its valence band is positive enough for the material to be a powerful oxidizing agent. Its band gap is larger than the standard Gibbs free energy change (1.23 eV) for water splitting, which allows it to separate water into H_2 and O_2 very efficiently under UV irradiation without the need of an external applied voltage. It shows very high stability in the presence of several different environments such as electrolyte solutions and in the presence of organic molecules. From all these characteristics, we may expect TiO_2 as the perfect material for photocatalysis. However, for its industrial application in either energy generation or the treatment of large amounts of water or air, TiO_2 remains inadequate because sunlight is very dispersed and thus, its energy density is low. In addition to that, its large band gap allows the harvesting of only a fraction of the sun spectrum. Because of this reasons, current research on the application of TiO_2 as a photocatalyst has left aside its application for water and air treatment, and instead, focused on degrading adsorbed species on two-dimensional surfaces, for which the weak UV light present in an ordinary environment would be a source of sufficient energy to clean surfaces with TiO_2 incorporation. These are the so-called self-cleaning surfaces.

Since TiO_2 has been proven not to be the best option to act as photocatalytic agent using sunlight for treating large quantities of water or air, the challenge remains open to find a suitable material able to perform efficient catalytic reactions under visible light irradiation.

3. IMPORTANCE OF THE WORK TO BE DEVELOPED

It has been established that the main limitation to implement TiO_2 to decontaminate large quantities of wastewater is due to titanium dioxide's large band gap that permits the harvesting of only UV light.

In principle, a material having its conduction and valence band edges well situated for oxidation or reduction, while maintaining a band gap smaller than 3 eV to be able to absorb visible light, is required for efficient photocatlysis under visible light radiation.

Many semiconducting materials, such as CdS and CdSe, with band gaps narrow enough to harvest light in the visible range, have been studied as photocatalysts, but their efficiency and stability were much lower than those of TiO_2.

$NiTiO_3$, having a sufficiently narrow band gap to harvest visible light, a great oxidizing potential (similar to that of TiO_2) and good chemical stability, is a promising candidate to be used to catalyze oxidation reactions in pollutants present in water.

As previously mentioned, regarding the optical characteristics of $NiTiO_3$, there are discrepancies with respect to the value of its band gap. Some publications report a band gap with a value in the range of 3 to 3.5 eV,[48–51] very similar to the band gap of TiO_2, but still visible-light activity is somehow reported.[51] Some other publications show that the value of the band gap for $NiTiO_3$ is located between 2.12 and 2.3 eV,[37,43,46,47] which is clearly suitable for visible-light photon absorption. These discrepancies suggest that insight into the optical characteristics of $NiTiO_3$ is still required.

From structural aspects, some questions remain open on the Raman vibrational active modes for this material and constitute a challenging task to deepen into these characteristics.

Thus, it is important to synthesize highly pure crystalline $NiTiO_3$, to characterize its physical peculiarities and properly understand the nature of those properties with the aim to identify the characteristics that promote efficient catalytic reactions.

4. OBJECTIVE OF THE WORK TO BE DEVELOPED

a. General objective

The general objective of this thesis work is the synthesis of highly pure and crystalline nickel titanate ($NiTiO_3$) powders and thin films, the characterization of their main physical features and testing the photocatalytic response of the synthesized materials.

b. Specific objectives

- Synthesizing $NiTiO_3$ powders by sol-gel and solid-state reaction and finding the best suitable technique based on its simplicity, cost and crystalline quality of the obtained materials.
- Growing crystalline $NiTiO_3$ thin films by radio frequency sputtering and optimizing the deposition conditions.
- Characterizing the synthesized materials in order to evaluate their physical properties and their suitability as potential photocatalysts.
- Conducting theoretical calculations in order to get insight into the physical properties of bulk and nanostructured $NiTiO_3$.
- Quantitative analysis of the physical properties of $NiTiO_3$ by correlating the experimental and the theoretical investigations.
- Testing $NiTiO_3$ as a photocatalyst by the degradation of methylene blue in charged solutions under visible light irradiation.
- Evaluating the electro-oxidation of methanol in alkaline medium using $NiTiO_3$ as anode in a three-electrode cell.

The realization of the specified objectives will help to bring insight into the understanding of the physical properties of nickel titanate and to clarify some possible misconceptions found in the literature concerning the electronic transitions and vibrational properties of $NiTiO_3$ in its ilmenite crystal structure. It will also demonstrate the potential of $NiTiO_3$ to induce visible light driven heterogeneous photocatalysis through the degradation of organic dyes, such as methylene blue, under visible light irradiation. Finally, it will also address the possibility to use $NiTiO_3$ in order to electro-oxidize methanol and the feasibility to implement it as anode in direct alkaline methanol fuel cells.

CHAPTER II - THEORETICAL CALCULATIONS

The study of nanosized systems, with regard to the critical role of the specific active surface in physical phenomena, is of great interest. The interface between the active material and the surrounding environment contributes critically to the efficiency of heterogeneous catalysis. Simultaneously, with a decrease of particle size the specific surface area of the catalyst increases and the charge transfer, between the catalyst and the pollutants molecules to be reduced or oxidized, is improved. In this case, the understanding of catalyst properties following their size dimensions decreasing to certain limit is very important. More precisely, the electronic and optical properties of catalytic materials are strongly affected by the size reduction due to quantum confinement size effect, and as a consequence, these properties significantly differ from the behavior of the bulk material. From the other side the efficiency of a photocatalytic reaction is directly related to the electronic and optical properties of the catalyst. Having a clear understanding of these features is of special interest and it may be realized with the support of computer modeling and quantum chemical simulations. As starting point, the modeling of bulk systems is important for development of the methodology to simulate structural, vibrational and electronic properties of nanostructures.

Previously, the related properties of several titanate oxides were investigated experimentally and theoretically. Among them, natural mineral as the $FeTiO_3$ was widely studied. The mentioned material is major source of titanium for the commercial production of TiO_2. The electronic, magnetic, structural and elastic properties of bulk $FeTiO_3$ have been computed using the density functional theory (DFT) formalism and ab initio methodologies.[53–55] Within such approaches, the electronic ground-state properties and the charge transfer processes involved in $FeTiO_3$ were determined by the strong coupling of the structure with the charge distribution. It has been found that the quantum-mechanical description of these features is very sensitive to the treatment of electronic exchange and correlation energies. This suggests that titanates are strongly correlated systems, and therefore the electron correlation part should be taken into account sufficiently.

In this chapter, the structural, electronic, optical and vibrational properties of bulk $NiTiO_3$ and nanostructured $(NiTiO_3)_n$ clusters are calculated by numerical models based on DFT and semi-empirical quantum chemistry codes. The quantum chemical calculations for the bulk

crystal were based on first-principles calculations using the ultrasoft pseudopotential of the plane wave methodology within the DFT formalism. The generalized gradient approximation extended by Hubbard parameters (GGA+U) was used to evaluate the electronic properties of the $NiTiO_3$ bulk crystal.

The clusters were built by using the initial atomic positions of crystalline ilmenite structure. The position of atoms was relaxed to ensure stable and energetically favorable geometries. The semi-empirical PM6 parameterization method was used to evaluate the HOMO–LUMO energy differences versus size of nanocrystals. The quantum confinement effect was exhibited following reduction of cluster size. Theoretically obtained UV-Vis absorption and Raman spectra show drastic influence of the surface characteristics on the electronic and the vibrational properties of the nanoclusters. Investigated changes in electronic and vibrational properties of nanoparticles were accurately described as a function of their structural features. Also the surface influence on the physical properties of clusters was demonstrated. The simulation of the electronic band structures clarified the charge transfer characteristics. The proposed approach paves the way to elucidating the mechanisms behind the photocatalytic activity of the nanosized $NiTiO_3$ materials. The theoretically obtained data were compared to the experimentally measured results described in further chapters.

CHAPTER II

1. THEORETICAL METHODOLOGIES BACKGROUND AND COMPUTATIONAL DETAILS

a. Density Functional Theory (DFT)

Density functional theory (DFT) is a computational quantum mechanical modeling method used in physics, chemistry and materials science to investigate the electronic and structural properties of many-body systems. The mentioned properties of a many-electron system can be determined by using different functionals describing a spatially dependent electron density.

The methodology of the DFT is based on two fundamental mathematical theorems proved by Kohn and Hohenberg and on equations implemented by Kohn and Sham. The first Hohenberg and Kohn theorem says that: "*The ground-state energy from the Schrodinger's equation is a unique functional of the electron density*". In other words, the ground-state electron density uniquely determines all properties of the many-body electron system. The second Hohenberg-Kohn theorem determine an important property of the functional as follow: "*The electron density that minimizes the energy of the overall functional is the true electron density corresponding to the full solution of the Schrodinger's equation*". Unfortunately, the mentioned functional is not known and depends on many parameters that are crucial for the system.

Starting from the first Hohenberg and Kohn theorem, one may describe a system by the known energy ($E_{known}[\{\psi_i\}]$), which takes involves the electron kinetic energy, the Coulomb interactions between the electrons and the nuclei, the Coulomb interactions between pairs of electrons and the Coulomb interactions between pairs of nuclei. Additionally, it should be added the energy described by the exchange-correlation functional ($E_{XC}[\{\psi_i\}]$). whose exact expression is unknown. Following the mentioned definition, the energy of the system can be described by the expression:

$$(E[\{\psi_i\}]) = (E_{known}[\{\psi_i\}]) + (E_{XC}[\{\psi_i\}]) \tag{2.1}$$

Finding the minimum energy solutions of the total energy functional (2.1) is not guaranteed to be easier than solving the Schrodinger's equation involving wave functions. To attend this

problem, Kohn and Sham proved that finding the right electron density could be expressed by solving a set of one electron equations. These are the so-called Kohn-Sham equations. The structure of the Kohn-Sham equations is in principle identical to the full Schrodinger's equation. The summations go through the electrons in the system. Thus, the solutions of the Kohn-Sham equations are single-electron wave functions that depend only on three spatial variables.

$$\left[\frac{h^2}{2m}\nabla^2 + V(r) + V_H(r) + V_{XC}(r)\right]\psi_i(r) = \epsilon_i\psi_i(r) \qquad (2.2)$$

In the Kohn-Sham equations (2.2) appear three potentials, $V(\boldsymbol{r})$, $V_H(\boldsymbol{r})$ and $V_{XC}(\boldsymbol{r})$. The first one defines the interaction between an electron and the collection of atomic nuclei. The second is called the Hartree potential and describes the Coulomb repulsion between the electron being considered in the Kohn-Sham equations and the total electron density defined by all electrons in the system. Because the electron considered in the Kohn-Sham equations is part of the total electron density, the Hartree potential involves a self-interaction between the electrons. The self-interaction is unphysical, and the correction for it is one of the effects that are lumped together into the third potential in the Kohn-Sham equations, which defines the exchange and correlation contributions to the single-electron equations.

b. Local Density Approximation (LDA)

Since the true form of the exchange–correlation functional, whose existence is guaranteed by the Hohenberg–Kohn theorems, is simply not known, an approximation is needed in order to be able to solve the Kohn-Sham equations. Fortunately, there is one case where this functional can be derived exactly. It is the uniform electron gas. In this situation, the electron density is constant at all points in space. The uniform electron gas provides a practical way to actually use the Kohn–Sham equations. To do this, the exchange–correlation potential at each position is set to be the known exchange–correlation potential from the uniform electron gas. This approximation uses only the local density to define the approximate

exchange-correlation functional and give us a way to completely define the Kohn-Sham equations.

c. Generalized Gradient Approximation (GGA)

The physical idea behind the GGA is that real electron densities are not uniform, so including information on the spatial variation in the electron density can create a functional with greater flexibility to describe real materials. The equations on which the GGA are based are valid for slowly varying densities. In the GGA, the exchange–correlation functional is expressed using both the local electron density and gradient in the electron density. Non-empirical GGA functionals satisfy the uniform density limit. Different functionals might give different results for any particular configuration of atoms. It is important to select the functional that best suits the characteristics of the system. An example of a non-empirical GGA functional is the Perdew-Burke-Ernzerhof (PBE) functional.

d. DFT+U Theory

The basic idea behind DFT+U is to treat the strong on-site Coulomb interaction of localized electrons, which is not correctly described by LDA or GGA approximations. The on-site Coulomb interactions are particularly strong for localized d and f electrons, but can be also important for p localized orbitals. The strength of the on-site interactions is usually described by Hubbard parameters U (on-site Coulomb) and J (on-site exchange). These parameters U and J can be extracted from ab-initio calculations, but usually are obtained semi-empirically.

The DFT+U corrections can be introduced in quantum chemical calculations in different ways. In Liechtenstein et al.[56] model the U and J enter as independent corrections in the calculations. The one proposed by Anasimov et al.,[57,58] defines only single effective $U_{eff} = U - J$ parameter accounts for the Coulomb interaction, neglecting thereby any higher multi-polar terms.

e. Semi-empirical Parametrization Method (PM6)

Semi-empirical methods are simplified versions of Hartree-Fock theory using empirical (derived from experimental data) corrections in order to shorter the calculation time and to improve performance. These methods are usually referred to through acronyms encoding some of the underlying theoretical assumptions. The most frequently used methods (MNDO, AM1, PM3) are all based on the Neglect of Differential Diatomic Overlap (NDDO) integral approximation. All three approaches belong to the class of Zero Differential Overlap (ZDO) methods, in which all two-electron integrals involving two-center charge distributions are neglected. A number of additional approximations are made to speed up calculations and a number of parameterized corrections. How the parameterization is performed characterizes the particular semi-empirical method. For MNDO, AM1, and PM3 the parameterization is performed in the way that the calculated energies are expressed as heats of formations instead of total energies.

PM6 is an extended and re-parameterized version of PM3 and it includes d-orbitals for second-row and higher elements. The PM6 parameterization has the capability to carry out calculations on molecules containing transition metals on elements up trough bismuth (excluding the rare earths). Some of the most important aspects of PM6 that differ from previous work include: careful examination and pruning of the experimental data to ensure quality and consistency, use of *ab initio* and DFT results where experimental data is lacking, inclusion of new experimental data in parameterization, addition of many pairwise interaction terms that adjust the core repulsion function, new method for computing 1-center 2-electron integrals for TMs, molecular mechanics correction terms for certain difficult cases. The general performance of PM6 is better than that for other semi-empirical methodologies.

f. Computational details and cluster building methodology

The crystal structures were computed for two different configurations of the material. One of them was considered to represent the bulk $NiTiO_3$ monocrystal crystallized in the ilmenite

phase; *i.e.* space group $R\bar{3}$ (no. 148).[59] The second was chosen to be a nanocrystalline cluster of varying size, possessing the ilmenite structure in the core. Therefore, the unit cell of ilmenite $NiTiO_3$ was built using the cell parameters a = b = 5.0289 Å, c = 13.7954 Å and the angular parameters α = β = 90° and γ = 120°. The positions of representative atoms within the unit cell are summarized in Table 2.1.

Table 2.1 *Lattice parameters and atomic fractional coordinates of the $NiTiO_3$ crystal structures*

Atom	**Atomic positions**		
	x/a	**y/b**	**z/c**
Ni	0	0	0.3499(1)
Ti	0	0	0.1441(1)
O	0.3263(7)	0.0214(10)	0.2430(3)
Cell parameters	a = b = 5.0289(1) Å α = β = 90°	c = 13.7954(2) Å γ = 120°	
Space group	$R\bar{3}$ (no. 148)		

The crystal structure of $NiTiO_3$ was built using the Materials Studio Program Package. The same simulation software was used to build the $(NiTiO_3)_n$ nanostructures with diameters from 0.6 nm up to 2.6 nm, associated with clusters composed of $(NiTiO_3)_2$ and $(NiTiO_3)_{183}$ units, respectively. Consequently, all of the investigated nanocrystals exhibited spherical shapes and stoichiometric compositions. According to a previous work on other classes of nanocrystalline systems by Makowska-Janusik et al.[60] dangling bonds were not specially saturated. The unit cell of the monocrystal and the morphology of the $(NiTiO_3)_{82}$ cluster are depicted in Fig. 2.1.

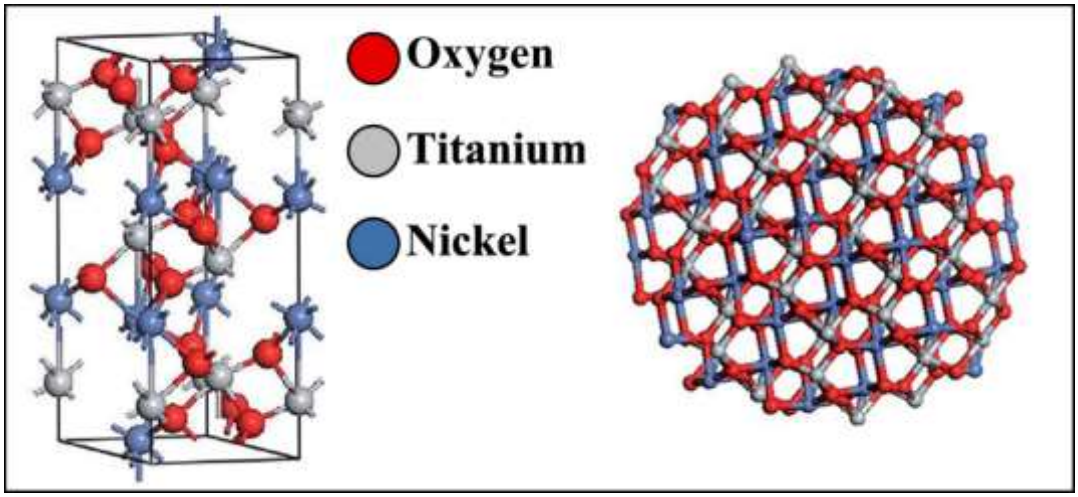

Fig. 2.1 *The unit cell of crystalline $NiTiO_3$ (left) and the unpassivated nanocrystalline structure made by the formula $(NiTiO_3)_{82}$ (right).*

The electronic properties of the $NiTiO_3$ single crystal were calculated using the DFT methodology. The quantum chemical calculations were performed using the Cambridge Serial Total Energy Package (CASTEP);[61] *i.e.* the module of the Materials Studio Program. The CASTEP is based on the evaluation and analysis of the total energy inferred from the plane-wave pseudopotential method. The first task deals with the geometry optimization of the investigated crystal structure, which is built and evaluated with respect to the total energy minimization within the Broyden–Fletcher–Goldfarb–Shanno (BFGS) algorithm.[62] During the geometry optimization procedure, the symmetry of the structure was frozen but the size of the unit cell was allowed to change. The convergence criteria for the optimization procedure were chosen as hereafter outlined. The convergence of the total energy during the geometry optimization procedure cannot be greater than 2×10^{-5} eV per atom, the force on the atom must be less than 0.01 eV $Å^{-1}$, the stress on the atom less than 0.02 GPa and the maximal atomic displacement no more than 5×10^{-4} Å. The electron exchange–correlation energy was treated within the framework of the generalized gradient approximation (GGA) using Perdew–Burke–Ernzerhof (PBE) potential.[63] To accelerate the computational runs, the ultrasoft pseudopotential formalism was used. In this frame, calculations were performed for Ti ($3d^2$ $4s^2$), Ni ($3d^8$ $4s^2$) and O ($2s^2$ $2p^4$) electrons. The cut-off energy of the plane-wave basis set was chosen to be equal to 500 eV. The integration by numerical sampling for specific directions over the Brillouin zone (BZ) were carried out using the Monkhorst–Pack

method with an 8 x 8 x 8 special *k*-point mesh. The total energy convergence criterion was assumed to be fulfilled when the self-consistent field (SCF) tolerance; *i.e.* equal to 10^{-5} eV per atom.

The electronic properties of the $NiTiO_3$ crystal were computed using the above-mentioned parameters, as specified for the geometry optimization procedure. The calculations were carried out in spin restricted as well as spin unrestricted procedures, applying the GGA/PBE potential and Heyd–Scuseria–Ernzerhof (HSE06) range-separated hybrid functional.[64,65] Hummer et al.[66] showed that the HSE06 functional yields the correct electronic band structure for the semiconductors of group-IV. Also the work of Spiewak et al.[67] shows that the HSE06 potential may better reproduce the electronic properties of Ge single crystals with defects. Contrary to this, other works indicate that the range-separated functionals show improvements for strong charge transfer systems.[68,69] It is generally known that classical DFT potentials do not correctly reproduce far-nucleus asymptotic behaviour[70,71] and underestimate the excitation energies, notably for charge transfer processes.[72] The range-separated potentials lead to the partitioning of the total exchange energy into short-range and long-range contributions:

$$E_x = E_x^{sr} + E_x^{lr} \tag{2.3}$$

To improve the exchange functional, in terms of calculating the long-range electron–electron interactions using the HF exchange integral, the standard error function is used. The repulsion electron operator is also divided into short-range and long-range parts and can be defined for two electrons at the r_{ij} distance as:

$$\frac{1}{r_{ij}} = \frac{1 - [\alpha - \beta \mathrm{erf}(\mu r_{ij})]}{r_{ij}} + \frac{\alpha - \beta \mathrm{erf}(\mu r_{ij})}{r_{ij}} \tag{2.4}$$

where the α and β parameters define the exact exchange percentages between the short and long-range exchange functional. μ represents the weighting factor, which controls the separation between the short-range exchange functional and the long-range part of the HF exchange integral.

The Kohn–Sham equation was also solved using the GGA/PBE functional extended by the Hubbard parameters. The introduced methodology contributes to precise insights into the electronic properties of the material. The major drawback of all functionals lies in the underestimation of the calculated electronic band gap.[73] This is frequently encountered due

to the approximate calculations of the electron self-interaction energies. Also, pure local density approximations (LDA),[74] generalized gradient approximations (GGA)[75] and even hybrid functionals[64,76,77] can lack precision in some instances, due to the so-called "strongly correlated" systems.

One relevant solution for describing correlated electrons in solids concerns the Hubbard model,[57] based on an extended LDA approach, also referred to as LDA+U. It decreases the electron self-interaction error by selectively adding an energy correction to localized electron states, such as d or f orbitals where the self-interaction is particularly large. To construct an appropriate functional, the LDA+U approach subdivides the charge density into two subsystems with delocalized and localized features. In the multiband Hubbard model the effective LDA+U energy functional is written as:

$$E_{LDA+U} = E_{LDA} + E_{HF}(n_{\mu\nu}) - E_{dc}(n_{\mu\nu}) \quad (2.5)$$

where E_{LDA} denotes the standard LDA energy functional, E_{HF} is the Hartree–Fock (HF) functional, E_{dc} is the double counting term and $n_{\mu\nu}$ is one particle density matrix. The HF part can be written as follows:

$$E_{HF}(n_{\mu\nu}) = \frac{1}{2}\sum (U_{1324} - U_{1342}) n_{12} n_{34} \quad (2.6)$$

where the U_{1324} terms represent the renormalized Coulomb integrals. In the LDA+U approach, the Kohn–Sham equation is supplemented by the non-local potential. On the other hand, the DFT/Hubbard method fails to compute the correct energy difference between systems with localized/correlated and delocalized/uncorrelated electronic states.[78] In such an approach, the LDA/GGA+U methodology has successfully been applied to compute the electronic properties of different ternary oxides, such as $CuAlO_2$,[79] $CuAl_2O_4$,[80] $Pr_2Ti_2O_7$ or $Ce_2Ti_2O_7$,[81] and $MnFe_2O_4$.[82] Based on the outlined theoretical framework, the influence of the Hubbard parameter U on the electronic properties of $NiTiO_3$ was investigated for the crystalline structure in bulk material or in nanosized clusters, taking into account the strong correlation of the d-orbital electrons.

In the present work, the electronic properties of the $(NiTiO_3)_n$ nanoclusters were calculated. The methodology requires two different calculation codes to perform the simulations and also to ensure their stability. Thus, the Gaussian09 and MOPAC (Molecular Orbital PACkage)[83] quantum chemistry programs were used. With regard to the size of the

investigated clusters, semi-empirical single point calculations were performed, applying the parameterized self-consistent restricted HF (SCF RHF) PM6 method.[84] The convergence of the SCF procedure was achieved with an energy uncertainty not greater than 10^{-6} hartrees and no more than 150 required iterations. Within such approaches, the electronic properties of two different cluster families were computed. The first one deals with $(NiTiO_3)_n$ clusters possessing an ilmenite crystal structure without any reconstruction. The second considers the same clusters as specified previously, but their geometries were optimized according to the total energy minimization. The geometry of all clusters was specified in Cartesian coordinates with C_1 symmetry. The gradient convergence tolerance was equal to 10^{-6} hartrees $bohr^{-1}$ using the quadratic approximation (QA) method,[85–87] updating the Hessian matrix during the optimization. The Hessian evaluation was performed to exclude the structures giving rise to negative frequency modes.

2. STRUCTURE AND ELECTRONIC PROPERTIES OF BULK ILMENITE $NiTiO_3$

The GGA/PBE functional was used to build the stable $NiTiO_3$ crystal geometry and to calculate the related physical responses. In the first step, the geometry optimization of the crystal structure was performed. The changes to the optimized atomic distances were less than 5% compared to the starting values from the defined crystallographic data. It is in agreement with the former report by Xin et al.[88] The noticed departures from these values could be attributed to the fact that the present calculations were performed at T = 0 K, whereas the experimental structural data measurements were generally performed at room temperature. Thus, the relatively low deviation between the optimized values and experimental structural data indicates that GGA/PBE is a suitable computational functional for the description of the structures of the $NiTiO_3$ crystal. Following the performed geometry optimization, one may conclude that the ilmenite $NiTiO_3$ structure appears as the layered organization depicted in Fig. 2.2 (left-hand panel), where Ti and Ni atoms form the layers separated by oxygen atoms.

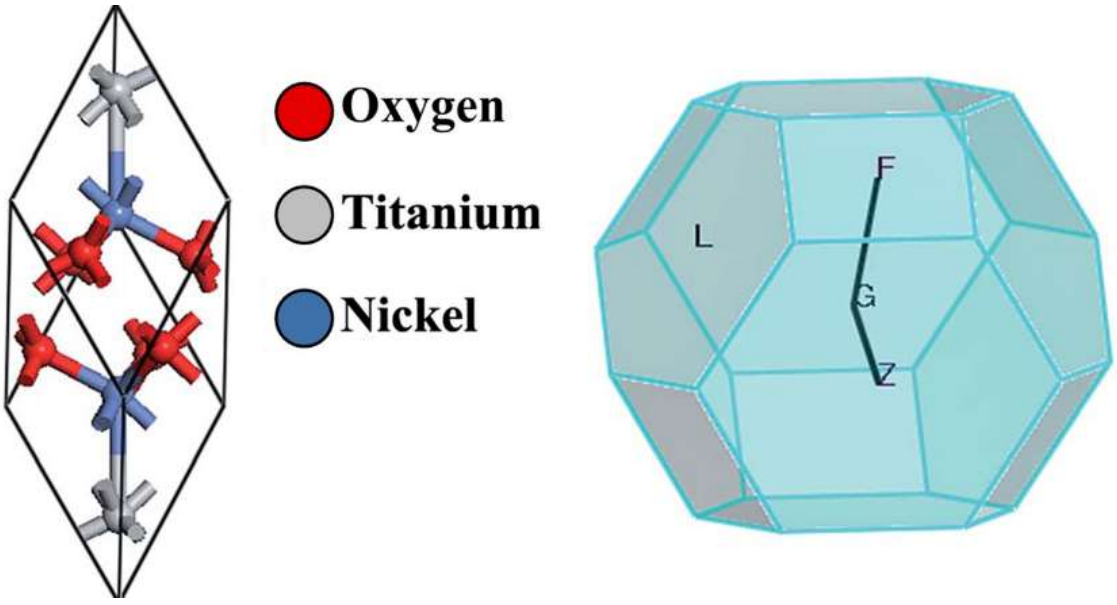

Fig. 2.2 *Primitive unit cell of $NiTiO_3$ (left) and the corresponding reciprocal lattice (right) with the coordinates of the special points of the BZ: F (1/2, 1/2, 0); G (0, 0, 0); K (1/4, 1/4, 1/4) and Z (1/2, 1/2, 1/2).*

The electronic properties of the $NiTiO_3$ crystal were computed within the spin polarized approach for a primitive unit cell (see Fig. 2.2). The band structure calculations were performed in the *k* space within the BZ directions shown in Fig. 2.2 (right-hand panel). The DFT/HSE06 functional gives unsatisfactory results. The obtained energy gap is equal to 1.23 eV, whereas the experimental data are within 2.18-2.3 eV.[47,89,90] Also, the DFT/PBE functional was considered with and without the Hubbard approximation. The mentioned functional without the Hubbard approximation and in the spin polarized regime gives an energy gap equal to 0.77 eV for the $NiTiO_3$ crystal. This shows that using non-empirically tuned range-separated DFT methods results in a significant improvement over traditional GGA functionals but does not give good results for the studied crystal. The large discrepancies suggest the presence of strongly correlated electrons from the considered (Ti and Ni) ions, leading to the necessity to explore the Hubbard approximation in such systems. Within the approach based on the DFT/PBE potential, the electron density depicted in Fig. 2.3 also informs us about the covalent character of the O–Ti, O–Ni and Ti–Ni bonds. This behavior indicates the nature of the strongly correlated system and the necessity to develop the theoretical functional to reconcile the predicted electronic features with the experimental findings.

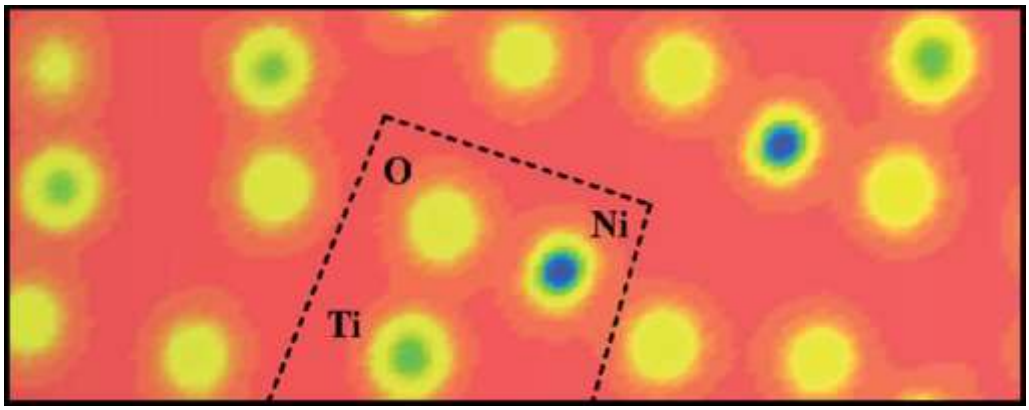

Fig. 2.3 *Electron density projection in a selected plane of the $NiTiO_3$ ilmenite structure.*

The functional modified by the Hubbard approximation uses parameters that can be chosen for Ti 3d and Ni 3d valence electrons in order to evaluate the energy band gap values. The influence of the chosen Hubbard parameter U on the obtained band gaps is demonstrated in the summary in Table 2.2.

Table 2.2 *Hubbard U parameter values for the Ti d and Ni d orbitals and the energy gap value calculated by the DFT/PBE + U methodology*

Ti 3d	Ni 3d	E_g[eV]
0	0	0.77
2.5	2.5	1.75
3.5	4.5	2.33
4.5	3.5	1.94
4.5	4.5	2.46

The correct evaluation of the electronic behavior, in agreement with experimental findings, requires fixed Hubbard parameters at 3.5 eV and 4.5 eV for Ti 3d and Ni 3d electrons, respectively. Thus, the DFT/PBE + U method may provide a satisfactory qualitative electronic structure calculation with the correct choice of the Hubbard parameters. The electronic band structure computed with U_{Ti} = 3.5 eV and U_{Ni} = 4.5 eV is presented in Fig. 2.4.

This plot indicates that the $NiTiO_3$ structure exhibits a direct semiconducting nature with an energy gap equal to 2.33 eV. Its spin polarized character is also included in the predicted electronic features. Thus, the top of the valence band is constituted by spin polarized alpha electrons while the bottom of the conduction band is composed of the beta state. In addition, the partial density of states depicted in Fig. 2.5 shows that the spin polarized alpha electrons with energies at the top of the valence band derive from the hybridization of Ni 3d and O 2p orbitals; while hybridization of the Ti 3d and Ni 3d states defines the electronic structure at the bottom of the conduction band, in agreement with the previous work of Salvador et al.[91]

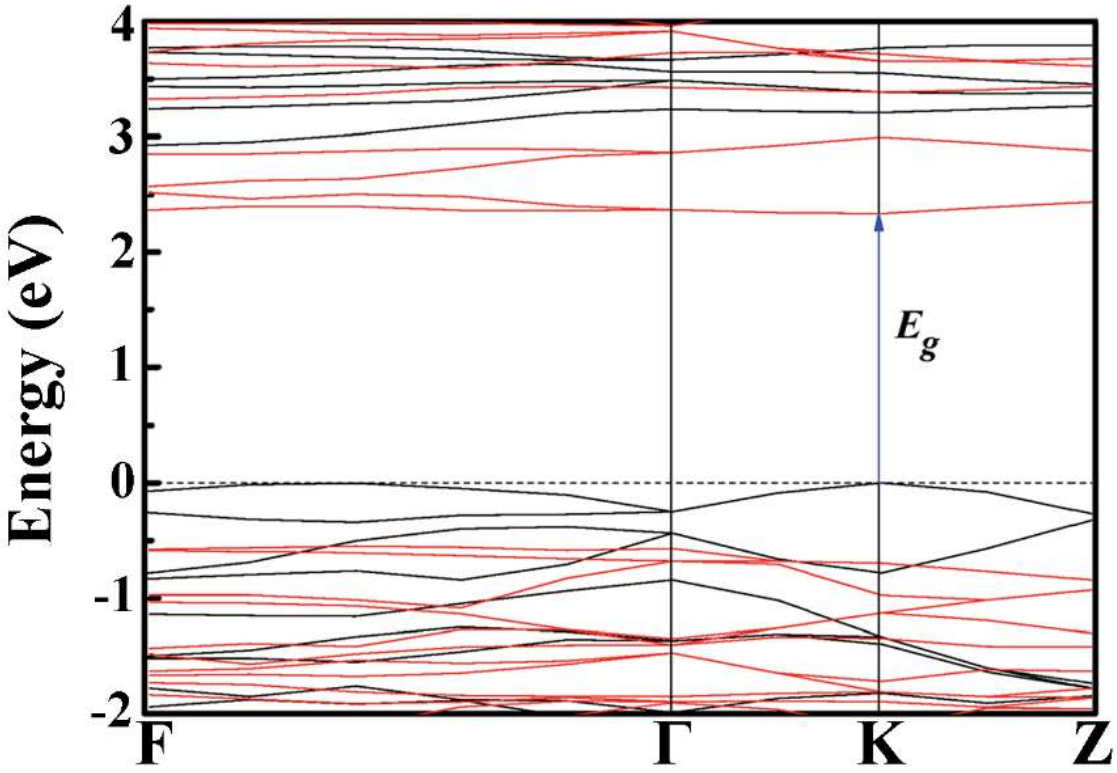

Fig. 2.4 *Electron band structure calculated by the DFT/PBE functional within the Hubbard approximation U. The energy levels with spin polarized alpha electrons (black) and energy levels with a beta state (red) are shown.*

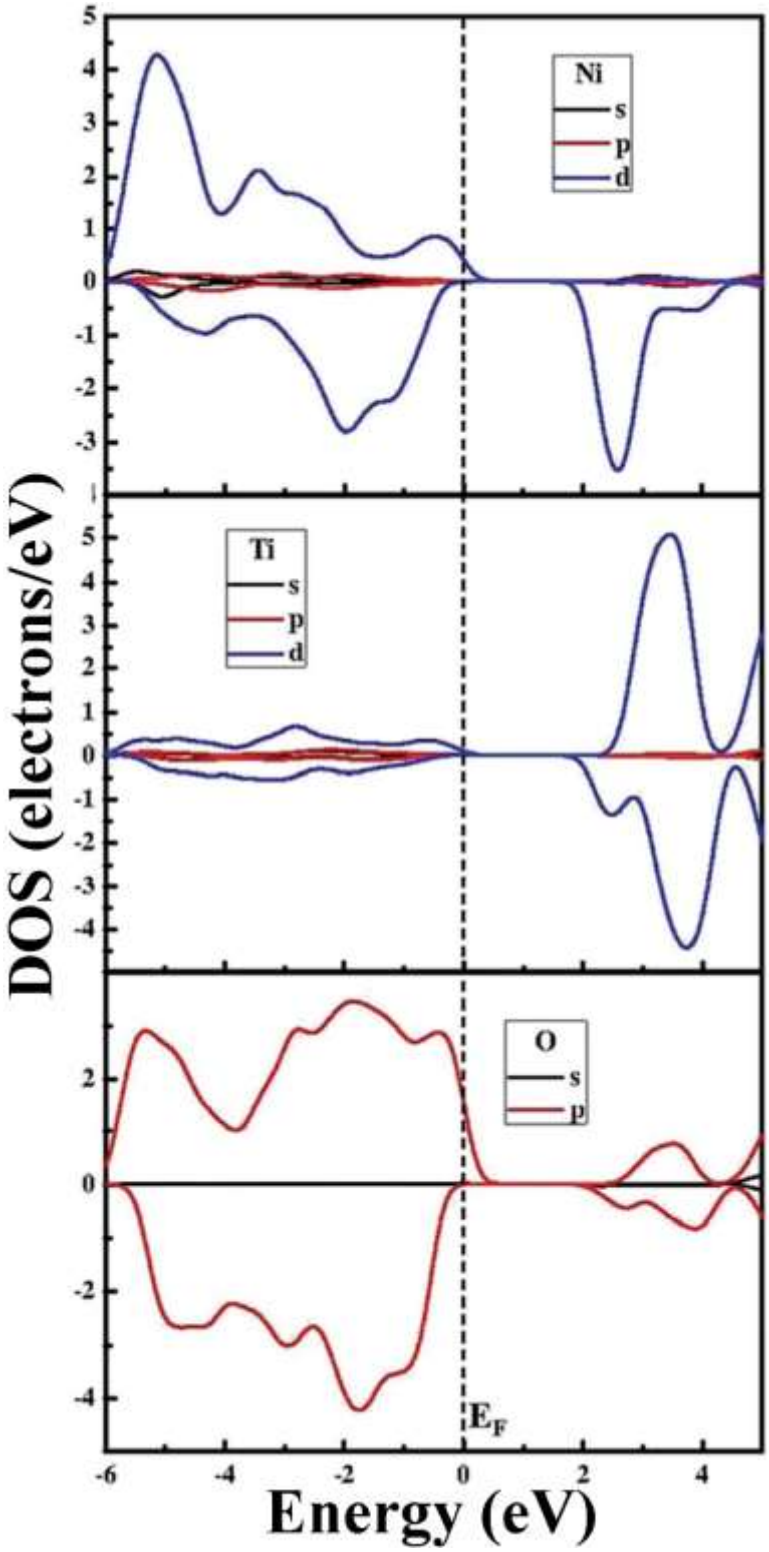

Fig. 2.5 *Electron density of state (DOS) calculated for the $NiTiO_3$ ilmenite structure by using the DFT/PBE functional augmented by the Hubbard approximation: polarized alpha electrons (top) and beta electrons (bottom).*

The energy dispersion of the electronic states allows us to calculate the effective masses of charge carriers. The diagonal elements of the effective mass tensor for electrons and holes are calculated as the energy derivatives around the K point of the BZ, following the equations:

$$\frac{1}{m^*_{e_{ij}}} = \frac{1}{\hbar^2}\frac{\partial^2 E_c(k)}{\partial k_i \partial k_j} \; and \; \frac{1}{m^*_{h_{ij}}} = \frac{1}{\hbar^2}\frac{\partial^2 E_v(k)}{\partial k_i \partial k_j} \tag{2.7}$$

The effective mass of electrons and holes is determined by fitting the conduction and valence bands (see Fig. 2.4), respectively, to parabolic functions. One may see that the top of the valence band and bottom of the conduction band are symmetric around the K point of the BZ. In this case, the calculated effective masses of the electrons and holes are equal to $m_e^* = 2.0986 m_e$ and $m_h^* = 0.683 m_e$, with the same values in both the K–Z and K–Γ directions of the BZ. The relatively high values of the reported parameters suggest that the mobility of charges in the investigated $NiTiO_3$ single crystal is relatively low. This result is of particular importance for the very low electrical conductivity (10^{-9} S m^{-1}) achieved in $NiTiO_3$ at moderate temperatures up to 200 °C.[37] The performed calculations confirm that in the studied material the electrical conduction observed at temperatures below 700 K seems to be extrinsic, governed by impurities, interstitial sites, etc. It takes place via the small polaron hopping mechanism.[89]

3. NANOCRYSTALLINE ILMENITE $NiTiO_3$ CLUSTERS

a. Structural and electronic features

Structural and electronic properties of $NiTiO_3$ nanocrystals were investigated for nanoparticles made of the ilmenite bulk material. The investigated nanostructures possess a spherical shape with a variable number of $(NiTiO_3)_n$ units, from n = 2 up to 183. The single point DFT/PBE and DFT/HSE06 calculations were performed for clusters with n from 2 up to 20, but the results did not show the correct behavior of the energy difference between the highest unoccupied molecular orbital (HOMO) and lowest unoccupied molecular orbital (LUMO) *versus* the size of the cluster. It is known that the standard DFT scheme is not useful for finite-sized objects because the asymptotic potential, absent in the bulk material, plays a crucial role in the cluster energy due to the addition and removal of electrons. This leads to the calculated energy gaps for finite-sized objects often being much smaller than the real gaps.[92] Contrary to the results obtained by DFT, the PM6 semi-empirical methodology was successfully applied for such clusters, leading to the correct estimation of the energy gap in nanosized $NiTiO_3$. In Fig. 2.6, the computed energy differences $\Delta E_{HOMO-LUMO}$ *versus* the cluster sizes are depicted. The reported energy gap splitting as a function of the $(NiTiO_3)_n$ units demonstrates the size induced quantum confinement effect. This is in agreement with the experimental report[51] on $NiTiO_3$ nanoparticles that give rise to a blue shift in the absorption spectra compared to the bulk material. The $\Delta E_{HOMO-LUMO}$ value reaches saturation for clusters comprising $n \geq 50$ $(NiTiO_3)_n$ units. The energy gap value for the large cluster saturates at 2.55 eV.

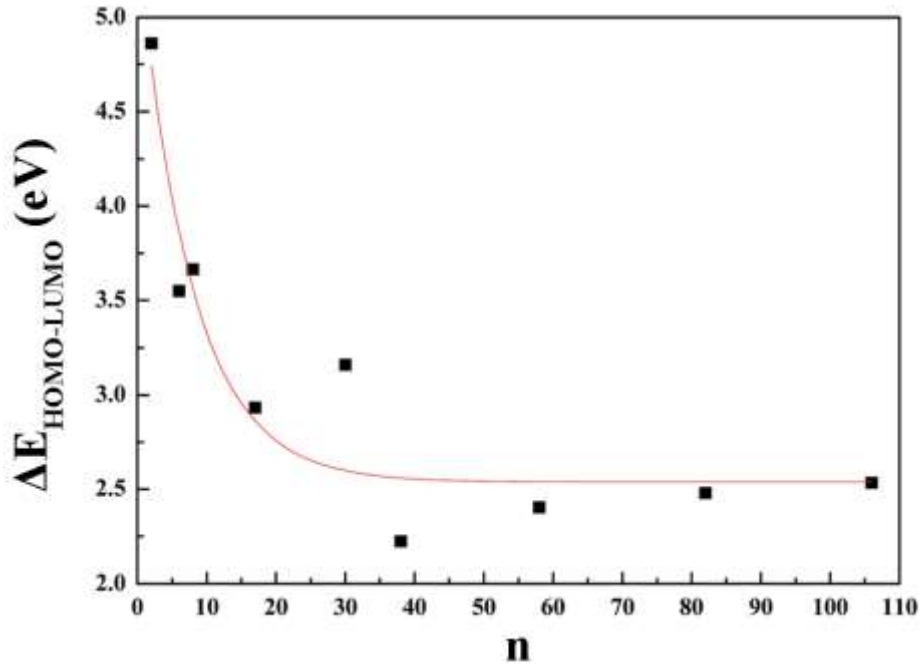

Fig. 2.6 *Evaluation of the $\Delta E_{HOMO-LUMO}$ energy splitting versus number n of $(NiTiO_3)_n$ units calculated by the PM6 methodology.*

Using the PM6 model, UV-Vis absorption spectra were computed for selected clusters, namely $(NiTiO_3)_2$, $(NiTiO_3)_8$ and $(NiTiO_3)_{17}$. Large clusters were not considered due to the memory limitations of the computer system. The calculated spectra are presented in Fig. 2.7, along with the experimental data. A good agreement is demonstrated between the spectrum calculated by the PM6 model for the $(NiTiO_3)_{17}$ cluster and the measured one for the crystalline powder of $NiTiO_3$. Increasing the cluster diameter (unit number n = 2–17), the position of the A band (see Fig. 2.7 left-hand panel) shifts to the red spectral range. The band labelled B, with pronounced intensity for small clusters, undergoes a red shift and decreases notably in intensity with increasing cluster size. For the cluster $(NiTiO_3)_{17}$ with a diameter of 1.20 nm an additional broad peak C develops in the range 750–900 nm. The broad band in that spectral range was also demonstrated experimentally.

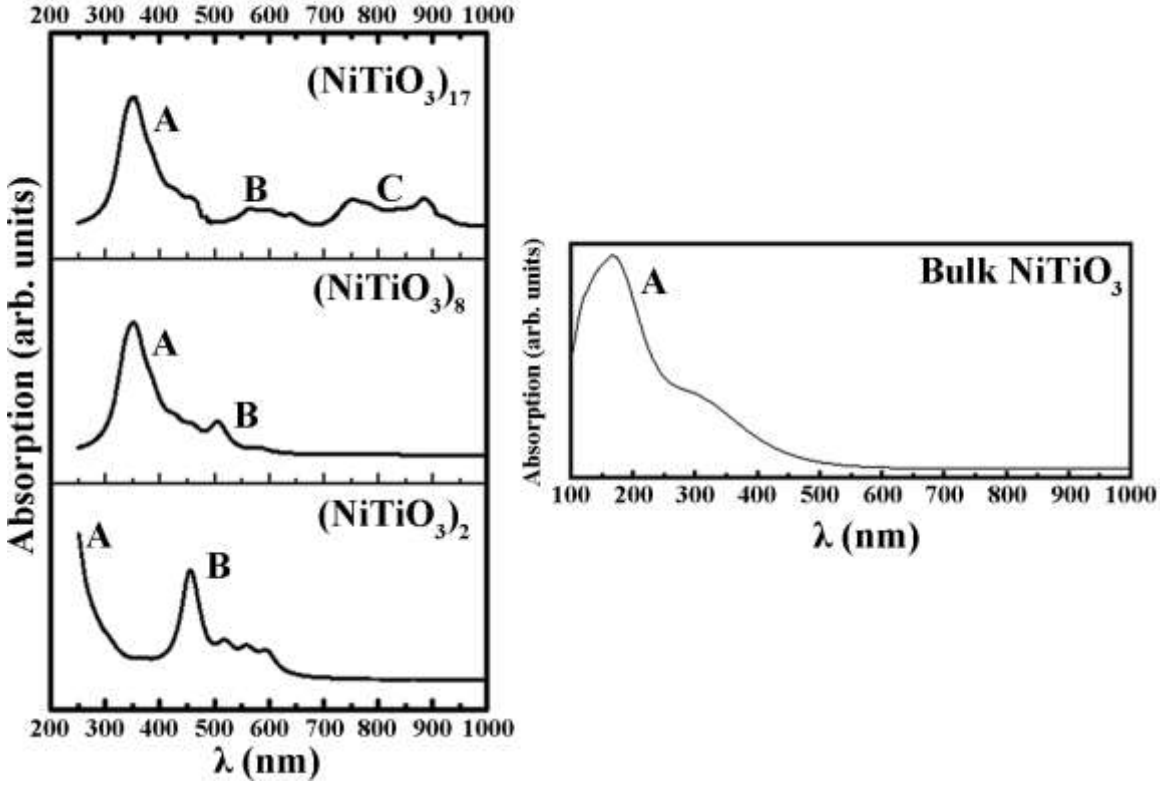

Fig. 2.7 *UV-Vis absorption spectra calculated by the PM6 model for different clusters (left-hand panel), and the spectrum calculated for the bulk crystal by using the DFT/PBE + U functional (right-hand panel).*

The UV-vis spectrum calculated for the bulk crystal $NiTiO_3$ by using the DFT/PBE + U functional (see Fig. 2.7, right-hand panel) did not match that obtained for the $(NiTiO_3)_{17}$ cluster in the high wavelength range, where the C band is involved. This confirms that the HOMO and LUMO orbitals separation, depicted in Fig. 2.8, contribute to the low energy absorption spectra. The separation feature between HOMO and LUMO orbitals is not seen for the bulk $NiTiO_3$, where the valence and conduction bands are attributed to the orbitals expanded through the volume of the crystal. The observed details suggest that the separation of the HOMO and LUMO orbitals gives rise to B and C bands.

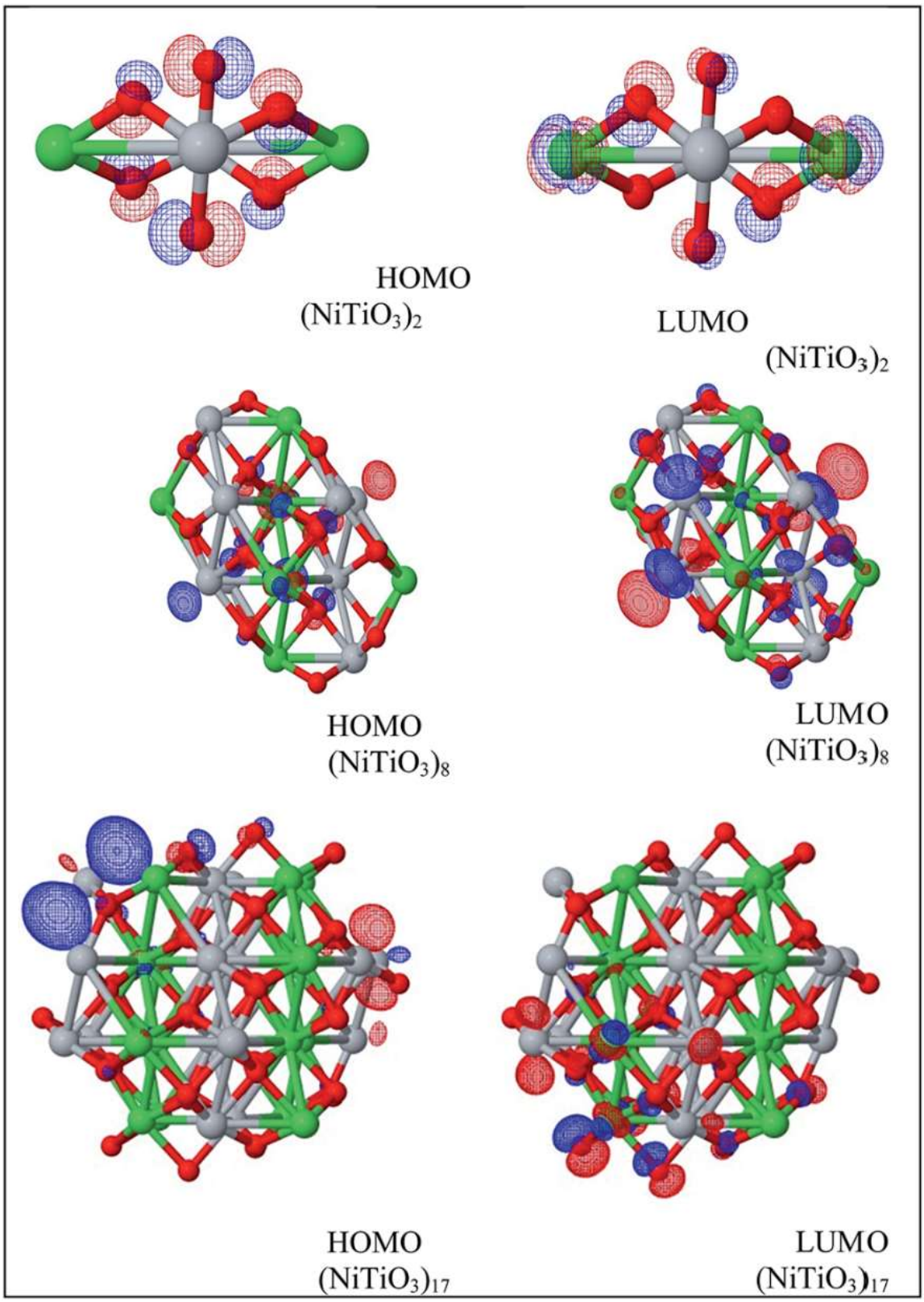

Fig. 2.8 *HOMO and LUMO orbitals calculated by the PM6 model for the $(NiTiO_3)_2$, $(NiTiO_3)_8$ and $(NiTiO_3)_{17}$ clusters.*

The theoretical UV-Vis absorption spectra of the $(NiTiO_3)_{17}$ nanocluster clearly indicates the interesting optical activity of the system in the UV and the visible range of the electromagnetic spectrum. A broad absorption edge situated at ~ 410 nm is associated with $O^{2-} \rightarrow Ti^{4+}$ charge transfer transitions. The higher wavelength shoulder is associated with the crystal field splitting of $NiTiO_3$, giving rise to the $Ni^{2+} \rightarrow Ti^{4+}$ transitions.[93] Thus, for the nanosized $NiTiO_3$, the photo-induced charge transfers that are required for photocatalytic reactions may be ensured by several electronic transitions covering the UV and visible light range. These contribute to the efficient photocatalytic activity. Finally, it is worth noting that the resolved details on the theoretical absorption spectra are induced by calculations performed without any influence from the temperature on the structural relaxation of the $NiTiO_3$ clusters. The possibility of reconciling the shapes of the absorption bands between the theory and experiments may be realized through the electron–phonon interactions and the Franck–Condon rule for the optical transition probabilities, as was used in our previous work.[94]

b. Raman spectroscopy of nanocrystalline $NiTiO_3$

Taking into account the effect of electron–phonon interactions, the evaluation of the Raman spectra related to the selected clusters were performed using the PM6 approach. The Raman spectra were calculated using the standard procedure implemented in the Gaussian program package. The calculations were performed on two $(NiTiO_3)_{17}$ clusters. In one of these, the ilmenite crystal structure was frozen and the other system possessed a surface reconstructed using the geometry optimization procedure according to the total energy minimization criterion. The last cluster was characterized by a completely amorphous network. The calculated Raman spectra modeled for the $(NiTiO_3)_{17}$ nanoclusters are depicted in Fig. 2.9.
For the cluster $(NiTiO_3)_{17}$ with a primarily ilmenite structure, the calculations show only a single mode at position C. The experimental Raman spectrum shows an intense band with a wavenumber position in agreement with the calculated value.
The C band is also the most intense detail in the experimental Raman spectrum. The titanates, such as $NiTiO_3$, $CoTiO_3$ and Na_4TiO_4, possess hexa-coordinated Ti–O–Ti groups and their Raman modes are associated with the main band, located at 705, 688, 737 cm^{-1},

respectively.[95–98] Therefore, it was established that the Ti–O–Ti stretching mode should appear in the vicinity of 700 cm^{-1}. For $NiTiO_3$, the band at 720 cm^{-1} corresponds to the Ti–O–Ti vibration of the crystal structure.

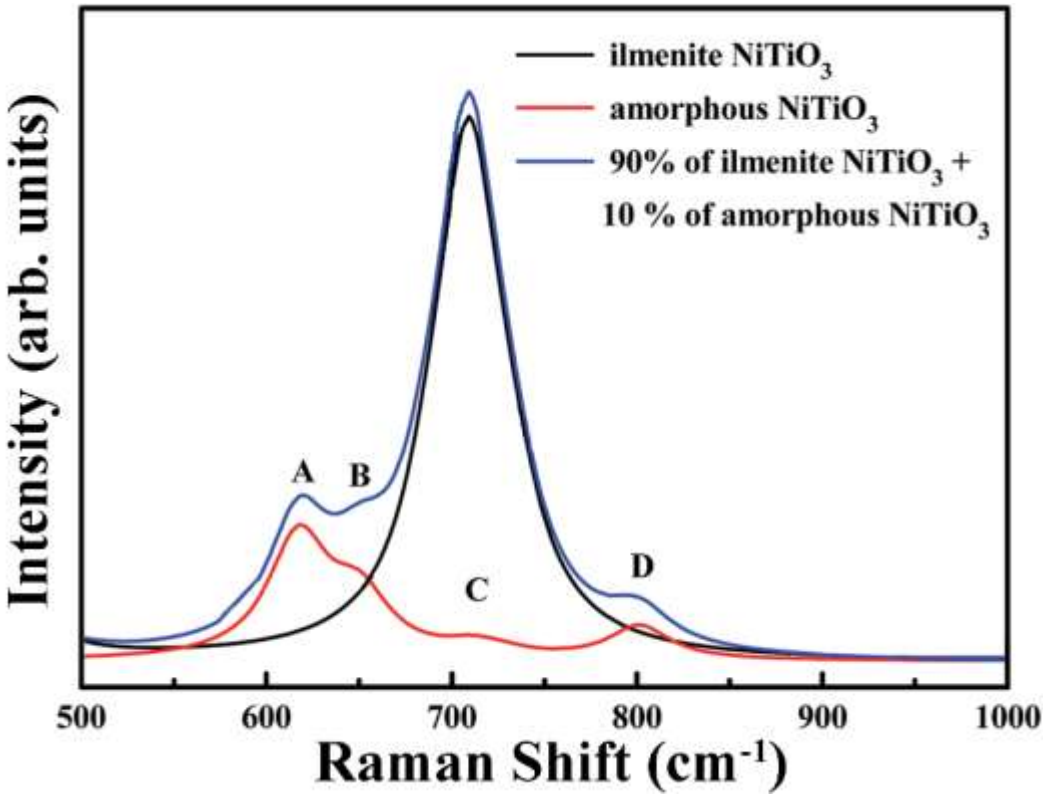

Fig. 2.9 *Raman spectra for the $(NiTiO_3)_{17}$ nanoparticles calculated by the parametrized PM6 method as well as experimental spectrum.*

The Raman bands named A, B and D, with relatively low intensities compared to the C band, are associated to the full optimization and relaxation of the nanocluster structures. This procedure, which leads to stable amorphous networks, ensures molecular bonding distortions, including changes to bond lengths and angles. Such structural changes modify the vibrational features and, as shown experimentally and theoretically, cause new Raman bands to appear. A superposition of the main Raman band (90%) for O–Ti–O stretching and the secondary bands (10%) related to the amorphous structure leads to a theoretical Raman spectrum that reproduces the features of the experimental one. It was proved that the bands located at 617 and 690 cm^{-1} originate from the stretching of Ti–O and bending of O–Ti–O bonds, while the contribution at 547 cm^{-1} results from Ni–O bonds.[51]

4. CONCLUSIONS

The electronic, optical and vibrational properties of $(NiTiO_3)_n$ nanostructures were investigated and compared to those of bulk ilmenite $NiTiO_3$. The investigated nanostructures possess a spherical shape with the number of $(NiTiO_3)_n$ units modified from n = 2 up to 183. The PM6 semi-empirical methodology was able to provide a valuable estimation of the energy gap in nanosized $NiTiO_3$ structures. The value of the $\Delta E_{HOMO-LUMO}$ saturates at 2.55 eV for the clusters comprising at least n = 50 $(NiTiO_3)_n$ units. The UV-Vis absorption spectra were calculated using the PM6 methodology for nanostructures. The obtained spectra confirm that the surface effects in $NiTiO_3$ nanoparticles contribute with additional band edges. The UV-Vis absorption spectra obtained for the $(NiTiO_3)_{17}$ nanocluster clearly indicates the promising optical activity of the system in the UV and the visible range of the solar spectrum. The $NiTiO_3$ nanoclusters also exhibit other relevant properties required for efficient photocatalysis.

The calculated Raman spectra for the $NiTiO_3$ clusters show the noticeable contribution of the surface to the vibrational properties. Among the features of the Raman spectra, those related to active modes of the ilmenite structure and those inferred from amorphous $NiTiO_3$ can be distinguished. The theoretical superposition of a Raman band that constitutes 90% of the band intensity, and is associated with the O–Ti–O stretching mode, and secondary less intense bands (10%), related to the amorphous structure, represents the main features of the experimental spectrum.

Finally, the present work points out the relevant optical properties of the $NiTiO_3$ clusters that allow them to harvest visible light for efficient photocatalytic reactions. However, the low mobility of charge carriers, demonstrated from the effective mass estimation, leaves open questions that can be solved using a doping procedure.

CHAPTER III: $NiTiO_3$ SYNTHESIS METHODOLOGIES AND CHARACTERIZATION DETAILS

Solid-State Reaction (SSR) has been the conventional method to synthesize nickel titanate powders in the past decades. This technique is simple, requiring only a solid mixture of the precursors (*e.g.* NiO and TiO_2) and an increase of the temperature, normally between 1000 and 1500 °C, to promote the reaction. [99] Among other factors, the surface area of the reactants plays an important role on the feasibility and rate of the reaction. Probably the main advantage of SSR is that it is easily scalable to obtain large quantities of the desired compound.

By contrast with the solid state reaction method, wet-chemistry synthesis techniques, including sol–gel, sol–precipitation, chemical co-precipitation, and others, are relatively more complicated to develop but at the same time offer many distinctive advantages over the traditional method such as controlling the average particle size, homogeneity, morphology control, lower reaction temperature, etc.

To mention some examples concerning wet-chemistry syntheses of $NiTiO_3$ structures, Zhou and Kang[100] have prepared nanostructured $NiTiO_3$ by the calcination at 900 ºC of the precipitate produced by $Ni(OH)_2$ and titanium dioxide powder (P-25) in etyltrimethylammonium bromide (CTAB) micelle solutions. Sadjadi et al.[101] implemented a sol–gel method using nickel stearate and tetra-*n*-butyl titanate as Ni and Ti sources, respectively, and stearic acid as the complexing reagent, calcinating at 750 ºC for 2 hours. A work that highlights itself from the rest is that one of Lopes et al.[93] in which a sol–gel route is followed, based on the polymerization of metallic citrate using ethylene glycol and also using citric acid as chelating agent in aqueous solution, obtaining $NiTiO_3$ powders varying the annealing temperature from 400 ºC to 1000 ºC during 2 hours in air. These results have shown that at annealing temperatures as low as 600 ºC the $NiTiO_3$ phase formation begins, in contrast with temperature above 1300 °C normally required in SSR. However, for annealing temperatures below 1000 ºC, in the case of their results, the lattice parameters of

the prepared nanocrystals differ significantly from the bulk crystalline powders according to the standard reference for ilmenite $NiTiO_3$ (JCPDS file 33-0960).

As mentioned before, SG has a series of advantages that should positively impact the properties of the synthesized materials for the specific application on mind, *i.e.* catalysis, but because of the simplicity of the SSR technique and despite the high temperatures required, we took on the task of testing if this method could result in $NiTiO_3$ powders presenting physical characteristics comparable to those of $NiTiO_3$ powders synthesized by sol-gel. In order to do this, $NiTiO_3$ powders were synthesized by both techniques and for each technique different annealing temperatures were tested.

On a parallel task, the deposition of $NiTiO_3$ thin films by a physical method was of interest. Radio frequency (rf)-sputtering deposition technique allows the deposition of nickel titanate as thin films without having to reach its evaporation temperature. In addition, sputtered films tend to have better adhesion to the substrate than evaporated films and the deposition rate is also easier to control. Using a $NiTiO_3$ target prepared from powders synthesized by SSR, taking advantage of its simplicity and the fact that a large amount of $NiTiO_3$ can be easily synthesized, $NiTiO_3$ thin films were grown by rf-sputtering after optimization of the deposition parameters.

Finally, following the above-mentioned points, the subject of this chapter is related to the synthesis details of $NiTiO_3$ powders by both sol–gel and solid-state reaction techniques, as well as the deposition conditions of $NiTiO_3$ thin films by rf-sputtering. In addition, the details of the characterizations performed on the different samples are described in this chapter. The characterization results and its analyses will be a matter of discussion for subsequent chapters.

CHAPTER III

1. EXPERIMENTAL SYNTHESIS PROCEDURES

a. $NiTiO_3$ powders synthetized by Sol-Gel (SG) and annealed at high temperatures: P1-SG-A1000C and P1-SG-A1350C

For synthesizing these powders, a sol–gel procedure was followed. The chemicals used were citric acid (Aldrich, 99% pure); titanium (IV) isopropoxide (ACRŌS Organics, 98% pure) and nickel acetate (ACRŌS Organics, 99% pure) as the metallic precursors; and ethylene glycol (J.T. Baker, 99% pure). In this method a solution of 5.76 g of citric acid in 92 ml of deionized water was prepared and, after this, 3 ml of titanium (IV) isopropoxide and 2.48 g of nickel acetate were added under constant stirring at room temperature (the molar ratio between citric acid:titanium (IV) isopropoxide:nickel acetate was 3:1:1). For homogenization, the solution was left under constant stirring for 1 hour. After this homogenization time, 68.4ml of ethylene glycol was added to the solution (weight percent ratio solution:ethylene glycol of 60:40). The resulting solution was stirred and heated at a temperature between 70 and 90 ºC for 3 h, and then it was put into an oven at 300 ºC in air, for 1 hour. The obtained powder was then calcinated at 1000 or 1350 ºC in air for 2 hours in a furnace where the temperature was increased at a rate of 5 ºC min^{-1} from room temperature up to the desired temperature.

After the annealing step, the furnace was cooled down at a slow rate to room temperature. Two different powders were thus obtained by this procedure, depending on the annealing temperature. They are labeled P1-SG-A1000C for the sample annealed at 1000 ºC and P1-SG-A1350C for the powder annealed at 1350 ºC.

b. $NiTiO_3$ synthetized by Solid-State Reaction (SSR): P2-SSR-A1000C and P2-SSR-A1350C

For the synthesis of these powders, the solid-state reaction method was used, for which stoichiometric quantities of nickel oxide and titanium dioxide (Aldrich, 99.9% pure) were

mixed in a mortar and ground by hand, until the mixture was homogeneous. This mixture presented a light gray color. In the same manner then for the previously described procedure, the obtained solid mixture was then heat treated at 1000 or 1350 ºC in air for 2 hours in a furnace increasing the temperature at a rate of 5 ºC min^{-1} from room temperature up to the desired temperature.

After annealing, the furnace was cooled down to room temperature. Two different powders were thus obtained by this procedure, depending on the annealing temperature. They are labeled P2-SSR-A1000C for the sample annealed at 1000 ºC and P2-SSR-A1350C for the powder annealed at 1350 ºC.

c. *$NiTiO_3$ powders synthesized by Sol-Gel (SG) and annealed at relative low temperature: P3-SG-A650C*

A different sol-gel route than the one described above is used to realize the synthesis of these powders.

In this case, the chelating agent used is hydrochloric acid (HNO_3); a tensoactive agent, commercially known as Brij58, is employed; and the metallic precursors for Ni and Ti are the same as before, *i.e.* nickel acetate (NA) and titanium isopropoxide (TIP). The reaction takes place in the presence of ethanol.

First, two solutions are prepared independently. A solution named “solution A”, which contains the metallic precursors, and “solution B” containing the tensoactive agent.

For solution A, 0.005 moles of NA, 0.016 moles of HNO_3, and 0.005 moles of TIP are dissolved in 0.08 moles of ethanol under magnetic stirring. The reactants are added in the order of appearance and waiting for them to dissolve completely before adding the next one. Once solution A is prepared, it is left under stirring for homogenization.

In the preparation of solution B, 0.012 moles of HNO_3 and $6.36x10^{-7}$ moles of Brij58 are dissolved in 0.556 moles of ethanol under magnetic stirring. Once again, the reactants are

added in the order of appearance and waiting for complete dissolving before adding the next one.

When both solutions are prepared and all the reactants have completely dissolved, solution A is added to solution B. The resulting solution is aged during 2 hours at room temperature (RT) under magnetic stirring. After the aging time, the temperature of the solution is raised to 90 ºC for the evaporation of the solvents. When the volume of the solution is a small fraction (~10 %) of the initial volume, a reaction takes place and a gel is formed in a foam-like structure. When this happens the volume of the gel increases considerably compared to the volume of the sol at the beginning of this reaction.

The foam-like gel is calcinated at 300 ºC for 2 hours, going from RT to 300 ºC at 5 ºC min^{-1} in air. The resulting green powder is annealed at 650 ºC during 1 hour in air to obtain crystalline $NiTiO_3$. With the purpose of future comparison with the powders described before, the powders detailed here are labeled P3-SG-A650C.

d. $NiTiO_3$ thin films (TF) by rf-sputtering

Synthesis of $NiTiO_3$ targets

The synthesis of $NiTiO_3$ targets was realized from stoichiometric commercial powders of NiO and TiO_2 from Aldrich with good purity (99.90%). After homogeneous mixing, shaped disks (diameter 30 mm and thickness 4 mm) were made by compressing the powder with a hydraulic press inside a mold, followed by a second compression process using an isostatic press. The pellets were sintered at 1100 °C for 6 hours in air to ensure, a homogenous $NiTiO_3$ composition with a good crystalline quality of the ilmenite structure.

Deposition of the $NiTiO_3$ thin films by rf-sputtering

The key parameters for rf-sputtering deposition of thin films consist of the argon/oxygen (Ar/O) flow, the partial pressure in the synthesis chamber, the rf-power and the substrate temperatures during the synthesis process. Different sets of parameters were tested in order

to determine the optimal values that promote good crystallinity of thin films. However, all the conditions lead to amorphous as-formed films and a post-synthesis annealing treatment is required to ensure a crystalline structure. The optimization of the synthesis parameters, giving rise to suitable stoichiometry and thickness, led to values of 94/0 sccm for the Ar/O flow, 0.1 mbar for the partial pressure, and 50 W for the rf-power and the silicon substrate temperature was fixed at room temperature. The films were deposited under the same conditions and during the same time. Thus, the same growth rate and thickness are expected for all synthesized films. The annealing process was conducted with a heating rate of 5 °C min^{-1} while the cooling rate was not fixed; the film was allowed to cool down at the natural rate of the oven. Typical cooling time from 1000 °C to ambient temperature was about 24 hours.

2. EXPERIMENTAL CHARACTERIZATIONS DETAILS

a. Scanning Electron Microscopy (SEM) and Energy-Dispersive X-ray Spectroscopy (EDS)

A JEOL-JECM-6360LV scanning electron microscope (SEM) was used for the morphological characterizations of the powder samples. In addition, semi-quantitative analyses were carried out using energy-dispersive X-ray spectroscopy with a JEOL detector inside the SEM chamber. The powders were deposited on a carbon conducting tape suited for the SEM and EDS observations. A low electron acceleration voltage (5 kV) was used in order to avoid charging the samples.

b. Transmission Electron Microscope (TEM)

TEM observations were carried out on powder samples using a JEOL ARM200F instrument operated at 200 kV accelerating voltage. A small quantity of powder sample was ultrasonically dispersed in ethanol and subsequently a drop of this dispersion was put on a copper grid. After the alcohol had evaporated, the grid was placed inside the vacuum chamber of the equipment for observation.

c. X-ray Diffraction (XRD)

XRD measurements were performed on all the samples in order to analyze their crystalline features including the presence of other secondary phases. The X-ray diffractometer was an Empyrean model from PANalytical. Measurements were carried out in a symmetrical coplanar geometry (theta-2theta) with 2theta ranging from 20° to 65°. In the special case of the thin films deposited by rf-sputtering, an offset between ω and 2θ was fixed equal to 5° in order to gather as much diffracted radiation as possible coming from the film along with a reduction of the reflection from the silicon substrate. X-rays were produced with a copper

tube ($K_{\alpha_1} = 1.54056$ Å, $K_{\alpha_2} = 1.54439$ Å) with 1/8° and 1/4° divergence slits, situated at 160 and 120 mm from the sample, respectively. A nickel filter was placed in the path of the reflected beam to avoid contamination in the data from the K_β wavelengths. A pixel 3D detector was used in all measurements. The observed data was refined with the Rietveld method[102], using the MAUD v2.33 software. This method was particularly useful for quantifying the volume fraction of each phase present in the samples, together with their crystalline structure.

d. Raman Spectroscopy

Raman spectrometry was also used to characterize the vibrational properties of the samples. The Raman scattering spectra were collected with a T64000 Horiba Jobin Yvon spectrometer, under a microscope (x50 LF objective) and coupled to a cooled CCD. The 514.5 nm wavelength of an Ar/Kr laser was used as the excitation line. A resolution of 0.7 cm^{-1} was used for all recorded spectra. The analysis of the Raman spectra was done with the help of the LabSpec software (v5.25.15) dedicated to identify the active Raman vibrational modes related to the involved crystalline structures.

e. Diffuse Reflectance Spectrometry (DRS)

The optical properties of the $NiTiO_3$ powders were investigated by using diffuse reflectance spectrometry based on an Ocean Optics Spectrometer with an integrating sphere and a Deuterium/Halogen Lamp (200–1400 nm) as the light source.

f. Atomic Force Microscopy (AFM)

The surface topography of the $NiTiO_3$ thin films deposited by rf-sputtering, was characterized by an Agilent 5500 AFM operating in tapping mode in an air atmosphere at

room temperature. A silicon AFM probe (Nanosensor PPPNCHR-W tip) was used and image processing was performed with Gwyddion Freeware (v2.27).

g. Optical Interferometry

Thickness and refractive index measurements were conducted on the $NiTiO_3$ thin films by optical interferometry with a setup from FILMETRICS F30 for white light interference fringe measurements. The setup uses an optical fiber that directs light in the spectral range from 400 to 3000 nm. The film on the Si substrate gives rise to an interferometry pattern, which can be analyzed by a fitting procedure to extract the film thickness and its refractive index (real and imaginary parts).

h. UV-Vis Spectrometry

The UV-vis absorption spectra of $NiTiO_3$ thin films deposited on quartz substrates were collected using an HR4000 Ocean Optics high resolution spectrometer with a deuterium–halogen lamp as the illumination source. The spectra were collected in the wavelength range of 200–1100 nm.

CHAPTER III

3. CONCLUSIONS

Nickel titanate ($NiTiO_3$) powders were synthesized by two different methods: sol-gel and solid-state reaction. For each method, a set of samples was annealed at 1000 ºC and another set was annealed at 1350 ºC. The intention for doing this is to compare the volume fraction of the crystalline phases present in the samples, and identify the synthesis method, as well as the post-synthesis treatment, that allows the obtaining of the highest fraction of the ilmenite phase and the lowest fraction of secondary phases, such as, anatase (TiO_2) and bunsenite (NiO).

A sol-gel route that permits the stabilization of the ilmenite crystal structure at a relative low temperature (*i.e.* 650 ºC) was developed.

A simple and fast synthesis route was developed to obtain $NiTiO_3$ thin films with a good crystalline quality and stable ilmenite structure. Solid-state reaction was performed to obtain crystalline powders used as targets for the rf-sputtering method. Appropriate deposition conditions and post-synthesis heat treatment were determined to obtain thin films with controlled features.

The experimental details of the characterization techniques employed for sample analyses were listed and the results of the characterization studies will be discussed in depth in the subsequent chapters.

CHAPTER IV: $NITIO_3$ POWDERS SYNTHESIZED BY SOL-GEL AND SOLID-STATE REACTION ANNEALED AT HIGH TEMPERATURE

The subject of this chapter is related to the synthesis of $NiTiO_3$ powders by both the sol–gel and the solid state reaction techniques as described in Chapter III, specifically the powders labelled P1-SG-A1000C, P1-SG-A1350C, P2-SSR-A1000C and P2-SSR-A1350C. The discussion also includes the investigation of their structural, morphological and optical features. Complementary experimental characterizations have been used to monitor their physical properties in order to make a comparison between these preparation techniques. In this way, the objective is to determine the best synthesis method according to the observed properties of the obtained powders from the photocactivity point of view.

These studies are indeed dedicated to create photoactive materials which offer competing alternatives to other systems based on titanium dioxide, typically applied in the area of clean energy (production of hydrogen) or environmental care (degradation of water and atmosphere pollutants).

Investigations of the structural, morphological and chemical properties were performed by techniques such as X-ray diffraction (XRD), Raman spectroscopy, scanning electron microscopy (SEM) and energy-dispersive X-ray spectroscopy (EDS). In addition, the UV–vis absorption curves, obtained from diffuse reflectance spectrometry (DRS), allowed the determination of the band-gap energy of the synthesized samples.

It will be shown that $NiTiO_3$ nanocrystalline powders were obtained in all cases. However, in contrast to the solid state reaction synthesis, the sol–gel route was found to be a more efficient method for obtaining the stabilized Ilmenite structure after a high temperature thermal treatment.

CHAPTER IV

1. STRUCTURE AND MORPHOLOGY

As described in Chapter III, the different powders were directly deposited on a carbon conducting tape in order to observe them with a (JEOL) scanning electron microscope. In Fig. 4.1 the images of the surfaces of samples P1-SG-A1000C, P1-SG-A1350C, P2-SSR-A1000C and P2-SSR-A1350C, are shown. As can be seen, the main difference is that the crystallite clusters are larger for the samples annealed at 1350 °C as compared to those annealed at 1000 °C. However, as will be explained below (from XRD) the coherently diffracting crystallites have dimensions of the same order (between 40 and 60 nm) in all cases.

The crystal structure as well as the phase volume fraction of the investigated samples are determined from the XRD patterns collected for each sample. Fig. 4.2 illustrates the XRD patterns. Reflections corresponding to the (0 1 2), (1 0 4), (1 1 0), (0 0 6), (1 1 3), (0 2 4), (1 1 6), (2 1 1), (0 1 8), (2 1 4) and (3 0 0) planes of the Ilmenite structure of $NiTiO_3$ with space group $R\bar{3}$ are identified. The hexagonal symmetry C_{3i}^2 was used to fit the data starting typically with lattice parameters a = b = 0.503 nm, c = 1.38 nm and α = β = 90°; γ ¼= 120° in agreement with the reference JCPDS 33-0960.

As shown in Fig. 4.2, the presence of secondary phases such as Bunsenite (NiO) and Rutile (TiO_2) is clearly seen. Table 4.1 shows the details for each sample with respect to the phases present in the samples. The volume fraction of these secondary phases (as determined by the Rietveld method) is reduced as the preparation temperature is increased.

P2-SSR-A1000C presents ~44% of the $NiTiO_3$ Ilmenite phase, ~40% of TiO_2 Rutile phase and ~16% of NiO Bunsenite phase. By increasing the temperature up to 1350 °C the volume fractions of these phases change drastically to 95 ± 5 % $NiTiO_3$, 3.3 ± 0.4 % TiO_2 and 1.9 % NiO within the uncertainty range. Thus, a higher annealing temperature strongly benefits to the formation of the $NiTiO_3$ phase in the solid state reaction method.

A similar effect is observed on the powders synthesized by sol-gel where annealing at 1000 °C (P1-SG-A1000C) leads to the coexistence of 86 ± 2 % for $NiTiO_3$, 8.4 ± 0.4 % for TiO_2 and 5.6 ± 0.4 % for NiO. Increasing the annealing temperature to 1350 °C (P1-SG-A1350C) contributes to having pure $NiTiO_3$ with the Ilmenite structure, within the uncertainty range.

In addition, the crystallite sizes increase for higher annealing temperatures as observed by the reduction of the full width at half maximum (FWHM) of the Bragg diffraction lines.

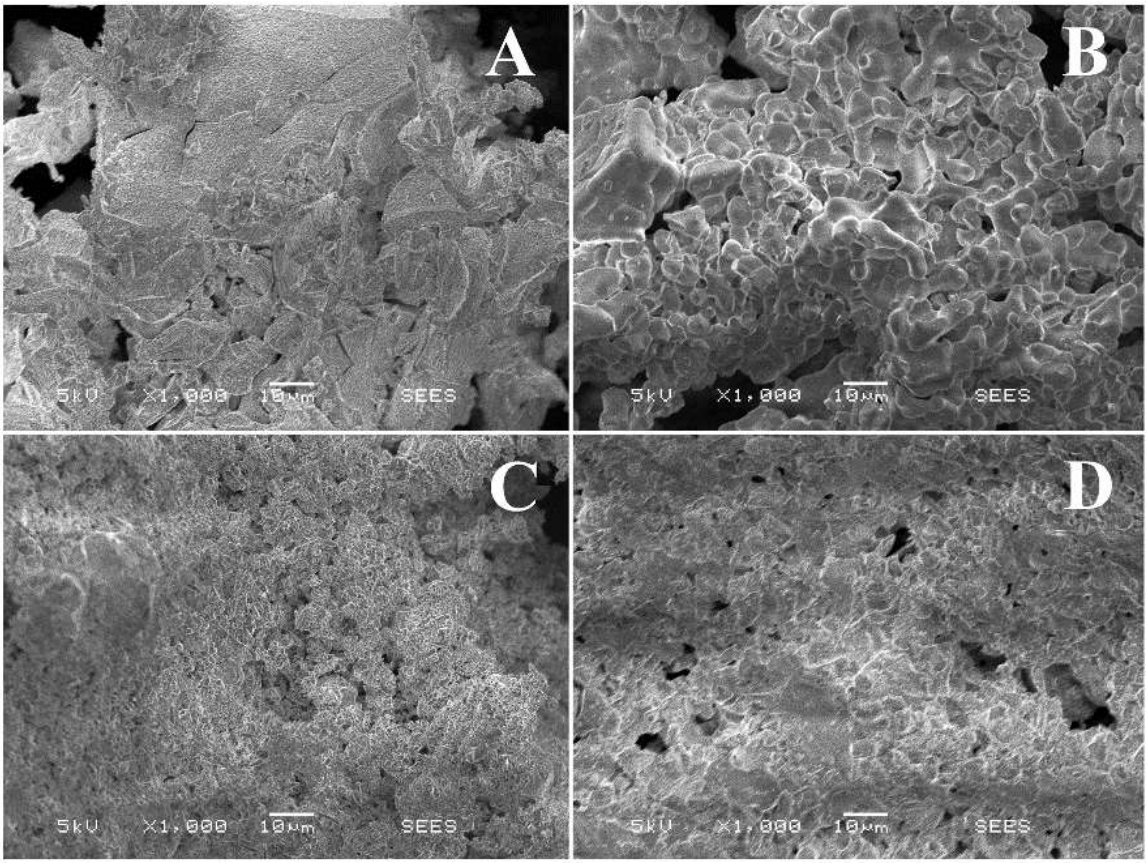

Fig. 4.1 *SEM image of the surface of P1-SG-A1000C (A); P1-SG-A1350C (B); P2-SSR-A1000C (C); P2-SSR-A1350C (D). Acceleration voltage set to 5kV, objective set to x1000, and the reference shown is 10 µm.*

Table 4.1 *Fraction of the phases present in the synthesized samples*

Sample	Phase volume fraction (%)		
	$NiTiO_3$ (Ilmenite)	TiO_2 (Rutile)	NiO (Bunsenite)
P1-SG-A1000C	86 ± 2	8.4 ± 0.4	5.6 ± 0.4
P1-SG-A1350C	98 ± 5	0	1.2 ± 2
P2-SSR-A1000C	44.2 ± 0.4	39.5 ± 0.4	16.3 ± 2
P2-SSR-A1350C	95 ± 5	3.3 ± 0.4	1.9 ± 2

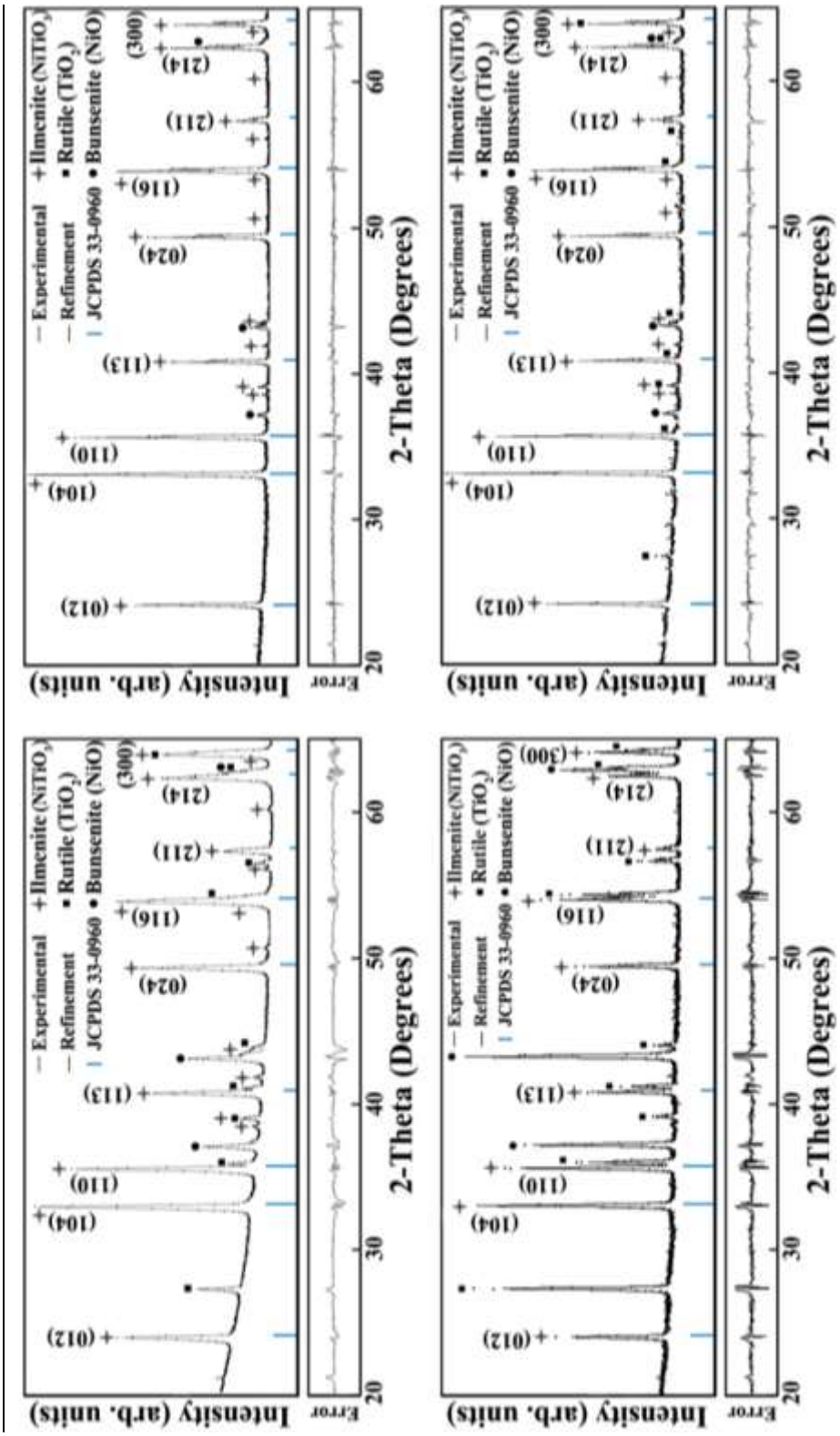

Fig. 4.2 *X-Ray Diffraction patterns of P1-SG-A1000C (top left), P1-SG-A1350C (top right), P2-SSR-A1000C (bottom left) and P2-SSR-A1350C (bottom right).*

The sizes for the crystallites oriented in the [1 0 4] direction were estimated by using the Scherrer equation[103], $D_{hkl} = K\lambda/(B_{hkl} \cdot \cos\theta)$, where λ is the wavelength of the X-rays, θ is the Bragg angle, D_{hkl} is the crystallite size in the direction perpendicular to the lattice planes under analysis, B_{hkl} is the FWHM of the diffraction peak in radians and K is a numerical factor frequently referred as the crystallite-shape factor. Considering spherical shaped particles the crystallite-shape factor was approximated to $K = 0.9$. [104,105] The obtained values for the crystallite sizes (D_{104}) are shown in Table 4.2.

Table 4.2 *$NiTiO_3$ mean crystallite size, estimated by the Scherrer formula for the crystallites oriented perpendicular to the (104) planes.*

Sample	Crystallite Size
P1-SG-A1000C	43.5
P1-SG-A1350C	59.5
P2-SSR-A1000C	56.6
P2-SSR-A1350C	61.6

Comparing the crystallite sizes for the different powders we can see that there is an increase of the size when the annealing temperature is increased from 1000 to 1350 °C. For the powders synthesized by sol-gel the size increases from 43.5 to 59.5 nm and for the powders synthesized by SSR it goes from 56.6 to 61.6 nm. We can also note the small difference in crystallite size between P1-SG- A1350C and P2-SSR-A1350C samples, particularly after the thermal treatment.

The lattice parameters were obtained from the Rietveld refinements with a very good correlation factor, as shown in Fig. 4.2. The lattice parameters obtained from this analysis are summarized in Table 4.3.

Table 4.3 *Lattice parameters of the $NiTiO_3$ phase of the synthesized samples.*

Sample	**$NiTiO_3$ lattice parameters (nm)**	
	a = b	**c**
P1-SG-A1000C	$0.503424 \pm 9 \times 10^{-6}$	$1.38098 \pm 4 \times 10^{-5}$
P1-SG-A1350C	$0.503289 \pm 3 \times 10^{-6}$	$1.37972 \pm 1 \times 10^{-5}$
P2-SSR-A1000C	$0.503293 \pm 4 \times 10^{-6}$	$1.37977 \pm 2 \times 10^{-5}$
P2-SSR-A1350C	$0.503249 \pm 3 \times 10^{-6}$	$1.37955 \pm 2 \times 10^{-5}$

2. CHEMICAL SEMI-QUANTITATIVE ANALYSIS

Energy-dispersive X-ray spectroscopy (EDS), shown in Fig. 4.3, has been used to determine the atomic percentages for each samples. For a 100 % pure nickel titanate sample, the atomic proportion should be 20 % nickel (Ni), 20 % titanium (Ti) and 60 % oxygen (O). However, taking into account the phase volume fractions (PVF) obtained from the Rietveld analysis (Table 4.1) we expect different atomic percentages of Ni, Ti and O. P1-SG-A1350C and P2-SSR-A1000C are located in the opposite PVF extremes. For P1-SG-A1350C, within the uncertainty errors, almost 100 % of the sample is composed of $NiTiO_3$ while for P2-SSR-A1000C, 44 % of $NiTiO_3$, 40 % of TiO_2 and 16 % of NiO was obtained. According to this result, the atomic proportion for P1-SG-A1350C should be ~20.2 % of Ni, ~19.7 % of Ti and ~60.2 % of O and for P2-SSR-A1000C we should get ~17 % of Ni, ~22 % of Ti and ~61 % of O. The atomic percentages for each sample are displayed in Table 4.4. These values are very close to those obtained by EDS, confirming the results obtained from the Rietveld refinements.

This fact also confirms that, within a small error, we have a pure $NiTiO_3$ phase in the case of P1-SG-A1350C.

Table 4.4 *Atomic percentages of the elements present in the samples, obtained by EDS.*

Element	Atomic proportion (%)			
	P1-SG-A1000C	**P1-SG-A1350C**	**P2-SSR-A1000C**	**P2-SSR-A1350C**
Ni	29.73 ± 0.81	22.33 ± 1.51	19.21 ± 1.93	27.89 ± 0.89
Ti	11.65 ± 0.44	19.05 ± 0.71	22.01 ± 0.86	11.85 ± 0.47
O	58.62 ± 0.24	58.62 ± 0.49	58.78 ± 0.66	60.26 ± 0.26

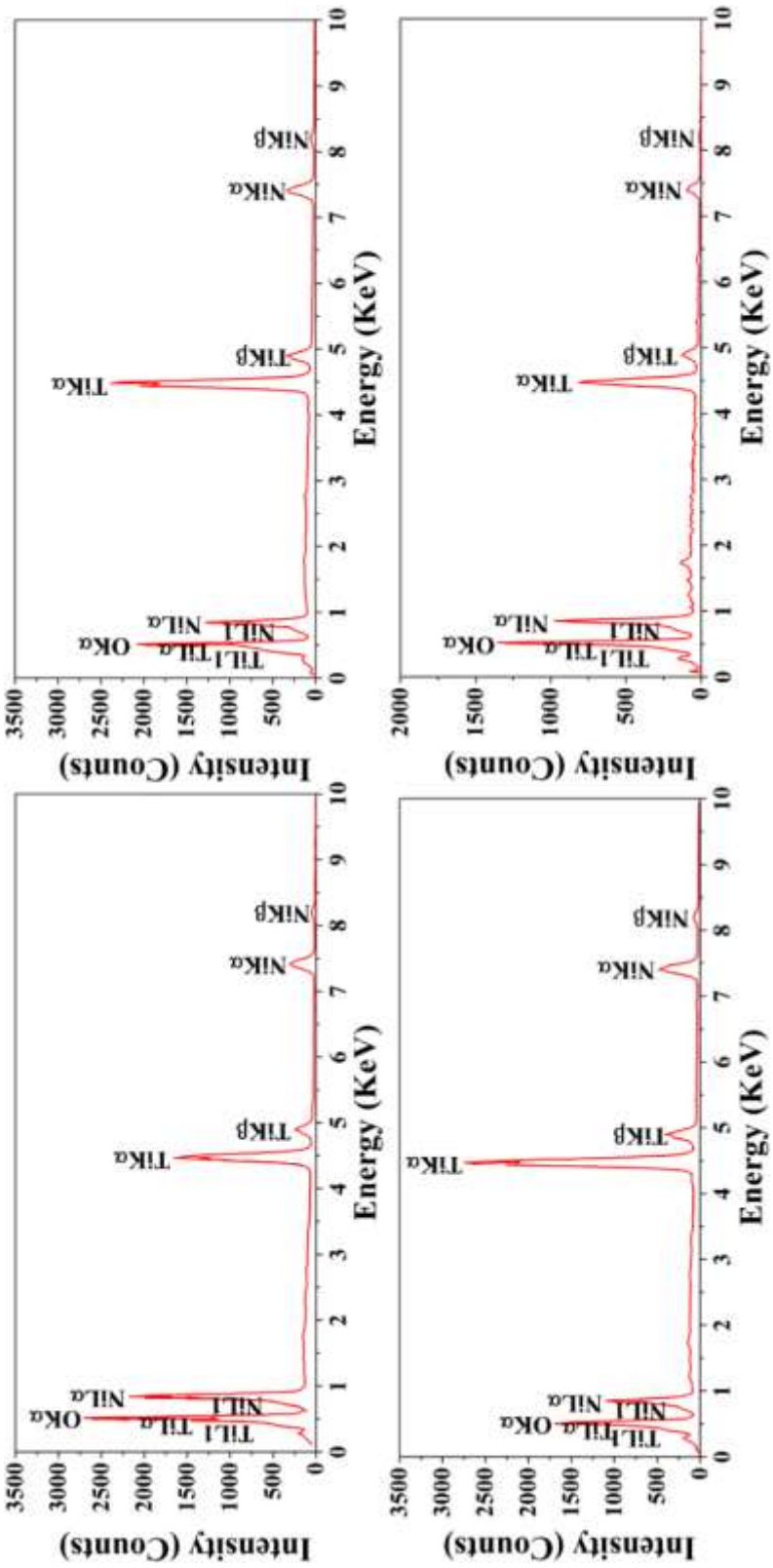

Fig. 4.3 *EDS signal of P1-SG-A1000C (top left), P1-SG-A1350C (top right), P2-SSR-A1000C (bottom left) and P2-SSR-A1350C (bottom right).*

3. RAMAN VIBRATIONAL ACTIVE MODES

From the above XRD analysis it was concluded that highly pure Ilmenite $NiTiO_3$ was achieved in the case of P1-SG-A1350C. In order to corroborate the above results, Raman spectrometry was used to analyze the vibrational properties of samples. For Ilmenite $NiTiO_3$, the oxygen atoms are tetra-coordinated to 2 Ti and 2 bivalent cations (Ni) in a C_1 symmetry site. Theoretically, we can expect ten active Raman modes ($\Gamma_{RAMAN} = 5A_g + 5E_g$), where each E_g mode is doubly degenerated ($E_g = E_{1g} + E_{2g}$) and eight IR active modes ($\Gamma_{IR} = 4A_u + 4E_u$). Additionally, this material should present two acoustic modes ($\Gamma_{AC} = A_u + E_u$) and no inactive modes. [96,98]

The Raman vibrational modes for $NiTiO_3$ are located at 192.2 (A_g), 229.8 (E_g), 246.9 (A_g), 291.3 (E_g), 345.4 (E_g), 394.5 (A_g), 465.3 (E_g), 484.5 (A_g), 613 (E_g) and 709.1 (A_g) cm^{-1}, as seen in Fig. 4.4. The assignment of the vibrational modes, as A_g or E_g, will be explained extensively in Chapters VI and VIII. Furthermore, in the samples containing a high fraction of Rutile (TiO_2), a contribution in the intensity is visible due to the vibrational modes of Rutile at 235, 445 and 610 cm^{-1}. Bunsenite's (NiO) contribution to the spectra is not noticeable in the analyzed spectral range.[106]

Notice that around 730 cm^{-1}, a mode of relatively low intensity appears as a shoulder of the more intense peak located 709.1 cm^{-1}. This vibrational mode has been wrongly considered before as one of the ten Raman modes for the Ilmenite symmetry. The work by Wang et al.[107] analyzes the Ilmenite-type $MgTiO_3$ and based on group theory, they calculated the Raman modes and concluded that this shoulder is not one of the ten expected modes. However, no explanation was given for it either. An explanation for this Raman mode will be proposed in Chapter VIII.

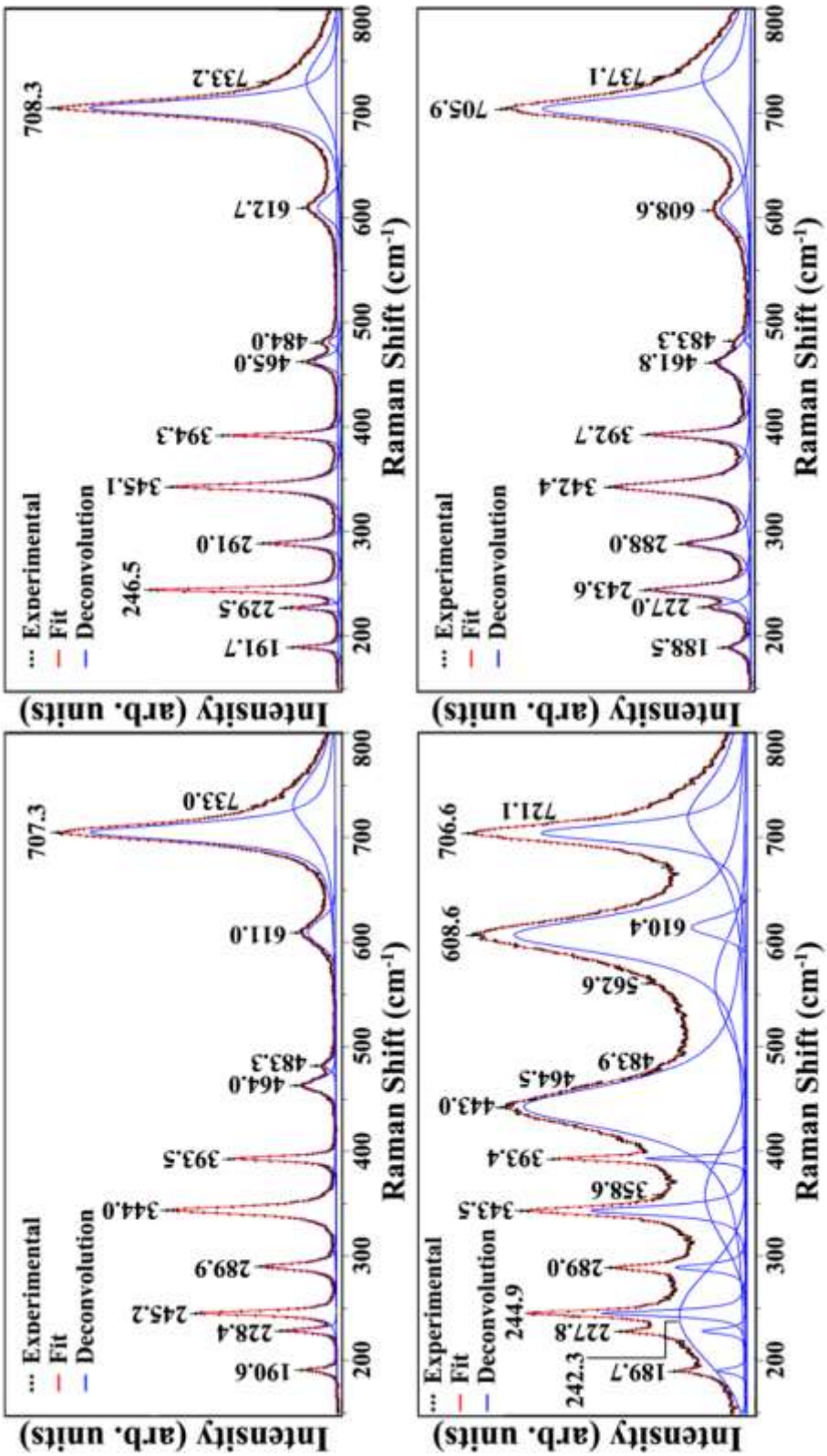

Fig. 4.4 *Raman active vibrational modes of P1-SG-A1000C (top left), P1-SG-A1350C (top right), P2-SSR-A1000C (bottom left) and P2-SSR-A1350C (bottom right).*

CHAPTER IV

4. OPTICAL PROPERTIES

The optical properties were caracterized by diffuse reflectance measurements for the different powders discussed in this chapter. The experimental spectra were analyzed using the Kubelka–Munk (K–M) model.[108] In this frame, the Kubelka–Munk function $F(R_{inf})$ is introduced and depends on the K–M effective absorption coefficient (K) and the K–M effective scattering coefficient (S):

$$F(R_{inf}) = \frac{(1 - R_{inf})^2}{2R_{inf}} = \frac{K}{S} \tag{4.1}$$

The K–M effective absorption coefficient (K) is proportional to the usual absorption coefficient (α) according to $K = \varepsilon\alpha$, and the K–M effective scattering coefficient (S) is related to the usual scattering coefficient (s) by $S = 2(1 - \varsigma)s$. When the material scatters in a perfectly diffuse manner the K–M effective absorption coefficient (K) becomes $K = 2\alpha$ and the K–M effective scattering coefficient (S) is exactly the same as the usual scattering coefficient (s), $S = s$.[109,110] Under this condition we can use the expression:

$$[F(R_{inf})h\nu]^2 = C_1(h\nu - E_g) \tag{4.2}$$

A plot of $[F(R_{inf})h\nu]^2$ vs $h\nu$ allows us to obtain the band-gap energy (E_g) values following the well-known Tauc plot.[111,112]

From the curves shown in Fig. 4.5, two absorption band edges related to two electronic transitions have been identified at approximately 2.25 eV and 2.50 eV, respectively. Table 4.5 shows the band-gaps, associated to the lower energy electronic transitions obtained from the Tauc plots for the different samples.

Table 4.5 *Band gap of the $NiTiO_3$ samples as determined from the Tauc plots of UV-Vis absorbance.*

Sample	Band-gap (eV)
P1-SG-A1000C	2.29 ± 0.03
P1-SG-A1350C	2.26 ± 0.01
P2-SSR-A1000C	2.26 ± 0.02
P2-SSR-A1350C	2.25 ± 0.01

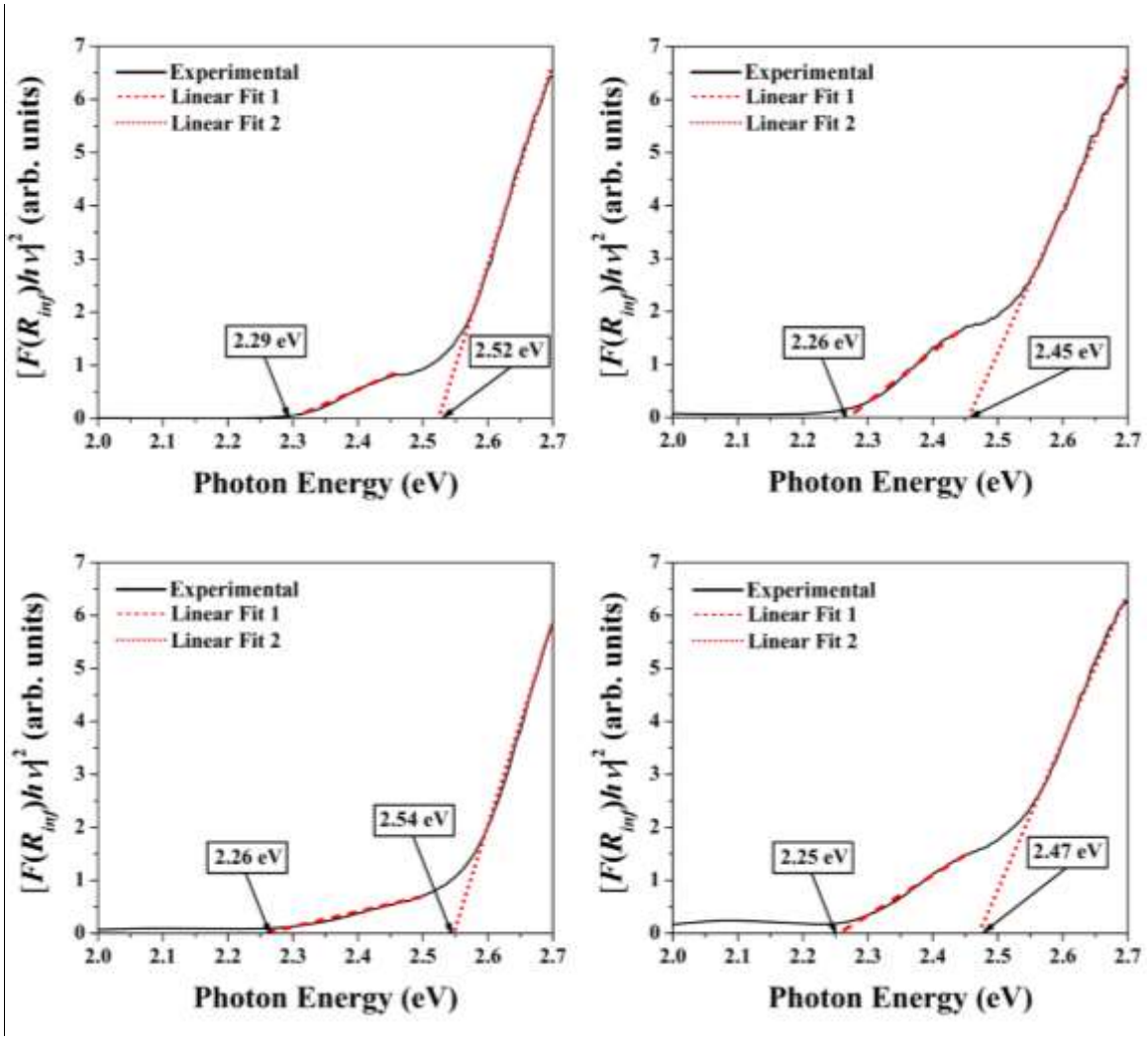

Fig. 4.5 *Tauc plots of P1-SG-A1000C (top left), P1-SG-A1350C (top right), P2-SSR-A1000C (bottom left) and P2-SSR-A1350C (bottom right).*

In Fig. 4.6 we can see the absorption spectra for each sample, where two absorption bands are clearly identified at 400 and 800 nm, respectively. Rossman et al.[113] give an explanation for the absorption bands found in $NiTiO_3$ after studying several compounds containing Ni^{2+} ions. In their paper, the general features of Ni^{2+} absorption have been described in terms of a ligand field theory. In a rigorously octahedral environment, Ni^{2+} will have three prominent absorption bands, arising from transitions from the $^3A_{2g}$ ground state to the $^3T_{2g}$, $^3T_{1g}(F)$, and $^3T_{1g}(G)$ states. These correspond to the prominent absorption bands in the 1400, 800 and 400 nm regions, respectively. Strong spin-orbit coupling together with antiferromagnetic interactions is believed to increase the intensity of the transition to the ^1E_g, state at ~720-740 nm such that it becomes more intense than the spin-allowed transition to the $^3T_{1g}$ state in the case of NiO. Likewise the transition to the $^1T_{1g}$ state at 378 nm is more intense than the 415 nm $^3T_{1g}$ band in NiO. The greatest absorption band intensities in the 400 nm region are associated with metal ion absorption bands in proximity to an ultraviolet wavelength tail due to charge transfer. The most intense bands are about an order of magnitude more intense than for NiO. Proximity to a charge transfer ultraviolet tail has been recognized to be an important factor in determining the intensities of electronic transitions of metal ions in general through the mechanism of "intensity stealing". The extent to which the ultraviolet charge transfer band extends into the visible region depends in part on the ion with which the Ni^{2+} shares oxygen ions. Easily reduced ions such as Ti^{4+} produce a charge transfer tail which extends well into the visible region, whereas hardly reduced ions such as P^{5+} and Si^{4+} do not. Site symmetry influences the color of Ni^{2+} compounds. The degeneracy of the $^3T_{1g}$, $^3T_{2g}$, and ^1E_g states of Ni^{2+} in octahedral geometry are lifted and multiple-absorption bands occur when Ni^{2+} is situated in a coordination environment of low symmetry.

Bands split by low symmetry will show peak wavelengths which are polarization dependent. Band intensities often increase in response to low site symmetry.

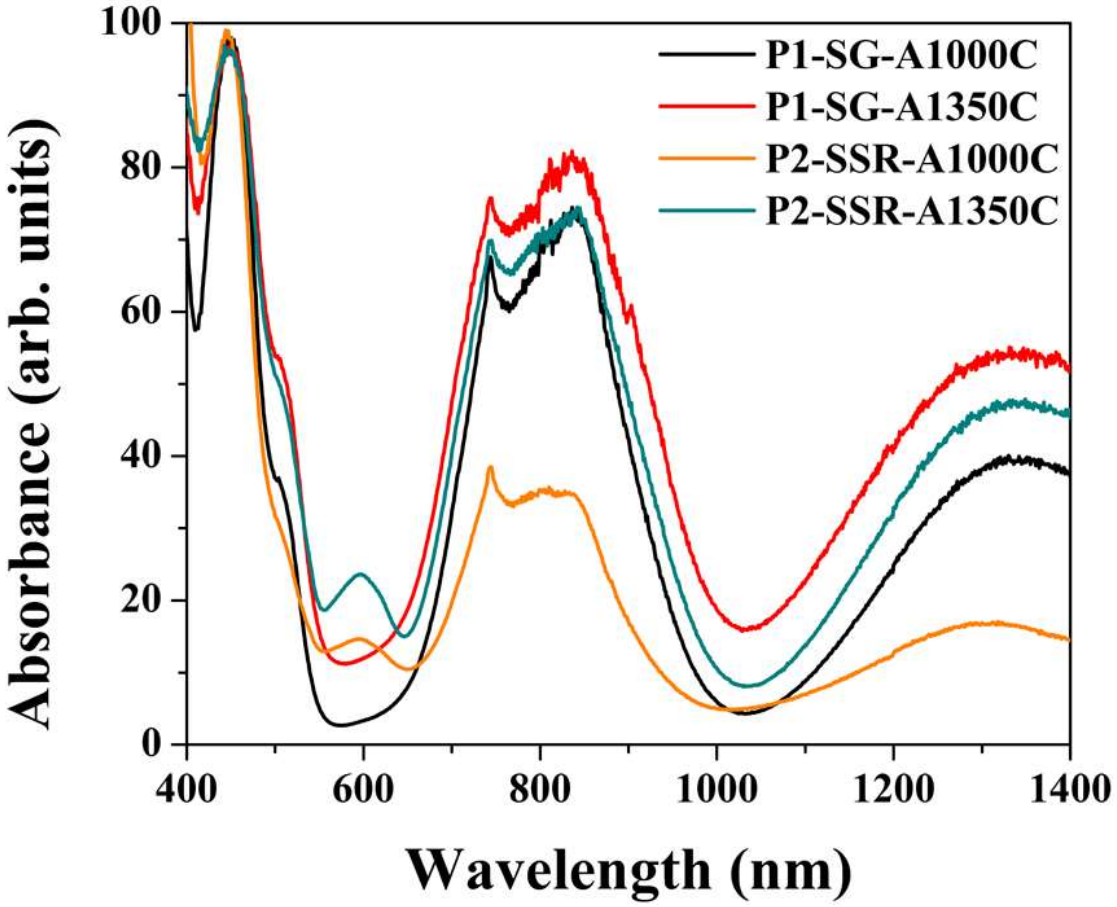

Fig. 4.6 *Absorption bands of P1-SG-A1000C (Black), P1-SG-A1350C (Red), P2-SSR-A1000C (Orange) and P2-SSR-A1350C (Green).*

In summary, all of the above measurements and characterizations show that we have obtained $NiTiO_3$ powders by the two proposed methods: sol–gel and solid state reaction, after annealing the samples at 1350 °C in air for two hours. It is clear that the sol–gel method is better than the solid state reaction method because an even more pure $NiTiO_3$ crystalline phase is obtained in the former case.

CHAPTER IV

5. CONCLUSIONS

Nickel titanate ($NiTiO_3$) powders were synthesized by two different routes: sol–gel and solid-state reaction. The synthesized powders were characterized by EDS, XRD, Raman spectroscopy and diffuse reflectance spectrometry. An analysis of the EDS and XRD results has shown that the sol–gel route with an additional annealing at 1350 °C for 2 hours, in air atmosphere, leads to a highly pure nickel titanate phase without any further purification step. A band-gap of 2.26 ± 0.01 eV was determined for this sample from diffuse reflectance spectroscopy. The EDS and XRD results were consistent between themselves for all the samples, showing that the powders obtained by the sol–gel route and annealed at 1350 °C, during 2 hours, are pure polycrystalline $NiTiO_3$ with the ilmenite structure (hexagonal symmetry with lattice parameters around a = b = 0.5 nm and c = 1.38 nm). In addition, the observed 10 active Raman modes confirmed the presence of the Ilmenite phase of $NiTiO_3$. Finally, the absorption spectra as determined from UV–Vis diffuse reflectance spectrometry, shows the presence of at least 3 absorption bands that could be explained by the main (HOMO–LUMO) transitions plus two other bands related to charge transfer from O^{2-} to Ti^{4+} and Ni^{2+} to Ti^{4+}. It can be expected that these photo-activated charge transfer phenomena will provide a high photo-catalytic activity to this material. All of the above results show that the sol–gel route allows the preparation of pure nanocrystalline $NiTiO_3$ powders. Our EDS, XRD and Raman spectroscopy results also show that the solid-state reaction route does not provide pure powders, since they have a volumetric fraction of the Rutile TiO_2 phase, even after annealing them for 2 hours in air at 1350 °C. Possibly longer annealing times are required when using this technique.

CHAPTER IV

CHAPTER V: $NITIO_3$ POWDERS SYNTHESIZED BY SOL-GEL ANNEALED AT RELATIVE LOW TEMPERATURE

In the last chapter, highly pure ilmenite $NiTiO_3$ structure was achieved by both Sol-Gel and Solid-State Reaction methodologies. The best results were those obtained following the Sol-Gel route after annealing at 1350 °C during 2 hours (sample P1-SG-A1350C). For this sample, it can be considered that pure $NiTiO_3$ was obtained, having no secondary phases within the uncertainty range. Also, a band gap of 2.2 eV was determine for this sample.

However, 1350 °C is a high temperature that requires adapted furnaces and obviously costly energetic needs. Such requirements make the material inadequate for potential application with fabrication process at a wide scale. For these reasons, it is relevant to stabilize $NiTiO_3$ in its ilmenite phase at lower temperatures.

Additionally, exposing the material to lower temperatures during short heating time durations might contribute to improve the efficiency of photocatalytic processes through the reduced particle sizes enhancing the specific surfaces. Such aspects will be demonstrated later on.

Thus, obtaining nanosized particles (*e.g.* less than 50 nm) could benefit to the catalytic reactions because the active surface area would be dramatically increased in comparison to larger particles, such as the obtained for the samples investigated in Chapter IV.

A modified Sol-Gel route was used for the synthesis of the $NiTiO_3$ nanoparticles described in this chapter. The details of the synthesis are explained in detail in Chapter III. It will be shown that less than half the temperature than the one needed before is sufficient to obtain highly pure $NiTiO_3$ powders possessing a band gap energy of 2.28 eV and that the mean size of the involved particles is around 25 nm. The electrocatalytic activity of this sample was evaluated for the electro-oxidation of methanol in alkaline medium by the cyclic voltammetry technique and will discussed in Chapter VII.

CHAPTER V

1. STRUCTURE AND MORPHOLOGY

An XRD analysis was carried out, in which the samples were heated *in-situ* inside the diffractometer and varying the temperature in the range between 420 °C and 800 °C (Fig. 5.1). This treatment determines the critical temperature at which the crystallization of the ilmenite phase of $NiTiO_3$ is obtained.

The diffraction patterns of the samples measured from room temperature up to 420 °C are identical between them. For this reason, measurements carried out at temperatures below 420 °C are not displayed in Fig. 5.1. At this temperature, broad peaks matching the bunsenite phase of NiO are observed. At 500 °C, occurs a very slight change in the relative intensity and FWHM.

Based on previous reports by other groups, the formation of the ilmenite phase was expected around 600 °C, and in order to determine the critical temperature with a good accuracy, the temperature was increased by steps of 10 °C from 550 °C to 700 °C. The results obtained for 420, 550, 600, 650, 660, 670, 680, 690, 700, 750 and 800 °C are displayed in Fig. 5.1. There, it can be seen that at 650 °C appears a diffraction peak at 25° corresponding to the anatase phase of TiO_2 (the fraction of this phase is not very high in any of the analyzed cases, and it decreases as the temperature goes beyond 670 °C, see Fig. 5.1, or as the annealing time increases while fixing the temperature at 650 °C, see Fig. 5.2. On the other hand, the diffraction lines, corresponding to the ilmenite phase, are also evident at 650 °C. For this reason, the critical temperature for the formation of the ilmenite phase was considered to be 650 °C.

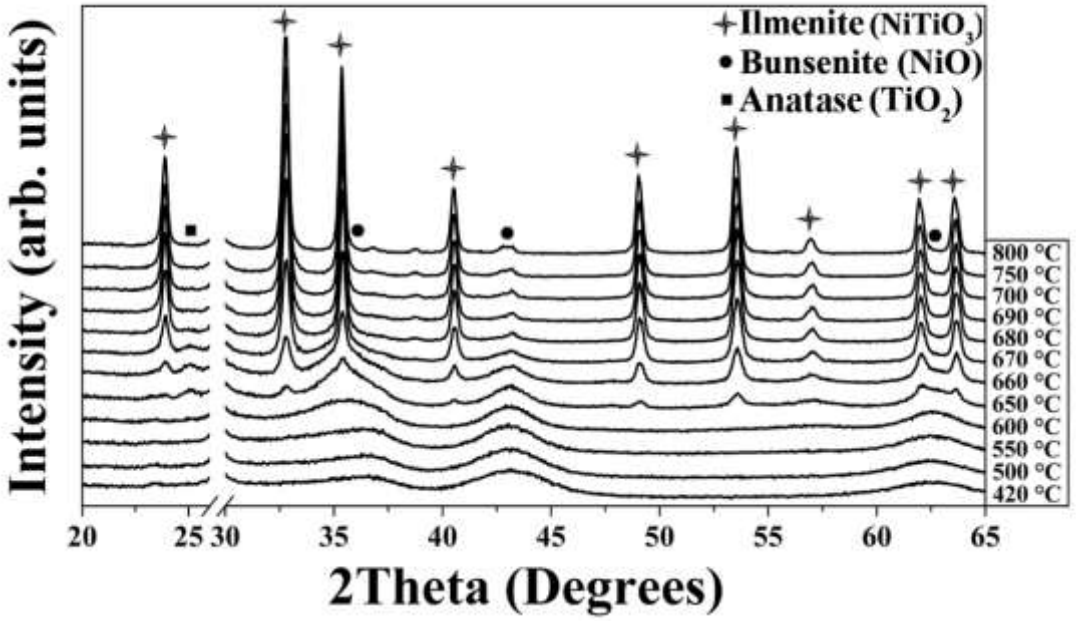

Fig. 5.1 *XRD patterns for samples annealed in-situ at temperatures ranging from 420 to 800 °C.*

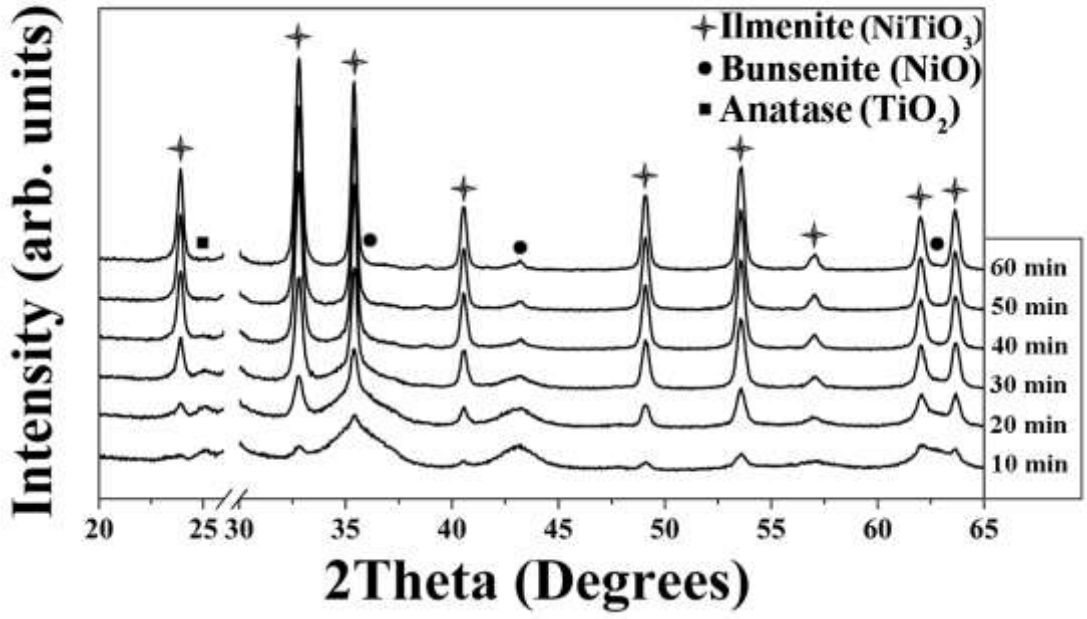

Fig. 5.2 *XRD patterns for samples annealed in-situ at a fixed temperature of 650 °C varying the annealing time.*

In addition, a second set of experiments were carried out in a similar manner with the temperature fixed at 650 °C and a scan was taken every 10 minutes. The results of this analysis can be seen in Fig. 5.2.

The next step was to determine the annealing time at which the presence of ilmenite is maximum and the presence of anatase and bunsenite is minimum. To do this, the area under the curve of the main reflection peaks was evaluated for the selected time durations of 10, 20, 30, 40, 50 and 60 minutes. The principal diffraction lines for each phase was considered to be 25° for anatase TiO2; 33° for ilmenite $NiTiO_3$; and 43° for bunsenite NiO. A plot of area under the curve vs annealing time is showed in Fig. 5.3.

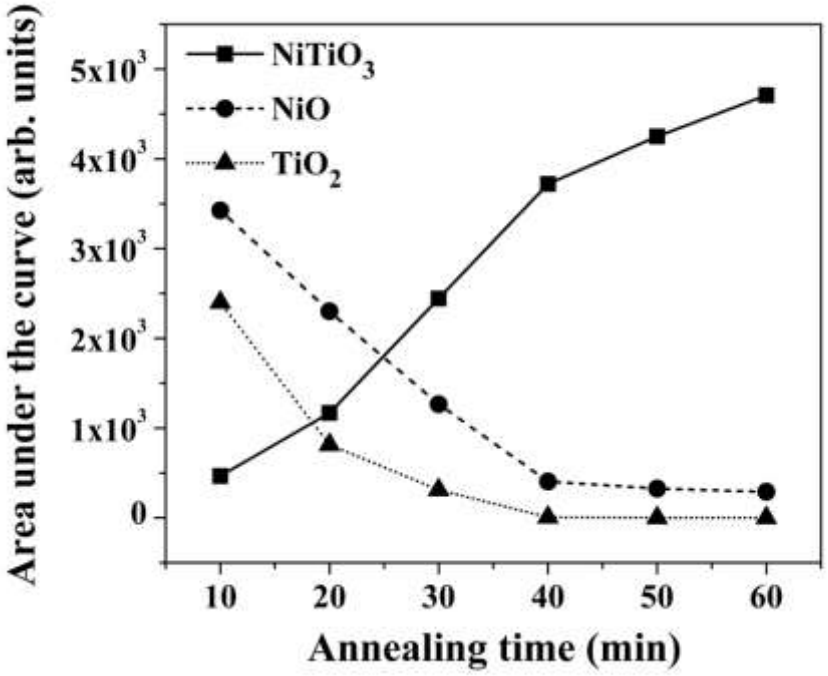

Fig. 5.3 *Area under the curve of the main diffraction peaks for each phase vs annealing time at a fixed temperature of 650 °C.*

According to the above analysis, it was determined that an annealing time of 60 minutes at 650 °C was enough to ensure the formation of the ilmenite phase of $NiTiO_3$ with very low traces of secondary phases, *i.e.* anatase (TiO_2) and bunsenite (NiO). The Rietveld method

was not used in this analysis because the low intensity and broadening of the diffraction lines, coming from anatase and bunsenite, made it difficult to distinguish these peaks from the background.

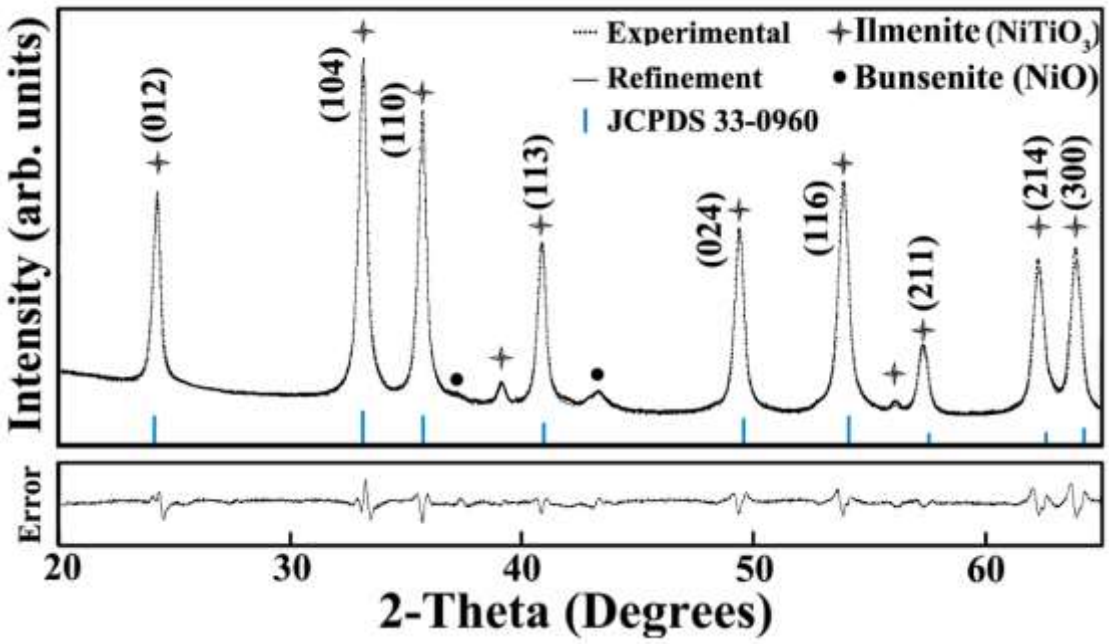

Fig. 5.4 *Rietveld analysis of the XRD patterns for sample P3-SG-A650C.*

For further reference, the powders annealed at 650 °C during 60 minutes will be labelled P3-SG-A650C. On this family of samples, *i.e.* P3-SG-A650C, a Rietveld refinement of the XRD spectra was performed (see Fig. 5.4), allowing the determination of the volume fraction of the phases present in the sample, the lattice parameters and the mean crystallite size. The volume fraction of the phases determined are: 97.8 ± 1.3 % of ilmenite and 2.2 ± 1.7 % of bunsenite. The lattice parameters are consistent with the ones of the previous samples and the standard reference JCPDS 33-0960, being, a = b = 5.0323 ± 2 x 10^{-4} and c = 13.8161 ± 7 x 10^{-4}. The mean value for the crystallite size was found to be 25.7 ± 1.1 nm. All these information is summarized in Table 5.1.

Table 5.1 *Phase volume fraction, lattice parameters and crystallite size for P1-SG-A1350C and P3-SG-A650C.*

Sample	Phase Volume Fraction (%)	
	$NiTiO_3$	NiO
P1-SG-A1350C	98 ± 5	1.2 ± 2
P3-SG-A650C	97.8 ± 1.3	2.2 ± 1.7

Sample	$NiTiO_3$ Lattice Parameters (nm)		Crystal Size
	a = b	c	
P1-SG-A1350C	$0.503289 \pm 3x10^{-6}$	$1.37972 \pm 3x10^{-5}$	59.5
P3-SG-A650C	$5.0323 \pm 2x10^{-4}$	$13.8161 \pm 7x10^{-4}$	25.7

Observations by Electron Transmission Microscopy (TEM), Fig. 5.5, give sustainability to the results obtained by XRD. The TEM image at the 200 nm scale allows to observe the homogeneity of the particle size distribution, and the image at 50 nm scale exemplifies a particle having a size very close to the mean crystallite size determined by XRD. This confirms that the P3-SG-A650C particles seen by TEM are individually monocrystalline and that they are significantly smaller than the particles described in Chapter IV that reached greater sizes by agglomeration.

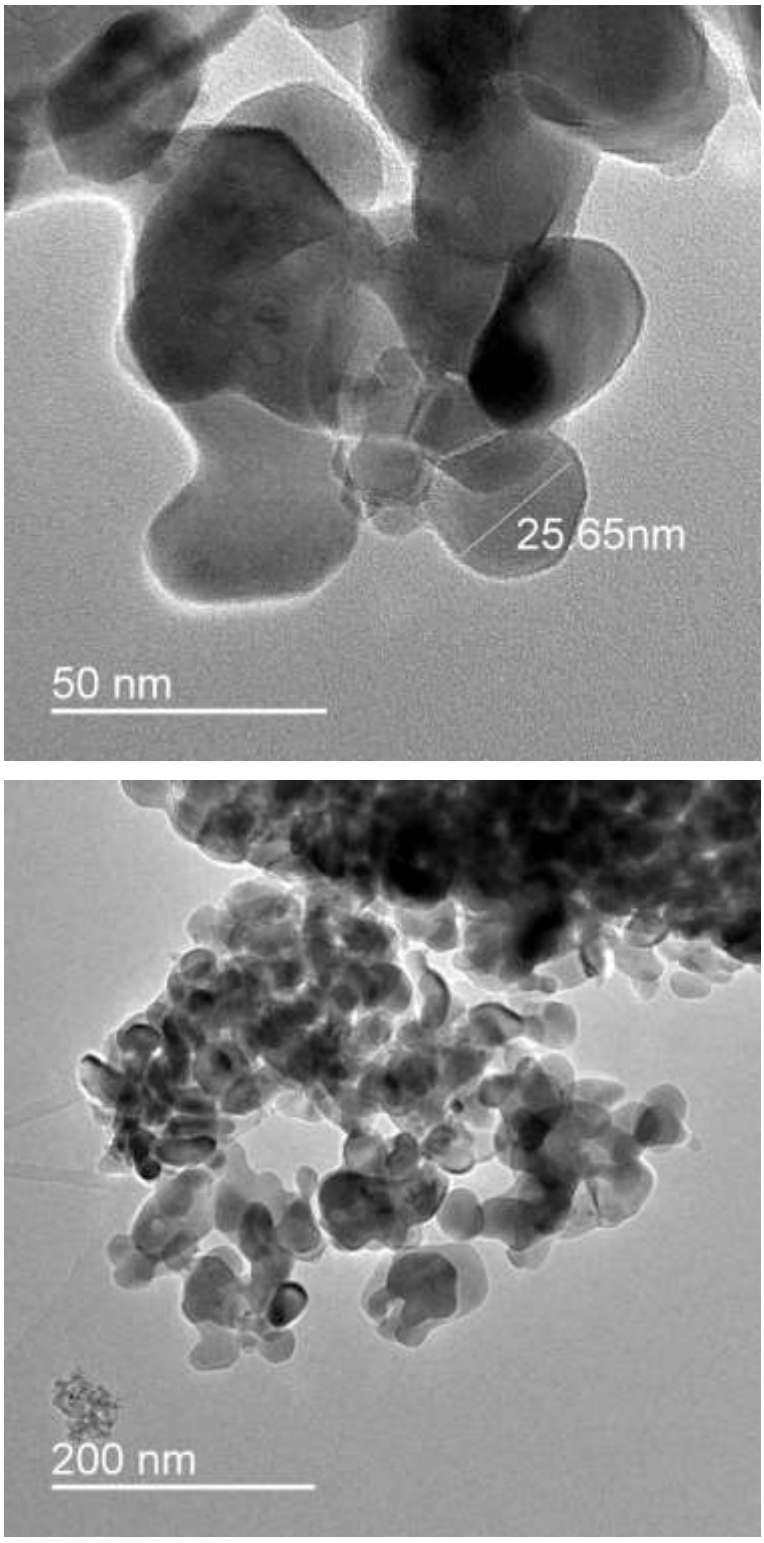

Fig. 5.5 *TEM images of sample P3-SG-A650C. On the bottom 200 nm scale is shown, on the top a 50 nm scale is displayed.*

2. RAMAN VIBRATIONAL ACTIVE MODES

The 10 active Raman vibrational modes of the ilmenite structure are situated as follows in powder P3-SG-A650C: 188.2 (A_g), 226.8 (E_g), 242.6 (A_g), 289.6 (E_g), 343.8 (E_g), 392.4 (A_g), 461.7 (E_g), 481.1 (A_g), 605.9 (E_g) and 705.5 (A_g) cm^{-1}. The experimental spectrum can be found in Fig. 5.6. By comparison with the Raman spectrum of sample P1-SG-A1350C (Chapter IV, Fig. 4.4, top right quadrant), the similarity is evident.

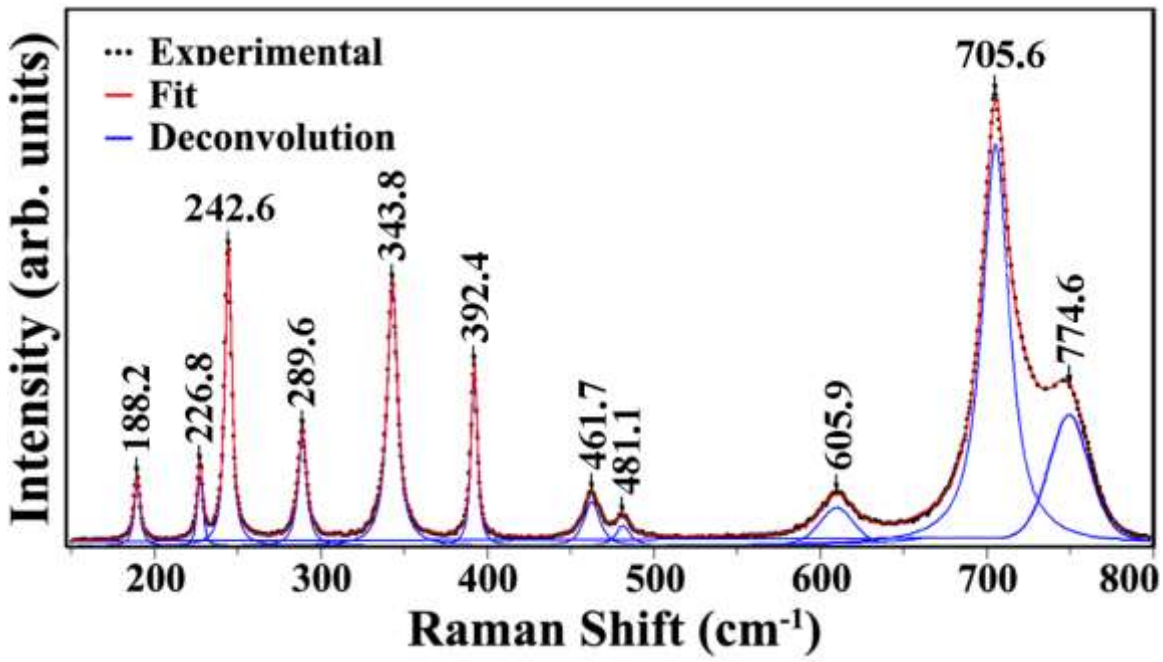

Fig. 5.6 *Raman active modes for sample P3-SG-A650C.*

The intensity of the Raman modes for both samples is almost identical. Only a small difference of a few cm^{-1} is observed in the position of the 10 active Raman lines between these samples.

The largest deviation between the two samples lies in the "shoulder" situated at 733.2 cm^{-1} for P1-SG-A1350C, and at 774.6 cm^{-1} for P3-SG-A650C. This Raman peak, whose the origin remains matter of debate, appears considerably more intense as well as shifted to the right for P3-SG-A650C relative to P1-SG-A1350C. A possible explanation for this peak, based on the theoretical calculations of Chapter II will be given in Chapter VII.

3. OPTICAL PROPERTIES

Following the same procedure used in the last chapter, the optical absorption bands were obtained by implementing the Kubelka-Munk model for diffuse reflectance spectroscopy. The absorption spectra for P3-SG-A650C and P1-SG-A1350C are displayed in Fig. 5.7. In both cases, three absorption bands can be clearly identified and located at approximately 400 nm, 800 nm and 1400 nm.

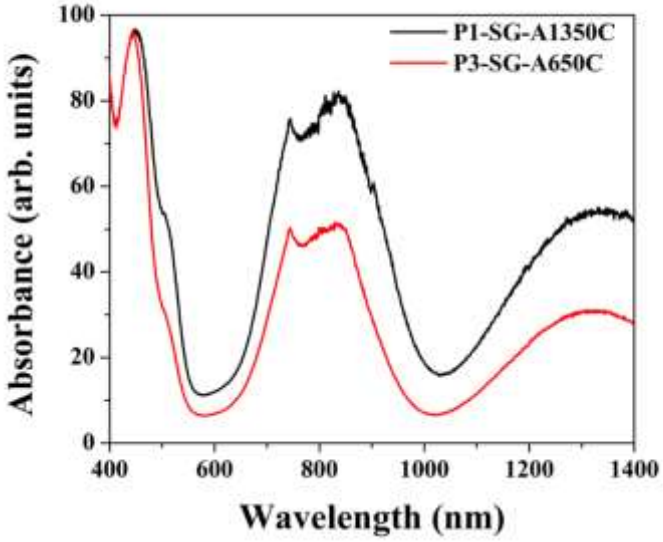

Fig. 5.7 *Optical absorption spectra of P3-SG-A650C (red) and P1-SG-A1350C (black).*

The Kubleka-Munk function ($F(R_{inf})$) was determined from the diffuse reflectance data and was used to plot it versus the photon energy, in this way, linear approximations were performed and the energy necessary for the electronic transitions at the absorption band edges was determined from the equation:

$$\left[F\left(R_{inf}\right)h\nu\right]^2 = C_1\left(h\nu - E_g\right) \tag{5.1}$$

The plot of equation (5.1) can be seen in Fig. 5.8 for P3-SG-A650C as well as for P1-SG-A1350C. In the case of P3-SG-A650C, two energy values corresponding to two electronic transitions are identified at approximately 2.28 and 2.53 eV as found in Table 5.2.

Table 5.2 *Band gap of the $NiTiO_3$ samples P1-SG-A1350C and P3-SG-A650C as determined from the Tauc plots of UV-Vis absorbance.*

Sample	Band-gap (eV)
P1-SG-A1350C	2.26 ± 0.01
P3-SG-A650C	2.28 ± 0.02

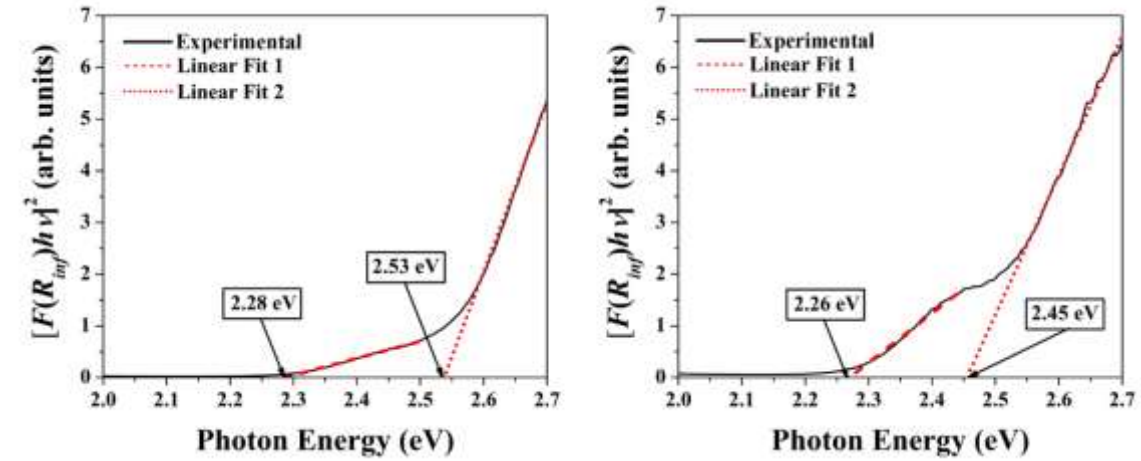

Fig. 5.8 *Tauc plot for P3-SG-A650C (left) and P1-SG-A1350C (right).*

Once again, the results of the samples annealed at 650 °C resemble the ones obtained for the samples annealed at 1350 °C.

CHAPTER V

4. CONCLUSIONS

The XRD and Raman results confirm the formation of nickel titanate powders with a high dregree of purity (~98%) after an annealing process at 650 °C for 60 minutes. The synhtesized powders present uniform particle size distribution of around 25 nm, which was observed in TEM images. By correlating TEM and XRD observations, the conclusion is that the particles observed by TEM are individually monocrystalline. From UV-Vis difuse reflectance measurements, a band gap of approximately 2.28 eV was determined, meaning that these samples are suited for visible light absorption.

The structural, vibrational and optical characteristics are very similar to those of sample P1-SG-A1350C from Chapter IV, with the advantage of requirering an annealing step at half the temperature and half the time. The lower temperature and shorter time length contribute to having considerable smaller particle sizes than the powders described in Chapter IV, which as a direct consecuence, would also improve the area-volume ratio, necessary for an efficient catalyst.

The catalytic response of P3-SG-A650C is discussed in Chapter VII.

CHAPTER V

CHAPTER VI: $NITIO_3$ THIN FILMS BY RF-SPUTTERING

Polycrystalline nickel titanate thin films were deposited on silicon substrates by the radio-frequency (rf) sputtering method using $NiTiO_3$ targets, which in turn were sintered from powders obtained by solid state reaction. The deposition parameters such as rf-powers, partial pressures of argon and oxygen, as well as substrate temperatures were optimized to ensure the homogeneous and stoichiometric composition of $NiTiO_3$ thin films. Post-synthesis annealing at suitable temperatures and time durations was realized to stabilize the ilmenite structure with improved crystalline features deduced from structural and vibrational investigations by using XRD and Raman spectroscopy. The surface roughness and thin film microstructure were characterized by AFM which points out the organization of the film surface. Representative films with ilmenite structure and defined surface microstructure and optical absorbance were tested as visible light driven heterogeneous photocatalysts for the degradation of organic dyes, these results will be discussed in Chapter VII.

CHAPTER VI

1. STRUCTURAL INVESTIGATIONS

The synthesized and annealed $NiTiO_3$ thin films were investigated by XRD as a function of the synthesis conditions and the annealing treatments performed at different temperatures and durations. The synthesis parameters leading to homogeneous films with an appropriate thickness were optimized at 94/0 sccm for Ar/O flow, 0.1 mbar for pressure and 50 W for rf-power, respectively, with deposition at room temperature. Different films were investigated for different annealing temperatures at 800 °C, 900 °C, 1000 °C and 1100 °C for 2 hours. In addition, a sample annealed for 4 hours at 800 °C and another annealed for 6 hours at 900 °C were also characterized in order to observe the role of annealing conditions in the crystalline order. The XRD patterns summarized in Fig. 6.1 indicate the occurrence of a good crystalline structure for annealing at 1000 °C for 2 hours under air. When the temperature is increased up to 1100 °C, the structure seems to be degraded (in comparison with the film annealed at 1000 °C) and an intense peak at $2\theta = 21.7°$ appears. This peak has been attributed to the formation of a crystalline layer of SiO_2 with a cristobalite structure (JCPDS PDF no. 39-1425) at the interface between the $NiTiO_3$ film and the silicon substrate. This was confirmed from the XRD patterns of thin films deposited by a complex process of co-sputtering from two metallic targets (Ni, Ti) on fused quartz substrates, well stable at temperature higher than 1100 °C.[114]

The quantitative analysis of the XRD patterns from the rf-sputtered thin films shows well defined and intense peaks located at 2θ positions of 24.2°, 33.2°, 35.7°, 40.9°, 49.5°, 54.11°, 57.5°, 62.55°, and 64.17°. According to the standard structural reference JCPDS No. 33-0960 related to the ilmenite $NiTiO_3$ phase, the above data are assigned to the planes (012), (104), (110), (113), (024), (118), (211), (214) and (300), respectively. Fig. 6.2 shows the XRD patterns of the $NiTiO_3$ thin film with optimized deposition conditions and annealed at 1000 °C for 2 hours under air. This film will be referred below as the representative film and will be investigated by Raman, AFM, and optical methods and tested in photocatalytic reactions.

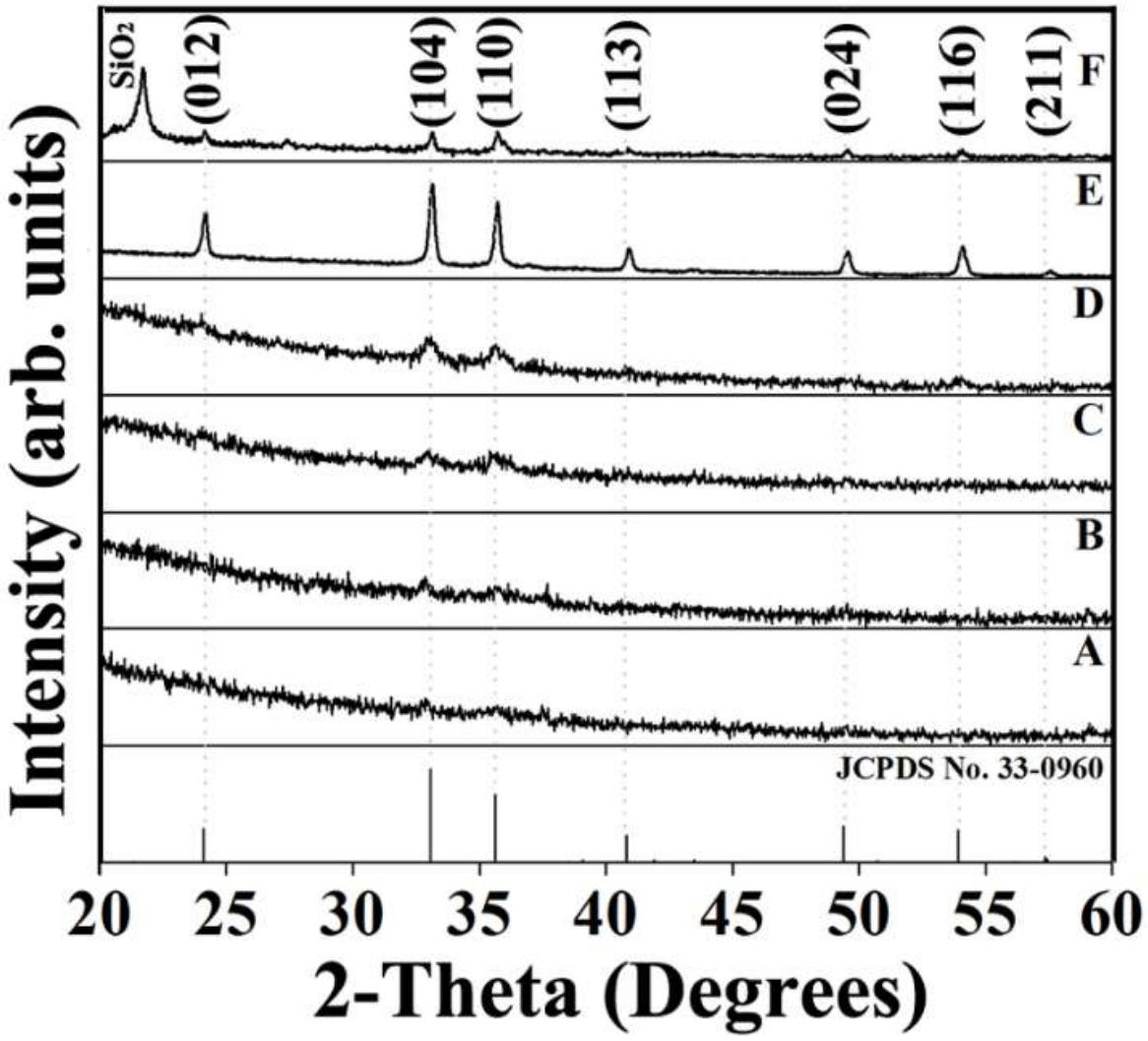

Fig. 6.1 *XRD patterns of $NiTiO_3$ thin films deposited on Si substrates annealed at different temperatures and durations under air. A) Annealed at 800 °C for 2 hours. B) Annealed at 800 °C for 4 hours. C) Annealed at 900 °C for 2 hours. D) Annealed at 900 °C for 6 hours. E) Annealed at 1000 °C for 2 hours. F) Annealed at 1100 °C for 2 hours.*

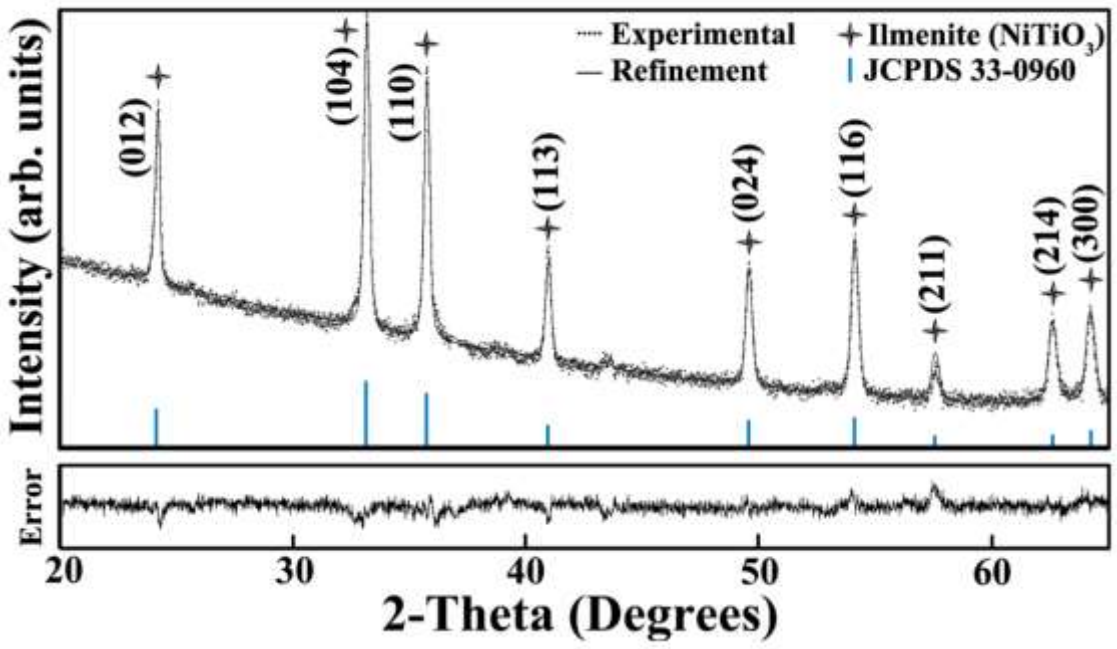

Fig. 6.2 *XRD refinement of a representative $NiTiO_3$ thin film deposited on a Silicon substrate and annealed at 1000 °C for 2 hours in air as a pure ilmenite phase by using the Rietveld method. The standard reference JCPDS No. 33-0960 is shown.*

The software Material Analysis Using Diffraction (MAUD) v2.33 was used for the refinement of the XRD patterns of the representative $NiTiO_3$ film. As seen in Fig. 6.2, the diffraction patterns did not show any secondary phases such as rutile (TiO_2) or bunsenite (NiO) along with the ilmenite phase of nickel titanate. The refinement data summarized in Table 6.1 for the film features are 154 ± 3 nm for the average crystallite domain size, 1.4×10^{-3} for the microstrain, and the lattice parameters were close to the standard values for the ilmenite structure, *i.e.* a = b = 5.03 Å and c = 13.80 Å. The 2θ positions of the diffraction lines are in agreement with those of the JCPDS reference for the ilmenite structure (Fig. 6.1). The analysis of the FWHM of the diffraction line yields an estimate of the crystalline domain sizes in the order of 154 nm. This value indicates the absence of size effects on the broadening of the diffraction line and with regard to the low value of microstrain (1.4×10^{-3}), we then conclude the good quality of the crystalline phase of the representative $NiTiO_3$ film.

Table 6.1 *Structural, morphological and optical features of the representative $NiTiO_3$ thin film obtained by rf-sputtering and annealed at 1000 °C under air.*

Sample	Crystal Size (nm)	Microstrain	$NiTiO_3$ Lattice Parameters (Å)	
			a = b	c
$NiTiO_3$	154 ± 3	$1.40(2)x10^{-3}$	5.0266(3)	13.7889(8)

Sample	Thickness (nm)	Roughness (nm)	Area (nm^2)	Refractive Index	Band Gap (eV)
$NiTiO_3$	1500	19.2	68.7	2.42	2.47

With the purpose of obtaining the optical transmission spectra, $NiTiO_3$ thin films were deposited on quartz substrates under the same conditions and with exactly the same post deposition annealing as the films deposited on Silicon substrates. As it was obtained for the films on silicon, pure ilmenite $NiTiO_3$ was obtained after an annealing at 1000 °C during 2 hours, with no traces of secondary phases. Nevertheless, some differences are obvious between them from the XRD patterns seen in Fig. 6.3.

Indeed, for the films deposited on quartz, a mean crystallite size is one order of magnitude smaller than the one for the films deposited on silicon. The crystallite size of the films on quartz was 18 nm in comparison to 150 nm for the films on silicon as seen in Table 6.1.

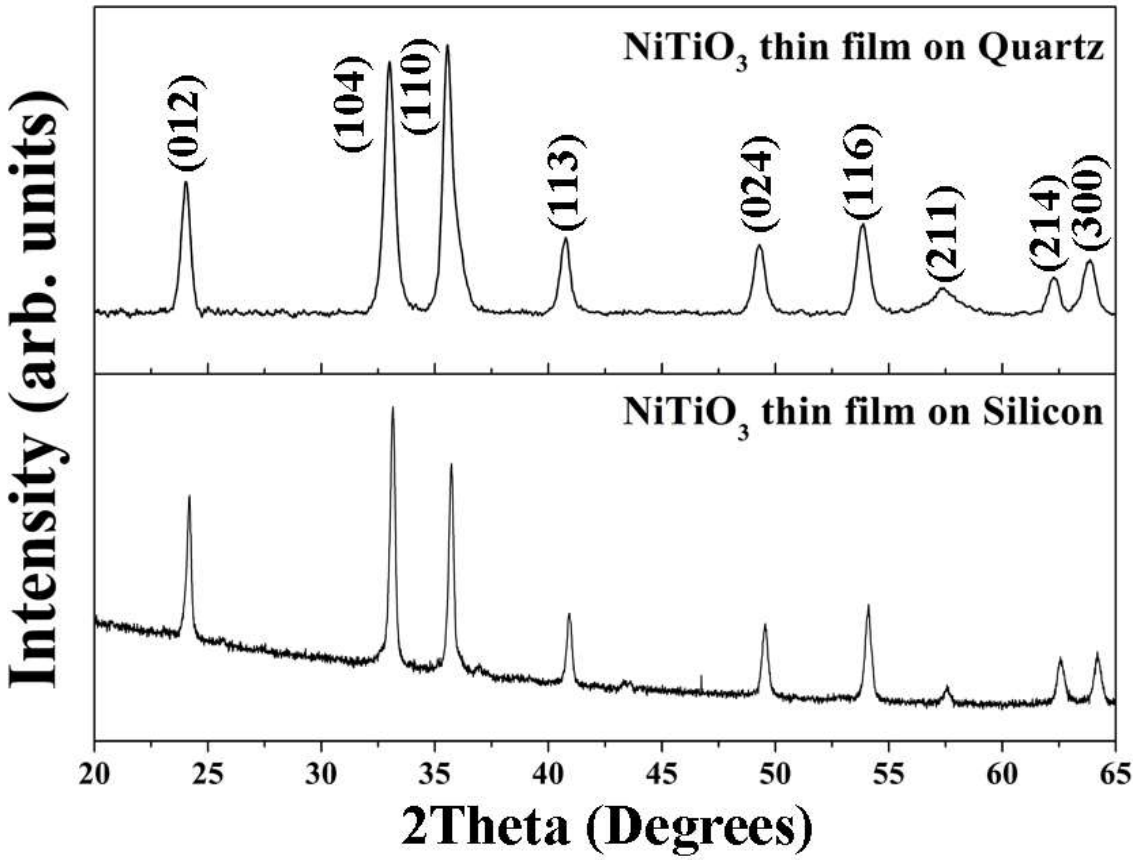

Fig. 6.3 *X-Ray diffraction patterns of the $NiTiO_3$ thin films deposited on quartz substrates (top) and silicon substrates (bottom).*

2. RAMAN INVESTIGATIONS OF VIBRATIONAL ACTIVE MODES

The ilmenite structure of $NiTiO_3$ possesses the space group $R\bar{3}$ (C_{3i}^2) with the oxygen atoms being tetra-coordinated to two tetravalent Ti and to two bivalent Ni cations (Fig. 6.4). It can be theoretically predicted that the optical normal modes of vibrations at the Brillouin zone center have the following symmetries $5A_g + 5E_g + 4A_u + 4E_u$ (in addition to the $A_u + E_u$ zero frequency acoustic modes).[96,98,107]

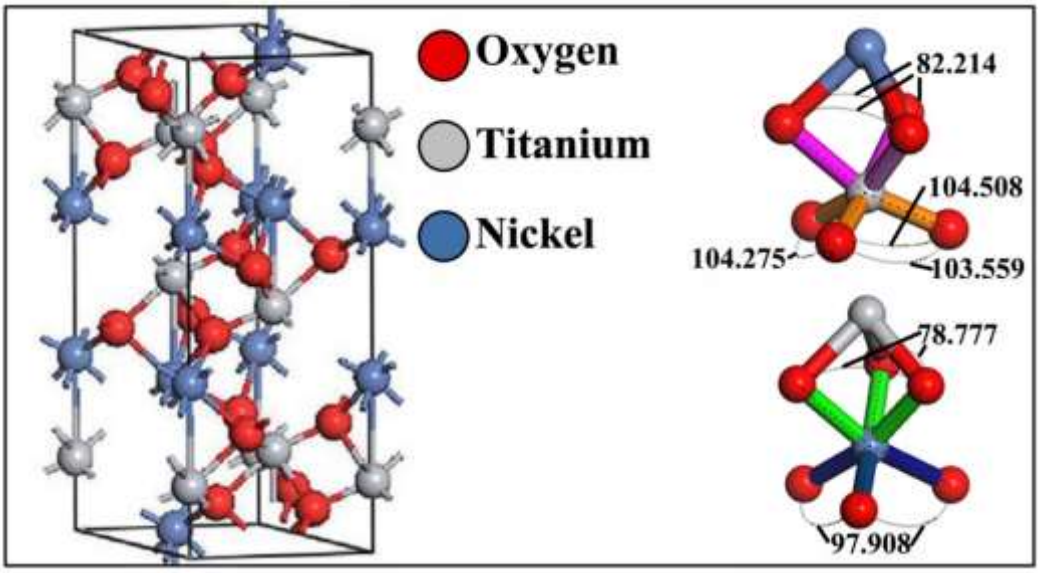

Fig. 6.4 *Representation of the $NiTiO_3$ ilmenite unit cell and local environments of Ti and Ni.*

Therefore, ten Raman active modes ($5A_g + 5E_g$) are expected with each E_g mode being twofold degenerated ($E_g = E1_g + E2_g$) along with the eight IR active modes ($4A_u + 4E_u$).

From the experimental spectra reported in Figs. 6.5 and 6.6, and excluding the 520 cm^{-1} band due to the silicon substrate, the Raman modes of $NiTiO_3$ are assigned as follows in cm^{-1}: 189.6 (A_g), 227.6 (E_g), 245.7 (A_g), 290.2 (E_g), 343.3 (E_g), 392.6 (A_g), 463.4 (E_g), 482.7 (A_g), 609.7 (E_g) and 705.9 (A_g).

This assignment is proposed by comparing the relative intensities of the Raman bands between parallel and cross polarizations (Fig. 6.6). The thickness of the sample (less than 1500 nm) prevents the occurrence of significant beam depolarization induced by

birefringence, as experimentally shown. On the other hand, for cubic symmetry, the diagonal elements of the Raman scattering tensors of A_g modes have the same value and the off-diagonal elements are zero, so that they vanish in cross polarization. In the case of ilmenite, with rhombohedral symmetry, the diagonal elements of the scattering tensor may be different but in view of the structure, they can be supposed to be fairly close to each other. Therefore, under cross polarization, the A_g Raman peaks are expected to undergo more important intensity decreases than the E_g ones, as observed in Fig. 6.6.

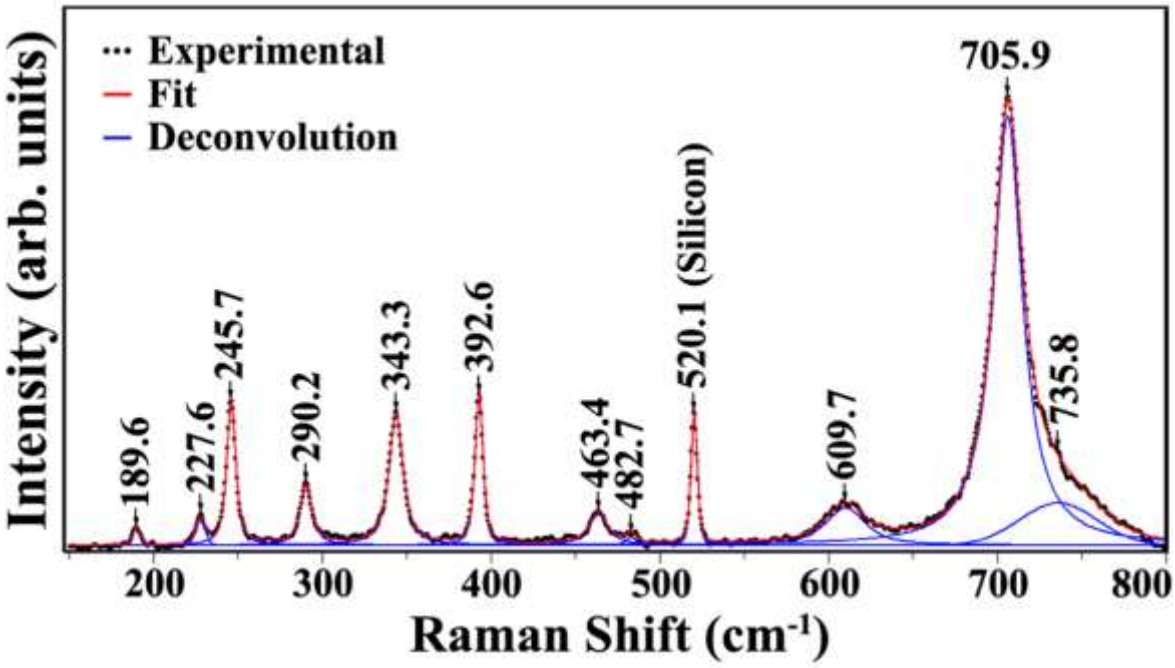

Fig. 6.5 *Experimental and simulation of the Raman spectrum of the representative $NiTiO_3$ thin film annealed at 1000 °C for 2 hours in air atmosphere.*

The Raman mode attribution can also be done by comparison with the Raman spectra of isomorphous $MgTiO_3$ as it was proposed by Wang et al.[107] In both materials, the Raman active modes can be described as symmetric Ti–O stretching vibrations, bond-bending of O–Ti–O, and translations of the divalent cations with respect to the oxygen groups.[115] The former vibrations are expected to be set in the same frequency range since the structures are close. On the other hand, the vibrations dominated by the divalent cation displacements are

expected to undergo frequency shifts related to mass effects and would be roughly proportional to the square root of the ratio between the Ni and Mg atomic masses. Thus, the A_g mode at 306 cm^{-1} in $MgTiO_3$ is predicted at 197 cm^{-1} in $NiTiO_3$ which matches fairly well with the experimental line measured at 189.6 cm^{-1}.

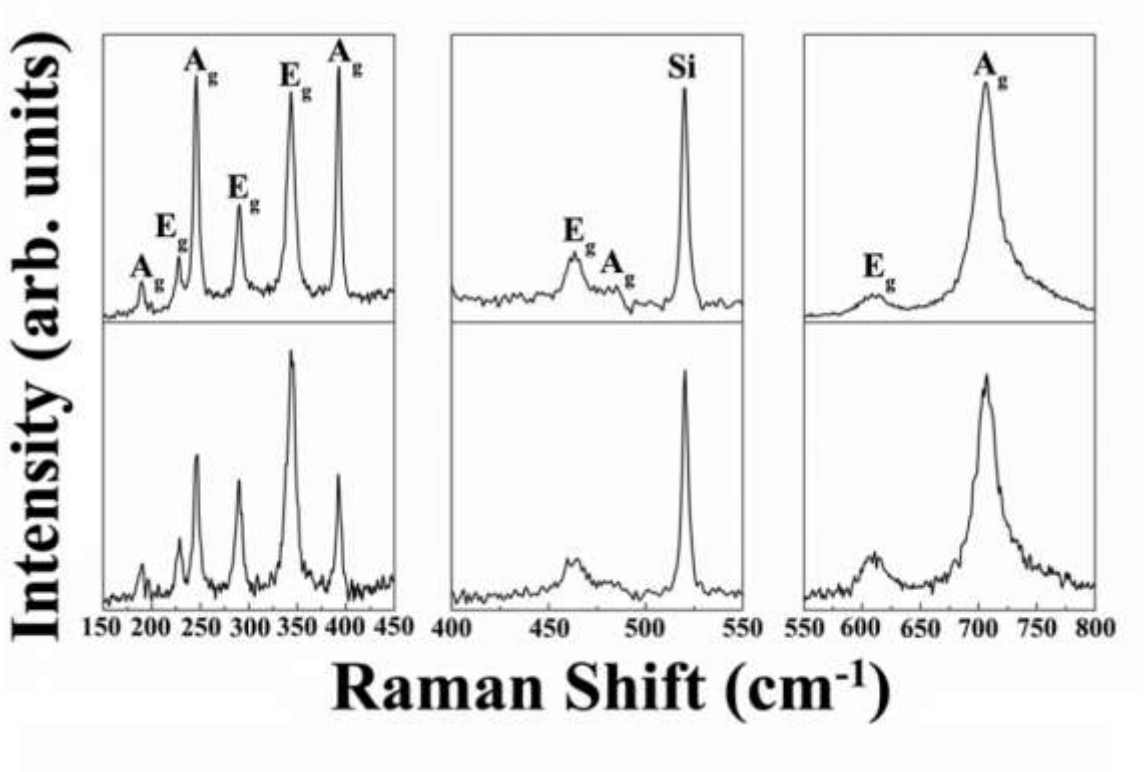

Fig. 6.6 *Raman spectra collected from a representative $NiTiO_3$ thin film annealed at 1000 °C for 2 hours in air atmosphere using: parallel polarization (top) and cross polarization (bottom).*

Since $MgTiO_3$ and $NiTiO_3$ are isostructural, the other modes that mostly involve Ti–O vibrations are expected in the same frequency range. Thus, the Ag mode at 245.7 cm^{-1} can be attributed to the vibrations of Ti atoms along the z axis and the Ag modes at 398 and 482.7 cm^{-1} can be assigned to a breathing-like stretching of the Ti centered oxygen octahedra.

A typical feature in the Raman spectra of the ilmenite structure lies in the appearance of a very strong band at high frequencies (*e.g.* 705.9 cm^{-1}). This Raman peak can be associated with a mode that is inactive in the similar but more symmetric corundum structure ($R\bar{3}c$ = D_{3d}^6 space group), which implies that this mode arises from the symmetric stretching of TiO_6

octahedra.[98] The Eg mode at 227.6 cm^{-1} can be considered as the asymmetric breathing vibration of the oxygen octahedra and the ones at 290.2 and 343.3 cm^{-1} can be described by the twist of oxygen octahedra due to vibrations of the Ni and Ti atoms parallel to the xy plane. The E_g modes at 463.4 and 609.7 cm^{-1} are assigned to the asymmetric breathing and twist of the oxygen octahedra with the cationic vibrations parallel to the xy plane.

In addition to these first-order Raman lines, a weak and broad signal (already reported) is observed around 735.8 cm^{-1}. A similar signal that appears as a shoulder of the highest frequency mode is also observed in the isomorphous $MgTiO_3$.[96,98,107] Its origin remains a matter of debate. In our recent work dealing with theoretical modelling and numerical simulations of the structural, vibrational and electronic structures of $NiTiO_3$,[115] our analysis suggests that this signal may arise from the occurrence of a small fraction of an amorphous phase. The involvement of vibrational density of states gives rise to broad features that would lead to the asymmetry of the A_g band, *i.e.* similar to the observed shoulder in the considered Raman band. The amorphous fraction may be accounted for by the high specific surface of the grains that compose the films as illustrated below by AFM observations.

3. SURFACE CHARACTERISTICS

In the case of heterogeneous photocatalysis, the contact surface between the photocatalyst and the surrounding media plays a key role in the efficiency of the photocatalytic reactions. The microstructure and morphologies of the grains define the roughness of the surface that monitors the contact between the active media. Also, the characterization of the topology of the film is an important factor and atomic force microscopy can be used for its evaluation versus the synthesis and treatment conditions. Thus, the representative sputtered thin film was investigated by AFM. The value of the roughness and the probed surface area for the optimized thin films were estimated to be 19.2 nm and 68.7 μm^2, respectively. The relevant morphology values are summarized in Table 6.1, and Fig. 6.7 shows the surface image of the representative $NiTiO_3$ thin film. The AFM observations indicate the occurrence of a rough surface organized as nano-islands with high specific surfaces. Such organization may contribute to the enhancement of the photocatalysis efficiency of such thin films as discussed below.

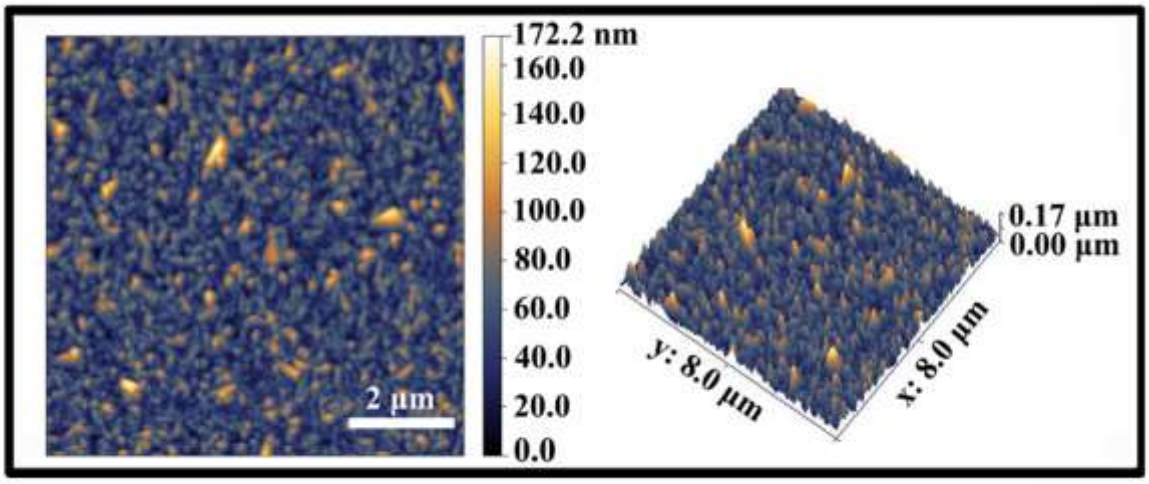

Fig. 6.7 *AFM surface image of a representative $NiTiO_3$ thin film annealed at 1000 °C for 2 hours in air atmosphere, RMS = 19.2 nm, area = 68.7 μm^2.*

CHAPTER VI

4. OPTICAL PROPERTIES

The experimental interferometry diagram was recorded on the ilmenite structure of the representative $NiTiO_3$ thin film by using Filmetrics equipment monitored by the related software. Fig. 6.8 reports an example of the experimental and simulated interference diagram from the representative film. The fitting parameters were deduced as 1500 nm and 2.42 for the thin film thickness and refractive index, respectively. The relevance of the estimated thickness was confirmed by profilometry measurements.

For the optical absorption measurements, $NiTiO_3$ thin films deposited on quartz substrates were used. The absorption coefficient (α) was extracted from the UV-Vis optical spectra and used to plot $(\alpha h\nu)^2$ versus the photon energy ($h\nu$) in order to determine accurately the band gap of the material. From the Tauc plot depicted in Fig. 6.9, the extrapolation of the linear behavior to the ($h\nu$) axis allows us to determine a band gap of 2.47 eV. With such values, the obtained thin films absorb a fraction of visible range for photocatalysis reactions discussed in the forthcoming part. It is worth noting that the band gap about 2.25 eV is indeed involved in bulk 3D crystalline materials. For the representative film in this work, the roughness of about 19 nm and the mean crystallite size of 18 nm may lead to quantum confinement effects able to modify the band gap compared to the infinite crystal.

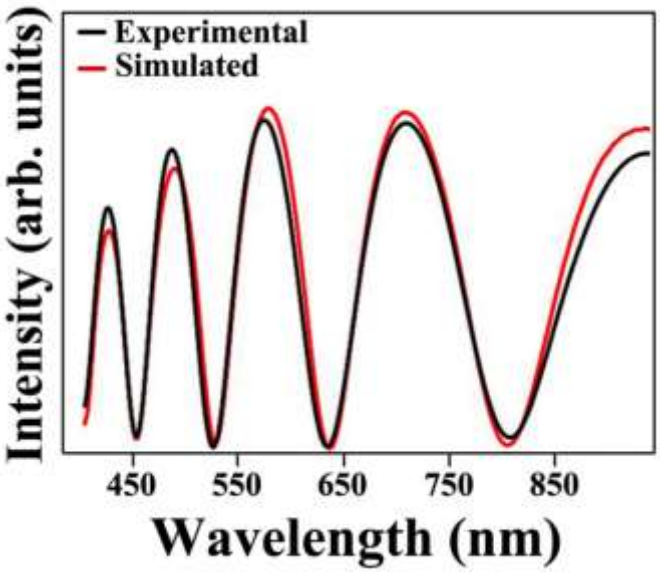

Fig. 6.8 *Representation of the optical interferometry pattern made by a $NiTiO_3$ thin film annealed at 1000 °C for 2 hours in air atmosphere. The values of the fit are summarized in Table 6.1.*

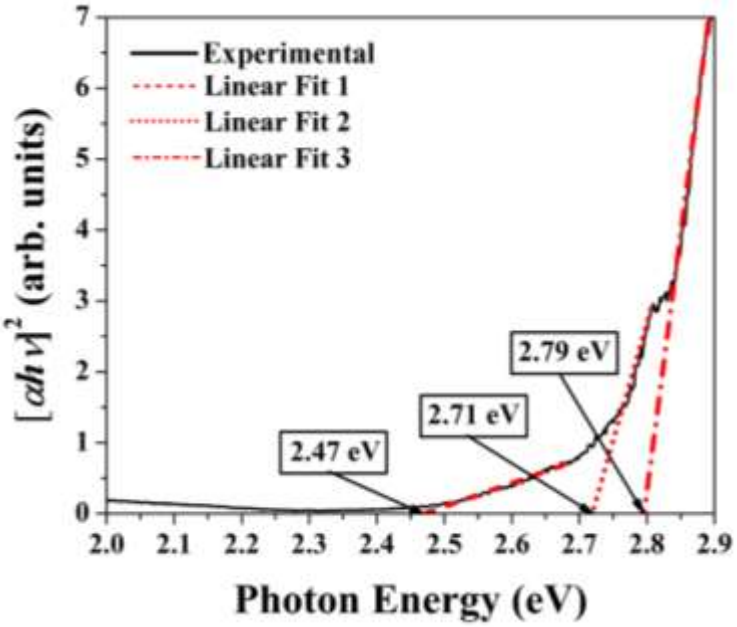

Fig. 6.9 *Tauc plot of a $NiTiO_3$ thin film deposited on a quartz substrate; the film was annealed at 1000 °C under air and exhibits the ilmenite structure.*

CHAPTER VI

5. CONCLUSIONS

A simple and fast synthesis route was developed to obtain $NiTiO_3$ thin films with a good crystalline quality and stable ilmenite structure. Solid state reaction was performed to obtain crystalline powders used as targets for the rf-sputtering method. Appropriate deposition conditions and post-synthesis treatment were determined to obtain thin films with controlled features. Thus, optimized deposition conditions and annealing lead to diffraction patterns of the ilmenite structure without any additional phase. Vibrational properties were investigated by Raman spectroscopy with the identification and exhaustive discussion of the assignment made for all the active modes related to the $R\bar{3}$ space group. The surface morphology and roughness were characterized by AFM microscopy. These features characterize the contact surface which can be exploited in the photocatalysis reactions considered in this work through the degradation of organic dyes in aqueous solutions discussed in Chapter VII.

CHAPTER VII: PHOTOCATALYTIC AND ELECTROCATALYTIC RESPONSES OF $NITIO_3$

In precedent chapters the fabrication methods and major physical features of nickel titanate powders and thin films were described. It was shown that the synthesized materials present features that are suitable for photocatalysis.

It has also been discussed in Chapter I that in order to test the photocatalytic potential of certain material it is possible to use solutions with organic dyes as probe molecules and measure their degradation by analyzing the decrease in intensity of the absorption spectra of the solution containing the dyes.

The first section of this chapter is dedicated to discuss the degradation of methylene blue (MB) using $NiTiO_3$ thin films (as described in Chapter VI) as photocatalysts irradiated by visible light.

In a related matter, the electrochemical oxidation of methanol has been discussed in Chapter I and it has been mentioned that methanol can be used in alkaline fuel cells (AFC) based on selective catalyst.[116]

The finding of a material capable of oxidizing methanol that is not based on platinum is a topic of intense research. Pt-based alloys have been considered the most active electrodes for the electro-oxidation of methanol, however, in addition to the high cost and limited supply of Pt, Pt-based electrodes generally become less active due to surface degradation by the reaction intermediates.[117,118] Therefore, investigating low cost non-noble metal-based materials for catalysis is of great interest. In this sense, Nickel has been used to enhance the electrocatalytic activity in oxidation reactions of diverse molecules in alkaline media due to its surface oxidation properties. In sight of these facts, the electro-oxidation of methanol has been tested using the $NiTiO_3$ powders described in chapter V (P3-SG-A650C) as catalyst in alkaline medium, since an alkaline media is considered to be superior in comparison to an acid solution from the point of view of kinetics and material stability.[118] The second part of this chapter is related to these investigations.

CHAPTER VII

1. PHOTOCATALYTIC ACTIVITY OF $NiTiO_3$

The discussion in Chapter VI concerns the obtaining of polycrystalline nickel titanate thin films deposited on silicon substrates by the radio-frequency (rf) sputtering method. The deposition parameters of the rf-sputtering such as rf-power, partial pressures of argon and oxygen, as well as substrate temperatures were optimized to ensure the homogeneous and stoichiometric composition of $NiTiO_3$ thin films. Post-synthesis annealing at suitable temperatures and time durations was realized to stabilize the ilmenite structure with improved crystalline features deduced from structural and vibrational investigations by using XRD and Raman spectroscopy. The surface roughness and thin film microstructure were characterized by AFM which points out the organization of the film surface. It was concluded that $NiTiO_3$ thin films with the ilmenite structure and a defined surface microstructure and optical absorbance suited for visible absorption were obtained. In the forthcoming paragraph, the test of representative thin films as visible-light-driven heterogeneous photocatalysts for the degradation of methylene blue will be discussed to evaluate the photocatalytic efficiency for this class of material.

a. Experimental details

Photocatalytic reactions were investigated through the degradation of methylene blue (MB) by $NiTiO_3$ films immersed in aqueous solutions and irradiated by a UV-vis 200 W Xenon arc lamp (set at 60 W). The initial concentration of the MB contaminant was 10^{-5} M. The degradation of the dyes was evaluated by means of collecting the absorption spectrum of the colored solution every 30 minutes during a period of 5 hours. The experimental setup consists of a glass beaker containing the MB solution with the specified molar concentration (under continuous magnetic stirring to ensure the homogenization of the MB charged solution). The thin film was set in a holder with its top surface directed in front of the collimated light beam. This setup can be visualized in Fig 7.1.

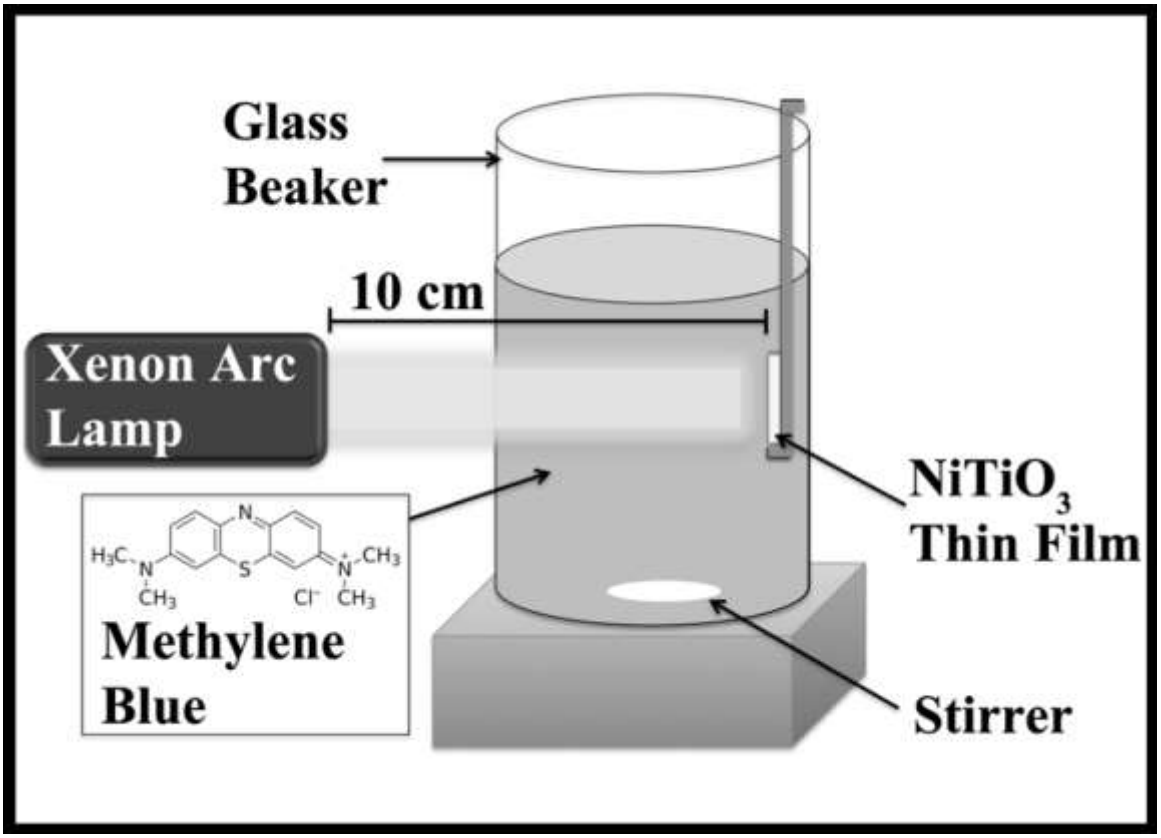

Fig. 7.1 *Photocatalytic experimental setup.*

b. Results and discussion

The photocatalysis experiments were carried out by using MB dyes with a concentration of 10^{-5} M in water and a representative $NiTiO_3$ thin film as a photocatalyst. Under light radiation from a Xenon arc lamp (UV-Vis-60 W) directed on the sample surface about 4 cm^2, the degradation of MB was monitored by the optical absorption measured at steps of 30 minutes for 5 hours. As shown in Fig. 7.2, left panel, the absorption spectra undergo a continuous decrease as a function of the light exposure time and demonstrate the photocatalytic activity of $NiTiO_3$. It can be seen that after 5 hours of irradiation, 60% of the initial concentration of MB dyes was destroyed in the solution.

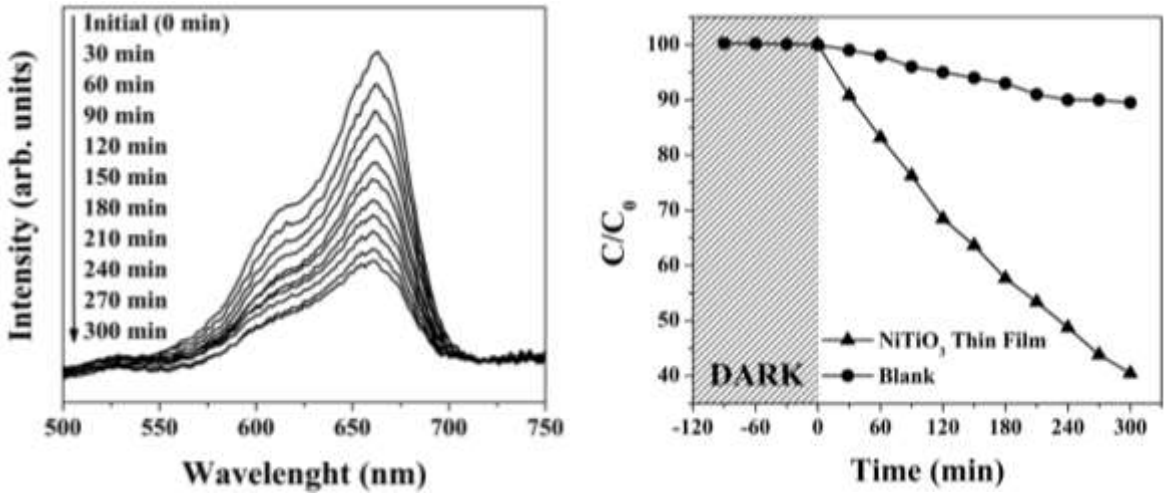

Fig. 7.2 *Optical absorption spectra of the MB charged solution during the photocatalytic process (left panel). Absolute MB concentration vs time (right panel). The dashed plot area shows the results in dark conditions and the white section displays the experimental measurements under illumination.*

The ratio between the absolute concentration at a given time (C) and the initial concentration (C_0) was plotted versus time in the logarithmic scale

$$\ln\left[\frac{C}{C_0}\right] = f(t) \tag{7.1}$$

The behavior seen on the experiments is typical of a Langmuir-Hinshelwood kinetics.

$$r = \frac{dC}{dt} = \frac{a \cdot K_{ads}^{LH} \cdot C}{1 + K_{ads}^{LH} \cdot C} = kC \tag{7.2}$$

Where K_{ads}^{LH} is the Langmuir-Hinshelwood adsorption equilibrium constant, a is the pseudo-first order rate constant, and k is an observable rate constant defined as:

$$k = \frac{a \cdot K_{ads}^{LH}}{1 + K_{ads}^{LH} \cdot C} \tag{7.3}$$

Thus,

$$\ln\left[\frac{C}{C_0}\right] = kt \tag{7.4}$$

The linear semi-logarithmic plot was adjusted by using a first order kinetics as:

$$C = C_0 e^{-kt} \tag{7.5}$$

with the observable reaction rate constant estimated from the experiment (Fig. 7.3) to be $k = 0.3\text{x}10^{-2}$ min^{-1}.

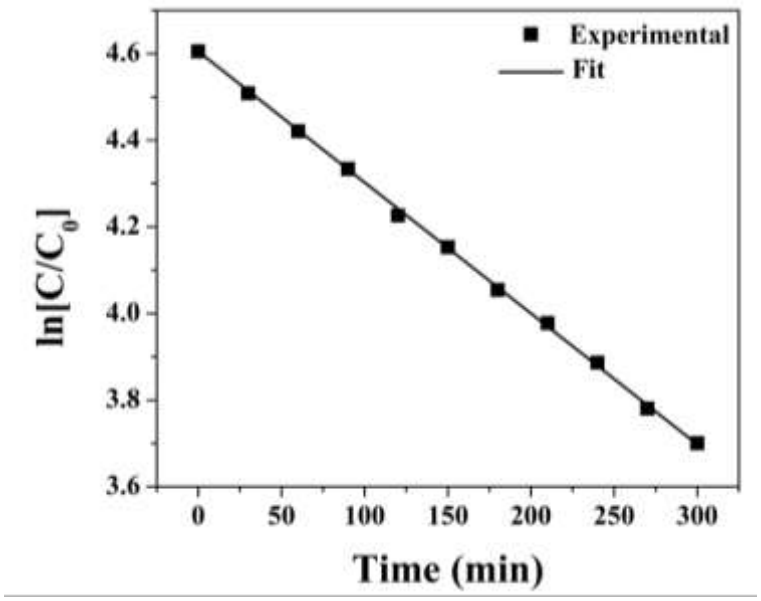

Fig. 7.3 *Kinetics of the photocatalytic degradation of MB by visible light irradiated $NiTiO_3$. The graph reports the semi-logarithmic plot of the normalized concentration C/C_0 versus irradiation time.*

The visible-light-driven photoactivity of $NiTiO_3$ is thus demonstrated in $NiTiO_3$ obtained by a simple synthesis procedure followed by suitable treatments to ensure ilmenite structure with a good crystalline quality. The photocatalytic efficiency is a matter of improvement through the increase of the concentration of photogenerated charge carriers and their lifetime. Increasing the charge carriers may be realized by suitable doping as metallic elements. In this context, substitutional doping is able to modulate the electronic structure of the host material. A second configuration of the metal doping process leads to the formation of clusters where critical phenomena such as surface plasmon resonance contribute to the enhancement of the efficiency of the photocatalytic reactions based on $NiTiO_3$.

2. ELECTROCATALYTIC ACTIVITY OF $NiTiO_3$

In Chapter V the formation of highly pure ilmenite $NiTiO_3$ by a modified Sol-Gel route with similar characteristics to that of sample P1-SG-A1350C (see Chapter IV) is described. The advantage of these new samples is that they require a post synthesis heat treatment at half the temperature and time than before.

Having a mean particle size considerably smaller, the catalytic activity of P3-SG-A650C should be better than its larger particle sized counterparts. Besides, the nanometric dimensions of the particles would also make it possible to distribute homogenously in a suspension for long time. This feature can be exploited to deposit a layer of $NiTiO_3$ on a support by drop-casting and use it as an electrode to evaluate the electrocatalytic activity of the sample. Specifically, the electro-oxidation of methanol has been selected as the reaction to be analyzed.

For the above-mentioned reasons, the electro-oxidation of methanol in alkaline media using P3-SG-A650C as catalyst will be discussed in this section.

a. Experimental details

The electrocatalytic activity of $NiTiO_3$ has been evaluated for the electro-oxidation of methanol in alkaline medium using cyclic voltammetry (CV) technique with sample P3-SG-650C as catalyst.

The electrochemical characterization was performed using a conventional three-electrode cell with a NaOH 0.1 M solution as the support electrolyte. The potential interval was fixed from -0.5 to 0.72 V/Ag/AgCl. The reference electrode (RE) and counter electrode (CE) were Ag/AgCl and a graphite bar, respectively. The working electrode (WE) contains a layer of the $NiTiO_3$ catalyst and it consists on a glass substrate coated on one face by a commercial conductive transparent oxide (*i.e.* ITO supplied by Sigma Aldrich) thin film, and a layer of $NiTiO_3$. For the deposition of the $NiTiO_3$ layer, a suspension was prepared, consisting on 20

mg of P3-SG-A650C, 700 µL of deionized water, 300 µL of ethanol and 80 µL of nafion. An aliquot of 100 µL was deposited on the conductive side of the substrate. The solvents were then evaporated at 100 °C during 15 minutes. The working surface of the electrodes was of 1 cm^2.

Methanol was used as probe molecule. The methanol concentration was varied from 0.001 to 1 M. The solutions were degasified using an Ar flow during 5 minutes in order to remove the dissolved oxygen. A scan rate of 20 mV/s was used for all measurements. The external potential was controlled with a potentiostat VersaStat 3 (Princeton Applied Research).

b. Results and discussion

In Fig. 7.4 the cyclic voltammetry of P3-SG-A650C in NaOH 0.1 M is shown. From this characteristic can be inferred that the electrochemical behavior of the $NiTiO_3$ electrode in alkaline solution is similar to that of metallic Ni.[119] Two peaks, located at 0.48 V (positive-going scan) and 0.4 V (negative-going scan), corresponding to the redox-couple processes Ni^{2+}/Ni^{3+} are clearly observed in Fig. 7.4. This redox process can be written as shown in equation (7.6).

$$Ni^{2+}(OH)_2 + HO^- \leftrightarrow Ni^{3+}(OH) + H_2O + e^- \quad (7.6)$$

The peak at 0.48 V (A_I), in the anodic region, corresponds to the transformation of the $Ni(OH)_2$ species to NiO(OH), *i.e.* the oxidation of Ni^{2+} to Ni^{3+}, and the peak located at 0.4 V (C_I), in the cathodic region, corresponds to the inverse process.[120,121] Passivation processes due to the spontaneous formation of NiO species (-0.3 V/Ag/AgCl) are not observed. The process around 0.55 V/Ag/AgCl is associated to OH^- species in excess that remained adsorbed on the surface due to the medium, followed by the evolution of oxygen.[122]

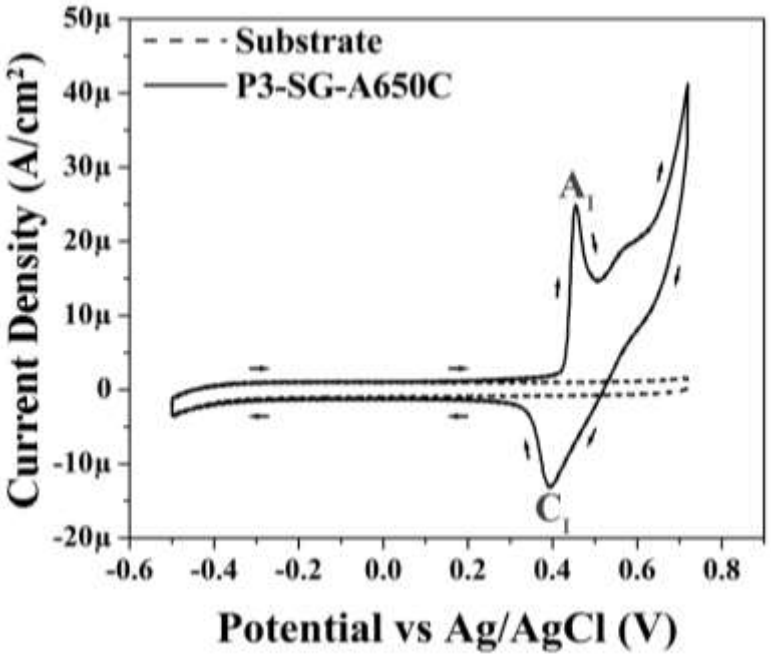

Fig. 7.4 *Cyclic Voltammetry of the ITO/Glass substrate (dashed line) and the P3-SG-A650C catalyst (solid line). NaOH 0.1 M was used supporting electrolyte. Scan rate of 20 mV/s.*

The oxidation of methanol (CH_3OH) was studied. This reaction could follow different paths obtaining CO_2 as product in all cases. However, depending on the selectivity of the catalyst, the reaction might stop at an intermediate step leading to different products other than CO_2, such as CO, $H_2C(OH)_2$, $HCOOCH_3$, or even a mixture of one of these with CO_2. The simplest reaction possible is expressed by equation (7.7).

$$CH_3OH + 6OH^- \rightarrow CO_2 + 5H_2O + 6e^- \qquad (7.7)$$

The cyclic voltammetry using methanol (CH_3OH) at different concentrations in alkaline media can be seen in Fig. 7.5, left panel. The effect of methanol concentration on the response is clear, it is observed that the intensity of the anodic peak increases considerably as the concentration of methanol does, going from ~70 µA at a methanol concentration of 0.001 M to ~1 mA at a methanol concentration of 1 M. When the methanol is introduced a new anodic peak appears at a more positive value of potential, corresponding to the oxidation of methanol, and this peak predominates over the Ni^{2+}/Ni^{3+} process.[123]

This leads to the conclusion of the occurrence of the electro-oxidation of methanol and that it takes place after the complete oxidation of $Ni(OH)_2$ to NiO(OH), meaning that the oxidation of methanol happens on the Ni^{3+} surface and that Ni^{3+} is the catalyst of the electro-oxidation of methanol, see equation (7.8).[124] This explains the reduction of the cathodic peak C_I with the increasing concentration of methanol, as seen in Fig. 7.5, right panel.

$$6Ni^{3+}(OH) + CH_3OH + 6e^- \rightarrow CO_2 + 6Ni^{2+} + 5H_2O \qquad (7.8)$$

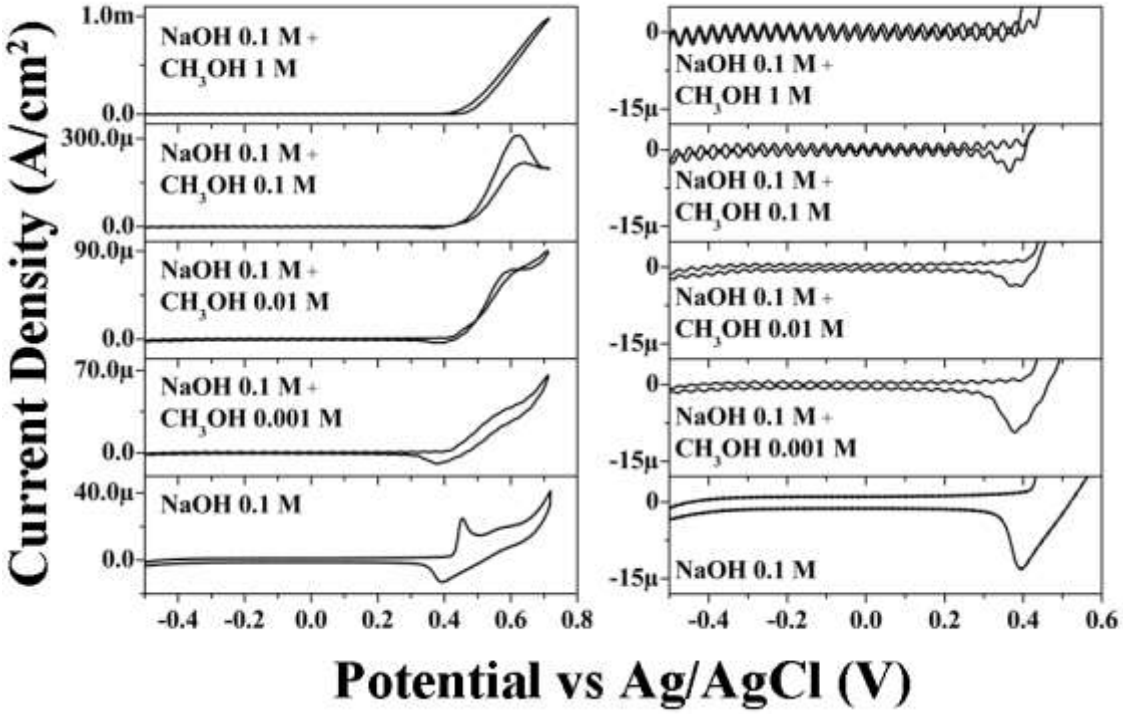

Fig. 7.5 *Cyclic Voltammetry of the P3-SG-A650C in the presence of Methanol. The activation in NaOH 0.1 M is showed as a reference. NaOH 0.1 M + Methanol 0.001 M, 0.01 M, 0.1 M and 1 M are displayed. The left-hand panel shows the reactions taking place. The right-hand panel allows to observe the change in intensity of the cathodic peak at 0.4 V with respect to methanol concentration. Scan rate 20 mV/s.*

Defining peak current density (J_p) as the current density value at the center of the anodic peak attributed to methanol oxidation and by plotting logarithm of peak current density

(Log[J_p]) vs logarithm of methanol Molar concentration (Log[C]) (Fig. 7.6, left panel), a linear behavior is observed. This linear behavior indicates that the peak current is proportional to the concentration of methanol as depicted by equation (7.9)

$$J_p = kC^{\gamma} \tag{7.9}$$

where J_p is peak current, k is a proportionality constant associated to the reaction rate, C is the Molar concentration of methanol, and γ is the order of the reaction.

$$\log J_p = \log k + \gamma \log C \tag{7.10}$$

By fitting the experimental results according to equation (7.10), the reaction rate is $k \approx 1x10^{-3}$ $[(A \cdot L)/(mol \cdot cm^2)]$, and the order of the reaction is $\gamma \approx 0.5$. In the right panel of Fig. 7.6, a curve of peak current density vs methanol Molar concentration was plotted using equation (7.9). In this plot, the simulated curve matches very well the experimental points and allows to visualize the tendency of the peak current for methanol.

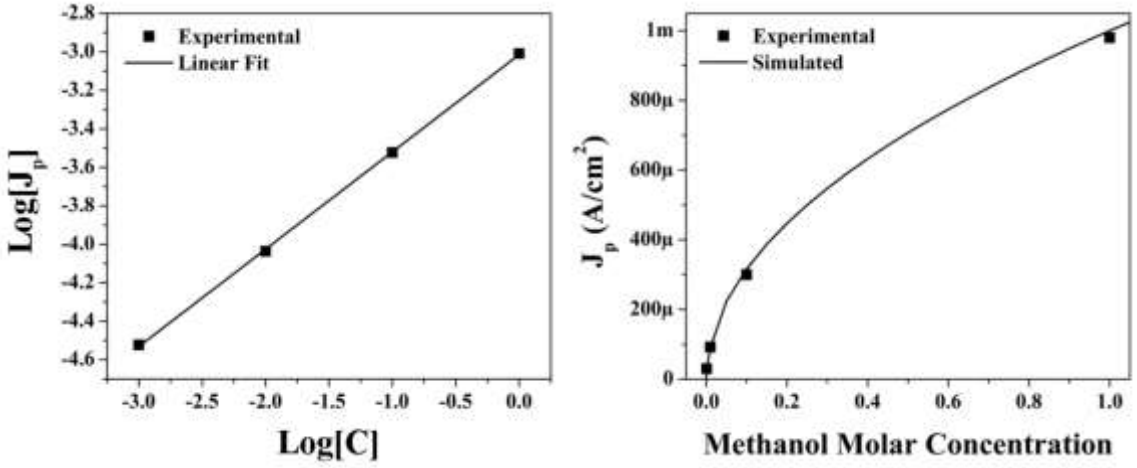

Fig. 7.6 Logarithm of peak current density (J_p) vs logarithm of methanol concentration (C) showing a linear behavior (left panel). Peak current density (J_p) vs methanol concentration (C) displaying the simulated behavior of peak current (right panel).

CHAPTER VII

3. CONCLUSIONS

The photocatalytic activity of $NiTiO_3$ has been demonstrated by using rf-sputtered thin films under visible-light in degrading methylene blue. After analyzing the degradation of the colorant over time, a reaction constant rate $k = 0.3\text{x}10^{-2}$ min^{-1} was determined. This value is in the order of the one obtained under the same conditions for co-sputtering synthesized films from metallic targets Ti and Ni.[114] The photoactivity of $NiTiO_3$ can be improved by modulation of its electronic and optical properties.

In addition to the degradation of methylene blue, the catalytic potential of $NiTiO_3$ has been demonstrated by oxidizing methanol when an external potential is applied in dark conditions. The Ni ions present in $NiTiO_3$ have been identified as the active species and the oxidation of the organic molecules to take place on the surface of Ni^{3+} in a similar manner as if metallic Ni particles were being used. $NiTiO_3$ has shown great stability during the catalytic process. The electro-oxidation of methanol opens the possibility to implement $NiTiO_3$ as anode in direct alkaline methanol fuel cells (DAMFC) for energy generation.

CHAPTER VII

CHAPTER VIII: HIGHLIGHTS, CONCLUSIONS AND FUTURE PERSPECTIVES

The carried work on $NiTiO_3$ associates several contributions such as different synthesis methods for powders and thin films and experimental investigations of physical features correlated with theoretical analysis of structural and electronic properties for the bulk and nanosized materials. The photocatalytic responses of the different $NiTiO_3$ were carried out and discussed on the basis of material features (morphologies, band gap, crystalline quality). The final chapter of this thesis is dedicated to underline the major achieved contributions and to draw the relevant conclusions and further development on $NiTiO_3$ based photocatalysts.

1. NICKEL TITANATE'S OPTICAL ABSORPTION AND ELECTRONIC TRANSITIONS

The photocatalytic performance requires deep insight on the optical properties of the considered materials. From the former chapters, experimental absorption spectra for the different synthesized forms of $NiTiO_3$ were reported and discussed for powders and thin films. The main characteristics of these spectra are hereafter compared by considering the theoretical approaches and numerical simulations reported in chapter II. Fig. 8.1 summarizes the experimental UV-Vis absorption spectra considered in this purpose.

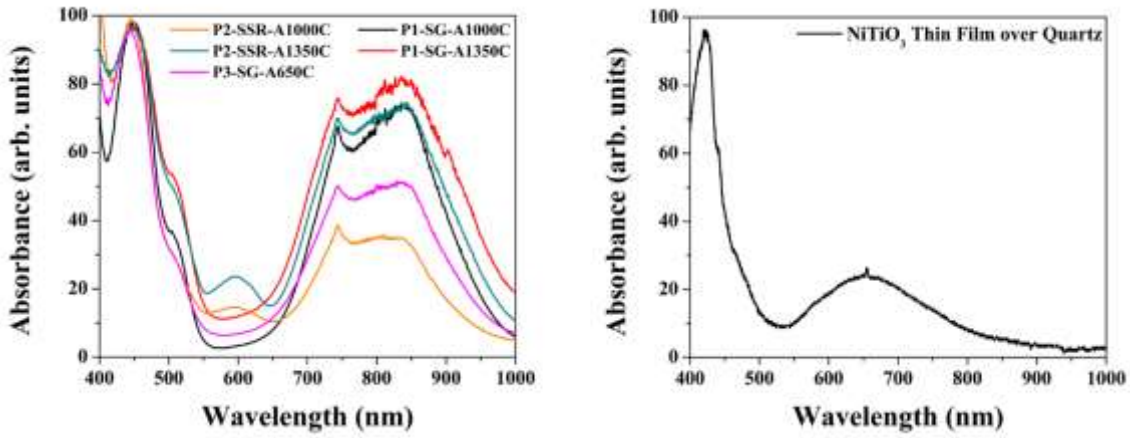

Fig. 8.1 *UV-Vis absorption spectra obtained experimentally for the different $NiTiO_3$ powders (left) and the $NiTiO_3$ Thin Film deposited on quartz (right).*

From theoretical approach, the UV-Vis absorption spectra for three different $NiTiO_3$ nanoclusters (*i.e.* $(NiTiO_3)_2$, $(NiTiO_3)_8$ and $(NiTiO_3)_{17}$) were simulated using semi-empirical PM6 model. The details of the calculations are specified in Chapter II. In Fig. 8.2 the calculated spectra for the three different clusters and the bulk material are shown, along with the spectrum obtained for the powder samples P1-SG-A1350C and P3-SG-A650C in representation of the experimental data. A good agreement is demonstrated between the calculated spectrum for the $(NiTiO_3)_{17}$ cluster and the experimental ones associated to the crystalline powders. The simulation results show that three main absorption bands, labelled below as A, B and C, are involved and their features depend on the $(NiTiO_3)_n$ cluster size. With increasing cluster size, the position of the A band, shifts to longer wavelengths and the

same behavior occurs for B band which undergoes a red shift and decreases notably in intensity. The third band C, appears for the cluster $(NiTiO_3)_{17}$ in the range 750–900 nm.

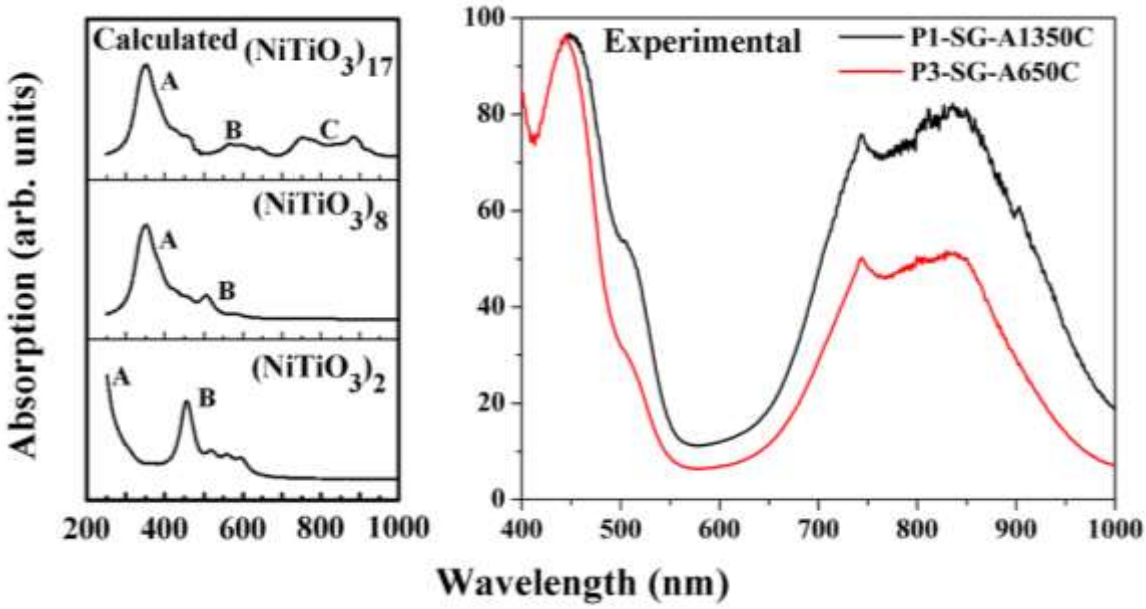

Fig. 8.2 *UV-Vis absorption spectra calculated by the PM6 model for different clusters (left panel) and the experimental spectrum obtained for samples P1-SG-A1350C and P3-SG-A650C (right panel, black and red respectively).*

The HOMO and LUMO orbitals, depicted in Fig. 8.3, for the investigated clusters $(NiTiO_3)_2$, $(NiTiO_3)_8$ and $(NiTiO_3)_{17}$, show their explicit separation and contribute to the low energy absorption spectra. The observed details suggest that the separation of the HOMO and LUMO orbitals gives rise to B and C bands.

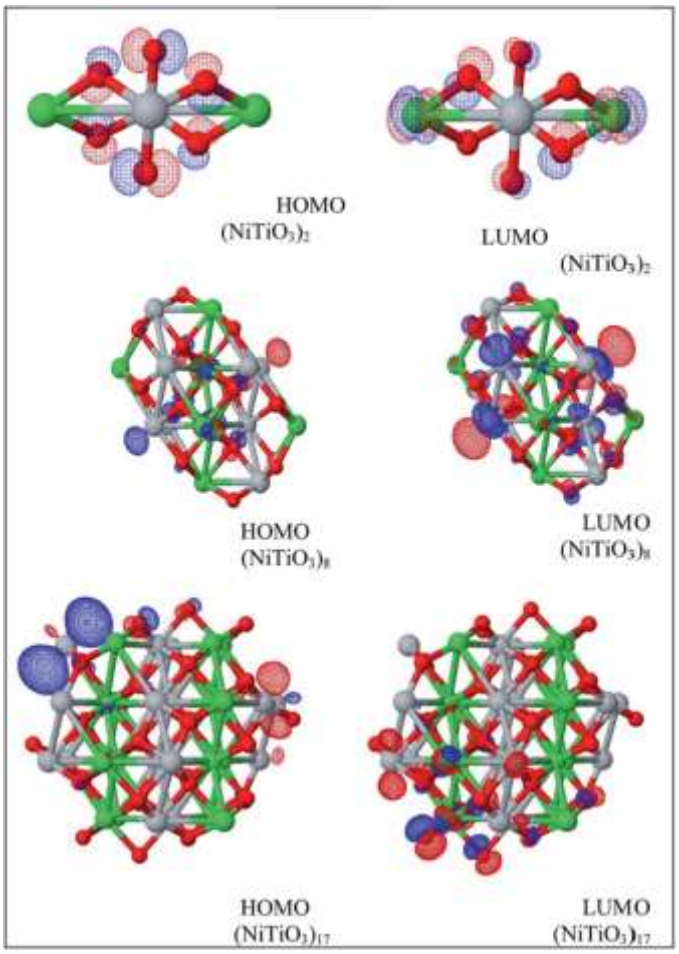

Fig. 8.3 *HOMO and LUMO orbitals calculated by the PM6 model for the $(NiTiO_3)_2$, $(NiTiO_3)_8$ and $(NiTiO_3)_{17}$ clusters. (Larger version in Chapter II, Fig. 2.8)*

The comparison of the theoretical and the experimental UV-Vis absorption spectra of the $(NiTiO_3)_{17}$ cluster clearly indicates the interesting optical activity of the system in the UV and the visible range of the electromagnetic spectrum. A broad absorption edge situated at ~ 410 nm is associated with $O^{2-} \rightarrow Ti^{4+}$ charge transfer transitions. The higher wavelength shoulder is associated with the crystal field splitting of $NiTiO_3$, giving rise to the $Ni^{2+} \rightarrow Ti^{4+}$ transitions.[93] Thus, for the nanosized $NiTiO_3$, the photo-induced charge transfers required for photocatalytic reactions may be ensured by several electronic transitions covering the UV and visible light range, contributing to efficient photocatalytic activity. Finally, it is worth noting that the resolved details on the theoretical absorption spectra are induced by calculations performed without any influence from the temperature on the structural relaxation of the $NiTiO_3$ clusters. The possibility of reconciling the shapes of the

absorption bands between the theory and experiments may be realized through the electron–phonon interactions and the Franck–Condon rule for the optical transition probabilities, as was used in a previous work by Kassiba et al.[94]

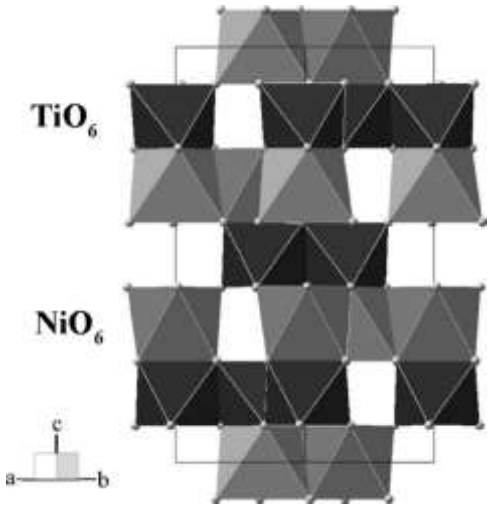

Fig. 8.4 *Crystal structure of $NiTiO_3$ showing the NiO_6 (light gray) and TiO_6 (dark grey) octahedral.*

In a related matter, the energies of the identified electronic transitions were determined by the Tauc analysis. Mainly, two electronic transition energies can be observed at approximately 2.25 and 2.50 eV, seen in Fig. 8.5 and listed in Table 8.1.

The ilmenite structure is an ordered corundum structure in which Ni^{2+} and Ti^{4+} form alternating layers along the rhombohedral axis of the crystal, with oxygen layers between them. Thus, the origin of the observed transitions can be related to the TiO_6 and NiO_6 octahedral arrangement of the structure (Fig. 8.4).

Table 8.1 *Band gap of the $NiTiO_3$ samples as determined from the Tauc plots of UV-Vis absorbance.*

Sample	Band-gap (eV)
P1-SG-A1000C	**2.29**
P1-SG-A1350C	**2.26**
P2-SSR-A1000C	**2.26**
P2-SSR-A1350C	**2.25**
P3-SG-A650C	**2.28**
Thin Films	**2.47**

Radtke et al.[125] conducted an investigation on the electronic structure of a series of compounds belonging to the $ATiO_3$ ilmenite family using electron energy loss spectroscopy (EELS). The high resolution of the equipment utilized (*e.g.* 0.20-0.25 eV) allowed them to unambiguously determine the formal valence and spin-state of the transition metals from the analysis of the L_{23} and O-K edges with theoretical ligand field calculations. Their conclusion is that in all the cases exists an $O^{2-} \rightarrow Ti^{4+}$ transition, corresponding to the 2.50 eV energy observed experimentally. A second transition involving the divalent cation as Ni^{2+} in our case, was discussed. This transition depends on the interatomic distances between the divalent cation and the oxygen atoms. Indeed, the interatomic distances decrease as the atomic number of the involved metallic ions increases. The resulting transition occurs at energy which correlates with the interatomic distance between the divalent cation and the oxygen atoms. In the case of $NiTiO_3$ the energy of this transition is around 2.25 eV, matching very well with the electronic transition observed experimentally in Fig. 8.5.

It is worth noting that, as mentioned in chapter VI, the smallest electronic transition determined for the $NiTiO_3$ thin films is about ~2.47 eV. The difference compared to the powder samples is most likely due to quantum effects arising from the very small mean crystallite sizes (*e.g.* 18 nm) determined from XRD spectra of thin films deposited over quartz substrates. Quantum confinement effects may occur and induce the blue shift of the optical absorption band.

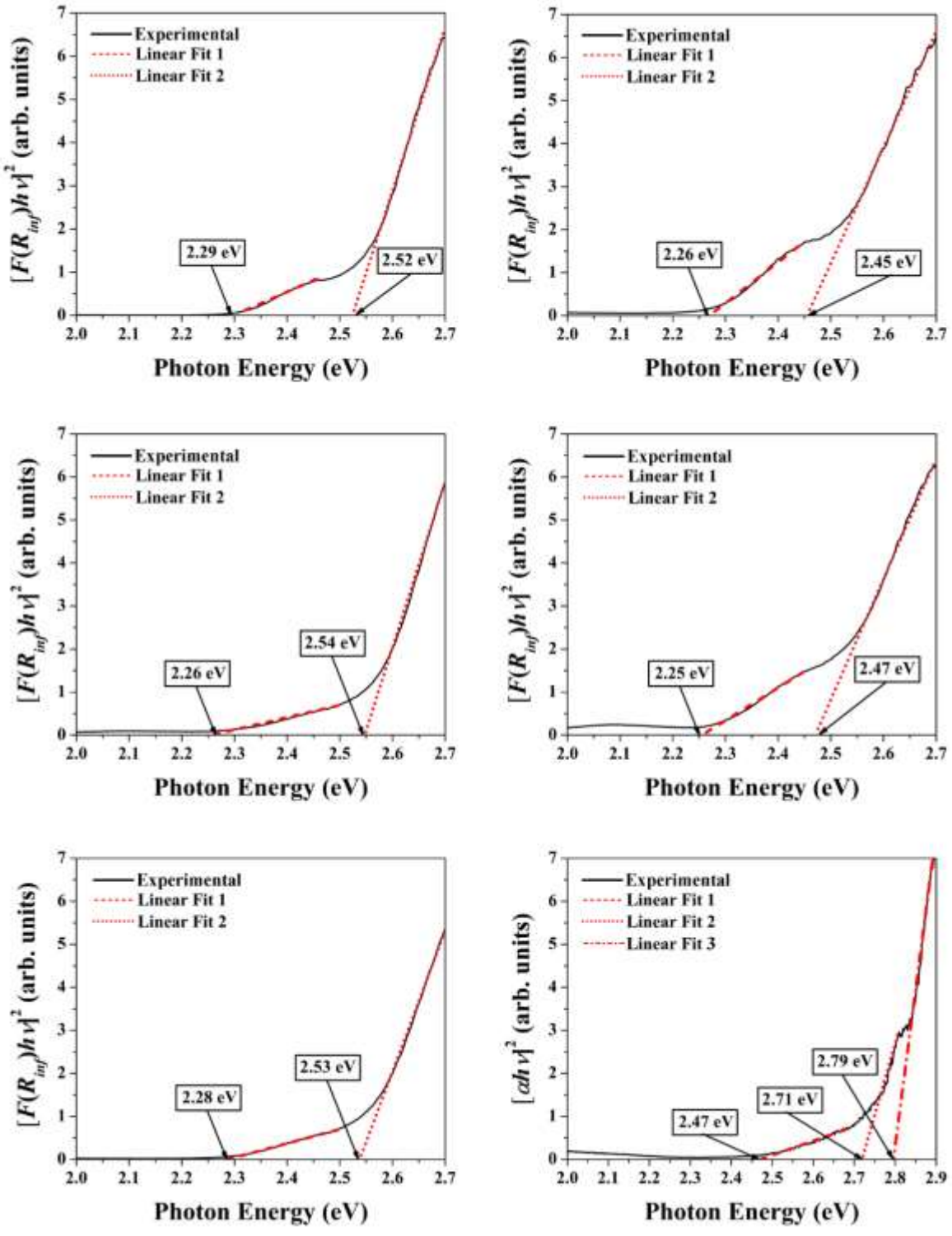

Fig. 8.4 *Tauc plots of P1-SG-A1000C (top left), P1-SG-A1350C (top right), P2-SSR-A1000C (middle left, P2-SSR-A1350C (middle right), P3-SG-A650C (bottom left) and Thin Film (bottom right).*

2. ORIGIN OF THE ACTIVE RAMAN VIBRATIONAL MODES OF NICKEL TITANATE

In former chapters (IV-VI), the Raman vibrational characteristics obtained for $NiTiO_3$ powders and thin films were discussed. As mentioned before, the ilmenite structure of $NiTiO_3$ possesses the space group $R\bar{3}$ (C_{3i}^2) with the oxygen atoms being tetra-coordinated to two tetravalent Ti and to two bivalent Ni cations. Furthermore, ten Raman active modes ($5A_g + 5E_g$) are expected with each E_g mode being twofold degenerated ($E_g = E_{1g} + E_{2g}$) along with the eight IR active modes ($4A_u + 4E_u$).

An extensive analysis of the Raman vibrational properties conducted on $NiTiO_3$ thin films was detailed in Chapter VI. The analysis consisted in using parallel and cross polarizations for the Raman measurements in order to assign the mode of vibrations. Excluding the 520 cm^{-1} band due to the silicon substrate, the Raman modes of $NiTiO_3$ were assigned as follows in cm^{-1}: 189.6 (A_g), 227.6 (E_g), 245.7 (A_g), 290.2 (E_g), 343.3 (E_g), 392.6 (A_g), 463.4 (E_g), 482.7 (A_g), 609.7 (E_g) and 705.9 (A_g) (Figs. 8.6 and 8.7).

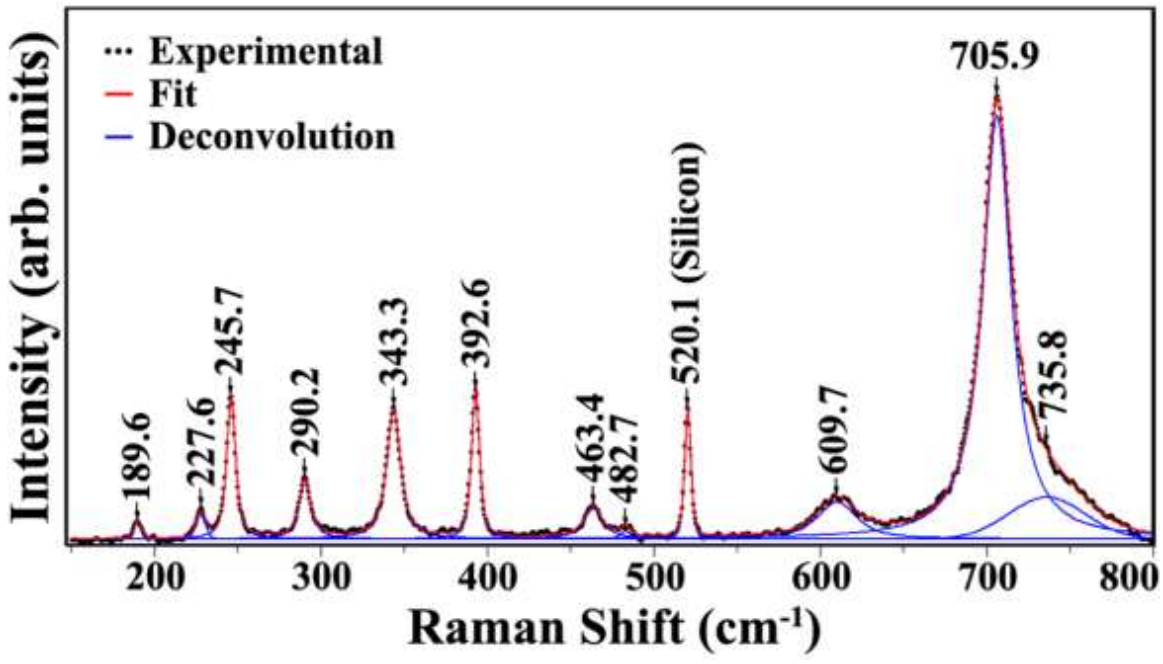

Fig. 8.6 *Experimental and simulation of the Raman spectrum of the representative $NiTiO_3$ thin film annealed at 1000 °C for 2 hours in air atmosphere.*

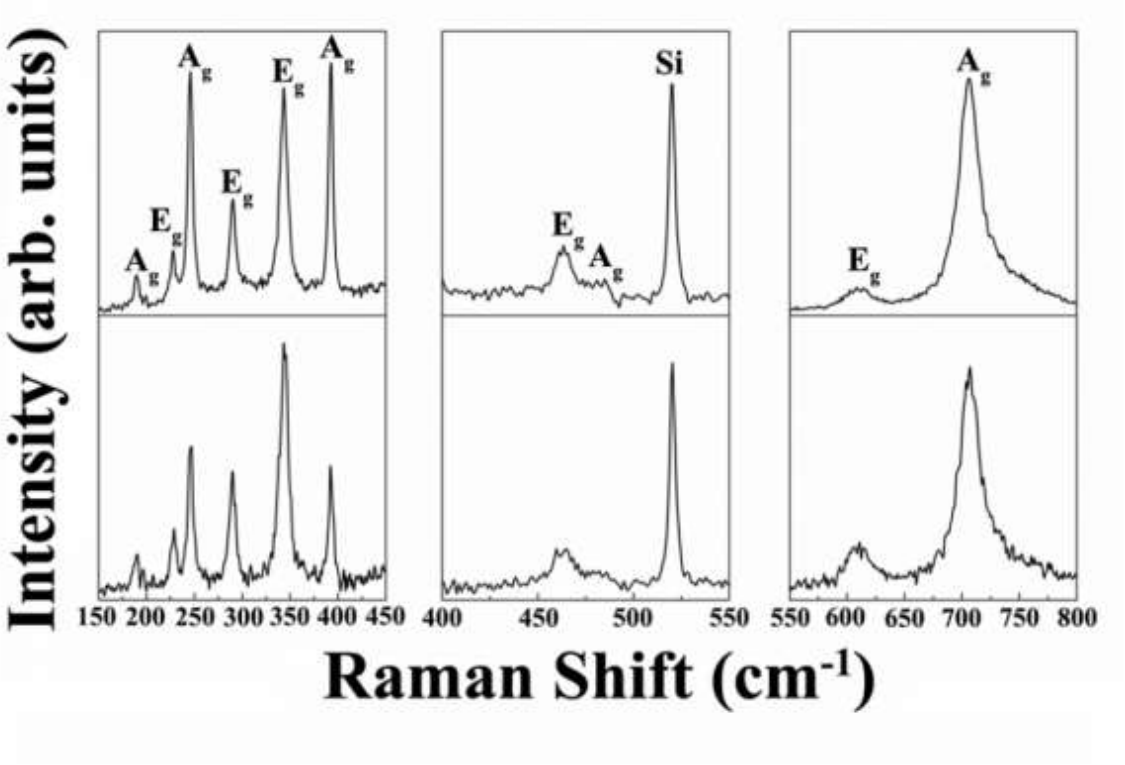

Fig. 8.7 *Raman spectra collected from a representative $NiTiO_3$ thin film annealed at 1000 °C for 2 hours in air atmosphere using: parallel polarization (top) and cross polarization (bottom).*

The Raman active modes can be described as symmetric Ti–O stretching vibrations, bond-bending of O–Ti–O, and translations of the Ni^{2+} cations with respect to the oxygen groups.[115] The Ag mode at 245.7 cm^{-1} can be attributed to the vibrations of Ti atoms along the z axis and the Ag modes at 398 and 482.7 cm^{-1} can be assigned to a breathing-like stretching of the Ti centered oxygen octahedra. The strong band at high frequencies at 705.9 cm^{-1} arises from the symmetric stretching of TiO_6 octahedra.[98] The Eg mode at 227.6 cm^{-1} can be considered as the asymmetric breathing vibration of the oxygen octahedra and the ones at 290.2 and 343.3 cm^{-1} can be described by the twist of oxygen octahedra due to vibrations of the Ni and Ti atoms parallel to the xy plane. The E_g modes at 463.4 and 609.7 cm^{-1} are assigned to the asymmetric breathing and twist of the oxygen octahedra with the cationic vibrations parallel to the xy plane.

In addition to these first-order Raman lines, a weak and broad signal is observed around 735.8 cm^{-1}. The origin of this signal has not been explained before and its interpretation remains a matter of debate.

In Chapter II, the analysis regarding the theoretical modelling and numerical simulations of the vibrational properties of $NiTiO_3$,[115] suggests that this signal may arise from the occurrence of a small fraction of an amorphous phase. In this analysis the Raman spectra related to selected clusters were performed using the PM6 approach. The Raman spectra were calculated using the standard procedure implemented in the Gaussian program package. The calculations were performed on three $(NiTiO_3)_{17}$ clusters. For the first cluster, the ilmenite crystal structure was frozen; the geometry of the second cluster was optimized according to the total energy minimization criterion while the last cluster consisted in a completely amorphous network. The theoretical results were compared to experimental data. The Raman spectrum from the powder sample P3-SG-A650C was selected in representation of the Raman vibrational properties of $NiTiO_3$ because for this sample the Raman line of interest is well resolved with higher intensity. The experimental and calculated Raman spectra modeled for the $(NiTiO_3)_{17}$ nanoclusters and for the $NiTiO_3$ powder are showed in Fig. 8.8.

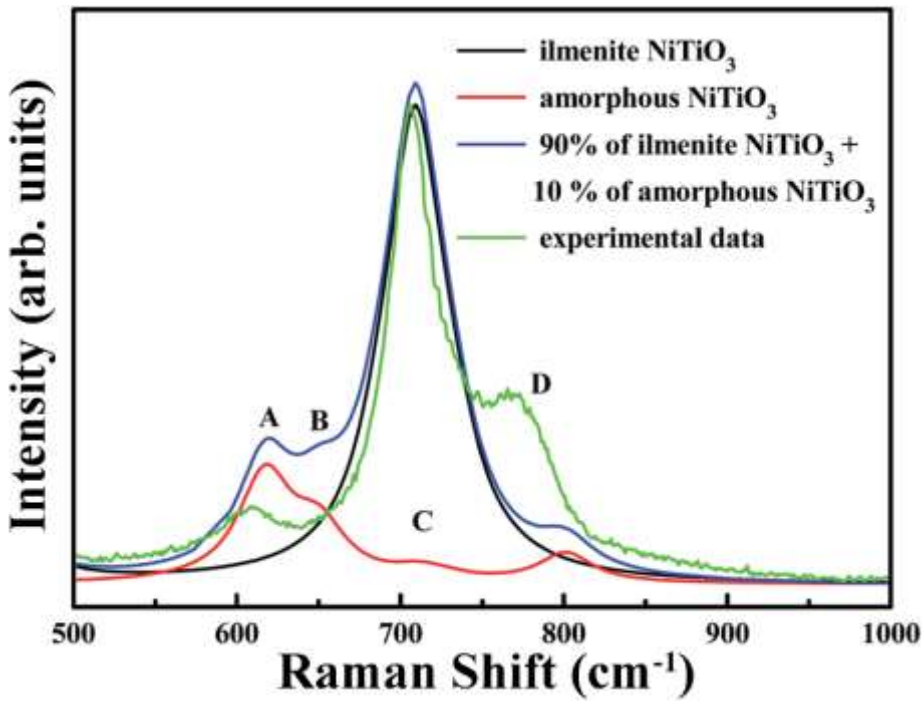

Fig. 8.8 *Raman spectra for the $(NiTiO_3)_{17}$ nanoparticles calculated by the parametrized PM6 method as well as experimental spectrum.*

A superposition of the main Raman band (90%) for O–Ti–O stretching and the secondary bands (10%) related to the amorphous structure leads to a theoretical Raman spectrum that reproduces the features of the experimental one. The slight departures from the experimental band positions may be explained by the fact that anharmonic vibration terms were not considered in the calculation model. The main origin may be related to bond frequency distributions due to "amorphization" or the occurrence of vacancies or antisites contributing to the damping and frequency shifts of Raman modes.[114,126] In this frame, it was proved that the bands located at 617 and 690 cm^{-1} originate from the stretching of Ti–O and bending of O–Ti–O bonds, while the contribution at 547 cm^{-1} results from Ni–O bonds.[51] As illustrated from the theoretical analysis and the experimental Raman investigations, the organization of the powder material is fully accounted for in the analysis that has been carried out. The particle core brings the signature features of the infinite and bulk crystal, while the outermost particle surface accounts for the amorphous features. This is presumably due to the manifestation of surface states with the relaxation and reconstruction of the outermost particle layers.

CHAPTER VIII

3. CONCLUSIONS

The thesis work is devoted to the synthesis of $NiTiO_3$ semiconducting structures as powders or thin films and the investigation of their related physical properties with the aim to apply them as photocatalysts. The synthesis of $NiTiO_3$ powders has been achieved by sol-gel and solid state reaction, while $NiTiO_3$ thin films have been grown by rf-sputtering. Characterizations on their structural, vibrational and optical properties confirm the stabilization of $NiTiO_3$ in its ilmenite phase, without the presence of secondary phases irrespective to the form of the samples as powders or thin films.

Theoretical studies supported by numerical simulations of the electronic, vibrational and optical properties of bulk and nanosized $NiTiO_3$ structures have been carried out in order to ensure quantitative insights for understanding the experimental peculiarities. An analysis of the simulated and experimental absorption spectra of the investigated materials, revealed two intense absorption bands at 400 and 800 nm that have been associated to $O^{2-} \rightarrow Ti^{4+}$ and Ni^{2+}-related electronic transitions, respectively. In the same context, an extensive Raman analysis along with theoretical results allowed the identification of the physical nature of the active Raman modes that can be described as symmetric Ti–O stretching vibrations, bond-bending of O–Ti–O, and translations of the Ni^{2+} cations with respect to the oxygen groups. A weak vibrational mode, commonly misinterpreted as one of the 10 theoretically expected active modes, has been proposed to arise from the presence of a small fraction of an amorphous phase at the surface of the material.

The determination of the band gap in the order of 2.25 eV suggests the feasibility to exploit the synthesized materials as visible-light-active photocatalysts. This feature has been tested in the degradation of Methylene Blue in aqueous solutions using rf-sputtered $NiTiO_3$ thin films irradiated with visible light, achieving the degradation of 60% of the initial concentration of the colorant in 300 minutes.

In addition, the electro-oxidation of methanol has been accomplished by applying an external voltage on an electrode containing $NiTiO_3$ powders in alkaline media. The Ni ions present in the catalyst have been identified as the active species and the oxidation of the organic molecules to happen on the surface of Ni^{3+} sites.

In summary, $NiTiO_3$ has been synthesized as powders and thin films, the main physical features investigated by complementary experiments and explained quantitatively by theoretical approaches and numerical simulations. We also demonstrate the relevant characteristics for efficient heterogeneous photocatalysis and the catalytic capabilities of $NiTiO_3$ through the photodegradation of Methylene Blue and the electro-oxidation of methanol.

CHAPTER VIII

4. PROPOSAL OF FUTURE WORK

The stabilization of pure $NiTiO_3$ phase with ilmenite structure and its application as a photocatalyst constitute the main motivation of the present work. Nevertheless, improvement of the photocatalytic capabilities of $NiTiO_3$ could be done by combining different strategies able to enhance the absorption of photons for the generation of charge carriers (electron, hole) with high densities, the separation and migration of the photogenerated excitons charge carriers, as well as the charge transfer involved in the redox reactions.

- The efficiency of a catalytic reaction is strongly related to the "selectivity" of the catalyst under study. This means that a certain catalyst which might be very efficient to induce redox reactions on defined probe molecules and inefficient to degrade others. In this frame, it is important to test the photocatalytic activity of $NiTiO_3$ on the degradation of a variety of probe molecules.
- The photocatalytic reactions occur on the contact surface between the catalyst and the surrounding media charged by targeted molecules. Therefore, increasing the active area would enhance the catalytic activity. During a sol-gel synthesis process, it is possible to use surfactants in the aim to realize mesoporous organization of the materials with high specific surfaces. It is even possible to perform an evaporation induced self-assembly (EISA) process, in which solution from the sol-gel synthesis is deposited over a substrate forming a mesoporous thin films with organized porous structure.[127–129]
- Doping processes with selected ions has been successfully used to improve the photocatalytic activity in several families of materials, including TiO_2. An important contribution by Aahi *et al*. discusses titanium dioxide doped with nitrogen being active in the visible range of the electromagnetic spectrum.[130] Another work by Soni and colleagues, combines the organized mesoporous approach along with doping the material with nitrogen, achieving the decomposition of Methylene Blue under visible light.[131] The titanate family has also benefited from the doping process, the photocatalytic activity of wide band gap perovskites, like $SrTiO_3$, have been reported

to improve while showing enhanced chemical stability and H_2 and /or O_2 evolution induced by UV irradiation.[132] In a similar manner, doping might improve the overall photocatalytic process of $NiTiO_3$ notably by increasing the density of charge carriers as well as the lifetime of photogenerated electron-hole pairs. An advance on this approach has already been made by our group, growing N-doped $NiTiO_3$ thin films by co-sputtering Ti and Ni metallic targets in a controlled argon, oxygen and nitrogen atmosphere.[114] The results of that study show slight improvement in the photocatalytic degradation of methylene blue over non-doped $NiTiO_3$ thin films. A further step could be realized to implement a co-doping process in order to control the valence states of the doped metal cations and to reduce the lattice defects.[18] Before the actual experimental doping, it would be important to perform theoretical calculations in order to obtain the electronic and optical properties of $NiTiO_3$ doped with different elements and subsequently select the ones that show the best features.

- In the area of photocatalysis for water splitting, the construction of a Z-scheme system is worthy of interest consisting of $NiTiO_3$ and a second photocatalysts. The idea behind this approach is that since it is difficult to have a material with a narrow band gap while maintaining the band edges in the proper positions for both oxygen and hydrogen efficient evolution, then coupling two different materials, each having specific band edge positions that can induce oxidation or reduction reactions with enhanced efficiency might improve the photocatalytic efficiency.

CHAPTER VIII

BIBLIOGRAPHY

1. Fujishima, A., Hashimoto, K. & Watanabe, T. *TiO_2 photocatalysis: Fundamentals and applications*. (BKC, 1999).

2. Cook, T. R. *et al.* Solar Energy Supply and Storage for the Legacy and Nonlegacy Worlds. *Chem. Rev.* **110,** 6474–6502 (2010).

3. Izumi, Y. Recent advances in the photocatalytic conversion of carbon dioxide to fuels with water and/or hydrogen using solar energy and beyond. *Coord. Chem. Rev.* **257,** 171–186 (2013).

4. Tahir, M. & Amin, N. S. Recycling of carbon dioxide to renewable fuels by photocatalysis: Prospects and challenges. *Renew. Sustain. Energy Rev.* **25,** 560–579 (2013).

5. Pelaez, M. *et al.* A Review on the Visible Light Active Titanium Dioxide Photocatalysts for Environmental Applications. *Appl. Catal. B Environ.* **125,** 331–349 (2012).

6. Dalrymple, O. K., Stefanakos, E., Trotz, M. A. & Goswami, D. Y. A review of the mechanisms and modeling of photocatalytic disinfection. *"Applied Catal. B, Environ.* **98,** 27–38 (2010).

7. Gamage, J., Zhang, Z., Gamage, J. & Zhang, Z. Applications of Photocatalytic Disinfection. *Int. J. Photoenergy* **2010,** 1–11 (2010).

8. Bickley, R. I. & Vishwanathan, V. Photocatalytically induced fixation of molecular nitrogen by near UV radiation. *Nature* **280,** 306–308 (1979).

9. Guo, C. *et al.* The visible-light driven photocatalytic destruction of $NO_{(x)}$ using mesoporous TiO_2 spheres synthesized via a "water-controlled release process". *Nanoscale* **5,** 8184–91 (2013).

10. Zhao, J. & Yang, X. Photocatalytic oxidation for indoor air purification: a literature review. *Build. Environ.* **38,** 645–654 (2003).

11. Lasek, J., Yu, Y. H. & Wu, J. C. S. Removal of NO_x by photocatalytic processes. *Journal Photochem. Photobiol. C Photochem. Rev.* **14,** 29–52 (2013).

12. Tan, Y. N. *et al.* An Overview on the Photocatalytic Activity of Nano-Doped TiO_2 in the Degradation of Organic Pollutants. *ISRN Mater. Sci.* **2011,** 1–18 (2011).

13. Konstantinou, I. K. & Albanis, T. A. TiO_2-assisted photocatalytic degradation of azo dyes in aqueous solution: kinetic and mechanistic investigations A review. *Appl. Catal. B Environ.* **49,** 1–14 (2004).

14. Tayade, R. J., Surolia, P. K., Kulkarni, R. G. & Jasra, R. V. Photocatalytic degradation of dyes and organic contaminants in water using nanocrystalline anatase and rutile TiO_2. *Sci. Technol. Adv. Mater.* **8,** 455–462 (2007).

15. Fujishima, A., Zhang, X. & Tryk, D. A. TiO_2 photocatalysis and related surface phenomena. *Surf. Sci. Rep.* **63,** 515–582 (2008).

16. Hashimoto, K., Irie, H. & Fujishima, A. TiO_2 Photocatalysis: A Historical Overview and Future Prospects. *Jpn. J. Appl. Phys.* **44,** 8269–8285 (2005).

17. Fujishima, A., Rao, T. N. & Tryk, D. A. Titanium dioxide photocatalysis. *J. Photochem. Photobiol. C Photochem. Rev.* **1,** 1–21 (2000).

18. Yin, W. J. *et al.* Band structure engineering of semiconductors for enhanced photoelectrochemical water splitting: The case of TiO_2. *Phys. Rev. B - Condens. Matter Mater. Phys.* **82,** 1–6 (2010).

19. Yamashita, H. *et al.* Degradation of propanol diluted in water under visible light irradiation using metal ion-implanted titanium dioxide photocatalysts. *J. Photochem. Photobiol. A Chem.* **148,** 257–261 (2002).

20. In, S. *et al.* Effective visible light-activated B-doped and B,N-codoped TiO_2 photocatalysts. *J. Am. Chem. Soc.* **129,** 13790–13791 (2007).

21. Niu, Y., Xing, M., Zhang, J. & Tian, B. Visible light activated sulfur and iron co-doped TiO_2 photocatalyst for the photocatalytic degradation of phenol. *Catal. Today* **201,** 159–166 (2013).

22. Yang, J. *et al.* Heterostructured TiO_2/WO_3 porous microspheres: Preparation, characterization and photocatalytic properties. *Catal. Today* **201,** 195–202 (2013).

23. Liu, X., Pan, L., Lv, T., Sun, Z. & Sun, C. Enhanced photocatalytic reduction of Cr(VI) by ZnO-TiO_2-CNTs composites synthesized via microwave-assisted reaction. *J. Mol. Catal. A Chem.* **363–364,** 417–422 (2012).

24. Hussein, A. M. *et al.* Mesoporous coupled ZnO/TiO_2 photocatalyst nanocomposites for hydrogen generation. *J. Renew. Sustain. Energy* **5,** 1–13 (2013).

25. Chandrade, G., Roy, A. M. & Bhattacharya, S. S. Effect of n-Si on the photocatalytic production of hydrogen by Pt-loaded CdS and CdS/ZnS catalyst. *Int. J. Hydrogen Energy* **21,** 19–23 (1996).

26. Hwang, D. W., Kim, J., Park, T. J. & Lee, J. S. Mg-Doped WO_3 as a Novel Photocatalyst for Visible Light-Induced Water Splitting. *Catal. Letters* **80,** 53–57 (2002).

27. Kim, H. G., Hwang, D. W. & Lee, J. S. An Undoped, Single-Phase Oxide Photocatalyst Working under Visible Light. *J. Am. Chem. Soc.* **126,** 8912–8913 (2004).

28. Merupo, V. I. *et al.* Structural and optical characterization of ball-milled copper-doped bismuth vanadium oxide ($BiVO_4$). *CrystEngComm* **17,** 3366–3375 (2015).

29. Merupo, V. I., Velumani, S., Kassiba, A. & Garcia-Sanchez, M. A. Structural and optical properties of molybdenum-doped bismuth vanadate powders. *11th International Conference on Electrical Engineering, Computing Science and Automatic Control (CCE)* 1–5 (IEEE, 2014). doi:10.1109/ICEEE.2014.6978299

30. Merupo, V. I., Velumani, S., Oza, G., Makowska-Janusik, M. & Kassiba, A. Structural, electronic and optical features of molybdenum-doped bismuth vanadium oxide. *Mater. Sci. Semicond. Process.* **31,** 618–623 (2015).

31. Navrotsky, A. Energetics and Crystal Chemical Systematics among Ilmenite, Lithium Niobate, and Perovskite Structures. *Chem. Mater.* **10,** 2787–2793 (1998).

32. Giaquinta, D. M. & Zur Loye, H. C. Structural Predictions in the ABO_3 Phase Diagram. *Chem. Mater.* **6,** 365–372 (1994).

33. Neil, J. M., Navrotsky, A. & Kleppa, O. J. The enthalpy of ilmenite-perovskite transformation in cadmium titanate. *Inorg. Chem.* **10,** 2076–2077 (1971).

34. Kanhere, P. & Chen, Z. A review on visible light active perovskite-based photocatalysts. *Molecules* **19,** 19995–20022 (2014).

35. Jia, Q., Iwase, A. & Kudo, A. $BiVO_4$–Ru/$SrTiO_3$:Rh composite Z-scheme photocatalyst for solar water splitting. *Chem. Sci.* **5,** 1513 (2014).

36. Li, T. *et al.* Conductivity relaxation in $NiTiO_3$ at high temperatures. *Curr. Appl. Phys.* **13,** 1728–1731 (2013).

37. Yuvaraj, S. *et al.* Investigations on the temperature dependent electrical and magnetic properties of $NiTiO_3$ by molten salt synthesis. *Mater. Res. Bull.* **48,** 1110–1116 (2013).

38. Fujishima, A. & Honda, K. Electrochemical Photolysis of Water at a Semiconductor Electrode. *Nature* **238,** 37–38 (1972).

39. Kawai, T. & Sakata, T. Conversion of carbohydrate into hydrogen fuel by a photocatalytic process. *Nature* **286,** 474–476 (1980).

40. Bhalla, A. S., Guo, R. & Roy, R. The perovskite structure - A review of its role in ceramic science and technology. *Mater. Res. Innov.* **4,** 3–26 (2000).

41. Zhang, W. F., Tang, J. & Ye, J. Photoluminescence and photocatalytic properties of $SrSnO_3$ perovskite. *Chem. Phys. Lett.* **418,** 174–178 (2006).

42. Lin, W. H., Cheng, C., Hu, C. C. & Teng, H. $NaTaO_3$ photocatalysts of different crystalline structures for water splitting into H_2 and O_2. *Appl. Phys. Lett.* **89,** 211904 (2006).

43. Yong, X. & Schoonen, M. A. A. The absolute energy positions of conduction and valence bands of selected semiconducting minerals. *Am. Mineral.* **85,** 543–556 (2000).

44. Yao, W. F. *et al.* Photocatalytic property of perovskite bismuth titanate. *Appl. Catal. B Environ.* **52,** 109–116 (2004).

45. Kim, J. *et al.* Nickel-loaded $La_2Ti_2O_7$ as a bifunctional photocatalyst Jindo. *Chem. Commun.* 2488–2489 (2002). doi:10.1088/0256-307X/27/4/047203

46. Pelaez, M. *et al.* A review on the visible light active titanium dioxide photocatalysts for environmental applications. *"Applied Catal. B, Environ.* **125,** 331–349 (2012).

47. Qu, Y. *et al.* Facile preparation of porous $NiTiO_3$ nanorods with enhanced visible-light-driven photocatalytic performance. *J. Mater. Chem.* **22,** 16471 (2012).

48. de Haart, L. G. J., de Vries, A. J. & Blasse, G. Photoelectrochemical properties of $MgTiO_3$ and other titanates with the ilmenite structure. *Mater. Res. Bull.* **19,** 817–824 (1984).

49. Sadjadi, M. S., Mozaffari, M., Enhessari, M. & Zare, K. Effects of $NiTiO_3$ nanoparticles supported by mesoporous MCM-41 on photoreduction of methylene blue under UV and visible light irradiation. *Superlattices Microstruct.* **47,** 685–694 (2010).

50. Zhou, L., Zhang, S., Cheng, J., Zhang, L. & Zeng, Z. Optical absorptions of nanoscaled CoTiO, and $NiTiO_3$. *Mater. Sci. Eng. B* **49,** 117–122 (1997).

51. Vijayalakshmi, R. & Rajendran, V. Effect of Reaction Temperature on Size and Optical Properties of $NiTiO_3$ Nanoparticles. *E-Journal Chem.* **9,** 282–288 (2012).

52. Shu, X., He, J. & Chen, D. Visible-Light-Induced Photocatalyst Based on Nickel Titanate Nanoparticles. *Ind. Eng. Chem. Res.* **47,** 4750–4753 (2008).

53. Wilson, N., Russo, S., Muscat, J. & Harrison, N. High-pressure phases of $FeTiO_3$ from first principles. *Phys. Rev. B* **72,** 24110 (2005).

54. Wilson, N., Muscat, J., Mkhonto, D., Ngoepe, P. & Harrison, N. Structure and properties of ilmenite from first principles. *Phys. Rev. B* **71,** 75202 (2005).

55. Chen, S. W. *et al.* Orbital structure of $FeTiO_3$ ilmenite investigated with polarization-dependent X-ray absorption spectroscopy and band structure calculations. *Appl. Phys.*

Lett. **102,** 42107 (2013).

56. Liechtenstein, A. I., Anisimov, V. I. & Zaanen, J. Density-functional theory and strong interactions: Orbital ordering in Mott-Hubbard insulators. *Phys. Rev. B* **52,** R5467–R5470 (1995).

57. Anisimov, V. I., Zaanen, J. & Andersen, O. K. Band theory and Mott insulators: Hubbard U instead of Stoner I. *Phys. Rev. B* **44,** 943–954 (1991).

58. Anisimov, V. I., Solovyev, I. V, Korotin, M. A., Czyzyk, M. T. & Sawatzky, G. A. No Title. *Phys. Rev. B* **48,** 929 (1993).

59. Anjana, P. S. Investigations on ceria based dielectric ceramic materials for wireless communication. (2008).

60. Makowska-Janusik, M., Gladii, O., Kassiba, A., Bouclé, J. & Herlin-Boime, N. Cluster approach to model titanium dioxide as isolated or organic dye sensitized nano-objects. *J. Phys. Chem. C* **118,** 6009–6018 (2014).

61. Clark, S. J. *et al.* First principles methods using CASTEP. *Zeitschrift fur Krist.* **220,** 567–570 (2005).

62. Pfrommer, B. G., Cote, M., Louie, S. G. & Cohen, M. L. Relaxation of crystals with the quasi-Newton method. *J. Comput. Phys.* **131,** 233–240 (1997).

63. Perdew, J. P., Burke, K. & Ernzerhof, M. Generalized Gradient Approximation made simple. *Phys. Rev. Lett.* **77,** 3865–3868 (1996).

64. Heyd, J., Scuseria, G. E. & Ernzerhof, M. Hybrid functionals based on a screened Coulomb potential. *J. Chem. Phys.* **118,** 8207–8215 (2003).

65. Heyd, J., Scuseria, G. E. & Ernzerhof, M. Erratum: Hybrid functionals based on a screened Coulomb potential [J. Chem. Phys.118, 8207 (2003)]. *J. Chem. Phys.* **124,** 219906 (2006).

66. Hummer, K., Harl, J. & Kresse, G. Heyd-Scuseria-Ernzerhof hybrid functional for calculating the lattice dynamics of semiconductors. *Phys. Rev. B - Condens. Matter Mater. Phys.* **80,** (2009).

67. Śpiewak, P., Vanhellemont, J. & Kurzydłowski, K. J. Improved calculation of vacancy properties in Ge using the Heyd-Scuseria-Ernzerhof range-separated hybrid functional. *J. Appl. Phys.* **110,** 63534 (2011).

68. Foster, M. E. & Wong, B. M. Nonempirically tuned range-separated DFT accurately predicts both fundamental and excitation gaps in DNA and RNA nucleobases. *J. Chem. Theory Comput.* **8,** 2682–2687 (2012).

69. Wong, B. M., Piacenzab, M. & Della Sala, F. Absorption and fluorescence properties of oligothiophene biomarkers from long-range-corrected time-dependent density functional theory. *Phys. Chem. Chem. Phys.* **11,** 4498 (2009).

70. Almbladh, C. O. & Pedroza, A. C. Density-functional exchange-correlation potentials and orbital eigenvalues for light atoms. *Phys. Rev. A* **29,** 2322–2330 (1984).

71. Levy, M., Perdew, J. P. & Sahni, V. Exact differential equation for the density and ionization energy of a many-particle system. *Phys. Rev. A* **30,** 2745–2748 (1984).

72. Dreuw, A., Weisman, J. L. & Head-Gordon, M. Long-range charge-transfer excited states in time-dependent density functional theory require non-local exchange. *J. Chem. Phys.* **119,** 2943–2946 (2003).

73. Hybertsen, M. S. & Louie, S. G. Electron correlation in semiconductors and insulators: Band gaps and quasiparticle energies. *Phys. Rev. B* **34,** 5390–5413 (1986).

74. Kohn, W. & SHAM, L. J. Self-Consistent Equations Including Exchange and Correlation Effects. *Phys. Rev.* **140,** A1133–A1138 (1965).

75. Langreth, D. C. & Perdew, J. P. Theory of nonuniform electronic systems. {I}. Analysis and a generalization that works. *Phys. Rev. B* **21,** 5469–5493 (1980).

76. Stephens, P. J., Devlin, F. J., Chabalowski, C. F. & Frisch, M. J. Ab Initio Calculation of Vibrational Absorption and Circular Dichroism Spectra Using Density Functional Force Fields: A Comparison of Local, Nonlocal, and Hybrid Density Functionals. *J. Phys. Chem.* **98,** 11623–11627 (1994).

77. Perdew, J. P., Ernzerhof, M. & Burke, K. Rationale for mixing exact exchange with

density functional approximations. *J. Chem. Phys.* **105,** 9982 (1996).

78. Jain, A. *et al.* Formation enthalpies by mixing GGA and GGA + U calculations. *Phys. Rev. B - Condens. Matter Mater. Phys.* **84,** 45115 (2011).

79. Laskowski, R., Christensen, N. E., Blaha, P. & Palanivel, B. Strong excitonic effects in $CuAlO_2$ delafossite transparent conductive oxides. *Phys. Rev. B - Condens. Matter Mater. Phys.* **79,** 165209 (2009).

80. Liu, Q. J. & Liu, Z. T. First-principles generalized gradient approximation + U study of cubic $CuAl_2O_4$. *Appl. Phys. Lett.* **99,** 91902 (2011).

81. Sayede, A., Khenata, R., Chahed, A. & Benhelal, O. Electronic and optical properties of layered $RE_2Ti_2O_7$ (RE = Ce and Pr) from first principles. *J. Appl. Phys.* **113,** 173501 (2013).

82. Huang, J. R. & Cheng, C. Cation and magnetic orders in $MnFe_2O_4$ from density functional calculations. *J. Appl. Phys.* **113,** 33912 (2013).

83. MOPAC2012: Stewart, J. J. P. Stewart Computational Chemistry, Colorado Springs: CO, http://OpenMOPAC.net.

84. Stewart, J. J. P. Optimization of parameters for semiempirical methods V: Modification of NDDO approximations and application to 70 elements. *J. Mol. Model.* **13,** 1173–1213 (2007).

85. Baker, J. An algorithm for the location of transition states. *J. Comput. Chem.* **7,** 385–395 (1986).

86. Helgaker, T. Transition-state optimizations by trust-region image minimization. *Chem. Phys. Lett.* **182,** 503 (1991).

87. Culot, P., Dive, G., Nguyen, V. H. & Ghuysen, J. M. Theoretica Chimica Acta A quasi-Newton algorithm for first-order saddle-point location. *Theor Chim Acta* **82,** 189–205 (1992).

88. Xin, C. *et al.* Electronic, magnetic and multiferroic properties of magnetoelectric $NiTiO_3$. *J. Alloys Compd.* **613,** 401–406 (2014).

89. Singh, R. S., Ansari, T. H., Singh, R. A. & Wanklyn, B. M. Electrical conduction in $NiTiO_3$ single crystals. *Mater. Chem. Phys.* **40,** 173–177 (1995).

90. Wang, J., Li, Y., Byon, Y., Mei, S. & Zhang, G. Synthesis and characterization of $NiTiO_3$ yellow nano pigment with high solar radiation re fl ection ef fi ciency. *Powder Technol.* **235,** 303–306 (2013).

91. Salvador, P., Gutierrez, C. & Goodenough, J. B. Photoresponse of n-type semiconductor $NiTiO_3$. *Appl. Phys. Lett.* **40,** 188–190 (1982).

92. Stein, T., Eisenberg, H., Kronik, L. & Baer, R. Fundamental gaps in finite systems from eigenvalues of a generalized Kohn-Sham method. *Phys. Rev. Lett.* **105,** 266802 (2010).

93. Lopes, K. P. *et al.* $NiTiO_3$ powders obtained by polymeric precursor method: Synthesis and characterization. *J. Alloys Compd.* **468,** 327–332 (2009).

94. Kassiba, A. *et al.* Photoluminescence features on the Raman spectra of quasistoichiometric SiC nanoparticles: Experimental and numerical simulations. *Phys. Rev. B* **66,** 155317 (2002).

95. Su, Y., Balmer, M. Lou & Bunker, B. C. Raman Spectroscopic Studies of Silicotitanates. *J. Phys. Chem. B* **104,** 8160–8169 (2000).

96. Busca, G., Ramis, G. & Piaggio, P. FT Raman and FTlR Studies of Titanias and Metatitanate Powders. *J. Chem. Soc. Faraday Trans.* **90,** 3181–3190 (1994).

97. Llabrés Xamena, F. X., Damin, A., Bordiga ab, S. & Zecchina, A. Healing of defects in ETS-10 by selective UV irradiation: a Raman study. *Chem. Commun.* 1514–1515 (2003). doi:10.1039/b302773b

98. Baraton, M. I., Busca, G., Prieto, M. C., Ricchiardi, G. & Escribano, V. S. On the Vibrational Spectra and Structure of $FeCrO_3$ and of the Ilmenite-Type Compounds $CoTiO_3$ and $NiTiO_3$. *J. Solid State Chem.* **112,** 9–14 (1994).

99. Lerch, M., Boysen, H., Neder, R., Frey, F. & Laqua, W. Neutron scattering investigation of the high temperature phase transition in $NiTiO_3$. *J. Phys. Chem. Solids*

53, 1153–1156 (1992).

100. Zhou, G. & Soo Kang, Y. Synthesis and Characterization of the Nickel Titanate $NiTiO_3$ Nanoparticles in CTAB Micelle. *J. Dispers. Sci. Technol.* **27,** 727–730 (2006).

101. Sadjadi, M. S., Zare, K., Khanahmadzadeh, S. & Enhessari, M. Structural characterization of $NiTiO_3$ nanopowders prepared by stearic acid gel method. *Mater. Lett.* **62,** 3679–3681 (2008).

102. Lutterotti, L. & Scardi, P. Simultaneous structure and size–strain refinement by the Rietveld method. *J. Appl. Crystallogr.* **23,** 246–252 (1990).

103. Scherrer, P. Bestimmung der Grosse und der inneren Struktur von Kolloidteilchen mittels Rontgenstrahlen. *Math. Klasse 2* 98–100 (1918).

104. Klug, H. P. & Alexander, L. E. in *X-Ray Diffraction Procedures: For Polycrystalline and Amorphous Materials* (Wiley, 1974).

105. Cullity, B. D. *Elements of X Ray Diffraction*. (Addison-Wesley, 1956).

106. Mironova-Ulmane, N., Kuzmin, A., Sildos, I. & Pärs, M. Polarisation dependent Raman study of single-crystal nickel oxide. *Cent. Eur. J. Phys. @BULLET Cent. Eur. J. Phys.* **9,** 1096–1099 (2011).

107. Wang, C. H., Jing, X. P., Feng, W. & Lu, J. Assignment of Raman-active vibrational modes of $MgTiO_3$. *J. Appl. Phys.* **104,** 34112 (2008).

108. Kubelka, P. & Munk, F. Ein Beitrag zur Optik der Farbanstriche. *Z. Tech. Phys* **12,** 593–599 (1931).

109. Escobedo Morales, A., Sánchez Mora, E. & Pal, U. Use of diffuse reflectance spectroscopy for optical characterization of un-supported nanostructures. *Rev. Mex. Física S* **53,** 18–22 (2007).

110. Murphy, A. B. Band-gap determination from diffuse reflectance measurements of semiconductor films, and application to photoelectrochemical water-splitting. *Sol. Energy Mater. Sol. Cells* **91,** 1326–1337 (2007).

111. Tauc, J. Optical properties and electronic structure of amorphous Ge and Si. *Mat. Res. Bull.* **3,** 37–46 (1968).

112. Tauc, J., Grigorovici, R. & Vancu, a. Optical Properties and Electronic Structure of Amorphous Germanium. *Phys. Status Solidi* **15,** 627–637 (1966).

113. Rossman, G. R., Shannon, R. D. & Waring, R. K. Origin of the yellow color of complex nickel oxides. *J. Solid State Chem.* **39,** 277–287 (1981).

114. Bellam, J. B. *et al.* Visible-light photocatalytic activity of nitrogen-doped $NiTiO_3$ thin films prepared by a co-sputtering process. *RSC Adv.* **5,** 10551–10559 (2015).

115. Ruiz Preciado, M. A., Kassiba, A., Morales-Acevedo, A. & Makowska-Janusik, M. Vibrational and electronic peculiarities of $NiTiO_3$ nanostructures inferred from first principle calculations. *RSC Adv.* **5,** 17396–17404 (2015).

116. Brockis, J. M. & Reddy, K. N. in 561 (Kluwer Academic/Plenum Publishers, 2000).

117. Park, K. W., Choi, J. H., Ahn, K. S. & Sung, V. E. PtRu alloy and PtRu-WO_3 nanocomposite electrodes for methanol electrooxidation fabricated by a sputtering deposition method. *J. Phys. Chem. B* **108,** 5989–5994 (2004).

118. Parsons, R. & Vandernoot, T. J. The oxidation of small organic molecules: a survey of recent fuel cell related research. *J. Electroanal. Chem.* **257,** 9–45 (1998).

119. Danaee, I., Jafarian, M., Forouzandeh, F., Gobal, F. & Mahjani, M. G. Electrocatalytic oxidation of methanol on Ni and NiCu alloy modified glassy carbon electrode. *Int. J. Hydrogen Energy* **33,** 4367–4376 (2008).

120. El-Shafei, A. A. Electrocatalytic oxidation of methanol at a nickel hydroxide / glassy carbon modified electrode in alkaline medium. *J. Electroanal. Chem.* **471,** 89–95 (1999).

121. Singh, R. N., Singh, A. & Mishra, D. Influence of the nature of conductive support on the electrocatalytic activity of electrodeposited Ni films towards methanol oxidation in 1 M KOH. *Int. J. Hydrogen Energy* **33,** 6878–6885 (2008).

122. Oliver-Tolentino, M. A. *et al.* Electrochemical behavior of Ni_xW_{1-x} materials as

catalyst for hydrogen evolution reaction in alkaline media. *J. Alloys Compd.* **536,** S245–S249 (2012).

123. Wang, Y., Zhang, D., Peng, W., Liu, L. & Li, M. Electrochimica Acta Electrocatalytic oxidation of methanol at Ni – Al layered double hydroxide film modified electrode in alkaline medium. *Electrochim. Acta* **56,** 5754–5758 (2011).

124. Rahim, M. A. A., Hameed, R. M. A. & Khalil, M. W. Nickel as a catalyst for the electro-oxidation of methanol in alkaline medium. **134,** 160–169 (2004).

125. Radtke, G., Lazar, S. & Botton, G. A. High-resolution EELS investigation of the electronic structure of ilmenites. *Phys. Rev. B* **74,** 155117 (2006).

126. Scott, B. A. & Burns, G. Determination of stoichiometry Variations in $LiNbO_3$ and $LiTaO_3$ by Raman Powder Spectroscopy. *J. Am. Ceram. Soc.* **55,** 225–230 (1972).

127. Fall, S., Kulij, M. & Gibaud, A. X-ray analysis of mesoporous silica thin films templated by Brij58 surfactant. *J. Phys. Condens. Matter* **22,** 474005 (2010).

128. Henderson, M. J., Gibaud, A., Bardeau, J. F. & White, J. W. An X-ray reflectivity study of evaporation-induced self-assembled titania-based films. *J. Mater. Chem.* **16,** 2478–2484 (2006).

129. Fall, S., Pattier, B., Benyayia, L. & Gibaud, A. Binary Phase Diagram of Water/Brij58 Studied by SAXS. *Acta Phys. Pol. A* **121,** 388–396 (2012).

130. Asahi, R., Morikawa, T., Ohwaki, T., Aoki, K. & Taga, Y. Visible-light photocatalysis in Nitrogen-doped Titanium oxides. *Science* **293**, 269-271 (2001).

131. Soni, S. S., Henderson, M. J., Bardeau, J. F. & Gibaud, A. Visible-light photocatalysis in titania-based mesoporous thin films. *Adv. Mater.* **20**, 1493-1498 (2008).

132. Ikeda, S., Hirao, K., Ishino, S., Matsumura, M. & Ohtani, B. Preparation of platinized strontium titanate covered with hollow silica and its activity for overall water splitting in a novel phaseboundary photocatalytic system. *Catal. Today* **117,** 343–349 (2006).

BIBLIOGRAPHY

ANNEXES

1. CONGRESS COMMUNICATIONS

- XXIII International Materials Research Congress, Cancún, México. "Nickel titianate ($NiTiO_3$) powders fabricated by sol-gel and solid state reaction." M.A. Ruiz-Preciado, A. Kassiba, A. Gibaud, A. Morales-Acevedo
- XXIII International Materials Research Congress, Cancún, México. "Nickel titanate ($NiTiO_3$) thin films synthesis rf-sputtering for photocatalythic applications." M.A. Ruiz-Preciado, A. Kassiba, A. Gibaud, A. Morales-Acevedo
- XXIV International Materials Research Congress, Cancún, México. "Sol-Gel synthesis of Ilmenite $NiTiO_3$ nanoparticles at low temperature." M.A. Ruiz-Preciado, A. Morales-Acevedo, A. Gibaud, M. Makowska-Janusik, A. Kassiba
- XXV International Materials Research Congress, Cancún, México. "Synthesis and investigations of Nickel titanate ($NiTiO_3$) thin films for photocatalytic applications." M.A. Ruiz-Preciado, A. Bulou, A. Gibaud, M. Makowska-Janusik, A. Morales-Acevedo, A. Kassiba.

2. LIST OF PEER-REVIEWED JOURNAL PUBLICATIONS

- Ruiz-Preciado, M. A., Kassiba, A., Morales-Acevedo, A. & Makowska-Janusik, M. Vibrational and electronic peculiarities of $NiTiO_3$ nanostructures inferred from first principle calculations. *RSC Adv.* **5,** 17396–17404 (2015).
- Ruiz-Preciado, M. A., Kassiba, A., Gibaud, A. & Morales-Acevedo, A. Comparison of nickel titanate ($NiTiO_3$) powders synthesized by sol-gel and solid state reaction. *Mater. Sci. Semicond. Process.* **37,** 171–178 (2015).
- Ruiz-Preciado, M. A., Bulou, A., Makowska-Janusik, M., Gibaud, A., Morales-Acevedo, A. & Kassiba, A. Nickel Titanate ($NiTiO_3$) thin films: RF-sputtering synthesis and investigations of related features for photocatalysis. *CrystEngComm* **18,** 3229–3236 (2016).
- Bellam, J. B., Ruiz-Preciado, M. A., Edely, M., Szade, J., Jouanneaux, A. & Kassiba, A. Visible-light photocatalytic activity of nitrogen-doped $NiTiO_3$ thin films prepared by a co-sputtering process. *RSC Adv.* **5,** 10551–10559 (2015).

3. REPRINTS OF THE PEER-REVIEWED JOURNAL PUBLICATIONS

a. Vibrational and electronic peculiarities of $NiTiO_3$ nanostructures inferred from first principle calculations

RSC Advances

PAPER

View Article Online
View Journal | View Issue

CrossMark

Cite this: RSC Adv., 2015, 5, 17396

Vibrational and electronic peculiarities of $NiTiO_3$ nanostructures inferred from first principle calculations

M. A. Ruiz Preciado,[abc] A. Kassiba,[b] A. Morales-Acevedo[c] and M. Makowska-Janusik*[a]

Structural, electronic and vibrational properties of nanostructured $(NiTiO_3)_n$ clusters were calculated by numerical models based on DFT and semi-empirical quantum chemistry codes. The clusters were built by using the initial atomic positions of crystalline ilmenite, which were relaxed to ensure stable and energetically favourable geometries. For the electronic properties, the semi-empirical PM6 parameterisation method was used to evaluate the HOMO–LUMO energy differences versus nanocrystal sizes. The quantum confinement effect was induced with cluster size reduction. Theoretical UV-Vis absorption and Raman spectroscopy showed the drastic influence of the surface characteristics on the electronic and the vibrational properties of the nanoclusters. Theoretically, it was proved that powder $NiTiO_3$ exhibits a patchwork of the properties of the bulk ilmenite material, amorphous Ni–Ti–O structures and atoms located at the surface of the investigated cluster.

Received 15th December 2014
Accepted 30th January 2015

DOI: 10.1039/c4ra16400h

www.rsc.org/advances

Introduction

Photocatalytic processes have been intensively discussed and investigated in the last two decades, due to their potential applications in solving problems of waste in the environment or alternatively in creating new sources of energy.[1,2] For example, it can be mentioned that photocatalytic reactions contribute to the remediation of environmental pollution by the degradation of organic compounds or to the production of hydrogen by the dissociation of water for renewable energy.[3–5] These processes are based on photoinduced charge transfers caused by light sources (visible or UV) in the semiconducting oxides.

Beyond its applications in photovoltaic devices, titanium dioxide (TiO_2) is one of the most efficient materials for photocatalytic reactions and possesses the best performance, associated with its good stability, versatile applications, non-toxicity and low cost.[6–11] Photocatalytic reactions using TiO_2 under UV irradiation have been carried out to remove different types of impurities from wastewater.[12–16] The kinetics of the reactions are characterized by short relaxation times to achieve the complete removal of pollutants. However, the need for UV to induce the required charge transfer in the mentioned reactions limits the performance of TiO_2. Therefore, photocatalytic materials that operate under visible light irradiation are of interest, since the solar light spectrum can be exploited on a large scale to activate high performance photocatalytic reactions.

The perovskite-type oxides, such as tantalates and titanates, have recently attracted much attention, because of their high photocatalytic activities under UV irradiation and, more remarkably, under visible light.[17–19] These titanates, such as $ATiO_3$ (A = Ca, Bi, Pb, Fe, Co, Mn, Ni, Cu, and Zn) have been studied as functional inorganic materials with many applications as electrodes for solid oxide fuel cells, metal–air barriers, gas sensors, solid lubricants, and high-performance catalysts.[20–22] Among these materials, we consider the transition metal titanates, such as $FeTiO_3$, $CoTiO_3$, $MnTiO_3$, $NiTiO_3$, *etc.*, that crystallize in the ilmenite structure under atmospheric pressure.[23–26] They are of particular interest due to their versatile electrical and magnetic properties, such as their antiferromagnetic behavior.[27,28] The related properties of several titanate oxides have been investigated experimentally and theoretically. $FeTiO_3$ is of interest as a natural mineral and a major source of titanium for the commercial production of TiO_2. The electronic, magnetic, structural and elastic properties of bulk $FeTiO_3$ have been computed using the density functional theory (DFT) formalism and *ab initio* calculations.[23–25] Within such approaches, the electronic ground-state properties and the charge transfer involved in $FeTiO_3$ were determined by the strong coupling of the structure with the charge distribution. The quantum-mechanical description of these features is very sensitive to the treatment of electronic exchange and correlation energies. This allows us to conclude that the metal titanates are strongly correlated systems and therefore the electron correlation part should be taken into account sufficiently.

[a]Institute of Physics, Jan Długosz University in Częstochowa, Al. Armii Krajowej 13/15, 42200 Częstochowa, Poland. E-mail: m.makowska@ujd.czest.pl
[b]Institute of Molecules and Materials of Le Mans, Université du Maine, 72085 Le Mans, France
[c]Centro de Investigación y Estudios Avanzados del IPN, Unidad Zacatenco, Mexico

The present work reports theoretical approaches to model the nanostructures and simulate the electronic and vibrational properties of $NiTiO_3$ nanoclusters. Comparative studies were also performed by using bulk crystal, with its infinite and periodic structure. Previous theoretical approaches developed by Xin *et al.*[29] were used to compute the electronic properties of the bulk and infinite $NiTiO_3$ system. However, to the best of our knowledge no particular models have been developed to compute and predict the physical properties of the $NiTiO_3$ nanostructures. The study of nanosized systems, with regard to the critical role of the specific active surface in physical phenomena, is of great interest. Particularly, because the interfaces between the active material and the surrounding media contribute critically to the efficiency of heterogeneous catalysis. However, developing theoretical models and numerical simulations to predict the electronic, optical, structural, vibrational and related properties of nanoparticles is a challenging task. The numerical approach presented here was partially used in our former studies devoted to functional semiconducting systems.[30–32] The nanostructures were built from their native bulk crystals with specified atomic positions as involved in defined space groups. Also, in this work, the modeling of bulk systems is of primary importance in developing the methodology for establishing the structural, vibrational and electronic properties of nanostructures. The quantum chemical calculations were based on first-principles calculations using the ultrasoft pseudopotential of the plane-wave within the DFT formalism. The generalized gradient approximation extended by Hubbard parameters was used to evaluate the electronic properties of the $NiTiO_3$ bulk crystal.

The original task in this work consisted of modeling the crystal structure at the nanoscale, including the relaxation of the outermost surface atoms with suitable treatment. The changes in their electronic and vibrational properties were accurately described as a function of the structural features of the investigated nanoclusters. Also the influence of the surface on the physical properties of the clusters was demonstrated. The simulation of electronic band structures clarified the charge transfer characteristics. This approach paves the way to elucidating the mechanisms behind the photocatalytic activity of the nanosized $NiTiO_3$ materials. The theoretical results are compared to the data obtained by experimental investigations of the relevant features of $NiTiO_3$ nanostructures.

Computational details and cluster building methodology

The crystal structures were computed for two different configurations of the material. One of them was considered to represent the bulk $NiTiO_3$ monocrystal crystallized in the ilmenite phase; *i.e.* space group $R\bar{3}$ (no. 148).[33] The second was chosen to be a nanocrystalline cluster of varying size, possessing the ilmenite structure in the core. Therefore, the unit cell of ilmenite $NiTiO_3$ was built using the cell parameters $a = b = 5.0289$ Å, $c = 13.7954$ Å and the angular parameters $\alpha = \beta = 90°$ and $\gamma = 120°$. The positions of representative atoms within the unit cell are summarized in Table 1. The crystal structure of $NiTiO_3$ was built using the Materials Studio Program Package. The same simulation software was used to build the $(NiTiO_3)_n$ nanostructures with diameters from 0.6 nm up to 2.6 nm, associated with clusters composed of $(NiTiO_3)_2$ and $(NiTiO_3)_{161}$ units, respectively. Consequently, all of the investigated nanocrystals exhibited spherical shapes and stoichiometric compositions. According to our previous work on other classes of nanocrystalline systems, dangling bonds were not specially saturated.[31] The unit cell of the monocrystal and the morphology of the $(NiTiO_3)_{82}$ cluster are depicted in Fig. 1.

Table 1 Lattice parameters and atomic fractional coordinates of the $NiTiO_3$ crystal structures

Atom name	x/a	y/b	z/c
Ni	0	0	0.3499(1)
Ti	0	0	0.1441(1)
O	0.3263(7)	0.0214(10)	0.2430(3)
Cell parameters	$a = b = 5.0289(1)$ Å, $c = 13.7954(2)$ Å, $\alpha = \beta = 90°$, $\gamma = 120°$		
Space group	$R\bar{3}$ (no. 148)		

The electronic properties of the $NiTiO_3$ single crystal were calculated using the DFT methodology. The quantum chemical calculations were performed using the Cambridge Serial Total Energy Package (CASTEP)[34] *i.e.* the module of the Materials Studio Program. The CASTEP is based on the evaluation and analysis of the total energy inferred from the plane-wave pseudopotential method. The first task deals with the geometry optimisation of the investigated crystal structure, which is built and evaluated with respect to the total energy minimization within the Broyden–Fletcher–Goldfarb–Shanno (BFGS) algorithm.[35] During the geometry optimisation procedure, the symmetry of the structure was frozen but the size of the unit cell was allowed to change. The convergence criteria for the optimization procedure were chosen as hereafter outlined. The convergence of the total energy during the geometry optimization procedure cannot be greater than 2×10^{-5} eV per atom, the force on the atom must be less than 0.01 eV Å^{-1}, the stress on the atom less than 0.02 GPa and the maximal atomic displacement no more than 5×10^{-4} Å. The electron exchange–correlation energy was treated within the framework of the generalized gradient approximation (GGA) using Perdew–Burke–Ernzerhof (PBE)[36] potential. To accelerate the

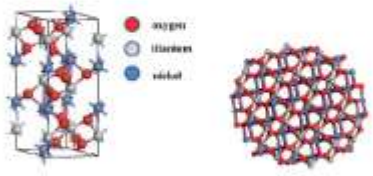

Fig. 1 The unit cell of crystalline $NiTiO_3$ (left) and the unpassivated nanocrystalline structure made by the formula $(NiTiO_3)_{82}$ (right).

computational runs, the ultrasoft pseudopotential formalism was used. In this frame, calculations were performed for Ti ($3d^3$ $4s^2$), Ni ($3d^8$ $4s^2$) and O ($2s^2$ $2p^6$) electrons. The cut-off energy of the plane-wave basis set was chosen to be equal to 500 eV. The integration by numerical sampling for specific directions over the Brillouin zone (BZ) were carried out using the Monkhorst–Pack method with an $8 \times 8 \times 8$ special k-point mesh. The total energy convergence criterion was assumed to be fulfilled when the self-consistent field (SCF) tolerance; *i.e.* equal to 10^{-5} eV per atom.

The electronic properties of the $NiTiO_3$ crystal were computed using the above-mentioned parameters, as specified for the geometry optimization procedure. The calculations were carried out in spin restricted as well as spin unrestricted procedures, applying the GGA/PBE potential and Heyd–Scuseria–Ernzerhof (HSE06) range-separated hybrid functional.[37,38] Hummer *et al.*[38] showed that the HSE06 functional yields the correct electronic band structure for the semiconductors of group-IV. Also the work of Śpiewak *et al.*[39] shows that the HSE06 potential may better reproduce the electronic properties of Ge single crystals with defects. Contrary to this, other works indicate that the range-separated functionals show improvements for strong charge transfer systems.[41,42] It is generally known that classical DFT potentials do not correctly reproduce far-nucleus asymptotic behaviour[43,44] and underestimate the excitation energies, notably for charge transfer processes.[45] The range-separated potentials lead to the partitioning of the total exchange energy into short-range and long-range contributions:

$$E_X = E_X^{sr} + E_X^{lr} \quad (1)$$

To improve the exchange functional, in terms of calculating the long-range electron–electron interactions using the HF exchange integral, the standard error function is used. The repulsion electron operator is also divided into short-range and long-range parts and can be defined for two electrons at the r_{ij} distance as:

$$\frac{1}{r_{ij}} = \frac{1 - [\alpha + \beta \mathrm{erf}(\mu r_{ij})]}{r_{ij}} + \frac{\alpha + \beta \mathrm{erf}(\mu r_{ij})}{r_{ij}} \quad (2)$$

where the α and β parameters define the exact exchange percentages between the short and long-range exchange functional. μ represents the weighting factor, which controls the separation between the short-range exchange functional and the long-range part of the HF exchange integral.

The Kohn–Sham equation was also solved using the GGA/PBE functional extended by the Hubbard parameters. The introduced methodology contributes to precise insights into the electronic properties of the material. The major drawback of all functionals lies in the underestimation of the calculated electronic band gap.[46] This is frequently encountered due to the approximate calculations of the electron self-interaction energies. Also, pure local density approximations (LDA),[47] generalized gradient approximations (GGA)[48] and even hybrid functionals[49–51] can lack precision in some instances, due to so-called "strongly correlated" systems.

One relevant solution for describing correlated electrons in solids concerns the Hubbard model,[52] based on an extended LDA approach, also referred to as LDA + U. It decreases the electron self-interaction error by selectively adding an energy correction to localized electron states, such as d or f orbitals where the self-interaction is particularly large. To construct an appropriate functional, the LDA + U approach subdivides the charge density into two subsystems with delocalized and localized features. In the multiband Hubbard model the effective LDA + U energy functional is written as:

$$E_{LDA+U} = E_{LDA} + E_{HF}(n_{\mu\sigma}) - E_{dc}(n_{\mu\sigma}) \quad (3)$$

where E_{LDA} denotes the standard LDA energy functional, E_{HF} is the Hartree–Fock (HF) functional, E_{dc} is the double counting term and $n_{\mu\sigma}$ is one particle density matrix. The HF part can be written as follows:

$$E_{HF}(n_{\mu\sigma}) = \frac{1}{2} \sum (U_{1324} - U_{1342}) n_{12} n_{34} \quad (4)$$

where the U_{1324} terms represent the renormalized Coulomb integrals. In the LDA + U approach, the Kohn–Sham equation is supplemented by the non-local potential. On the other hand, the DFT/Hubbard method fails to compute the correct energy difference between systems with localized/correlated and delocalized/uncorrelated electronic states.[53] In such an approach, the LDA/GGA + U methodology has successfully been applied to compute the electronic properties of different ternary oxides, such as $CuAlO_2$,[54] $CuAl_2O_4$,[55] $Pr_2Ti_2O_7$ or $Ce_2Ti_2O_7$,[56] and $MnFe_2O_4$.[57] Based on the outlined theoretical framework, the influence of the Hubbard parameter U on the electronic properties of $NiTiO_3$ was investigated for the crystalline structure in bulk material or in nanosized clusters, taking into account the strong correlation of the d-orbital electrons.

In the present work, the electronic properties of the $(NiTiO_3)_n$ nanoclusters were also calculated. To our knowledge, it is first time that nickel titanate nanostructures have been studied theoretically. The methodology requires two different calculation codes to perform the simulations and also to ensure their stability. Thus, the Gaussian09 and MOPAC (Molecular Orbital PACkage)[58] quantum chemistry programs were used. With regard to the size of the investigated clusters, semiempirical single point calculations were performed, applying the parameterized self-consistent restricted HF (SCF RHF) PM6 method.[59] The convergence of the SCF procedure was achieved with an energy uncertainty not greater than 10^{-6} hartrees and no more than 150 required iterations. Within such approaches, the electronic properties of two different cluster families were computed. The first one deals with $(NiTiO_3)_n$ clusters possessing an ilmenite crystal structure without any reconstruction. The second considers the same clusters as specified previously, but their geometries were optimised according to the total energy minimization. The geometry of all clusters was specified in Cartesian coordinates with $C1$ symmetry. The gradient convergence tolerance was equal to 10^{-6} hartrees $bohr^{-1}$ using the quadratic approximation (QA) method,[60–62] updating the Hessian matrix during the optimization. The Hessian

evaluation was performed to exclude the structures giving rise to negative frequency modes.

Results and discussion

Structure and electronic properties of bulk ilmenite $NiTiO_3$

The GGA/PBE functional was used to build the stable $NiTiO_3$ crystal geometry and to calculate the related physical responses. In the first step, the geometry optimization of the crystal structure was performed. The changes to the optimised atomic distances were less than 5% compared to the starting values from the defined crystallographic data. It is in agreement with the former report by Xin *et al.*[58] The noticed departures from these values could be attributed to the fact that the present calculations were performed at $T = 0$ K, whereas the experimental structural data measurements were generally performed at room temperature. Thus, the relatively low deviation between the optimized values and experimental structural data indicates that GGA/PBE is a suitable computational functional for the description of the structures of the $NiTiO_3$ crystal. Following the performed geometry optimization, one may conclude that the ilmenite $NiTiO_3$ structure appears as the layered organisation depicted in Fig. 2 (left-hand panel), where Ti and Ni atoms form the layers separated by oxygen atoms.

The electronic properties of the $NiTiO_3$ crystal were computed within the spin polarized approach for a primitive unit cell (see Fig. 2). The band structure calculations were performed in the k space within the BZ directions shown in Fig. 2 (right-hand panel). The DFT/HSE06 functional gives unsatisfactory results. The obtained energy gap is equal to 1.23 eV, whereas the experimental data are within 2.12–2.18 eV.[61–65] Also, the DFT/PBE functional was considered with and without the Hubbard approximation. The mentioned functional without the Hubbard approximation and in the spin polarized regime gives an energy gap equal to 0.77 eV for the $NiTiO_3$ crystal. This shows that using nonempirically tuned range-separated DFT methods results in a significant improvement over traditional GGA functionals but does not give good results for the studied crystal. The large discrepancies suggest the presence of strongly correlated electrons from the considered (Ti and Ni) ions, leading to the necessity to explore the Hubbard approximation in such systems. Within the approach based on the DFT/PBE potential, the electron density depicted in Fig. 3 also informs us about the covalent character of the O–Ti, O–Ni and Ti–Ni bonds. This behavior indicates the nature of the strongly correlated system and the necessity to develop the theoretical functional to reconcile the predicted electronic features with the experimental findings.

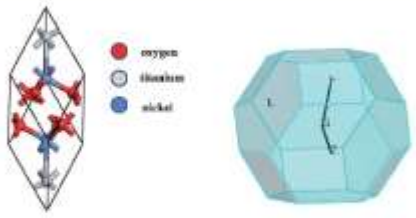

Fig. 2 Primitive unit cell of $NiTiO_3$ (left) and the corresponding reciprocal lattice (right) with the coordinates of the special points of the BZ: F (1/2, 1/2, 0); Γ (0, 0, 0); K (1/4, 1/4, 1/4) and Z (1/2, 1/2, 1/2).

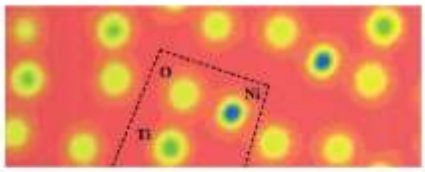

Fig. 3 Electron density projection in a selected plane of the $NiTiO_3$ ilmenite structure.

The functional modified by the Hubbard approximation uses parameters that can be chosen for Ti 3d and Ni 3d valence electrons in order to evaluate the energy band gap values. The influence of the chosen Hubbard parameter U on the obtained band gaps is demonstrated in the summary in Table 2. The correct evaluation of the electronic behaviour, in agreement with experimental findings, requires fixed Hubbard parameters at 3.5 eV and 4.5 eV for Ti 3d and Ni 3d electrons, respectively. Thus, the DFT/PBE + U method may provide a satisfactory qualitative electronic structure calculation with the correct choice of the Hubbard parameters. The electronic band structure computed with $U_{Ti} = 3.5$ eV and $U_{Ni} = 4.5$ eV is presented in Fig. 4. This plot indicates that the $NiTiO_3$ structure exhibits a direct semiconducting nature with an energy gap equal to 2.33 eV. Its spin polarized character is also included in the predicted electronic features. Thus, the top of the valence band is constituted by spin polarized alpha electrons while the bottom of the conduction band is composed of the beta state. In addition, the partial density of states depicted in Fig. 5 shows that the spin polarized alpha electrons with energies at the top of the valence band derive from the hybridization of Ni 3d and O 2p orbitals; while hybridization of the Ti 3d and Ni 3d states defines the electronic structure at the bottom of the conduction band, in agreement with the previous work of Salvador *et al.*[66]

The energy dispersion of the electronic states allows us to calculate the effective masses of charge carriers. The diagonal elements of the effective mass tensor for electrons and holes are calculated as the energy derivatives around the K point of the BZ, following the equations:

Table 2 Hubbard U parameter values for the Ti d and Ni d orbitals and the energy gap value calculated by the DFT/PBE + U methodology

Ti 3d	Ni 3d	E_g [eV]
0	0	0.77
2.5	2.5	1.75
3.5	4.5	2.33
4.5	3.5	1.94
4.5	4.5	2.46

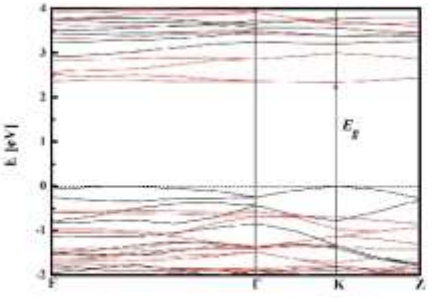

Fig. 4 Electron band structure calculated by the DFT/PBE functional within the Hubbard approximation U. The energy levels with spin polarized alpha electrons (black) and energy levels with a beta state (red) are shown.

$$\frac{1}{m_{h_{ij}}^*} = \frac{1}{\hbar^2}\frac{\partial^2 E_v(k)}{\partial k_i \partial k_j} \text{ and } \frac{1}{m_{h_{ij}}^*} = \frac{1}{\hbar^2}\frac{\partial^2 E_v(k)}{\partial k_i \partial k_j} \quad (5)$$

The effective mass of electrons and holes is determined by fitting the conduction and valence bands (see Fig. 4), respectively, to parabolic functions. One may see that the top of the valence band and bottom of the conduction band are symmetric around the K point of the BZ. In this case, the calculated effective masses of the electrons and holes are equal to $m_e^* = 2.0986m_e$ and $m_h^* = 0.6836m_e$, with the same values in both the K–Z and K–Γ directions of the BZ. The relatively high values of the reported parameters suggest that the mobility of charges in the investigated $NiTiO_3$ single crystal is relatively low. This result is of particular importance for the very low electrical conductivity (10^{-9} S m^{-1}) achieved in $NiTiO_3$ at moderate temperatures up to 200 °C.[67] The performed calculations confirm that in the studied material the electrical conduction observed at temperatures below 700 K seems to be extrinsic, governed by impurities, interstitial sites, *etc.* It takes place *via* the small polaron hopping mechanism.[64]

Nanocrystalline ilmenite $NiTiO_3$ clusters

Structural and electronic features. Structural and electronic properties of $NiTiO_3$ nanocrystals were investigated for nanoparticles made of the ilmenite bulk material. The investigated nanostructures possess a spherical shape with a variable number of $(NiTiO_3)_n$ units, from $n = 2$ up to 183. The single point DFT/PBE and DFT/HSE06 calculations were performed for clusters with n from 2 up to 20, but the results did not show the correct behaviour of the energy difference between the highest unoccupied molecular orbital (HOMO) and lowest unoccupied molecular orbital (LUMO) *versus* the size of the cluster. It is known that the standard DFT scheme is not useful for finite-sized objects because the asymptotic potential, absent in the bulk material, plays a crucial role in the cluster energy due to the addition and removal of electrons. This leads to the calculated energy gaps for finite-sized objects often being much smaller than the real gaps.[68]

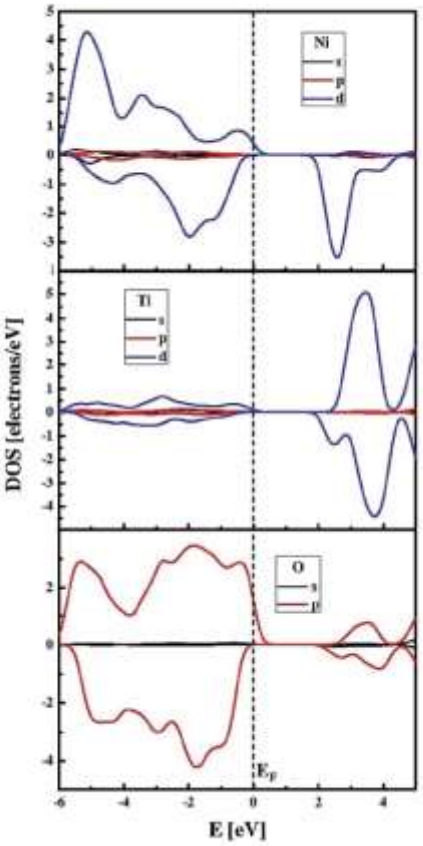

Fig. 5 Electron density of state (DOS) calculated for the $NiTiO_3$ ilmenite structure by using the DFT/PBE functional augmented by the Hubbard approximation: polarized alpha electrons (top) and beta electrons (bottom).

Contrary to the results obtained by DFT, the PM6 semi-empirical methodology was successfully applied for such clusters, leading to the correct estimation of the energy gap in nanosized $NiTiO_3$. In Fig. 6, the computed energy differences $\Delta E_{HOMO-LUMO}$ *versus* the cluster sizes are depicted. The reported energy gap splitting as a function of the $(NiTiO_3)_n$ units demonstrates the size induced quantum confinement effect. This is in agreement with the experimental report[69] on $NiTiO_3$ nanoparticles that give rise to a blue shift in the absorption spectra compared to the bulk material. The $\Delta E_{HOMO-LUMO}$ value reaches saturation for clusters comprising $n \geq 50$ $(NiTiO_3)_n$

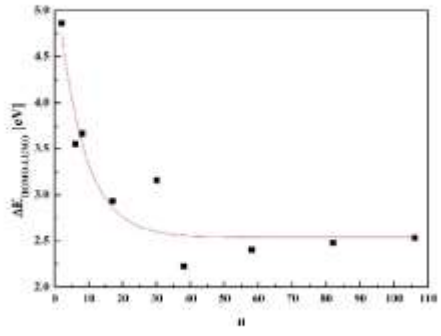

Fig. 6 Evaluation of the $\Delta E_{HOMO-LUMO}$ energy splitting versus number n of $(NiTiO_3)_n$ units calculated by the PM6 methodology.

units. The energy gap value for the large clusters saturates at 2.55 eV.

Using the PM6 model, UV-Vis absorption spectra were computed for selected clusters, namely $(NiTiO_3)_2$, $(NiTiO_3)_8$ and $(NiTiO_3)_{17}$. Large clusters were not considered due to the memory limitations of the computer system. The calculated spectra are presented in Fig. 7, along with the experimental data. A good agreement is demonstrated between the spectrum calculated by the PM6 model for the $(NiTiO_3)_{17}$ cluster and the measured one for the crystalline powder of $NiTiO_3$. Increasing the cluster diameter (unit number $n = 2$–17), the position of the A band (see Fig. 7 left-hand panel) shifts to the red spectral range. The band labelled B, with pronounced intensity for small clusters, undergoes a red shift and decreases notably in intensity with increasing cluster size. For the cluster $(NiTiO_3)_{17}$ with a diameter of 1.20 nm an additional broad peak C develops in the range 750–900 nm. The broad band in that spectral range was also demonstrated experimentally. The UV-Vis spectrum calculated for the bulk crystal $NiTiO_3$ by using the DFT/PBE + U functional (see Fig. 7, upper right-hand panel) did not match that obtained experimentally in the high wavelength range, where the C band is involved. This confirms that the surface effect in the experimental absorption spectrum of the $NiTiO_3$ powders plays a key role.

The HOMO and LUMO orbitals, depicted in Fig. 8, for the investigated clusters $(NiTiO_3)_2$, $(NiTiO_3)_8$ and $(NiTiO_3)_{17}$, show their explicit separation and contribute to the low energy absorption spectra. The separation feature between HOMO and LUMO orbitals is not seen for the bulk $NiTiO_3$, where the valence and conduction bands are attributed to the orbitals expanded through the volume of the crystal. The observed details suggest that the separation of the HOMO and LUMO orbitals gives rise to B and C bands.

The comparison of the theoretical and the experimental UV-Vis absorption spectra of the $(NiTiO_3)_{17}$ nanocluster clearly indicates the interesting optical activity of the system in the UV and the visible range of the solar spectrum. A broad absorption edge situated at ~410 nm is associated with $O^{2-} \rightarrow Ti^{4+}$ charge transfer transitions. The higher wavelength shoulder is associated with the crystal field splitting of $NiTiO_3$, giving rise to the $Ni^{2+} \rightarrow Ti^{4+}$ transitions.[76] Thus, for the nanosized $NiTiO_3$, the photoinduced charge transfers that are required for

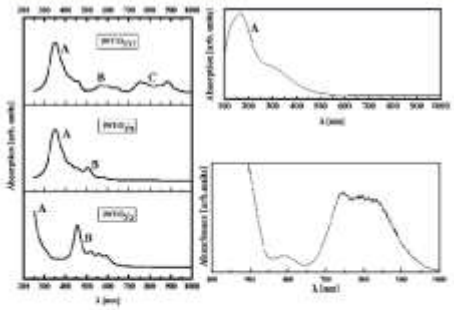

Fig. 7 UV-Vis absorption spectra calculated by the PM6 model for different clusters (left-hand panel), the spectrum calculated for the bulk crystal by using the DFT/PBE + U functional (upper right-hand panel) and the experimentally obtained data (lower right-hand panel).

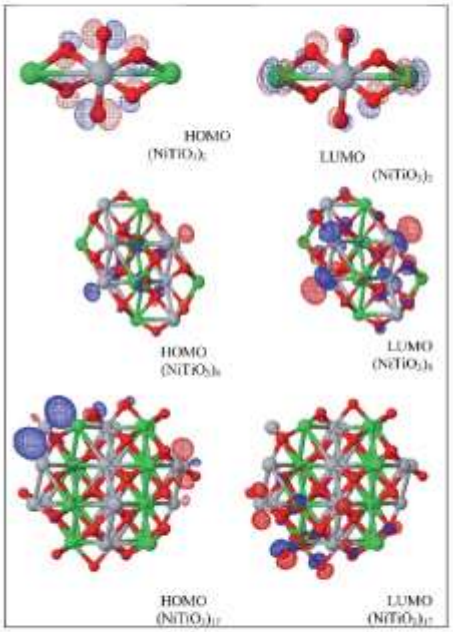

Fig. 8 HOMO and LUMO orbitals calculated by the PM6 model for the $(NiTiO_3)_2$, $(NiTiO_3)_8$ and $(NiTiO_3)_{17}$ clusters.

photocatalytic reactions may be ensured by several electronic transitions covering the UV and visible light range. These contribute to the efficient photocatalytic activity. Finally, it is worth noting that the resolved details on the theoretical absorption spectra are induced by calculations performed without any influence from the temperature on the structural relaxation of the $NiTiO_3$ clusters. The possibility of reconciling the shapes of the absorption bands between the theory and experiments may be realized through the electron–phonon interactions and the Franck–Condon rule for the optical transition probabilities, as was used in our previous work.[71]

Raman spectroscopy of nanocrystalline $NiTiO_3$. Taking into account the effect of electron–phonon interactions, the evaluation of the Raman spectra related to the selected clusters were performed using the PM6 approach. The Raman spectra were calculated using the standard procedure implemented in the Gaussian program package. The calculations were performed on two $(NiTiO_3)_{17}$ clusters. In one of these, the ilmenite crystal structure was frozen and the other system possessed a surface reconstructed using the geometry optimization procedure according to the total energy minimization criterion. The last cluster was characterized by a completely amorphous network. The experimental and calculated Raman spectra modeled for the $(NiTiO_3)_{17}$ nanoclusters and for the $NiTiO_3$ powder are depicted in Fig. 9.

For the cluster $(NiTiO_3)_{17}$ with a primarily ilmenite structure, the calculations show only a single mode at position C. The experimental Raman spectrum shows an intense band with a wavenumber position in agreement with the calculated value. The C band is also the most intense detail in the experimental Raman spectrum. The titanates, such as $NiTiO_3$, $CoTiO_3$ and Na_4TiO_4, possess hexacoordinated Ti–O–Ti groups and their Raman modes are associated with the main band, located at 705, 688, 737 cm^{-1}, respectively.[72–74] Therefore, it was established that the Ti–O–Ti stretching mode should appear in the vicinity of 700 cm^{-1}. For $NiTiO_3$, the band at 720 cm^{-1} corresponds to the Ti–O–Ti vibration of the crystal structure.

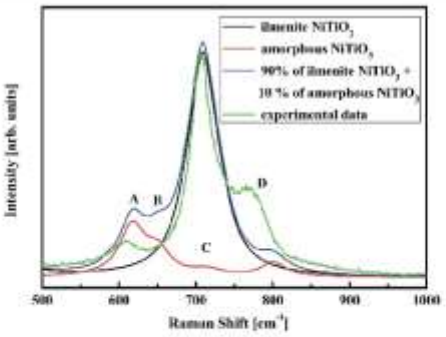

Fig. 9 Raman spectra for the $(NiTiO_3)_{17}$ nanoparticles calculated by the parametrised PM6 method as well as experimental spectrum.

The Raman bands named A, B and D, with relatively low intensities compared to the C band, are associated to the full optimization and relaxation of the nanocluster structures. This procedure, which leads to stable amorphous networks, ensures molecular bonding distortions, including changes to bond lengths and angles. Such structural changes modify the vibrational features and, as shown experimentally and theoretically, cause new Raman bands to appear. A superposition of the main Raman band (90%) for O–Ti–O stretching and the secondary bands (10%) related to the amorphous structure leads to a theoretical Raman spectrum that reproduces the features of the experimental one. The slight departures from the experimental band positions may be explained by the fact that anharmonic vibration terms were not considered in the calculation model. The main origin may be related to bond frequency distributions due to amorphization or the occurrence of vacancies or antisites contributing to the damping and frequency shifts of Raman modes.[75,76] In this frame, it was proved that the bands located at 617 and 690 cm^{-1} originate from the stretching of Ti–O and bending of O–Ti–O bonds, while the contribution at 547 cm^{-1} results from Ni–O bonds.[69]

As illustrated from the theoretical analysis and the experimental Raman investigations, the organization of the powder material is fully accounted for in the analysis that has been carried out. The particle core brings the signature features of the infinite and bulk crystal, while the outermost particle surface accounts for the amorphous features. This is presumably due to the manifestation of surface states with the relaxation and reconstruction of the outermost particle layers.

Conclusions

The electronic, optical and vibrational properties of $(NiTiO_3)_n$ nanostructures were investigated and compared to those of bulk ilmenite $NiTiO_3$. The investigated nanostructures possess a spherical shape with the number of $(NiTiO_3)_n$ units modified from $n = 2$ up to 183. The PM6 semi-empirical methodology was able to provide a valuable estimation of the energy gap in nanosized $NiTiO_3$ structures. The value of the $\Delta E_{HOMO\text{-}LUMO}$ saturates at 2.55 eV for the clusters comprising at least $n = 50$ $(NiTiO_3)_n$ units. The UV-Vis absorption spectra were calculated using the PM6 methodology for nanostructures and compared with those obtained experimentally. The obtained spectra confirm that the surface effects in $NiTiO_3$ powders contribute with additional band edges. The comparison of the theoretical and the experimental UV-Vis absorption spectra obtained for the $(NiTiO_3)_{17}$ nanocluster clearly indicates the promising optical activity of the system in the UV and the visible range of the solar spectrum. The $NiTiO_3$ nanoclusters also exhibit other relevant properties required for efficient photocatalysis.

The calculated Raman spectra for the $NiTiO_3$ clusters show the noticeable contribution of the surface to the vibrational properties. Among the features of the Raman spectra, those related to active modes of the ilmenite structure and those inferred from amorphous $NiTiO_3$ can be distinguished. The theoretical superposition of a Raman band that constitutes 90% of the band intensity, and is associated with the O–Ti–O

stretching mode, and secondary less intense bands (10%), related to the amorphous structure, represents the main features of the experimental spectrum.

Finally, the present work points out the relevant optical properties of the $NiTiO_3$ clusters that allow them to harvest visible light for efficient photocatalytic reactions. However, the low mobility of charge carriers, demonstrated from the effective mass estimation, leaves open questions that can be solved using a doping procedure. This is a matter of current development.

Acknowledgements

Calculations have been carried out in Wroclaw Center for Networking and Supercomputing <http://www.wcss.wroc.pl> (Grant no. 171). The MATERIALS STUDIO package was used under POLAND COUNTRY-WIDE LICENSE. The authors acknowledge the financial support of Polonium program 31300 TA – 2014 for researchers' mobility. Marco Ruiz acknowledges the doctoral school 3MPL and CONACyT-Mexico for the financial support.

Notes and references

1 L. Linsebigler, G. Lu and J. T. Yates Jr, *Chem. Rev.*, 1995, **95**, 735.
2 K. Nakata and A. Fujishima, *J. Photochem. Photobiol., C*, 2012, **13**, 169.
3 S. Bagwasi, B. Tian, J. Zhang and M. Nasir, *Chem. Eng. J.*, 2013, **217**, 108.
4 C. L. Torres-Martinez, R. Kho, O. I. Mian and R. K. Mehra, *J. Colloid Interface Sci.*, 2001, **240**, 525.
5 A. Di Paola, E. García-López, G. Marci and L. Palmisano, *J. Hazard. Mater.*, 2012, **211–212**, 3.
6 Y. Liu, G. Su, B. Zhang, G. Jiang and B. Yan, *Analyst*, 2011, **136**, 872.
7 D. Deng, S. T. Martin and S. Ramanathan, *Nanoscale*, 2010, **2**, 2685.
8 M. M. Khin, A. Sreekumaran Nair, V. Jagadeesh Babu, R. Murugan and S. Ramakrishna, *Energy Environ. Sci.*, 2012, **5**, 8075.
9 K. Ariga, S. Ishihara, H. Abe, M. Lia and J. P. Hill, *J. Mater. Chem.*, 2012, **22**, 2369.
10 X. B. Chen, L. Liu, P. Y. Yu and S. S. Mao, *Science*, 2011, **331**, 746.
11 J. Thomas, K. P. Kumar and S. Mathew, *Sci. Technol. Adv. Mater.*, 2011, **3**, 59.
12 X. J. Xu, X. S. Fang, T. Y. Zhai, H. B. Zeng, B. D. Liu, X. Y. Hu, Y. Bando and D. Golberg, *Small*, 2011, **7**, 445.
13 M. A. Lazar, S. Varghese and S. S. Nair, *Catalysts*, 2012, **2**, 572.
14 K. Hashimoto, H. Irie and A. Fuhjishima, *Jpn. J. Appl. Phys.*, 2005, **44**, 8269.
15 S. M. Gupta and M. Tripathi, *Chin. Sci. Bull.*, 2011, **56**, 1639.
16 Y. Ruzmanova, M. Ustundas, M. Stoller and A. Chianese, *Chem. Eng. Transac.*, 2013, **32**, 2233.
17 W. F. Yao, X. H. Xu, H. Wang, J. T. Zhou, X. N. Yang, Y. Zhang, S. Shang and B. B. Huang, *Appl. Catal., B*, 2004, **52**, 109.
18 J. Kim, D. W. Hwang, H. G. Kim, S. W. Bae, S. M. Ji and J. S. Lee, *Chem. Commun.*, 2002, 2488.
19 H. G. Kim, D. W. Hwang and J. S. Lee, *J. Am. Chem. Soc.*, 2004, **126**, 8912.
20 A. Navrotsky, *Chem. Mater.*, 1998, **10**, 2787.
21 D. M. Giaquinta and H.-C. zur Loye, *Chem. Mater.*, 1994, **6**, 365.
22 J. M. Neil, A. Navrotsky and O. J. Kleppa, *Inorg. Chem.*, 1971, **10**, 2076.
23 N. C. Wilson, J. Muscat, D. Mkhonto, P. E. Ngoepe and N. M. Harrison, *Phys. Rev. B: Condens. Matter Mater. Phys.*, 2005, **71**, 075202.
24 N. C. Wilson, S. P. Russo, J. Muscat and N. M. Harrison, *Phys. Rev. B: Condens. Matter Mater. Phys.*, 2005, **72**, 024110.
25 S. W. Chen, M. J. Huang, P. A. Lin, H. T. Jeng, J. M. Lee, S. C. Haw, S. A. Chen, H. J. Lin, K. T. Lu, D. P. Chen, S. X. Dou, X. L. Wang and J. M. Chen, *Appl. Phys. Lett.*, 2013, **102**, 042107.
26 F. J. Craig, *Phys. Rev. Lett.*, 2008, **100**, 167203.
27 P. B. Fabritchnyi, M. V. Korolenko, M. I. Afanasov, M. Danot and E. Janod, *Solid State Commun.*, 2003, **125**, 341.
28 P. B. Fabritchnyi, A. Wattiaux, M. V. Korolenko, M. I. Afanasov and C. Delmas, *Solid State Commun.*, 2009, **149**, 1535.
29 C. Xin, Y. Wang, Y. Sui, Y. Wang, X. Wang, K. Zhao, Z. Liu, B. Li and X. Liu, *J. Alloys Compd.*, 2014, **613**, 401.
30 M. Makowska-Janusik and A. Kassiba, Functional Nanostructures and Nanocomposites – Numerical Modeling Approach and Experiment, in *Handbook of Computational Chemistry*, ed. J. Leszczynski, Springer, 2012.
31 M. Makowska-Janusik, O. Gladii, A. Kassiba, J. Boucle and N. Herlin-Boime, *J. Phys. Chem. C*, 2014, **118**, 6009.
32 H. Melhem, P. Simon, J. Wang, C. Di Bin, B. Ratier, Y. Leconte, N. Herlin-Boime, M. Makowska-Janusik, A. Kassiba and J. Boucle, *Sol. Energy Mater. Sol. Cells*, 2013, **117**, 624.
33 P. S. Anjana and M. T. Sebastian, *J. Am. Ceram. Soc.*, 2006, **89**, 2114.
34 S. J. Clark, M. D. Segall, C. J. Pickard, P. J. Hasnip, M. J. Probert, K. Refson and M. C. Payne, *Z. Kristallogr.*, 2005, **220**, 567.
35 B. G. Pfrommer, M. Cate, S. G. Louie and M. L. Cohen, *J. Comput. Phys.*, 1997, **131**, 233.
36 J. P. Perdew, K. Burke and M. Ernzerhof, *Phys. Rev. Lett.*, 1996, **77**, 3865.
37 J. Heyd, G. E. Scuseria and M. Ernzerhof, *J. Chem. Phys.*, 2003, **118**, 8207.
38 J. Heyd, G. E. Scuseria and M. Ernzerhof, *J. Chem. Phys.*, 2006, **124**, 219906.
39 K. Hummer, J. Harl and G. Kresse, *Phys. Rev. B: Condens. Matter Mater. Phys.*, 2009, **80**, 115205.
40 P. Śpiewak, J. Vanhellemont and K. J. Kurzydłowski, *J. Appl. Phys.*, 2011, **110**, 063534.

41 M. E. Foster and B. M. Wong, *J. Chem. Theory Comput.*, 2012, **8**, 2682.
42 B. W. Wong, M. Piacenza and F. D. Sala, *Phys. Chem. Chem. Phys.*, 2009, **11**, 4498.
43 C. O. Almbladh and A. C. Pedroza, *Phys. Rev. A*, 1984, **29**, 2322.
44 M. Levy, J. P. Perdew and V. Sahni, *Phys. Rev. A*, 1984, **30**, 2745.
45 A. Dreuw, J. L. Weisman and M. Head-Gordon, *J. Chem. Phys.*, 2003, **119**, 2943.
46 M. S. Hybertsen and S. G. Louie, *Phys. Rev. B: Condens. Matter Mater. Phys.*, 1986, **34**, 5390.
47 W. Kohn and L. J. Sham, *Phys. Rev. A*, 1965, **140**, 1133.
48 D. C. Langreth and J. P. Perdew, *Phys. Rev. B: Condens. Matter Mater. Phys.*, 1980, **21**, 5469.
49 P. J. Stephenset, F. J. Devlin, C. F. Chabalowski and M. J. Frisch, *J. Phys. Chem.*, 1994, **98**, 11623.
50 J. P. Perdew, M. Ernzerhof and K. Burke, *J. Chem. Phys.*, 1996, **105**, 9982.
51 J. Heyd, G. E. Scuseria and M. Ernzerhof, *J. Chem. Phys.*, 2003, **118**, 8207.
52 V. I. Anisimov, J. Zaanen and O. K. Andersen, *Phys. Rev. B: Condens. Matter Mater. Phys.*, 1991, **44**, 943.
53 A. Jain, G. Hautier, S. P. Ong, C. J. Moore, C. C. Fischer, K. A. Persson and G. Ceder, *Phys. Rev. B: Condens. Matter Mater. Phys.*, 2011, **84**, 045115.
54 R. Laskowski, N. E. Christensen, P. Blaha and B. Palanivel, *Phys. Rev. B: Condens. Matter Mater. Phys.*, 2009, **79**, 165209.
55 Q. J. Liu and Z. T. Liu, *Appl. Phys. Lett.*, 2011, **99**, 091902.
56 A. Sayede, R. Khenata, A. Chahed and O. Benhelal, *J. Appl. Phys.*, 2013, **113**, 173501.
57 J. R. Huang and C. Cheng, *J. Appl. Phys.*, 2013, **113**, 033912.
58 MOPAC2012: Stewart, J. J. P. Stewart Computational Chemistry, Colorado Springs: CO, http://OpenMOPAC.net.
59 J. J. P. Stewart, *J. Mol. Model.*, 2007, **13**, 1173.
60 J. Baker, *J. Comput. Chem.*, 1986, **7**, 385.
61 T. Helgaker, *Chem. Phys. Lett.*, 1991, **182**, 503.
62 P. Culot, G. Dive, V. H. Nguyen and J. M. Ghuysen, *Theor. Chim. Acta*, 1992, **82**, 189.
63 Y. Qu, W. Zhou, Z. Ren, S. Du, X. Meng, G. Tian, K. Pan, G. Wanga and H. Fu, *J. Mater. Chem.*, 2012, **22**, 16471.
64 R. S. Singh, T. H. Ansari, R. A. Singh and B. M. Wanklyn, *Mater. Chem. Phys.*, 1995, **40**, 173.
65 J.-L. Wang, Y.-Q. Li, Y.-J. Byon, S.-G. Mei and G.-L. Zhang, *Powder Technol.*, 2013, **235**, 303.
66 P. Salvador, C. Gutierrez and J. B. Goodenough, *Appl. Phys. Lett.*, 1982, **40**, 188.
67 S. Yuvaraj, V. D. Nithya, K. Saiadali Fathima, C. Sanjeeviraja, G. Kalai Selvan, S. Arumugam and R. Kalai Selvan, *Mater. Res. Bull.*, 2013, **48**, 1110.
68 T. Stein, H. Eisenberg, L. Kronik and R. Baer, *Phys. Rev. Lett.*, 2010, **105**, 266802.
69 R. Vijayalakshmi and V. Rajendran, *E-J. Chem.*, 2012, **9**, 282.
70 K. P. Lopes, L. S. Cavalcante, A. Z. Simoes, J. A. Varela, E. Longo and E. R. Leite, *J. Alloys Compd.*, 2009, **468**, 327.
71 A. Kassiba, M. Makowska-Janusik, J. Boucle, J. F. Bardeau, A. Bulou and N. Herlin-Boime, *Phys. Rev. B: Condens. Matter Mater. Phys.*, 2002, **66**, 155317.
72 Y. Su and M. L. Balmer, *J. Phys. Chem. B*, 2000, **104**, 8160; G. Busca, G. Ramis, J. M. Gallardo Amores, V. Sanchez Escribano and P. Piaggio, *J. Chem. Soc., Faraday Trans.*, 1994, **90**, 3181.
73 F. X. Llabrés i Xamena, A. Damin, S. Bordiga and A. Zecchina, *Chem. Commun.*, 2003, 1514.
74 M. I. Baraton, G. Busca, M. C. Prieto, G. Ricchiardi and V. Sanchez Escribano, *J. Solid State Chem.*, 1994, **112**, 9.
75 B. A. Scott and G. Burns, *J. Am. Ceram. Soc.*, 1972, **55**, 225.
76 J. B. Bellam, M. A. Ruiz-Preciado, M. Edely, J. Szade, A. Jouanneaux and A. Kassiba, *RSC Adv.*, 2015, **5**, 10551.

ANNEXES

b. *Comparison of nickel titanate ($NiTiO_3$) powders synthesized by sol-gel and solid state reaction*

Materials Science in Semiconductor Processing 37 (2015) 171–178

Contents lists available at ScienceDirect

Materials Science in Semiconductor Processing

journal homepage: www.elsevier.com/locate/mssp

Comparison of nickel titanate ($NiTiO_3$) powders synthesized by sol–gel and solid state reaction

M.A. Ruiz-Preciado [a,b], A. Kassiba [a], A. Gibaud [a], A. Morales-Acevedo [b,*]

[a] Institut des Molécules et Matériaux du Mans, Université du Maine, Le Mans, France
[b] Centro de Investigación y de Estudios Avanzados del IPN, Electrical Engineering Department, Unidad Zacatenco, Mexico

ARTICLE INFO

Available online 18 March 2015

Keywords:
$NiTiO_3$ powders
Sol–gel
Photocatalysis

ABSTRACT

This work was concerned with the synthesis of $NiTiO_3$ powders by the sol–gel and the solid state reaction methods, and the investigation of their structural, electronic and optical properties required for their application in photocatalysis. The main goal was to determine which of these two synthesis methods was better for obtaining a pure $NiTiO_3$ crystalline phase. Synthesized powders were characterized by EDS, XRD, Raman and UV–vis diffuse reflectance spectroscopies. An analysis of the results shows that the sol–gel route with an annealing step at 1350 °C for 2 h in air atmosphere leads to a highly pure nickel titanate powder without any further purification step. A band gap of 2.2 eV was determined for this sample from diffuse reflectance spectroscopy. The solid state reaction route also allows the preparation of $NiTiO_3$ powders, but with a reduced purity (95%) as some TiO_2 and NiO phases are found in the powders, after the same thermal treatment as for the sol–gel samples. The EDS and XRD results were consistent between themselves for all samples, showing that the powders obtained by the sol–gel route and annealed at 1350 °C, during 2 h, are pure polycrystalline $NiTiO_3$ with the Ilmenite structure (hexagonal symmetry with lattice parameters around $a=b=0.5$ nm and $c=1.38$ nm). In addition, the observed 10 active Raman modes confirmed the presence of the Ilmenite phase of $NiTiO_3$. Finally, the absorption spectra as determined from UV–vis diffuse reflectance shows the presence of at least 3 absorption bands that could be explained by the main (HOMO–LUMO) transitions plus two other bands related to charge transfer from O^{2-} to Ti^{4+} and Ni^{2+} to Ti^{4+}. It can be expected that these photo-activated charge transfer phenomena will provide a high photo-catalytic activity to this material. All of the above results show that the sol–gel route allows the preparation of pure nano-crystalline $NiTiO_3$ powders.

1. Introduction

The development of visible-light-driven photocatalysis materials has been of great interest in the past decade because UV-light induced photocatalysis, like the one carried out by TiO_2, not only needs expensive light sources, but it is also inefficient in utilizing sunlight. Great efforts have been made to increase the wavelength range of UV-active oxides into the visible range by doping [1–4] or creating hetero-structures [5,6]. Also, attempts for developing new visible-light photocatalysts [7,8] have been made, but they are still deficient in either activity or stability. Perovskite-type oxides, such as tantalates and titanates, have recently attracted much attention because of their high photocatalytic activity under UV irradiation and, more remarkably, under visible light [9–11].

* Corresponding author.
E-mail address: amorales@solar.cinvestav.mx (A. Morales-Acevedo).

http://dx.doi.org/10.1016/j.mssp.2015.02.063
1369-8001/

The titanates $ATiO_3$ (A=Ni, Pb, Fe, Co, Mn, Cu, and Zn) have been studied as functional inorganic materials with many applications such as electrodes for solid oxide fuel cells, metal-air barriers, gas sensors, solid lubricants, and high-performance catalysts [12–14]. Nickel titanate ($NiTiO_3$), being an important member of the $ATiO_3$ family, has been attracting much attention in recent years because it holds tremendous promise for a wide range of applications, especially for semiconductor rectifiers, high temperature superconductors, gas sensors, and photocatalysts [15].

$NiTiO_3$ is an n-type semiconducting material with a band gap around 2.18 eV, which possess high electrical resistivity and high permittivity. A survey on the related reports on $NiTiO_3$ indicates that this material has both semiconducting and anti-ferromagnetic behavior [12–16]. Solid state reaction has been the conventional method to synthesize nickel titanate powders in the past decades and it requires a heat treatment step for a stoichiometric mixture of metallic Ni or NiO and TiO_2 at temperatures higher than 1000 °C [17]. By contrast with the solid state reaction method, wet-chemistry synthesis techniques, including sol–gel, sol–precipitation and chemical co-precipitation, among others, offer many distinctive advantages over the traditional method such as controlling the average particle size, homogeneity, morphology, etc. Zhou and Kang [18] have prepared nano-structured $NiTiO_3$ by the calcination at 900 °C of the precipitate produced by Ni $(OH)_2$ and titanium dioxide powder (P-25) in etyltrimethylammonium bromide (CTAB) micelle solutions. Sadjadi et al. [19] implemented a sol–gel method using nickel stearate and tetra-n-butyl titanate as Ni, Ti sources, respectively, and stearic acid as the complexing reagent, calcinating at 750 °C for 2 h. Lopes et al. [20] followed a sol–gel route based on the polymerization of metallic citrate using ethylene glycol and also using citric acid as chelating agent in aqueous solution, obtaining $NiTiO_3$ powders varying the annealing temperature from 400 °C to 1000 °C during 2 h in air. These results have shown that at annealing temperatures as low as 600 °C the $NiTiO_3$ phase formation begins. However, for annealing temperatures below 1000 °C, the lattice parameters of the prepared nano-crystals differ significantly from the bulk crystalline powders (JCPDS file 33-0960).

The subject of this work is related to the synthesis of $NiTiO_3$ powders by both the sol–gel and the solid state reaction techniques, and the investigation of their structural and optical properties required for their application in photocatalysis. Complementary experimental characterizations have been used to monitor their physical properties in order to make a comparison between these preparation techniques. In this way, we intend to determine the best synthesis method according to the observed properties of the obtained powders.

These studies are also dedicated to create photoactive materials which offer competing alternatives to other systems based on titanium dioxide, typically applied in the area of clean energy (production of hydrogen) or environmental care (degradation of water and atmosphere pollutants). Investigations of the structural, morphological and chemical properties were performed by techniques such as X-ray diffraction (XRD), Raman spectroscopy, scanning electron microscopy (SEM) and energy-dispersive X-ray spectroscopy (EDS). In addition, the UV–vis absorption curves, obtained from diffuse reflectance spectrometry (DRS), allowed us to determine the band-gap energy of the prepared powders.

It will be shown that $NiTiO_3$ nano-crystalline powders were obtained in all cases. However, in contrast to the solid state reaction synthesis, the sol–gel route was found to be a more efficient method for obtaining the stabilized Ilmenite structure after a high temperature thermal treatment.

2. Experimental details

2.1. Synthesis

$NiTiO_3$ powders were prepared by both the sol–gel and the solid state reaction techniques. Samples obtained by these two methods were labeled Powder1 and Powder2, respectively.

For making Powder1, the sol–gel procedure was followed. The chemicals used were citric acid (Aldrich, 99% pure), titanium (IV) isopropoxide (ACROS Organics, 98% pure), nickel acetate (ACROS Organics, 99% pure), ethylene glycol (J.T. Baker, 99% pure). In this method a solution of 5.76 g of citric acid in 92 ml of deionized water was prepared and, after this, 3 ml of titanium (IV) isopropoxide and 2.48 g of nickel acetate were added under constant stirring at room temperature (the molar ratio between citric acid:titanium (IV) isopropoxide:nickel acetate was 3:1:1). For homogenization, the solution was left under constant stirring for 1 h. After this homogenization time, 68.4 ml of ethylene glycol was added to the solution (weight percent ratio solution:ethylene glycol of 60:40). The resulting solution was stirred and heated at a temperature between 70° and 90 °C for 3 h, and then it was put into an oven at 300 °C in air, for 1 h. The obtained powder was then calcinated at 1000° or 1350 °C in air for 2 h in a furnace where the temperature was increased at a rate of 5 °C/min from room temperature up to the desired temperature.

After annealing (2 h), the furnace was cooled down at a slow rate to room temperature. Two different powders were thus obtained by this procedure, depending on the annealing temperature. They are labelled Powder1_A1000C for the sample annealed at 1000 °C and Powder1_A1350C for the powder annealed at 1350 °C.

For Powder2 synthesis, solid state reaction was used for which stoichiometric quantities of nickel oxide and titanium dioxide (Aldrich, 99.9% pure) were mixed in a mortar and ground by hand, until the mixture was homogeneous. This mixture presented a light gray color. The powder was then annealed in air in a similar way as described above for Powder1, i. e. starting at room temperature, the temperature was increased at a rate of 5 °C/min until the desired temperature was reached (1000° or 1350 °C). Then, the temperature was maintained constant for 2 h. After that time, the furnace was cooled down slowly to room temperature. In this case, the annealing temperature is specified in the label of the samples as Powder2_A1000C and Powder2_A1350C. In summary, 4 different powders were obtained: Powder1_A1000C, Powder1_A1350C, Powder2_A1000C and Powder2_A1350C.

2.2. Characterization

The characterization of the powders was made using the following techniques.

2.2.1. Scanning electron microscopy (SEM) and energy-dispersive X-ray spectroscopy (EDS)

A JEOL-JECM-6360LV scanning electron microscope (SEM) was used for the morphological characterizations of the samples. In addition, semi-quantitative analyses were carried out using energy-dispersive X-ray spectroscopy (EDS) with a JEOL detector inside the SEM chamber. The different powders were deposited on a carbon conducting tape suited for the SEM observations and EDS analysis. A low electron acceleration voltage (5 kV) was used in order to avoid charging these samples.

2.2.2. X-ray diffraction (XRD)

XRD measurements were performed on all the samples in order to analyze their crystalline features including the presence of other secondary phases. The X-ray diffractometer was an Empyrean model from PANalytical. Measurements were carried out in a symmetrical coplanar geometry (theta – 2theta) with 2theta ranging from 20° to 65°. X-rays were produced with a copper tube ($K_{\alpha1}$ = 1.54056 Å, $K_{\alpha2}$ = 1.54439 Å) with 1/8° and 1/4° divergence slits, situated at 160 and 120 mm from the sample, respectively. A nickel filter was placed in the path of the reflected beam to avoid contamination in the data from the K_β wavelengths. A pixel 3D detector was used in all measurements. The observed data was refined with the Rietveld method [21], using the MAUD v2.33 software. This method was particularly useful for quantifying the volume fraction of each phase present in the samples, together with their crystalline structure.

2.2.3. Raman spectroscopy

Raman spectrometry was also used to characterize the vibrational properties of the samples. The Raman scattering spectra were collected with a T64000 Horiba Jobin Yvon spectrometer, under a microscope (×50 LF objective) and coupled to a cooled CCD. The 514.5 nm wavelength of an Ar/Kr laser was used as the excitation line. A resolution of 0.7 cm^{-1} was used for all recorded spectra. The analysis of the Raman spectra was done with the help of the LabSpec software (v5.25.15) dedicated to identify the active Raman vibrational modes related to the involved crystalline structures.

2.2.4. Diffuse reflectance spectrometry (DRS)

The optical properties were investigated by using diffuse reflectance spectrometry based on an Ocean Optics Spectrometer with an integrating sphere and a Halogen Lamp (350–1000 nm) as the light source.

3. Experimental results

3.1. Scanning electron microscopy (SEM)

As described above, the different powders were directly deposited on a carbon conducting tape in order to observe them with a (JEOL) scanning electron microscope, having an EDS detector in the chamber. In Fig. 1 we show the images for only two samples, since in all cases the morphology was similar. As can be seen (Fig. 1), the main difference is that the crystallite clusters are larger for Powder1_A1350C as compared to those for Powder2_A1350C samples. However, as will be explained below (from XRD) the coherently diffracting crystallites have dimensions of the same order (around 60 nm) in both cases.

3.2. X-ray diffraction (XRD)

Fig. 2 illustrates the XRD patterns. Reflections corresponding to the (0 1 2), (1 0 4), (1 1 0), (0 0 6), (1 1 3), (0 2 4), (1 1 6), (2 1 1), (0 1 8), (2 1 4) and (3 0 0) planes of the Ilmenite structure of $NiTiO_3$ with space group $R\bar{3}$ are identified. The hexagonal symmetry C_{3i}^2 was used to fit the data starting typically with lattice parameters $a = b =$ 0.503 nm, $c = 1.38$ nm and $\alpha = \beta = 90°$, $\gamma = 120°$ in agreement with the JCPDS file 33-0960. As shown in Fig. 2, the presence of secondary phases such as Bunsenite (NiO) and Rutile (TiO_2) is clearly seen. Table 1 shows the details for each sample with respect to the phases present in the samples. The volume fraction of these secondary phases (as determined by the Rietveld method) is reduced as the preparation temperature is increased.

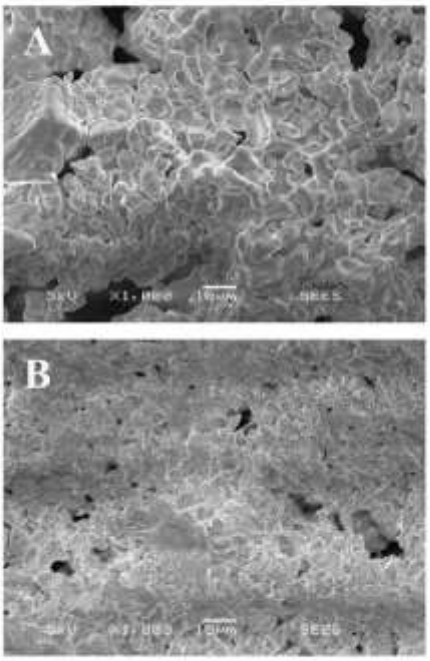

Fig. 1. SEM images of: (**A**) Powder1_A1350C with magnification × 1000. (B) Powder2_A1350C with magnification × 1000.

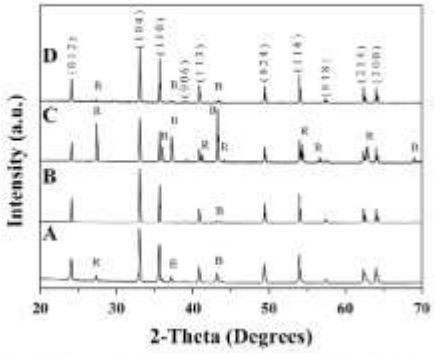

Fig. 2. XRD patterns of $NiTiO_3$ Powder1 and Powder2, annealed at different temperatures in air atmosphere. The letter "R" refers to the Rutile phase of TiO_2 and "B" to the Bunsenite phase of NiO. (A) Powder1_A1000C. (B) Powder1_A1350C. (C) Powder2_A1000C. (D) Powder2_A1350C.

Table 1
Fraction of the phases present in the synthesized sample.

Sample	Phase volume fraction (%)		
	$NiTiO_3$ (Ilmenite)	TiO_2 (Rutile)	NiO (Bunsenite)
Powder1_A1000C	86 ± 2	8.4 ± 0.4	5.6 ± 0.4
Powder1_A1350C	98 ± 5	0	1.2 ± 2
Powder2_A1000C	44.2 ± 0.4	39.5 ± 0.4	16.3 ± 2
Powder2_A1350C	95 ± 5	3.3 ± 0.4	1.9 ± 2

Powder2_A1000C presents ~44% of the $NiTiO_3$ Ilmenite phase, ~40% of TiO_2 Rutile phase and ~16% of NiO Bunsenite phase. By increasing the temperature up to 1350 °C the volume fractions of these phases change drastically to 95 ± 5% $NiTiO_3$, 3.3 ± 0.4% TiO_2 and 1.9% NiO within the uncertainty range. Thus, a higher annealing temperature strongly benefits to the formation of the $NiTiO_3$ phase in the solid state reaction method.

A similar effect is observed for Powder1 where annealing at 1000 °C (Powder1_A1000C) leads to the coexistence of 86 ± 2% for $NiTiO_3$, 8.4 ± 0.4% for TiO_2 and 5.6 ± 0.4% for NiO. Increasing the annealing temperature to 1350 °C (Powder1_A1350C) contributes to having pure $NiTiO_3$ with the Ilmenite structure, within the uncertainty range.

In addition, the crystallite sizes increase for higher annealing temperatures as observed by the reduction of the full width at half maximum (FWHM) of the Bragg diffraction lines. The sizes for the crystallites oriented in the [1 0 4] direction were estimated by using the Scherrer equation [22], $D_{hkl} = K\lambda/B_{hkl}\cos\theta$, where λ is the wavelength of the X-rays, θ is the Bragg angle, D_{hkl} is the crystallite size in the direction perpendicular to the lattice planes under analysis, B_{hkl} is the FWHM of the diffraction peak in radians and K is a numerical factor frequently referred as the crystallite-shape factor. Considering spherical shaped particles the crystallite-shape factor was approximated to $K = 0.9$ [23–24]. The obtained values for the crystallite sizes (D_{104}) are shown in Table 2. Comparing the crystallite sizes for the different powders we can see that there is an increase of the size when the annealing temperature is increased from 1000 to 1350 °C. For Powder1 the size increases from 43.5 to 59.5 nm and for Powder2 it goes from 56.6 to 61.6 nm. We can also note the small difference in crystallite size between Powder1_A1350C and Powder2_A1350C samples, particularly after the thermal treatment.

Table 2
NiTiO3 crystal size, estimated by the Scherrer formula for the crystallites oriented perpendicular to the (1 0 4) planes.

Sample	Crystal size (nm)
Powder1_A1000C	43.5
Powder1_A1350C	59.5
Powder2_A1000C	56.6
Powder2_A1350C	61.6

The lattice parameters were obtained from the Rietveld refinements with a very good correlation factor, as shown in Fig. 3 for Powder1_A1000C, Powder1_A1350C and Powder2_A1350C. The lattice parameters obtained from this analysis are summarized in Table 3.

3.3. *Energy-dispersive X-ray spectroscopy (EDS)*

The atomic percentages in the samples were determined by energy-dispersive X-ray spectroscopy (EDS). For a 100% pure nickel titanate sample, the atomic proportion should be 20% nickel (Ni), 20% titanium (Ti) and 60% oxygen (O). However, taking into account the phase volume fractions (PVF) obtained from the Rietveld analysis (Table 1) we expect different atomic percentages of Ni, Ti and O. Powder1_A1350C and Powder2_A1000C are located in the opposite PVF extremes. For Powder1_A1350C, within the uncertainty errors, almost 100% of the sample is composed of $NiTiO_3$ while for Powder2_A1000C, 44% of $NiTiO_3$, 40% of TiO_2 and 16% of NiO was obtained. According to this result, the atomic proportion for Powder1_A1350C should be ~20.2% of Ni, ~19.7% of Ti and ~60.2% of O and for Powder2_A1000C we should get ~17% of Ni, ~22% of Ti and ~61% of O. The atomic percentages for each sample are displayed in Table 4. These values are very close to those obtained by EDS, confirming the results obtained from the Rietveld refinements. This fact also confirms that, within a small error, we have a pure $NiTiO_3$ phase in the case of Powder1_A1350C.

3.4. *Raman spectroscopy*

From the above XRD analysis it was concluded that highly pure Ilmenite $NiTiO_3$ was achieved in the case of Powder1_A1350C. In order to corroborate the above results, Raman spectrometry was used to analyze the vibrational properties of samples. For Ilmenite $NiTiO_3$, the oxygen atoms are tetra-coordinated to 2 Ti and 2 bivalent cations (Ni) in a C_1 symmetry site. Theoretically, we can expect ten active Raman modes ($\Gamma_{RAMAN} = 5A_g + 5E_g$), where each E_g mode is doubly degenerated ($E_g = E_g^1 + E_g^2$) and eight IR active modes ($\Gamma_{IR} = 4A_u + 4E_u$). Additionally, this material

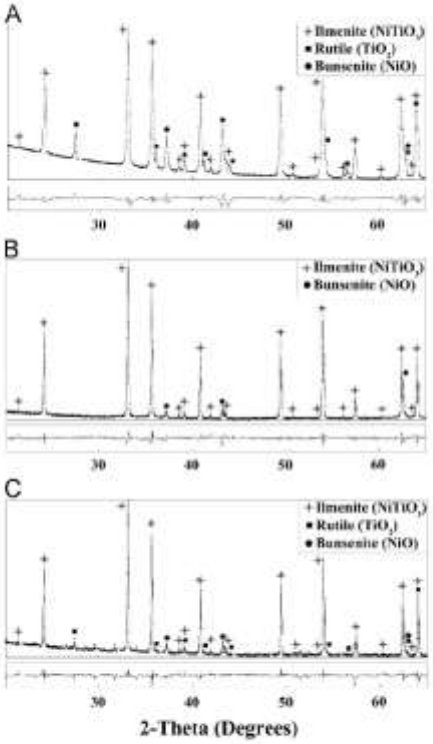

Fig. 3. XRD refinements of three of the samples, showing the presence of secondary phases. (A) Powder1_A1000C. (B) Powder1_A1350C. (C) Powder2_A1350C.

Table 3
Lattice parameters of the $NiTiO_3$ phase of the synthesized samples.

Sample	$NiTiO_3$ lattice parameters (nm)	
	$a=b$	c
Powder1_A1000C	$0.503424 \pm 9\times10^{-6}$	$1.38098 \pm 4\times10^{-5}$
Powder1_A1350C	$0.503289 \pm 3\times10^{-6}$	$1.37972 \pm 1\times10^{-5}$
Powder2_A1000C	$0.503293 \pm 4\times10^{-6}$	$1.37977 \pm 2\times10^{-5}$
Powder2_A1350C	$0.503249 \pm 3\times10^{-6}$	$1.37955 \pm 2\times10^{-5}$

should present two acoustic modes ($\Gamma_{ac}=A_u+E_u$) and no inactive modes [25,26].

The Raman vibrational modes for $NiTiO_3$ are located at 192.2 (A_g), 229.8 (E_g), 246.9 (A_g), 291.3 (E_g), 345.4 (E_g), 394.5 (A_g), 465.3 (E_g), 484.5 (A_g), 613 (E_g) and 709.1 (A_g) cm^{-1}, as seen in Fig. 4. In the samples containing a high fraction of Rutile (TiO_2), a contribution in the intensity is visible due to the vibrational modes of Rutile at 235, 445 and 610 cm^{-1}. Bunsenite's (NiO) contribution to the spectra is not noticeable in the analyzed spectral range [27]. Notice that around 730 cm^{-1}, a mode of relatively low intensity appears as a shoulder of the more intense peak located 709.1 cm^{-1}. This vibrational mode has been wrongly considered before as one of the ten Raman modes for the Ilmenite symmetry. The work by Wang et al. [28] analyzes the Ilmenite-type $MgTiO_3$ and based on group theory, they calculated the Raman modes and concluded that this shoulder is not one of the ten expected modes. However, no explanation was given for it either.

3.5. Diffuse reflectance spectrometry (DRS)

The optical properties characterization was conducted by diffuse reflectance measurements form the powders. The experimental spectra were analyzed using the Kubelka–Munk (K–M) model [29]. In this frame, the Kubelka–Munk function $F(R_{inf})$ is introduced and depends on the K–M effective absorption coefficient (K) and the K–M effective scattering coefficient (S):

$$F(R_{inf}) = \frac{(1-R_{inf})^2}{2R_{inf}} = \frac{K}{S} \quad (1)$$

The K–M effective absorption coefficient (K) is proportional to the usual absorption coefficient (α) according to $K=e\alpha$, and the K–M effective scattering coefficient (S) is related to the usual scattering coefficient (s) by $S=2(1-\zeta)s$. When the material scatters in a perfectly diffuse manner the K–M effective absorption coefficient (K) becomes $K=2\alpha$ and the K–M effective scattering coefficient (S) is exactly the same as the usual scattering coefficient (s), $S=s$ [30,31].

Under this condition we can use the expression:

$$[F(R_{inf})h\upsilon]^2 = C_1(h\upsilon - E_g) \quad (2)$$

A plot of $[F(R_{inf})h\upsilon]^2$ vs $h\upsilon$ allows us to obtain the band-gap energy (E_g) values following the well-known Tauc analysis [32,33].

From the plots shown in Fig. 5 we have determined the band-gap (HOMO–LUMO transitions for nanocrystalline clusters) for the different powders in the energy range

Table 4
Atomic percentages of the elements present in the samples obtained by EDS.

Element	Atomic proportion (%)			
	Powder1_A1000C	**Powder1_A1350C**	**Powder2_A1000C**	**Powder2_A1350C**
Ni	29.73 ± 0.81	22.33 ± 1.51	19.21 ± 1.93	27.89 ± 0.89
Ti	11.65 ± 0.44	19.05 ± 0.71	22.01 ± 0.86	11.85 ± 0.47
O	58.62 ± 0.24	58.62 ± 0.49	58.78 ± 0.66	60.26 ± 0.26

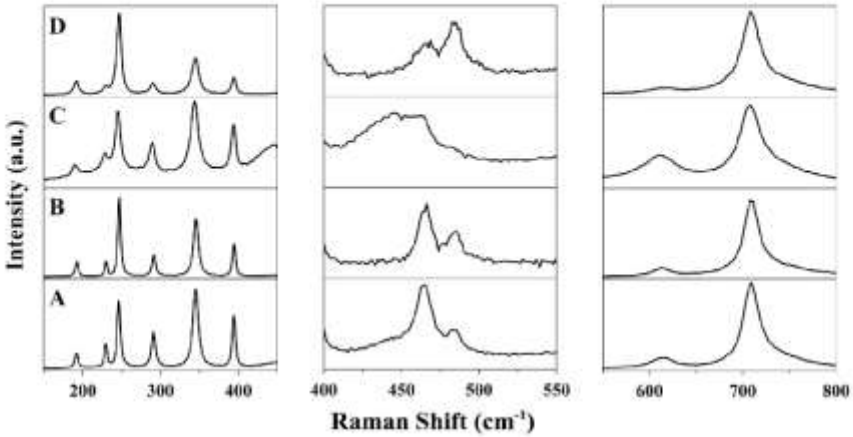

Fig. 4. Raman spectra for Powder1 and Powder2 samples divided into three regions in order to be able to distinguish the details corresponding to the specified range. Each region has a different scale. (A) Powder1_A1000C. (B) Powder1_A1350C. (C) Powder2_A1000C, (D) Powder2_A1350C.

between 2.2 and 2.5 eV. Table 5 shows the band-gaps obtained from the Tauc plots for the different samples.

In Fig. 6 we can see the absorption spectra for each sample, where two absorption bands are clearly identified at 400 and 800 nm, respectively. Rossman et al. [34] give an explanation for the absorption bands found in $NiTiO_3$ after studying several compounds containing Ni^{2+} ions. In their paper, the general features of Ni^{2+} absorption have been described in terms of a ligand field theory. In a rigorously octahedral environment, Ni^{2+} will have three prominent absorption bands, arising from transitions from the $^3A_{2g}$ ground state to the $^3T_{2g}$, $^3T_{1g}(F)$, and $^3T_{1g}(G)$ states. These correspond to the prominent absorption bands in the 1400, 800 and 400 nm regions, respectively. Because of equipment limitations we could obtain only the spectra corresponding to wavelengths in the range from 400 to 1000 nm, but Rossman's explanation for the 400 and 800 nm bands is still valid for our results. Strong spin-orbit coupling together with antiferromagnetic interactions is believed to increase the intensity of the transition to the ^1E_g, state at ~720–740 nm such that it becomes more intense than the spin-allowed transition to the $^3T_{1g}$ state in the case of NiO. Likewise the transition to the $^1T_{1g}$ state at 378 nm is more intense than the 415 nm $^3T_{1g}$ band in NiO. The greatest absorption band intensities in the 400 nm region are associated with metal ion absorption bands in proximity to an ultraviolet wavelength tail due to charge transfer. The most intense bands are about an order of magnitude more intense than for NiO. Proximity to a charge transfer ultraviolet tail has been recognized to be an important factor in determining the intensities of electronic transitions of metal ions in general through the mechanism of "intensity stealing". The extent to which the ultraviolet charge transfer band extends into the visible region depends in part on the ion with which the Ni^{2+} shares oxygen ions. Easily reduced ions such as Ti^{4+} produce a charge transfer tail which

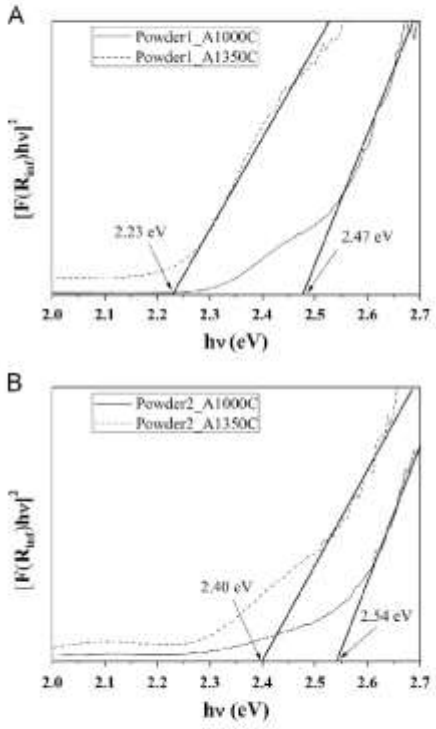

Fig. 5. Tauc plots of the samples analyzed. (A) Powder1_A1000C and Powder1_A1350C. (B) Powder2_A1000C and Powder2_A1350C.

Table 5
Band gap of the $NiTiO_3$ samples as determined from the Tauc plots of UV–vis absorbance.

Sample	Band-gap (eV)
Powder1_A1000C	$2.494 \pm 4 \times 10^{-3}$
Powder1_A1350C	$2.22 \pm 1 \times 10^{-2}$
Powder2_A1000C	$2.546 \pm 3 \times 10^{-3}$
Powder2_A1350C	$2.41 \pm 1 \times 10^{-2}$

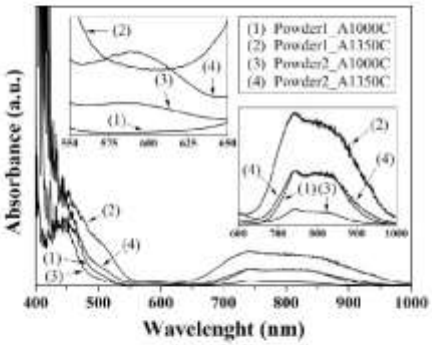

Fig. 6. Absorbance spectra of the samples, obtained from diffuse reflectance spectra.

extends well into the visible region, whereas hardly reduced ions such as P^{5+} and Si^{4+} do not. Site symmetry influences the color of Ni^{2+} compounds. The degeneracy of the $^3T_{1g}$, $^3T_{2g}$, and ^1E_g states of Ni^{2+} in octahedral geometry are lifted and multiple-absorption bands occur when Ni^{2+} is situated in a coordination environment of low symmetry. Bands split by low symmetry will show peak wavelengths which are polarization dependent. The brightest yellow color samples also have the most pronounced splitting of the absorption bands. Band intensities often increase in response to low site symmetry.

This is also consistent with recent molecular calculations based on the semi-empirical PM6 parameterization method [35] applied to $NiTiO_3$ nano clusters. This method was used to calculate the optical absorption of $NiTiO_3$ nano clusters and it was found that for large $NiTiO_3$ clusters (17 molecules of $NiTiO_3$), 3 absorption bands are calculated. A band "A" at wavelengths between 300 and 400 nm, a band "B" between 500 and 600 nm and a band "C" between 700 and 900 nm. The calculated band "B" would correspond to the less intense band, seen in the inset of fig. 6, between 550 and 650 nm. The calculated band "A" would be related to the most intense band observed experimentally around 400 nm. According to these calculations, the "A" band is related to optical transitions due to charge transfer from O^{2-} to Ti^{4+} and Ni^{2+} to Ti^{4+}, in a similar way as the explanation given by Rossman et al. [34].

In summary, all of the above measurements and characterizations show that we have obtained $NiTiO_3$ powders by the two proposed methods: sol–gel and solid state reaction, after annealing the samples at 1350 °C in air for two hours. It is clear that the sol–gel method is better than the solid state reaction method because an even more pure $NiTiO_3$ crystalline phase is obtained in the former case.

4. Conclusions

Nickel titanate ($NiTiO_3$) powders were synthesized by two different routes: sol–gel and solid state reaction. The synthesized powders were characterized by EDS, XRD, Raman spectroscopy and diffuse reflectance spectrometry. An analysis of the EDS and XRD results has shown that the sol–gel route with an additional annealing at 1350 °C for 2 h, in air atmosphere, leads to a highly pure nickel titanate phase without any further purification step. A band-gap of 2.22 ± 0.01 eV was determined for this sample from diffuse reflectance spectroscopy. The EDS and XRD results were consistent between themselves for all the samples, showing that the powders obtained by the sol–gel route and annealed at 1350 °C, during 2 h, are pure polycrystalline $NiTiO_3$ with the ilmenite structure (hexagonal symmetry with lattice parameters around $a=b=0.5$ nm and $c=1.38$ nm). In addition, the observed 10 active Raman modes confirmed the presence of the ilmenite phase of $NiTiO_3$. Finally, the absorption spectra as determined from UV–vis diffuse reflectance spectrometry, shows the presence of at least 3 absorption bands that could be explained by the main (HOMO–LUMO) transitions plus two other bands related to charge transfer from O^{2-} to Ti^{4+} and Ni^{2+} to Ti^{4+}. It can be expected that these photo-activated charge transfer phenomena will provide a high photo-catalytic activity to this material. All of the above results show that the sol–gel route allows the preparation of pure nano-crystalline $NiTiO_3$ powders. Our EDS, XRD and Raman spectroscopy results also show that the solid state reaction route does not provide pure powders, since they have a volumetric fraction of the Rutile TiO_2 phase, even after annealing them for 2 h in air at 1350 °C. Possibly longer annealing times are required when using this technique. Therefore, now we can study the photocatalytic properties of such structures when prepared by the sol–gel route after annealing at 1350 °C. These results also encourage us to further study the prepared nickel titanate powders for using it as a photocatalytic agent for water splitting or water/air purification.

Acknowledgements

We acknowledge CONACyT (Mexico) for the scholarship granted to M. A. Ruiz-Preciado for doing his PhD work as well as the facilities and support provided by the doctoral school ED3MPL in Université du Maine in the frame of PhD co-graduation with CINVESTAV. We also thank to Prof. Alain Bulou from Université du Maine for dedicating his valuable time and experience in Raman Spectroscopy, to Eng. Mathieu Edely from Université du Maine for all the help provided in the laboratory and to Dr. Gaspar Casados-Cruz for the SEM and EDS measurements at CINVESTAV-México.

References

[1] Wan-Jian Yin, Houwen Tang, Su-Huai Wei, Mowafak M. Al-Jassim, John Turner, Yanfa Yan, Phys. Rev. B: Condens. Matter 82 (2010) 045106.
[2] Hiromi Yamashita, Masaru Harada, Jimbo Misaka, Masato Takeuchi, Keita Ikeue, Masakazu Anpo, J. Photochem. Photobiol., A 148 (2002) 257–261.
[3] Suil In, Alexander Orlov, Regina Berg, Felipe Garcia, Sergio Pedrosa-Jimenez, Mintcho S. Tikhov, Dominic S. Wright, Richard M. Lambert, J. Am. Chem. Soc. 9 129 (45) (2007) 13790–13791.
[4] Yuxiao Niu, Mingyang Xing, Jinlong Zhang, Baozhu Tian, Catal. Today 201 (2013) 159–166.
[5] Jikai Yang, Ximiong Zhang, Hong Liu, Changhua Wang, Shuping Liu, Panpan Sun, Lingling Wang, Yichun Liu, Catal. Today 201 (2013) 195–202.
[6] Xinjuan Liu, Likun Pana, Tian Lva, Zhao Sun, Changqing Sun, J. Mol. Catal. A: Chem. 363-364 (2012) 417–422.
[7] Gobinda Chandra De, Asadi Mohan Roy, Bhattacharya Sitansu Sekhar, Int. J. Hydrogen Energy 21 (1996) 19–23.
[8] Dong Won Hwang, Jindo Kim, Tae Jin Park, Jae Sung Lee, Catal. Lett. 80 (2002) 53–57.
[9] Wei Feng Yao, Xiao Hong Xu, Hong Wang, Jing Tao Zhou, Xue Na Yang, Yin Zhang, Shu Xia Shang, Bai Biao Huang, Appl. Catal., B 52 (2004) 109–116.
[10] Jindo Kim, Dong Won Hwang, Hyun-Gyu Kim, Sang Won Bae, Sang Min Ji, Jae Sung Lee, Chem. Commun. (21) (2002) 2488–2489.
[11] Hyun Gyu Kim, Dong Won Hwang, Lee Jae Sung, J. Am. Chem. Soc. 126 (2004) 8912–8913.
[12] Alexandra Navrotsky, Chem. Mater. 10 (1998) 2787–2793.
[13] Daniel M. Giaquinta, Hans-Conrad Zur Loye, Chem. Mater. 6 (1994) 365–372.
[14] J.M. Xeil, A. Navrotsky, O.J. Klepp, Inorg. Chem. 10 (1971) 2076–2077.
[15] Teng Li, Chun Chang Wang, Chang Mei Lei, Xiao Hong Sun, Guo Jing Wang, Liu Liu Na, Curr. Appl Phys. 13 (2013) 1728–1731.
[16] S. Yuvaraj, V.D. Nithya, K. Saiadali Fathima, C. Sanjeeviraja, G. Kalai Selvan, S. Arumugam, R. Kalai Selvan, Mater. Res. Bull. 48 (2013) 1110–1116.
[17] M. Lerch, H. Boysen, R. Neder, F. Frey, W. Laqua, J. Phys. Chem. Solids 53 (1992) 1153–1156.
[18] Guo-Wei Zhou, Young Soo Kang, J. Dispersion Sci. Technol. 27 (2006) 727–730.
[19] M.S. Sadjadi, K. Zare, S. Khanahmadzadeh, M. Enhessari, Mater. Lett. 62 (2008) 3679–3681.
[20] K.P. Lopes, L.S. Cavalcante, A.Z. Simoes, J.A. Varela, E. Longoh, E.R. Leite, J. Alloys Compd. 468 (2009) 327–332.
[21] Luca Lutterotti, Paolo Scardi, J. Appl. Crystallogr. 23 (1990) 246–252.
[22] Paul Scherrer, Mathematisch-Physikalische Klasse 2 (1918) 98–100.
[23] H.P. Klug, L.E. Alexander, X-Ray Diffraction Procedures Ch. 9, second ed. Wiley, 1974.
[24] B.D. Cullity, Elements of X-ray Diffraction, second ed. Addison-Wesley, 1978.
[25] Guido Busca, Giangiulo Ramis, Jose M. Gallardo Amores, Vicente Sanchez Escribano, Paolo Piaggio, J. Chem. Soc., Faraday Trans. 90 (1994) 3181–3190.
[26] M.I. Baraton, G. Busca, M.C. Prieto, G. Ricchiardi, V. Sanchez Escribano, J. Solid State Chem. 112 (1994) 9–14.
[27] Nina Maunuva-Ulmane, Alexei Kuzmin, Ilmo Sildos, Martti Pärs, Cent. Eur. J. Phys. 9 (2011) 1096–1099.
[28] Chun-Hai Wang, Xi-Ping Jing, Wei Feng, Jing Lu, J. Appl. Phys. 104 (2008) 034112. 034112.
[29] P. Kubelka, F. Munk, Z. Tech. Phys. 12 (1931) 593–599.
[30] A. Escobedo Morales, E. Sanchez Mora, U. Pal, Revista Mexicana de Fisica S 53 (2007) 18–22.
[31] A.B. Murphy, Sol. Energy Mater. Sol. Cells 91 (2007) 1326–1337.
[32] Jan Tauc, Mater. Res. Bull. 3 (1968) 37–46.
[33] J. Tauc, R. Grigorovic, A. Vancu, Phys. Status Solidi B 15 (1966) 627–637.
[34] George R. Rossman, Robert D. Shannon, Robert K. Waring, J. Solid State Chem. 39 (1981) 277–287.
[35] M.A. Ruiz Preciado, A. Kassiba, A. Morales-Acevedo, M. Makowska-Janusik, RSC Adv. 5 (2015) 17396–17404.

c. *Nickel titanate ($NiTiO_3$) thin films: RF-sputtering synthesis and investigation of related features for photocatalysis*

CrystEngComm

PAPER

View Article Online

Cite this: DOI: 10.1039/c6ce00306k

Nickel titanate ($NiTiO_3$) thin films: RF-sputtering synthesis and investigation of related features for photocatalysis

M. A. Ruiz-Preciado,[ab] A. Bulou,[a] M. Makowska-Janusik,[c] A. Gibaud,[a] A. Morales-Acevedo[b] and A. Kassiba*[a]

Received 4th February 2016,
Accepted 29th March 2016

DOI: 10.1039/c6ce00306k

www.rsc.org/crystengcomm

Polycrystalline nickel titanate thin films were deposited on silicon substrates by the radio-frequency (rf) sputtering method using $NiTiO_3$ targets, which in turn were sintered from powders obtained by solid state reaction. The deposition parameters such as rf-powers, partial pressures of argon and oxygen, as well as substrate temperatures were optimized to ensure the homogeneous and stoichiometric composition of $NiTiO_3$ thin films. Post-synthesis annealing at suitable temperatures and time durations was realized to stabilize the ilmenite structure with improved crystalline features deduced from structural and vibrational investigations by using XRD and Raman spectroscopy. The surface roughness and thin film microstructure were characterized by AFM which points out the organisation of the film surface. Representative films with ilmenite structure and defined surface microstructure and optical absorbance were tested as visible light driven heterogeneous photocatalysts for the degradation of organic dyes.

Introduction

Water dissociation for hydrogen production or degradation of pollutants involved in wastewater or in confined atmospheres requires photocatalytic reactions that can be driven by light radiation within a defined spectral range. Among the most exploited photocatalysts, TiO_2 is worthy of interest with regard to the efficient photogeneration of excitonic states with high concentrations and long lifetimes.[1] In heterogeneous photocatalysis based on TiO_2, the mechanisms of superoxide and hydroxyl radical formation and their interactions in aqueous solutions have been described exhaustively in several reports devoted to the degradation of organic groups or biological organisms.[1–3] However, the efficiency of TiO_2 in photocatalysis under UV irradiation remains an open problem since costly light sources are required or alternatively only a narrow spectral range of solar radiation (4–6%) can be used. Thus, the search for a competitive material has been performed to reduce the TiO_2 band gap (~3 eV). Among the approaches, suitable metallic doping has been used[4–7] to better harvest visible light for efficient photocatalytic activity.[8–11] In parallel, alternative photoactive semiconducting structures with low electronic band gaps constitute an interesting challenge.[12–16] As examples, bismuth-based semiconducting oxides such as $BiVO_4$ have demonstrated efficient activity in visible light photocatalysis.[17–19] The photogenerated excitons occur between hybridized Bi_{6s} and O_{2p} orbitals within the valence band and V_{3d} orbitals involved in the conduction band. The electronic energy gap close to 2.5 eV allows the harvesting of a large spectral range of solar radiation, thus promoting efficient photocatalytic reactions. In similar approaches, perovskite-type oxides, such as titanates, have also demonstrated photocatalytic activities under visible-light irradiation.[20] Thus, titanate oxides such as $ATiO_3$ (A = Ni, Pb, Fe, Co, Mn, Cu, and Zn) have been studied as functional inorganic materials with wide applications as electrodes for solid oxide fuel cells, metal-air barriers, gas sensors, and high-performance catalysts.[21–23] Among the considered compositions for photocatalysis, nickel titanate ($NiTiO_3$) with the ilmenite crystalline structure exhibits an optical absorption spectrum with a band gap around 2.18 eV, well adapted for visible-light-driven photocatalysis.[20,24]

Also, the present work concerns the synthesis of $NiTiO_3$ thin films by a simple procedure based on rf-sputtering and the investigation of their structure, morphology and optical properties with the aim of applying them in photocatalysis. The relevance of the experimental approach lies first in an effective simplification of the synthesis process compared to the one already experienced in our group by using co-sputtering techniques from metallic targets (Ti and Ni) following a very sophisticated procedure such as Plackett-

[a] Institut des Molécules et Matériaux du Mans, UMR-CNRS 6283, Université du Maine, Avenue O. Messiaen, 72085 Le Mans, France. E-mail: kassiba@univ-lemans.fr
[b] Centro de Investigación y de Estudios Avanzados del IPN, Unidad Zacatenco, Av. IPN No. 2508, 07360 México, D. F., Mexico
[c] Institute of Physics, Al. Armii Krajowej, 13/15, Jan Długosz University in Czestochowa, 42 200 Czestochowa, Poland

Burman design.[27] Second, a deep analysis including *polarization measurements* has been performed for the assignment of Raman active modes in the crystalline structure of $NiTiO_3$. Moreover, the realization of films with the ilmenite structure characterized by an electronic band gap in the order of 2.7 eV contributes to the harvesting of a fraction of visible light radiation as it was demonstrated by photocatalytic degradation of organic dyes.

Thus, experimental approaches were developed to optimize the key physical properties required for photoactive materials under visible radiation. In a first step, the parameters of the rf-sputtering deposition were determined to ensure the appropriate stoichiometry and thickness of the films. As the obtained films are amorphous, a post-synthesis annealing is required for crystal structure stabilization of the ilmenite polytype. Structural and vibrational investigations were carried out and analyzed as a function of the annealing conditions. The rf-sputtered thin films offering the appropriate physical features were obtained and their performance was tested in photocatalysis through the degradation of organic dyes dissolved in aqueous media, under visible light irradiation. The photocatalytic activity was evaluated through the reaction rate constant of dye degradation and insights into the key parameters which monitor such photocatalyst responses and the possible trend to improve their efficiency were obtained.

Experimental details

Synthesis of $NiTiO_3$ targets

The synthesis of $NiTiO_3$ targets was realized from stoichiometric commercial powders of NiO and TiO_2 with good purity (99.90%). After homogeneous mixing, shaped disks (diameter 30 mm and thickness 4 mm) were made by compressing the powder with a hydraulic press inside a mold, followed by a second compression process using an isostatic press. The pellets were sintered at 1100 °C for 6 hours in air to ensure, as demonstrated by X-ray diffraction studies, a homogenous $NiTiO_3$ composition with a good crystalline quality of the ilmenite structure.

Deposition of the $NiTiO_3$ thin films by rf-sputtering

The key parameters for rf-sputtering deposition of thin films consist of the argon/oxygen (Ar/O) flow, the partial pressure in the synthesis chamber, the rf-power and the substrate temperatures during the synthesis process. Different sets of parameters were tested in order to determine the optimal values that promote good crystallinity of thin films. However, all the conditions lead to amorphous as-formed films and a post-annealing treatment is required to ensure a crystalline structure. The optimization of the synthesis parameters giving rise to suitable stoichiometry and thickness led to values of 94/0 sccm for the Ar/O flow, 0.1 mbar for the partial pressure and 50 W for the rf-power and the silicon substrate temperature was fixed at room temperature. The films were deposited under the same conditions and during the same time. Thus, the same growth rate and thickness are expected for all synthesized films. The annealing process was conducted with a heating rate of 5 °C min^{-1} while the cooling rate was not fixed; the film was allowed to cool down at the natural rate of the oven. Typical cooling time from 1000 °C to ambient temperature was about 24 h.

Characterization techniques

X-ray diffraction (XRD)

XRD investigations were carried out by using an Empyrean diffractometer from PANalytical working with a Cu anticathode ($k_{\alpha 1}$ = 1.54056 Å, $K_{\alpha 2}$ = 1.54439 Å) with 1/4 and 1/8 degree divergence slits, situated at 160 and 120 mm, respectively, from the sample. A nickel filter was placed in the path of the reflected beam to avoid contamination of the data from K_β radiation. Symmetrical geometry (θ–2θ) was adopted within the 2θ range from 20° to 65°. The offset between ω and 2θ was fixed equal to 5° in order to gather as much diffracted radiation as possible coming from the film along with a reduction of the reflection from the silicon substrate. Refinement by the Rietveld method[28] has been done on the XRD pattern of the film with the best achieved crystalline order, referred to as the representative film. This refinement ensures quantitative analysis of the crystal structure, texture, strain, and size of the coherent diffracting domains. The software Materials Analysis Using Diffraction (MAUD) v2.33 was selected for its accuracy in structural refinement.

Raman spectroscopy

Raman spectrometry was used to analyze the vibrational properties of the films in close relation to the structural features. Raman scattering spectra were collected with a T64000 Horiba Jobin Yvon spectrometer, under a microscope (50× LF objective) coupled to a nitrogen-cooled CCD. The 514.5 nm wavelength of an Ar/Kr laser was used as the excitation source. The Raman spectra were analysed by the software LabSpec v5.25.15 to obtain the spectral parameters of the bands (Raman shifts and line widths). A resolution of 0.7 cm^{-1} was selected to record the Raman spectra.

Atomic force microscopy

The surface topography was characterized by an Agilent 5500 AFM operating in tapping mode in an air atmosphere at room temperature. A silicon AFM probe (Nanosensor PPP-NCHR-W tip) was used and image processing was performed with Gwyddion Freeware (v2.27).

Optical characterization

Thickness and refractive index measurements were conducted on $NiTiO_3$ films by optical interferometry with a setup from FILMETRICS F30 for white light interference fringe measurements. The setup uses an optical fibre which directs white light in the spectral range from 400 to 3000 nm. The film on the Si substrate gives rise to an interferometry

pattern which can be analysed by a fitting procedure to extract the film thickness and its refractive index (real and imaginary parts).

The UV-vis absorption spectra of $NiTiO_3$ thin films deposited on quartz substrates were collected using an HR4000 Ocean Optics high resolution spectrometer with a deuterium–halogen lamp as the illumination source. The spectra were collected in the wavelength range of 200–1100 nm.

Photocatalytic activity

Photocatalytic reactions were investigated through the degradation of Methylene Blue (MB) by $NiTiO_3$ films immersed in aqueous solutions and irradiated by a UV-vis 200 W Xenon arc lamp (set at 60 W). The initial concentration of the MB contaminant was 10^{-5} M. The degradation of the dyes was evaluated by means of collecting the absorption spectrum of the colored solution every 30 minutes during a period of 5 hours. The experimental setup consists of a glass beaker containing the MB solution with the specified molar concentration (under continuous magnetic stirring to ensure the homogenization of the MB charged solution). The thin film was set in a holder with its top surface directed in front of the collimated light beam.

Results and discussion

Structural investigations (XRD)

The synthesized and annealed $NiTiO_3$ thin films were investigated by XRD as a function of the synthesis conditions and the annealing treatments performed at different temperatures and durations. The synthesis parameters leading to homogeneous films with an appropriate thickness were optimized at 94/0 sccm for Ar/O flow, 0.1 mbar for pressure and 50 W for rf-power, respectively, with deposition at room temperature. Different films were investigated for different annealing temperatures at 800 °C, 900 °C, 1000 °C and 1100 °C for 2 hours. In addition, a sample annealed for 4 hours at 800 °C and another annealed for 6 hours at 900 °C were also characterized in order to observe the role of annealing conditions in the crystalline order. The XRD patterns summarized in Fig. 1 indicate the occurrence of a good crystalline structure for annealing at 1000 °C for 2 hours under air. When the temperature is increased up to 1100 °C, the structure seems to be degraded (in comparison with the film annealed at 1000 °C) and an intense peak at $2\theta = 21.7°$ appears. This peak has been attributed to the formation of a crystalline layer of SiO_2 with a cristobalite structure (JCPDS PDF no. 39-1425) at the interface between the $NiTiO_3$ film and the silicon substrate. This was confirmed from the XRD patterns of thin films deposited by a complex process of co-sputtering from two metallic targets (Ni, Ti) on fused quartz substrates, well stable at temperature higher than 1100 °C.[27]

The quantitative analysis of the XRD patterns from the rf-sputtered thin films shows well defined and intense peaks located at 2θ positions of 24.2°, 33.2°, 35.7°, 40.9°, 49.5°, 54.11°, 57.5°, 62.55°, and 64.17°. According to the standard

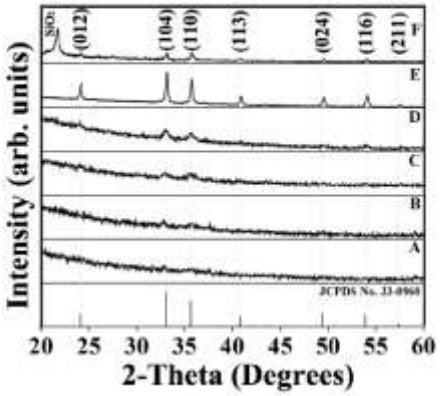

Fig. 1 XRD patterns of $NiTiO_3$ thin films annealed at different temperatures and durations under air. A) Annealed at 800 °C for 2 hours. B) Annealed at 800 °C for 4 hours. C) Annealed at 900 °C for 2 hours. D) Annealed at 900 °C for 6 hours. E) Annealed at 1000 °C for 2 hours. F) Annealed at 1100 °C for 2 hours.

structural reference JCPDS No. 33-0960 related to the ilmenite $NiTiO_3$ phase, the above data are assigned to the planes (012), (104), (110), (113), (024), (118), (211), (214) and (300), respectively. Fig. 2 shows the XRD patterns of the $NiTiO_3$ thin film with optimized deposition conditions and annealed at 1000 °C for 2 hours under air. This film will be referred below as the representative film and will be investigated by Raman, AFM, and optical methods and tested in photocatalytic reactions.

The software MAUD v2.33 (ref. 28) was used for the refinement of the XRD patterns of the representative $NiTiO_3$ film. As seen in Fig. 2, the diffraction patterns did not show any secondary phases such as rutile (TiO_2) or bunsenite (NiO) along with the ilmenite phase of nickel titanate. The refinement data summarized in Table 1 for the film features are 154 ± 3 nm

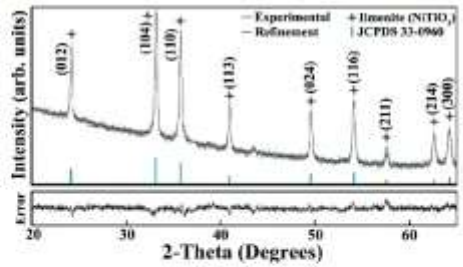

Fig. 2 XRD refinement of a representative $NiTiO_3$ thin film annealed at 1000 °C for 2 hours in air as a pure ilmenite phase by using the Rietveld method. The standard reference JCPDS No. 33-0960 is shown.

Table 1 Structural, morphological and optical features of the representative $NiTiO_3$ thin film obtained by rf-sputtering and annealed at 1000 °C under air

Sample	Crystal size (nm)	Microstrain	$NiTiO_3$ lattice parameters (Å)		Thickness (nm)	Roughness (nm)	Area (μm^2)	Refractive index	Band gap (eV)
			$a = b$	c					
$NiTiO_3$	154 ± 3	$1.40(2) \times 10^{-3}$	5.0266(3)	13.7889(8)	1500	19.2	68.7	2.42	2.71–2.79

for the average crystallite domain size, 1.4×10^{-3} for the microstrain, and the lattice parameters were close to the standard values for the ilmenite structure, *i.e.* $a = b = 5.03$ Å and $c = 13.80$ Å. The 2θ positions of the diffraction lines are in agreement with those of the JCPDS reference for the ilmenite structure (Fig. 1). The analysis of the FWHM of the diffraction line yields an estimate of the crystalline domain sizes in the order of 154 nm. This value indicates the absence of size effects on the broadening of the diffraction line and with regard to the low value of microstrain (1.4×10^{-3}), we then conclude the good quality of the crystalline phase of the representative $NiTiO_3$ film.

Raman investigations

The ilmenite structure of $NiTiO_3$ possesses the space group $R\bar{3}$ (C_{3i}^2) with the oxygen atoms being tetra-coordinated to two tetravalent Ti and to two bivalent Ni cations (Fig. 3). It can be theoretically predicted that the optical normal modes of vibrations at the Brillouin zone center have the following symmetries $5A_g + 5E_g + 4A_u + 4E_u$ (in addition to the $A_u + E_u$ zero frequency acoustic modes).[29–31]

Therefore, ten Raman active modes ($5A_g + 5E_g$) are expected with each E_g mode being twofold degenerated ($E_g = E_g^1 + E_g^2$) along with the eight IR active modes ($4A_u + 4E_u$).

From the experimental spectra reported in Fig. 4 and 5, and excluding the 520 cm^{-1} band due to the silicon substrate, the Raman modes of $NiTiO_3$ are assigned as follows in cm^{-1}: 189.6 (A_g), 227.6 (E_g), 245.7 (A_g), 290.2 (E_g), 343.3 (E_g), 392.6 (A_g), 463.4 (E_g), 482.7 (A_g), 609.7 (E_g) and 705.9 (A_g).

This assignment is proposed by comparing the relative intensities of the Raman bands between parallel and cross polarizations (Fig. 5). The thickness of the sample (less than 1500 nm) prevents the occurrence of significant beam depolarization induced by birefringence, as experimentally shown. On the other hand, for cubic symmetry, the diagonal elements of the Raman scattering tensors of A_g modes have the same value and the off-diagonal elements are zero, so that they vanish in cross polarization. In the case of ilmenite, with rhombohedral symmetry, the diagonal elements of the scattering tensor may be different but in view of the structure, they can be supposed to be fairly close to each other. Therefore, under cross polarization, the A_g Raman peaks are expected to undergo more important intensity decreases than the E_g ones, as observed in Fig. 5.

The Raman mode attribution can also be done by comparison with the Raman spectra of isomorphous $MgTiO_3$ as it was proposed by Wang *et al.*[10] In both materials, the Raman active modes can be described as symmetric Ti–O stretching vibrations, bond-bending of O–Ti–O, and translations of the divalent cations with respect to the oxygen groups.[32] The former vibrations are expected to be set in the same frequency range since the structures are close. On the other hand, the vibrations dominated by the divalent cation displacements are expected to undergo frequency shifts related to mass effects and would be roughly proportional to the square root of the ratio between the Ni and Mg atomic masses. Thus, the A_g mode at 306 cm^{-1} in $MgTiO_3$ is predicted at 197 cm^{-1} in $NiTiO_3$ which fairly well matches with the experimental line measured at 189.6 cm^{-1}.

Since $MgTiO_3$ and $NiTiO_3$ are isostructural, the other modes that mostly involve Ti–O vibrations are expected in the same frequency range. Thus, the A_g mode at 245.7 cm^{-1}

Fig. 3 Representation of the $NiTiO_3$ ilmenite unit cell and local environments of Ti and Ni.

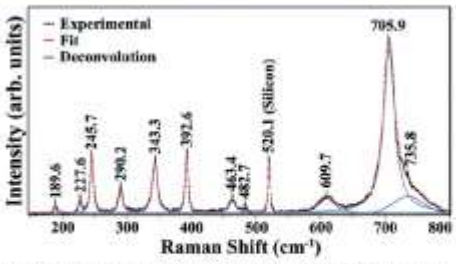

Fig. 4 Experimental and simulation of the Raman spectrum of the representative $NiTiO_3$ thin film annealed at 1000 °C for 2 hours in air atmosphere.

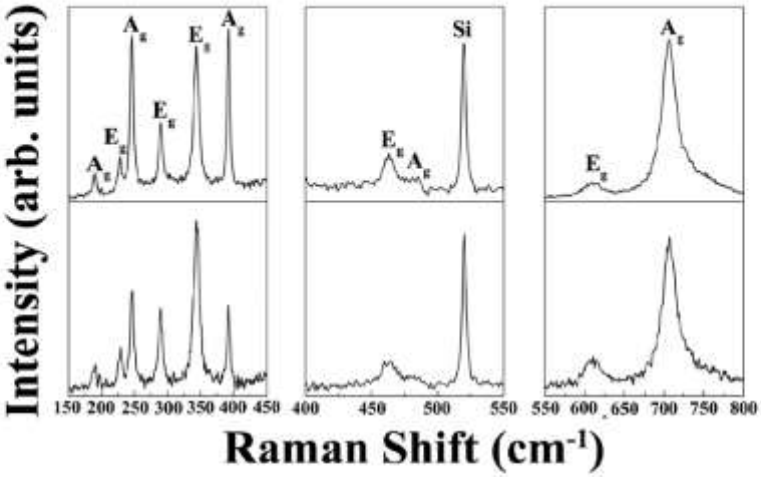

Fig. 5 Raman spectra collected from a representative $NiTiO_3$ thin film annealed at 1000 °C for 2 hours in air atmosphere using: parallel polarization (top) and cross polarization (bottom).

can be attributed to the vibrations of Ti atoms along the *z* axis and the A_g modes at 398 and 482.7 cm^{-1} can be assigned to a breathing-like stretching of the Ti centered oxygen octahedra.

A typical feature in the Raman spectra of the ilmenite structure lies in the appearance of a very strong band at high frequencies (*e.g.* 705.9 cm^{-1}). This Raman peak can be associated with a mode that is inactive in the similar but more symmetric corundum structure ($R\bar{3}c$ = D^6_{3d} space group), which implies that this mode arises from the symmetric stretching of TiO_6 octahedra.[21] The E_g mode at 227.6 cm^{-1} can be considered as the asymmetric breathing vibration of the oxygen octahedra and the ones at 290.2 and 343.3 cm^{-1} can be described by the twist of oxygen octahedra due to vibrations of the Ni and Ti atoms parallel to the *xy* plane. The E_g modes at 463.4 and 609.7 cm^{-1} are assigned to the asymmetric breathing and twist of the oxygen octahedra with the cationic vibrations parallel to the *xy* plane.

In addition to these first-order Raman lines, a weak and broad signal (already reported) is observed around 735.8 cm^{-1}. A similar signal that appears as a shoulder of the highest frequency mode is also observed in the isomorphous $MgTiO_3$.[29–31] Its origin remains a matter of debate. In our recent work dealing with theoretical modelling and numerical simulations of the structural, vibrational and electronic structures of nitrogen doped $NiTiO_3$,[32] our analysis suggests that this signal may arise from the occurrence of a small fraction of an amorphous phase. The involvement of vibrational density of states gives rise to broad features that would lead to the asymmetry of the A_g band, *i.e.* similar to the observed shoulder in the considered Raman band. The amorphous fraction may be accounted for by the high specific surface of the grains that compose the films as illustrated below by AFM observations.

Atomic force microscopy

In the case of heterogeneous photocatalysis, the contact surface between the photocatalyst and the surrounding media plays a key role in the efficiency of the photocatalysis reactions. The microstructure and morphologies of the grains define the roughness of the surface that monitors the contact between the active media. Also, the characterization of the topology of the film is an important factor and atomic force microscopy can be used for its evaluation *versus* the synthesis and treatment conditions. Thus, the representative sputtered thin film was investigated by AFM. The value of the roughness and the probed surface area for the optimized thin films were estimated to be 19.2 nm and 68.7 μm^2, respectively. The relevant morphology values are summarized in Table 1, and Fig. 6 shows the surface image of the representative $NiTiO_3$ thin film. The AFM observations indicate the occurrence of a rough surface organized as nano-islands with high specific surfaces. Such organization may contribute to the enhancement of the photocatalysis efficiency of such thin films as discussed below.

Optical characterization. The experimental interferometry diagram was recorded on the ilmenite structure of the representative $NiTiO_3$ thin film by using Filmetrics equipment monitored by the related software. Fig. 7 reports an example of the experimental and simulated interference diagram from the representative film. The fitting parameters were deduced

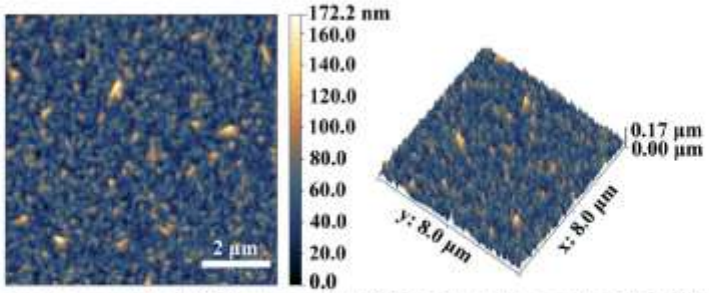

Fig. 6 AFM surface image of a representative $NiTiO_3$ thin film annealed at 1000 °C for 2 hours in air atmosphere, RMS = 19.2 nm, area = 68.7 μm^2.

as 1500 nm and 2.42 for the thin film thickness and refractive index, respectively. The relevance of the estimated thickness was confirmed by profilometry measurements. For the optical absorption measurements, the absorption coefficient (α) was deduced from the UV-vis optical spectra and used to plot $(\alpha h\nu)^2$ *versus* the photon energy ($h\nu$) in order to determine accurately the band gap of the material. From the Tauc plot depicted in Fig. 8, the extrapolation of the linear behaviour to the ($h\nu$) axis allows us to determine the band gap in the range 2.71 to 2.79 eV. With such values, the obtained thin films absorb a fraction of visible range for photocatalysis reactions discussed in the forthcoming part. It is worth noting that the band gap about 2.18 eV is indeed involved in bulk 3D crystalline materials. For the representative film in this work, the roughness of about 19 nm may lead to surface effects able to modify the band gap compared to the infinite crystal.

Photocatalytic activity of $NiTiO_3$ thin films. The photocatalysis experiments were carried out by using MB dyes with a concentration of 10^{-5} M as pollutants in water and the representative $NiTiO_3$ thin film as the photocatalyst. Under light radiation from a Xenon arc lamp (UV-vis-60 W) directed on the sample surface about 4 cm^2, the degradation of MB was monitored by the optical absorption measured at steps of 30 minutes for 5 hours. As shown in Fig. 9, the absorption spectra undergo a continuous decrease as a function of the light exposure time and demonstrate the photocatalytic activity of $NiTiO_3$. It can be seen that after 5 hours of irradiation, 60% of the initial concentration of MB dyes was destroyed in the solution.

The ratio between the absolute concentration at a given time (C) and the initial concentration (C_0) was plotted *versus* time in the logarithmic scale $\ln\left[\frac{C}{C_0}\right] = f(t)$ (Fig. 10). The linear semi-logarithmic plot was adjusted by using a first order kinetics as $C = C_0 e^{-kt}$ with the reaction rate constant estimated from the experiment (Fig. 10) to be $k = 0.3 \times 10^{-2}$ min^{-1}. The visible light driven photoactivity of $NiTiO_3$ is thus demonstrated in $NiTiO_3$ obtained by a simple synthesis

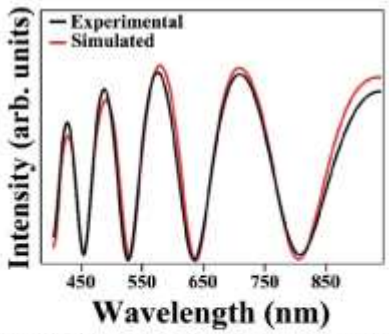

Fig. 7 Representation of the optical interferometry pattern made by a $NiTiO_3$ thin film annealed at 1000 °C for 2 hours in air atmosphere. The values of the fit are summarized in Table 1.

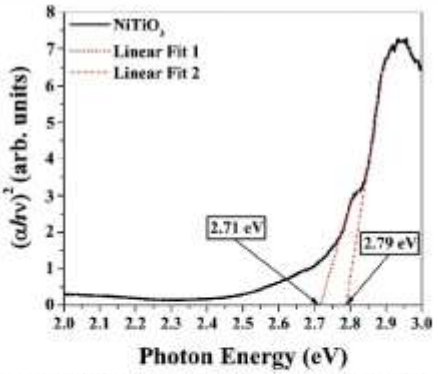

Fig. 8 Tauc plot of a $NiTiO_3$ thin film deposited on a quartz substrate; the film was annealed at 1000 °C under air and exhibits the ilmenite structure.

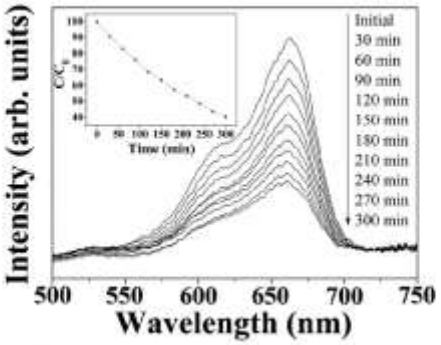

Fig. 9 Optical absorption spectra of the MB charged solution during the photocatalytic process. The inset reports the absolute MB concentration vs. time.

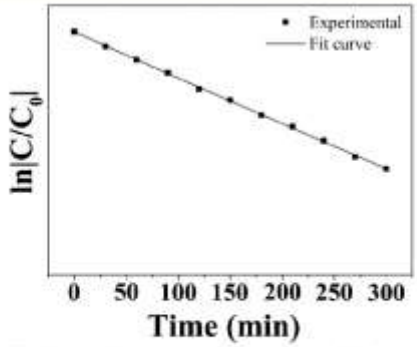

Fig. 10 Kinetics of the photocatalytic degradation of MB by visible light irradiated $NiTiO_3$. The graph reports the semi-logarithmic plot of the normalized concentration C/C_0 versus irradiation time.

procedure followed by suitable treatments to ensure ilmenite structure with a good crystalline quality. The photocatalytic efficiency is a matter of improvement through the increase of the concentration of photogenerated charge carriers and their lifetime. Increasing the charge carriers may be realized by suitable doping as metallic elements. In this context, substitutional doping is able to modulate the electronic structure of the host material. A second configuration of the metal doping process leads to the formation of clusters where critical phenomena such as surface plasmon resonance contribute to the enhancement of the efficiency of the photocatalytic reactions based on $NiTiO_3$. Such approaches are currently under consideration.

Conclusions

A simple and fast synthesis route was developed to obtain $NiTiO_3$ thin films with a good crystalline quality and stable ilmenite structure. Solid state reaction was performed to obtain crystalline powders used as targets for the rf-sputtering method. Appropriate deposition conditions and post-synthesis treatment were determined to obtain thin films with controlled features. Thus, optimized deposition conditions and annealing lead to diffraction patterns of the ilmenite structure without any additional phase. Vibrational properties were investigated by Raman spectroscopy with the identification and exhaustive discussion of the assignment made for all the active modes related to the $R\bar{3}$ space group. The surface morphology and roughness were characterized by AFM microscopy. These features characterize the contact surface which can be exploited in the photocatalysis reactions considered in this work through the degradation of organic dyes in aqueous solutions. We demonstrate the photoactivity of the representative film with the reaction constant rate $k = 0.33 \times 10^{-2}$ min^{-1}. This value is in the order of the one obtained under the same conditions on the co-sputtering synthesized films from metallic targets Ti and Ni.[27] The photoactivity of $NiTiO_3$ can be improved by modulation of its electronic and optical properties. The doping process using suitable metallic or nonmetallic ions is a matter of interest which is currently under development by the simple synthesis approach discussed in the present report.

Acknowledgements

M. A. Ruiz-Preciado is thankful to CONACYT for granting the doctoral scholarship to perform his Ph.D. thesis in the frame of collaboration between the Université du Maine and CINVESTAV. He is also thankful to the doctoral school of the Université du Maine ED3MPL for the allocated financial support. The authors are thankful to Dr. Nicolas Delorme for the AFM images reported in this article.

References

1 A. Fujishima, X. Zhang and D. A. Tryk, *Surf. Sci. Rep.*, 2008, **63**, 515–582.
2 K. Hashimoto, H. Irie and A. Fujishima, *Jpn. J. Appl. Phys.*, 2005, **44**(12), 8269–8285.
3 A. Fujishima, T. N. Rao and D. A. Tryk, *J. Photochem. Photobiol., C*, 2000, **1**, 1–21.
4 W.-J. Yin, H. Tang, S.-H. Wei, M. M. Al-Jassim, J. Turner and Y. Yan, *Phys. Rev. B: Condens. Matter Mater. Phys.*, 2010, **82**, 045106.
5 H. Yamashita, M. Harada, J. Misaka, M. Takeuchi, K. Ikeue and M. Anpo, *J. Photochem. Photobiol., A*, 2002, **148**, 257–261.
6 S. In, A. Orlov, R. Berg, F. Garcia, S. Pedrosa-Jimenez, M. S. Tikhov, D. S. Wright and R. M. Lambert, *J. Am. Chem. Soc.*, 2007, **129**(45), 13790–13791.
7 Y. Niu, M. Xing, J. Zhang and B. Tian, *Catal. Today*, 2013, **201**, 159–166.
8 J. Yang, X. Zhang, H. Liu, C. Wang, S. Liu, P. Sun, L. Wang and Y. Liu, *Catal. Today*, 2013, **201**, 195–202.

9 X. Liu, L. Pana, T. Lva, Z. Sun and C. Sun, *J. Mol. Catal. A: Chem.*, 2012, **363–364**, 417–422.
10 A. M. Hussein, L. Mahoney, R. Peng, H. Kibombo, C.-M. Wu, R. T. Koodali and R. Shende, *J. Renewable Sustainable Energy*, 2013, **5**, 033118.
11 G. C. De, A. M. Roy and S. S. Bhattacharya, *Int. J. Hydrogen Energy*, 1996, **21**, 19–23.
12 D. W. Hwang, J. Kim, T. J. Park and J. S. Lee, *Catal. Lett.*, 2002, **80**, 53–57.
13 W. F. Yao, X. H. Xu, H. Wang, J. T. Zhou, X. N. Yang, Y. Zhang, S. X. Shang and B. B. Huang, *Appl. Catal., B*, 2004, **52**, 109–116.
14 J. Kim, D. W. Hwang, H.-G. Kim, S. W. Bae, S. M. Ji and J. S. Lee, *Chem. Commun.*, 2002(21), 2488–2489.
15 H. G. Kim, D. W. Hwang and J. S. Lee, *J. Am. Chem. Soc.*, 2004, **126**, 8912–8913.
16 M. A. Ruiz-Preciado, A. H. Kassiba, A. Gibaud and A. Morales-Acevedo, *Mater. Sci. Semicond. Process.*, 2015, **37**, 171–178.
17 V. I. Merupo, V. Subramaniam, K. Ordon, N. Errien, J. Szade and A. Kassiba, *CrystEngComm*, 2015, **17**, 3366–3375.
18 V. I. Merupo, S. Velumani, A. h. Kassiba and M. A. García-Sánchez, *2014 11th International Conference on Electrical Engineering, Computing Science and Automatic Control IEEE*, DOI: 1109/ICEEE 2014 6978299.
19 V. I. Merupo, S. Velumani, G. Oza, M. Makowska-Janusik and A. Kassiba, *Mater. Sci. Semicond. Process.*, 2015, **31**, 618–623.
20 P. Kanhere and Z. Chen, *Molecules*, 2014, **19**, 19995–20022.
21 A. Navrotsky, *Chem. Mater.*, 1998, **10**(10), 2787–2793.
22 D. M. Giaquinta and H.-C. Z. Loye, *Chem. Mater.*, 1994, **6**, 365–372.
23 J. M. Xeil, A. Navrotsky and O. J. Klepp, *Inorg. Chem.*, 1971, **10**, 2076–2077.
24 Y. Xu and M. A. A. Schoonen, *Am. Mineral.*, 2000, **85**, 543–556.
25 T. Li, C. Ch. Wang, C. M. Lei, X. H. Sun, G. J. Wang and L. N. Liu, *Curr. Appl. Phys.*, 2013, **13**, 1728–1731.
26 S. Yuvaraj, V. D. Nithya, K. Saiadali Fathima, C. Sanjeeviraja, G. Kalai Selvan, S. Arumugam and R. Selvan, *Mater. Res. Bull.*, 2013, **48**, 1110–1116.
27 J. B. Bellam, M. A. Ruiz-Preciado, M. Edely, J. Szade, A. Jouanneaux and A. H. Kassiba, *RSC Adv.*, 2015, **5**, 10551–10559.
28 L. Lutterotti and P. Scardi, *J. Appl. Crystallogr.*, 1990, **23**, 246–252.
29 G. Busca, G. Ramis, J. M. G. Amores, V. S. Escribano and P. Piaggio, *J. Chem. Soc., Faraday Trans.*, 1994, **90**, 3181–3190.
30 C.-H. Wang, X.-P. Jing, W. Feng and J. Lu, *J. Appl. Phys.*, 2008, **104**, 034112–034112.
31 M.-I. Baraton, G. Busca, M. del Carmen Prieto, G. Ricchiardi and V. S. Escribano, *J. Solid State Chem.*, 1994, **112**, 9–14.
32 M. A. R. Preciado, A. Kassiba, A. Morales-Acevedo and M. Makowska-Janusik, *RSC Adv.*, 2015, **5**, 17396–17404.

d. Visible-light photocatalytic activity of nitrogen-doped $NiTiO_3$ thin films prepared by a co-sputterring process

RSC Advances

PAPER

View Article Online
View Journal | View Issue

CrossMark

Cite this: RSC Adv., 2015, 5, 10551

Visible-light photocatalytic activity of nitrogen-doped $NiTiO_3$ thin films prepared by a co-sputtering process

Jagadeesh Babu Bellam,[a] Marco Alejandro Ruiz-Preciado,[ab] Mathieu Edely,[a] Jacek Szade,[c] Alain Jouanneaux[a] and Abdel Hadi Kassiba*[a]

Nickel titanate ($NiTiO_3$) thin films were grown by a radio frequency magnetron co-sputtering process using metal (Ni and Ti) targets on fused quartz substrates at a substrate temperature of 400 °C. Annealing of as-deposited (amorphous) films was performed at 1100 °C for 2 hours to realize a stable crystalline phase. The effect of the Ti target power (200 and 250 W) and nitrogen doping on the structural, morphological and optical properties of post-annealed $NiTiO_3$ thin films were investigated besides photocatalytic activity under visible light irradiation. X-ray diffraction measurement on the films revealed a pure ilmenite phase at 250 W Ti power. Preferential orientation changed from [104] to [110] as Ti power increased from 200 to 250 W. Raman studies on $NiTiO_3$ thin films showed almost all the active modes ($5A_g + 5E_g$) of a crystalline structure. Two different microstructures were observed by scanning electron microscopy. films showed rounded (250 nm) grains at 200 W Ti target power while facet forms (500 nm) develop in the films deposited at 250 W. Chemical bonding and valence states of the involved ions such as Ni 2p, Ti 2p and O 1s were investigated by X-ray photoelectron spectroscopy. Nitrogen doping modifies the rms roughness from 12 nm to 17 nm as demonstrated on 200 W grown films and contributes also to modify the indirect optical band gap from 2.50 to 2.43 eV in films obtained at 250 W Ti target power. As a crucial role of nitrogen doping, photocatalytic activity in a broad visible light range was observed with a good efficiency for the degradation of methylene blue by nitrogen doped $NiTiO_3$ thin films.

Received 16th October 2014
Accepted 5th January 2015

DOI: 10.1039/c4ra12516a

www.rsc.org/advances

1. Introduction

Development of visible light driven photocatalysts has been of great interest in the past decade because ultra violet (UV) light induced photocatalysis not only needs expensive light sources but it is also inefficient in exploiting a large spectrum of solar radiation. TiO_2 shows relatively high reactivity and chemical stability under UV light, whose energy exceeds the band gap of 3.3 eV. Several approaches for TiO_2 modification have been employed such as metal (Ag, Fe, V, Au, Pt, Ni, Co, Cu, Nb)-ion implanted TiO_2,[1,2] non-metal (N, S, C, B, P, I, F) doped TiO_2 (ref. 1 and 3) and mixed oxides with p–n junction characteristics.[4] Attempts have also been made to develop new visible-light photocatalysts such as CdS, WO_3, $BiVO_4$ and $Bi_2O_2CO_3$.[5–9] However, the resulting photocatalysts are deficient in either activity or stability.

A suitable high efficiency semiconductor for visible-light-driven photocatalysis should have sufficiently narrow band gap (E_g < 3.0 eV) to harvest visible light, but large enough (E_g > 1.23 eV) to provide energetic electrons.[10] In this context $NiTiO_3$ with a band gap of 2.2 eV has recently attracted much attention because of its high photocatalytic activity under UV irradiation and more remarkably under visible light.[11–13] To the best of our knowledge, most published works have been focused on visible-light photocatalysis of pure or metal doped $NiTiO_3$ nanoparticles, nanorods and nanowires.[11,12,14] To enhance the visible light absorption in $NiTiO_3$, non-metal doping can be one of the simple and low cost option. This approach was successfully applied for TiO_2 where nitrogen doping shifts the absorption edge to lower energies and hence increase the visible light absorption.[3,15]

$NiTiO_3$ is the only ternary phase with ilmenite structure in the NiO–TiO_2 based materials.[16,17] For $NiTiO_3$ (ABO_3), cation arrangement along the c-axis occurs as A–B–Vac–B–A–Vac–A–B… (Vac = Vacancy) as also observed along the plane perpendicular to the c-axis.[18,19] Moreover, $NiTiO_3$ fulfills all conditions such as tolerance factor, electro-negativity difference and octahedral factor to adopt a stable ilmenite structure.[20] Thus good stability and related features of ilmenite $NiTiO_3$ contribute to a wide range of applications for this compound such as tribological

[a]Institute of Molecules and Materials, UMR-CNRS 6283, University of Maine, Avenue O. Messiaen, F-72085 Le Mans, France. E-mail: kassiba@univ-lemans.fr; Fax: +33 243833518; Tel: +33 243833512

[b]Department of Electrical Engineering-SEES, CINVESTAV-IPN, Zacatenco, D.F., C.P. 07360, Mexico

[c]A. Chelkowski Institute of Physics and Silesian Centre of Education and Interdisciplinary Research – University of Silesia, Ul. Uniwersytecka 4, 40-007 Katowice, Poland

coating,[21] pigment,[22] photocatalyst,[11,12,23] catalyst[24] and gas sensor.[25] However, the above properties depend on the synthesis method. So far different methods have been developed to obtain $NiTiO_3$ nanoparticles and thin films by different wet chemical methods such as polymer pyrolysis,[19,26] sol–gel dip coating,[23,27] stearic acid gel,[28] auto-combustion method,[24] co-precipitation,[3,13] solid state methods like molten salt synthesis[19,29] and aerosol assisted chemical vapor deposition.[30]

Efficiency of photocatalytic reactions is critically dependent on the imperfections of the crystalline structure. All the chemical methods require metal–organic molecules, solvents and longer time to reach desired composition and most of above studies involve only powders. Reports concerning the characteristics of $NiTiO_3$ based thin films deposited by physical vapor depositions are generally lacking. Herein we perform for first time the deposition of nitrogen doped $NiTiO_3$ thin films by radio frequency magnetron co-sputtering using Ti and Ni metal targets under argon and oxygen atmosphere as well as nitrogen for doped films. An achievement of good crystalline structure of the synthesized $NiTiO_3$ films was realized as well as the nitrogen doping. Exhaustive studies of structural and optical properties were carried out. The photocatalytic activity tested on methylene blue (MB) solutions shows enhanced efficiency in nitrogen doped film compared to un-doped structures.

2. Experimental details

$NiTiO_3$ thin films were deposited onto fused quartz substrates using Plassys MP 500S multi-target sputtering unit consisting of two 13.56 MHz, 300 W radio frequency (RF) magnetron sources, as schematically shown in Fig. 1. Double side polished clean 2 cm × 2 cm quartz substrates were introduced into deposition chamber without any pre-cleaning treatment, except removing the dust particles with an air jet. A 2 inch pure Ni (99.99%) and Ti (99.7%) metal targets with a thickness of 4 and 1 mm, respectively were used. Sputtering chamber was evacuated by turbo molecular pump to a base pressure of 5×10^{-8} mbar. Argon is used as processing gas, oxygen played reactive gas role and nitrogen doping requires defined nitrogen partial pressure in the deposition chamber. Pre-sputtering was carried out at a RF power of 50 W for 5 minutes in the presence of processing gas with closed shutters. The substrate was mounted apart from target at a distance of 100 mm on a rotating disc. Detailed deposition conditions of nitrogen doped and un-doped $NiTiO_3$ thin films are listed in Table 1. Deposition parameters value was chosen from a set of 12 experiments (L_{12}) designed by Plackett–Burman screening design and from preliminary depositions, which is not reported in this work. The as-deposited films were annealed at 1100 °C for 120 minutes with a heating rate of 5 °C $minute^{-1}$ in air.

Structural characterization of $NiTiO_3$ thin films were carried out using PANalytical Empyrean X-Ray Diffractometer operating at 40 kV, 30 mA with Cu $K_{\alpha1}$ (λ = 1.5406 Å) and Cu $K_{\alpha2}$ (λ = 1.5444 Å) lines in grazing incidence (ω = 0.3°) mode. X-ray diffraction (XRD) patterns were recorded in the scanning range of 20–65° with a scan step size of 0.03°. The XRD pattern was analyzed by the Rietveld method with the Fullprof program (version 5.40).[31,32] Refinement was carried out by considering space group and lattice parameters from Joint Committee on Powder Diffraction Standards (JCPDS) database for ilmenite (033-0960) and bunsenite (47-1049). The quality of Rietveld refinement was evaluated in terms of weighted profile residual error (R_{wp}) and profile residual factor (R_p). Confocal Raman scattering was performed with T64000 Jobin-Yvon multichannel spectrometer in simple configuration with 1800 lines per mm grating coupled to a CCD detector. The spectra were collected in the backscattering geometry, under microscope (50× objective) using the 514.5 nm wavelength of Ar–Kr laser source with a

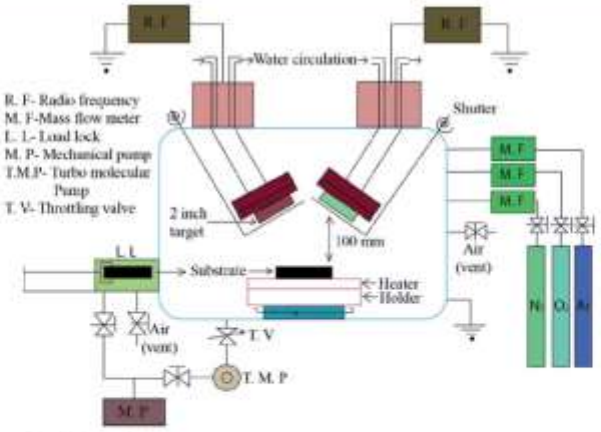

Fig. 1 Schematic of two target sputtering system.

Table 1 RF co-sputtering conditions for $NiTiO_3$ thin films

Deposition parameters	Sample identification			
	QNTL84A	QNTL86A	QNTN84A	QNTN86A
Power of Ni target (W)	40	40	40	40
Power of Ti target (W)	200	250	200	250
Deposition time (minutes)	120	120	120	120
Argon flow rate (sccm)	60	60	60	60
Oxygen flow rate (sccm)	10	10	10	10
Nitrogen flow rate (sccm)	—	—	2	2
Substrate temperature (°C)	400	400	400	400
Working pressure (mbar)	0.02	0.02	0.02	0.02
Annealing temperature (°C)	1100	1100	1100	1100
Annealing time (minutes)	120	120	120	120

power of 200 mW. Surface morphology was captured using JEOL JSM-6510LV scanning electron microscopy (SEM) at an operating voltage of 10 kV with a spot size of 30 nm. Composition of all the films were determined using Oxford X-Max energy dispersive analysis of X-ray (EDAX) system attached to a secondary electron microscope with an accelerating voltage of 10 kV.

The chemical states of $NiTiO_3$ thin film and nitrogen doping value were studied by using X-ray photoelectron spectroscopy (XPS) measurement performed on SSX-100 (Surface Science Instrument Inc.,) with monochromatic A1 Kα radiation. Binding energies were calibrated relative to the C 1s peak (284.6 eV). Topography images were obtained on an Agilent 5500 atomic force microscopy (AFM) operating in tapping mode in air at room temperature with a silicon AFM probe. Optical properties of $NiTiO_3$ thin films were recorded using Cary 100 double beam spectrophotometer in the wavelength range of 200–800 nm. Photocatalytic study was performed under visible light using the degradation of MB as the test reaction. The visible light source was a 240 W high-pressure mercury lamp (100 mm long). A quantity of 50 ml MB blue solution with a concentration of 1×10^{-5} mol L^{-1} under continuous magnetic stirring is taken in a glass beaker and the thin film is placed vertically in the container at a distance of 100 mm from the slit of incident light beam. At regular time intervals, a solution is collected in cuvette and analyzed by measuring the absorption at 661 nm (maximum absorption for MB) using an ulice SPID-PCH UV-vis spectrophotometer.

3. Results and discussion

3.1 Structural features

XRD patterns of $NiTiO_3$ thin films deposited at 200 and 250 W Ti target power with and without nitrogen atmosphere are depicted in Fig. 2. Fused quartz used as substrate lead to amorphous-like broad diffraction line at lower angle. With 250 W deposition power, all diffraction peaks were matched to JCPDS card no. 033-0960 (trigonal, $a = b = 5.03$ Å, $c = 13.79$ Å, $V = 301.69$ Å^3). The diffraction planes (102), (104), (110), (113), (024), (116), (018), (214) and (300) are situated at 24.34°, 33.33°, 35.94°, 41.07°, 49.66°, 54.36°, 57.80°, 62.64° and 64.30°, respectively,

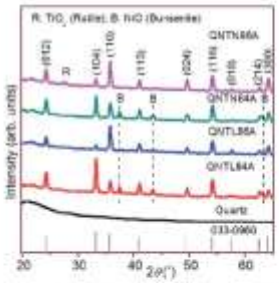

Fig. 2 XRD patterns of $NiTiO_3$ thin films deposited at different Ti power (200 W (QNTL84A) and 250 W (QNTL86A)) with nitrogen doping (QNTN84A and QNTN86A).

reveal single ilmenite phase $NiTiO_3$ without any secondary phases. Oppositely, in the case of films deposited at 200 W Ti power with or without doping, three diffraction lines (111), (200) and (220) at 37.48°, 43.66° and 62.98°, respectively were observed corresponding to JCPDS card no. 47-1049 (cubic, $a = 4.178$ Å, $V = 72.93$ Å^3) along with ilmenite phase for bunsenite phase NiO.

The observed, calculated and difference profiles of Rietveld refined XRD pattern of QNTL84A are illustrated in Fig. 3. Owing to a low signal-to-noise ratio in the diffraction pattern, a limited number of eight refined parameters were used in the refinement process and consist in scale factors, zero-point value, cell constants and two parameters only for the Thompson–Cox–Hastings pseudo-Voigt function.[33] The atomic coordinates and temperature factors were kept fixed. After Rietveld refinement, lattice parameters and volume of unit cell of two phases were determined as $a = b = 5.02$ Å, $c = 13.77$ Å, $V = 301.39$ Å^3 for $NiTiO_3$ and $a = 4.172$ Å, $V = 72.63$ Å^3 for NiO. Although there are some changes in the lattice parameters and unit cell volume, they are less than 1%. Changes in the parameters can be attributed to the stress induced by lattice mismatch between the substrate and the film.[34] The final R-factors (not corrected for background values) were R_I ($NiTiO_3$) = 15.3%, R_I (NiO) = 23.5%, R_p = 6.7%, R_{wp} = 8.4% and R_{exp} = 6.7%. The weight fractions

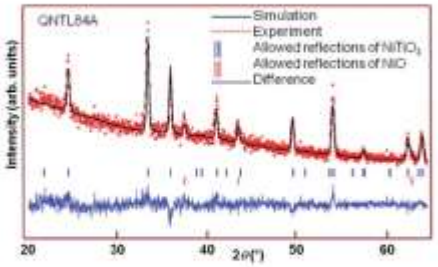

Fig. 3 Rietveld refinement for XRD pattern of $NiTiO_3$ thin film deposited at 200 W Ti power using FullProf software.

deduced from the Rietveld refinement results are 92 (4)% and 8 (1)% for $NiTiO_3$ and NiO, respectively. This suggests that these films are nickel rich compared to the one deposited at 250 W Ti power. It is obvious from the phase diagram[47] that NiO coexists with $NiTiO_3$ phase at higher Ni/Ti ratio. However the film deposited at 250 W Ti power with nitrogen doping showed an extra reflection (110) at 27.66° corresponding to rutile phase (TiO_2; JCPDS card 21-1276). As Ti power increased from 200 W to 250 W, preferential orientation on the film changed from [104] to [110] plane. Influence of nitrogen doping on structural features of $NiTiO_3$ were not noticed probably due to low doping rates.

Fig. 4 shows Raman spectra in the wavenumber range of 150–900 cm^{-1} for the $NiTiO_3$ films deposited at 200 and 250 W Ti power and with and without nitrogen doping. In the case of ilmenite structure, 10 Raman active modes ($5A_g + 5E_g$) were observed and assigned to C_{3i}^2 symmetry with $R\bar{3}$ space group.[26,27,33] These modes are characteristics of $NiTiO_3$ and confirm the rhombohedral structure in agreement with the reported literature.[26,27] The peak positions are located at 193.1, 230.5, 247.6, 292.0, 345.5, 395.2, 465.3, 485.2, 609.6 and 706.8 cm^{-1}. According to Baraton *et al.* at least nine Raman active fundamental modes can be observed without any difficulty in good crystalline structure.[33] The remaining mode can be unresolved due to low intensity or overlapping with a closer bands. However, we were able to observe all the active modes in all the samples. Though it's low intensity band, the A_g mode at 485.2 cm^{-1} was also observed. The Raman band at 706.8 cm^{-1} is the highest frequency for fundamental mode of ilmenite phase. This mode arises from the vibrational mode of MO_6 octahedra that is the symmetric stretching mode.[33] The assignment of the modes to vibration motions was made in agreement with the similar structure of $R\bar{3}$ space group reported by Wang *et al.* for $MgTiO_3$ structure.[26]

3.2 Morphology and composition

Surface morphology of $NiTiO_3$ thin films deposited at 200 and 250 W Ti target power and with nitrogen doping are shown in Fig. 5. As witnessed from XRD results, orientation of grains changed from round shape to facets along with pores as power of Ti target increases. Average grain size was measured to be 200–250 nm at 200 W Ti power while two different grain size distributions were observed at 250 W. Grains with similar sizes as seen in 200 W Ti power synthesized films coexist with greater grains up to 500 nm. The atomic concentrations of the investigated films obtained from EDAX are presented in Table 2. Increasing Ti target power from 200 to 250 W contributes to lower the ratio of Ni/Ti from 1.7 to 1.2, approaching then the stoichiometry. It's worth noting that EDAX spectrum (Fig. 6) was not able to evaluate the nitrogen content due to the low doping values as well as the oxygen content due to overlapping of energy lines of Ti Lα (0.452 keV) and O Kα (0.525 keV). On the hand, Ni/Ti ratio is of primary importance to define the stoichiometry of the films.

The XPS analysis of $NiTiO_3$ thin film deposited at 250 W Ti target power with nitrogen doping (QNTN86A) has been surveyed in the 0–1200 eV range of binding energies as shown in Fig. 7(a). No contamination species were observed within the sensitivity of the instrument, apart from the adsorbed atmospheric carbon and silicon from the substrate. Peaks corresponding to Ni, Ti and O exist in the sample and nitrogen peak was missing from the

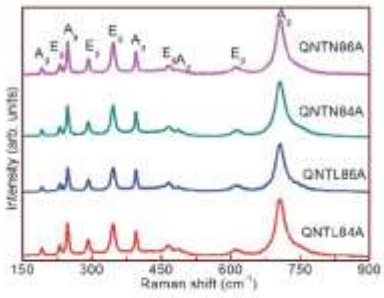

Fig. 4 Raman spectra of $NiTiO_3$ thin films deposited at different Ti power (200 W (QNTL84A) and 250 W (QNTL86A)) with nitrogen doping (QNTN84A and QNTN86A).

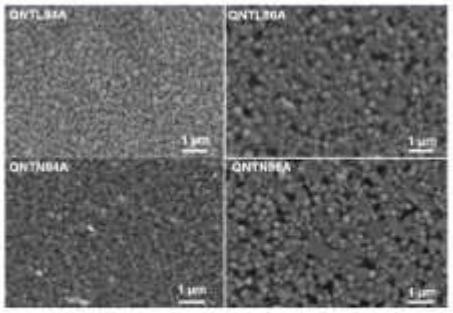

Fig. 5 SEM micrographs of $NiTiO_3$ thin films deposited at 200 and 250 W Ti power with nitrogen doping.

Table 2 EDAX analysis of $NiTiO_3$ thin films

Sample identification	Atomic concentration of Ni (at%)	Ti (at%)	O (at%)
QNTL84A	17.36	10.24	72.39
QNTL86A	15.02	12.39	72.59
QNTN84A	17.33	10.20	72.47
QNTN86A	15.13	12.12	72.76

spectrum probably because of lower doping levels. The high resolution XPS spectrum of Ni 2p, O 1s and Ti 2p are shown in Fig. 7(b)–(d), respectively. The peaks in Fig. 7(b) located at 856 and 874 eV corresponds to the Ni $2p_{3/2}$ and Ni $2p_{1/2}$ states.[14,17] The broad satellite peaks at 862 eV and 882 eV are characteristic of divalent Ni (Ni^{2+}).[27] The position of Ti $2p_{3/2}$ and Ti $2p_{1/2}$ lines at 458.6 eV and 464.2 eV shown in Fig. 7(d) indicates to Ti^{4+} oxidation state.[3,37] As shown in Fig. 7(c), the peak at about 530.3 eV of O 1s can be attributed to $NiTiO_3$ while the high energy peak at 532.6 eV corresponds to the surface contaminations.[3] Atomic concentration of Ni, Ti and O from XPS analysis were 12.06, 12.20 and 75.74 at%, respectively showing Ni/Ti ratio as 0.99. Ti excess compared to the Ni is the source for rutile phase observed in this film as presented in Fig. 2. However stoichiometric composition was not extracted from the sample because of signals coming from contamination and the substrate.

Fig. 8 shows surface topography of nitrogen doped and undoped $NiTiO_3$ thin films deposited at 200 and 250 W Ti target power under nitrogen atmosphere. The rms roughness was evaluated as 16.9 nm (QNTN84A) and 19.6 nm (QNTN86A) for the films deposited with nitrogen doping and 12.2 nm (QNTL84A) and 21.0 nm (QNTL86A) for the films deposited without doping. The difference in the surface roughness was observed in all the films and seems to be due to the deposition conditions which monitor drastically the film features. This fact was also noticed for the grain size variation with the increase in Ti target power or under nitrogen partial pressure required for doping. AFM images shown in Fig. 8 indicate dense, uniform films with columnar grown morphology along *c*-axis.

3.3 Optical and electronic features

Fig. 9 illustrates the absorption properties of $NiTiO_3$ thin films in the spectral range (200–800 nm). Films deposited at 200 W

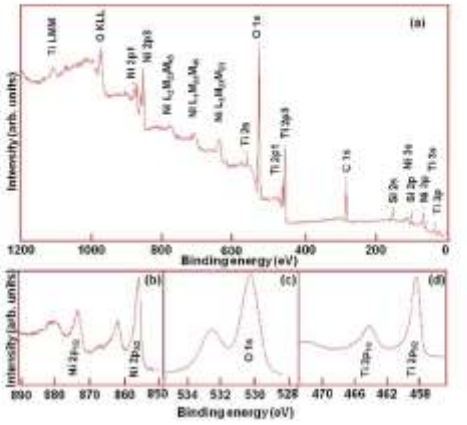

Fig. 7 (a) XPS survey spectrum of $NiTiO_3$ thin film deposited at 250 W Ti target power with nitrogen doping (QNTN86A); high resolution XPS spectrum for (b) Ni 2p, (c) O 1s and (d) Ti 2p regions.

Ti power show three absorption edges; one at lower wavelength region at about 300 nm (~4 eV) related to NiO interbands transition indicating the presence of NiO in the sample as noticed from XRD results. Suppression of this band edge occurs in the 250 W grown films which are free from NiO content. The second absorption edge is located at around 400 nm (~3 eV) related to direct electronic transition between the upper edge of O 2p valence band and the lower edge of Ti 3d conduction band. Finally a broad absorption edge appeared in the visible region near 600 nm according to the light yellow colored $NiTiO_3$ film.[14] An inset in Fig. 9 shows pale yellow color of post-annealed film deposited at 200 W Ti power without nitrogen doping. This indicates that these films indeed absorb visible light in agreement with optical band gap in pure $NiTiO_3$. With nitrogen doping, slight red shift occurs on the optical absorption spectrum indicating that these films have better visible light response to the ones without doping.

According to Agui and Mizumaki, who studied the intermetallic charge transfer and band gap of $MTiO_3$ (M = Fe, Mn,

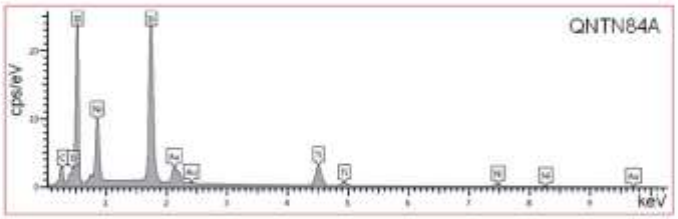

Fig. 6 EDAX spectrum of $NiTiO_3$ thin film deposited at 200 W Ti power with nitrogen doping.

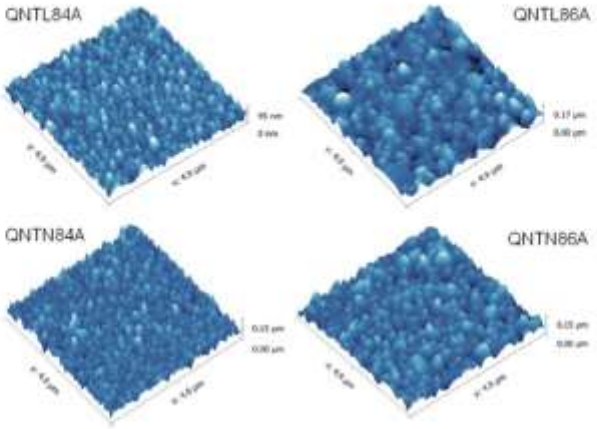

Fig. 8 AFM images of $NiTiO_3$ thin films deposited at 200 and 250 W Ti power with nitrogen doping.

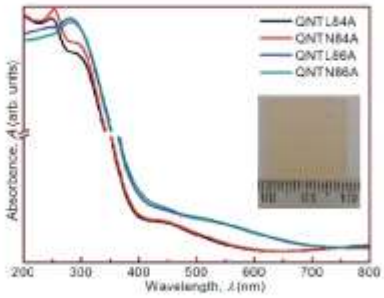

Fig. 9 Absorption spectra of $NiTiO_3$ thin films deposited at different Ti power (200 W (QNTL84A) and 250 W (QNTL86A)) with nitrogen doping (QNTN84A and QNTN86A). An inset shows post-annealed film deposited at 200 W Ti power without nitrogen doping.

Co and Ni), three types of electronic transitions exist in $NiTiO_3$.[38] They are represented as O 2p → Ti 3d, Ni 3d → Ti 3d and Ni 3d → O 2p. Here also two significant absorption edges can be observed due to the crystal field splitting of defined $NiTiO_3$ bands. Indeed, the one associated with Ni^{2+} that the $3d^8$ ions contributes to splitting of two sub-bands which can be called $Ni^{2+} \rightarrow Ti^{4+}$ charge transfer bands. The second broad absorption edge at shorter wave length is attributed to the $O^{2-} \rightarrow Ti^{4+}$ charge-transfer interactions[44,59] In order to obtain optical band gap of $NiTiO_3$ thin films, the absorbance spectra were fitted by using Tauc's equation given as $(\alpha h\nu)^F = A(h\nu - E_g)$, where A is proportionality constant. From the absorption spectra and the Tauc's equation, the results plotted in Fig. 10, leads to an evaluation of the band gaps.

The largest band gap for the four investigated samples is related to the direct electronic transition between the upper edge of O 2p valence band and the lower edge of Ti 3d

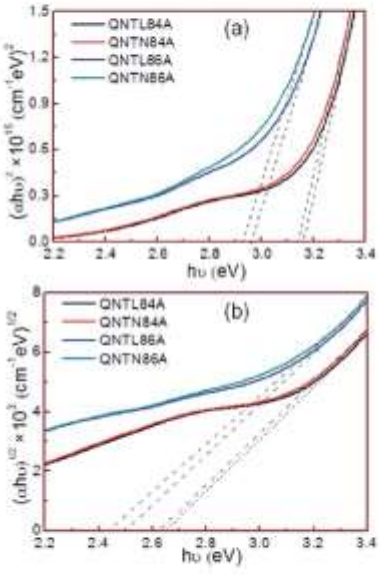

Fig. 10 Transformed absorption spectra of $NiTiO_3$ thin films deposited at different Ti power (200 W (QNTL84A) and 250 W (QNTL86A)) with nitrogen doping (QNTN84A and QNTN86A) showing (a) direct and (b) indirect band gap energies.

conduction band. The calculated values at 3.16, 3.14, 2.96 and 2.92 eV for QNTL84A, QNTN84A, QNTL86A and QNTN86A respectively, are close to those of TiO_2 structures.[48] The lower energy occurs from indirect transitions due to correlated electron states in the band gap, which could correspond to Ni^{2+} $3d^8$ band.[49] Therefore, the visible light response in the $NiTiO_3$ films would be due to the transition between the Ni^{2+} $3d^8$ band and Ti^{4+} 3d conduction band. The band gap values for these indirect transitions are around 2.65, 2.63, 2.50 and 2.43 eV for QNTL84A, QNTN84A, QNTL86A and QNTN86A as shown in Fig. 10. According to Zhao *et al.* nitrogen doping in TiO_2 induces two characteristics deep levels resulting band gaps of 1.0 eV and 2.5 eV due to oxygen vacancy and acceptor state of N 2p impurity, respectively.[5] The acceptor state is located at the top of the valence band and responsible for reduction in the band gap of nitrogen doped TiO_2. Similarly we noticed a slight drop in the optical band gap of $NiTiO_3$ films doped with nitrogen and this should improve the visible light photocatalytic activity.

3.4 Photocatalytic investigations

Photocatalytic process is based on the photo-generated electron–hole pairs, which can give rise to redox reactions with molecular species adsorbed on the surface of the catalysts. In this frame, photodegradation of methylene blue (MB) solutions was performed on the nitrogen doped and un-doped $NiTiO_3$ thin films under visible light irradiation. Fig. 11 shows the evolution of absorbance of MB *versus* wavelength with respect to the irradiation time. As shown in Fig. 11, the rapid decrease in the band intensity at 661 nm for QNTL86A compared to blank solution suggests that the chromophore responsible for characteristic color of MB is mineralized as the irradiation time increases. The change in the solution during photocatalysis reaction is illustrated in the inset of Fig. 11. No blue shift was observed for the absorption at 661 nm, but a gradual decrease in the absorption intensity was noticed, indicating that the large conjugated π-system has been destroyed.[11] We may note however, that a shoulder around 610 nm in MB solution was previously reported as a consequence of MB monomer and dimmer formations during the reaction.[51]

Fig. 12(a) shows the decrease in relative concentration of MB under visible light irradiation with time. For comparison, MB photolysis without any catalyst (blank solution) was also performed and plotted along with the degradation results. This proves that the decolorization of the MB solution is actually due to the photocatalytic decomposition of the dyes and the extent of decomposition achieved was 60% (Fig. 12(b)) for the sample deposited at 250 W Ti power without nitrogen doping. A slight increase in the photocatalytic efficiency was observed for the sample deposited at 250 W Ti power with nitrogen doping. The pseudo first order rate constant (k) values related to $NiTiO_3$ photocatalytic reaction is given by the following equation in terms of logarithmic ratio of MB concentration at time t (C) and at initial time (C_0).[52]

$$-\ln(C/C_0) = kt \quad (1)$$

The k values for $NiTiO_3$ thin films deposited at 250 W Ti power with (QNTN86A) and without (QNTL86A) nitrogen doping were estimated to be 5.83×10^{-3} and 5.75×10^{-3} per minutes, respectively from the slopes of straight line obtained by plotting $-\ln(C/C_0)$ *versus* irradiation time as shown in Fig. 12(c). The initial degradation rate of MB over these films decreased with nitrogen doping and better photocatalytic activity was observed with film doped with nitrogen. Fig. 12(d) shows surface topography of the $NiTiO_3$ thin film deposited at 250 W Ti target power (QNTL86A) after photocatalytic reaction. Rms roughness of the film decreased from 21 to 16.6 nm after 150 minutes of reaction. It can be noticed that the used films as photocatalysts are suitable for re-cycling.

Enhanced visible light photocatalytic activity of nitrogen doped TiO_2 films were reported earlier by Zhao *et al.* and the degradation efficiency on MB solution is given as 47.2%.[5] Y. J. Lin reported photo-degradation of MB on $NiTiO_3$ powders doped with Ag under visible light irradiation and the time taken for similar degradation efficiency reported in that study is about 60 hours.[53] X. Shu *et al.* achieved degradation efficiencies of 63 and 73% for $NiTiO_3$ and TiO_2 coupled $NiTiO_3$ nanoparticles, respectively after 6 hours of irradiation under visible light,[52] whereas we report almost equal efficiencies within 2.5 hours.

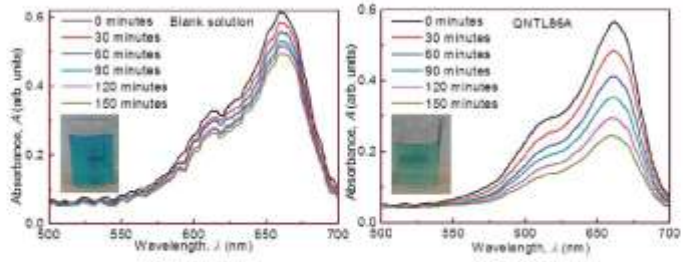

Fig. 11 Absorption changes of MB solution on blank (without sample) and $NiTiO_3$ thin films deposited at 250 W Ti power without nitrogen doping. A photograph of MB solution in the inset shows the de-colorization of the solution before and after the reaction.

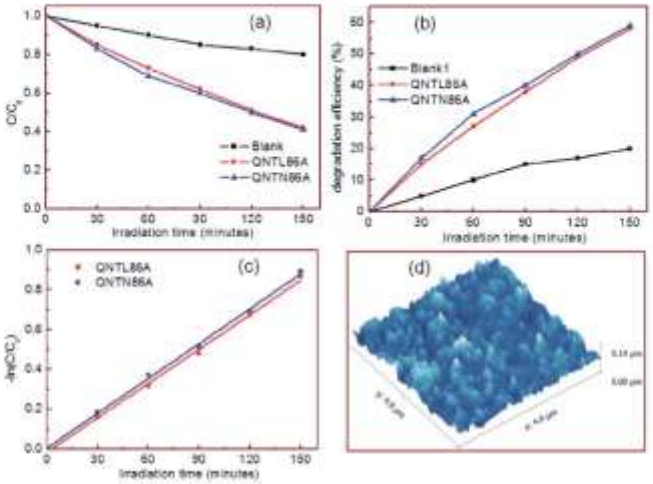

Fig. 12 (a) Photodegradation of MB monitored as the normalized concentration change, (b) de-colorization percentage, (c) linear transforms $-\ln(C/C_0)$ versus irradiation time under visible light irradiation for $NiTiO_3$ thin films deposited at 250 W Ti power (QNTL86A) and with nitrogen doping (QNTN86A) and (d) AFM image of QNTL86A after photocatalytic reaction.

Though the efficiencies obtained in our work are comparable with former reports, the kinetics of the reactions is characterized by shorter times. Thus effective photocatalytic degradation efficiency can be achieved easily (no further purification of the degraded solution is required) by pure $NiTiO_3$ thin films deposited on quartz substrates at 250 W Ti power. We obtained suitable characteristics of deposited films to act as efficient photocatalyst. For instance structural order is important to achieve crystalline films with defined optical characteristics. This optical band gap is crucial in the photoactivity of films under visible light irradiation and the nitrogen doping enhances the absorbance of these films in visible range contributing then to more efficient photocatalysts.

4. Conclusions

From the performed work, we demonstrate that pure ilmenite phase $NiTiO_3$ thin films with nitrogen doping can be grown on quartz substrate, thanks to co-sputtering process using multiple metal targets under partial pressure of oxygen and nitrogen atmosphere. XRD patterns under grazing incidence and well resolved Raman modes revealed high quality of the crystalline structure in investigated films. Formation of facets with porous structure was observed by SEM and AFM on films deposited at higher RF-sputtering power for the titanium target. XPS analysis determined the chemical bonding involved between the constitutive elements and their valence states. Effective effect of nitrogen doping consists in a reduction of the optical band gap of $NiTiO_3$ films and enhanced absorption in the visible light range. Improvement of the visible light driven photocatalytic activity was achieved from the degradation of MB by nitrogen doped $NiTiO_3$ thin film. The observed photocatalytic efficiency was attributed to synergetic effects of electronic structure modification induced by nitrogen doping combined with thin film morphology where higher specific surface and porous structure are involved. Potential exploitation is inferred from this work about the relevance of nitrogen doped $NiTiO_3$ as alternative to TiO_2 based heterogeneous photocatalysts.

Acknowledgements

The authors would like to thank Dr Nadia Haneche (IMMM) for SEM imaging. Special thanks to Prof. A. Gibaud and Prof. A. Bulou for helpful discussion on XRD and Raman measurements, respectively.

References

1 A. Zaleska, *Recent Pat. Eng.*, 2008, **2**, 157.
2 I. Ganesh, A. K. Gupta, P. P. Kumar, P. S. C. Sekhar, K. Radha, G. Padmanabham and G. Sundararajan, *Sci. World J.*, 2012, 1, DOI: 10.1100/2012/127326.
3 L. Zhao, Q. Jiang and J. Lian, *Appl. Surf. Sci.*, 2008, **254**, 4620.
4 (*a*) T. Sreethawong, S. Ngamsinlapasathian and S. Yoshikawa, *Chem. Eng. J.*, 2012, **192**, 292; (*b*) D. Li, Y. Zhang, W. Wu and C. Pan, *RSC Adv.*, 2014, **4**, 18186.
5 G. C. De, A. M. Roy and S. S. Bhattacharya, *Int. J. Hydrogen Energy*, 1996, **21**, 19.
6 D. W. Hwang, J. Kim, T. J. Park and J. S. Lee, *Catal. Lett.*, 2002, **80**, 53.

7 S. D. Scott, J. H. Richard and S. S. Kenneth, *J. Phys. Chem. C*, 2009, **113**, 11980.
8 R. Venkatesan, S. Velumani and A. Kassiba, *Mater. Chem. Phys.*, 2012, **135**, 842.
9 P. Madhusudan, J. Zhang, B. Cheng and G. Liu, *CrystEngComm*, 2013, **15**, 231.
10 Y. Qu, W. Zhou, L. Jiang and H. Fu, *RSC Adv.*, 2013, **3**, 18305.
11 X. Shu, J. He, D. Chen and Y. Wang, *J. Phys. Chem. C*, 2008, **112**, 4151.
12 X. Shu, J. He and D. Chen, *Ind. Eng. Chem. Res.*, 2008, **47**, 4750.
13 Y. J. Lin, Y. H. Chang, G. J. Chen, Y. S. Chang and Y. C. Chang, *J. Alloys Compd.*, 2009, **479**, 785.
14 (*a*) Y. Qu, W. Zhou, Z. Ren, S. Du, X. Meng, G. Tian, K. Pan, G. Wang and H. Fu, *J. Mater. Chem.*, 2012, **22**, 16471; (*b*) P. Jing, W. Lan, Q. Su, M. Yu and E. Xie, *Sci. Adv. Mater.*, 2014, **6**, 1.
15 (*a*) S. S. Soni, M. J. Henderson, J. F. Bardeau and A. Gibaud, *Adv. Mater.*, 2008, **20**, 1493; (*b*) L. Gomathi Devi and R. Kavitha, *RSC Adv.*, 2014, **4**, 28265.
16 K. T. Jacob, V. S. Saji and S. N. S. Reddy, *J. Chem. Thermodyn.*, 2007, **39**, 230.
17 A. T. Qiu, L. J. Liu, W. Pang, X. G. Lu and C. H. Li, *Trans. Nonferrous Met. Soc. China*, 2011, **21**, 1808.
18 M. Ohgaki, K. Tanaka, F. Marumo and H. Takei, *Mineral. J.*, 1988, **14**, 133.
19 S. Yuvaraj, V. D. Nithya, K. S. Fathima, C. Sanjeeviraja, G. Kalai Selvan, S. Arumugam and R. Kalai Selvan, *Mater. Res. Bull.*, 2013, **48**, 1110.
20 X. C. Liu, R. Hong and C. Tian, *J. Mater. Sci.: Mater. Electron.*, 2009, **20**, 323.
21 D. J. Taylor, P. F. Fleig, S. T. Schwab and R. A. Page, *Surf. Coat. Technol.*, 1999, **120**, 465.
22 J. L. Wang, Y. Q. Li, Y. J. Byon, S. G. Mei and G. L. Zhang, *Powder Technol.*, 2013, **235**, 303.
23 M. Kharkwal, S. Uma and R. Nagarajan, *Ind. Eng. Chem. Res.*, 2010, **49**, 1995.
24 G. A. Traistaru, C. I. Covaliu, V. Matei, D. Cursaru and I. Jitaru, *Dig. J Nanomater. Bios.*, 2011, **6**, 1257.
25 E. D. Gaspera, M. Pujatti, M. Guglielmi, M. L. Post and A. Martucci, *Mater. Sci. Eng., B*, 2011, **176**, 716.
26 K. P. Lopes, L. S. Cavalcante, A. Z. Simoes, J. A. Varela, E. Longo and E. R. Leite, *J. Alloys Compd.*, 2009, **468**, 327.
27 S. H. Chuang, M. L. Hsieh, S. C. Wu, H. C. Lin, T. S. Chao and T. H. Hou, *J. Am. Ceram. Soc.*, 2011, **94**, 250.
28 M. S. Sadjadi, K. Zare, S. Khanahmadzadeh and M. Enhessari, *Mater. Lett.*, 2008, **62**, 3679.
29 T. Li, C. C. Wang, C. M. Lei, X. H. Sun, G. J. Wang and L. N. Liu, *Curr. Appl. Phys.*, 2013, **13**, 1728.
30 A. A. Tahir, M. Mazhar, M. Hamid, K. G. U. Wijayantha and K. C. Molloy, *Dalton Trans.*, 2009, 3674.
31 H. M. Rietveld, *J. Appl. Crystallogr.*, 1969, **2**, 65.
32 J. Rodriguez-Carvajal, *Phys. B*, 1993, **192**, 55.
33 P. Thompson, D. E. Cox and J. B. Hastings, *J. Appl. Crystallogr.*, 1987, **20**, 79.
34 M. M. Shirolkar, D. Phase, V. Sathe, J. Rodriguez-Carvajal, R. J. Choudhary and S. K. Kulkarni, *J. Appl. Phys.*, 2011, **109**, 123512.
35 (*a*) M. I. Baraton, G. Busca, M. C. Prieto, G. Riechiardi and V. Sanchez Escribano, *J. Solid State Chem.*, 1994, **112**, 9; (*b*) G. Busca, G. Ramis, J. M. Gallardo Amores, V. Sanchez Escribano and P. Piaggio, *J. Chem. Soc., Faraday Trans.*, 1994, **90**, 3181.
36 C. H. Wang, X. P. Jing, W. Feng and J. Lu, *J. Appl. Phys.*, 2008, **104**, 034112.
37 G. Yang, W. Chang and W. Yan, *J. Sol-Gel Sci. Technol.*, 2014, **69**, 473.
38 A. Agui and M. Mizumaki, *J. Electron Spectrosc. Relat. Phenom.*, 2011, **184**, 463.
39 S. Moghiminia, H. Farsi and H. Raissi, *Electrochim. Acta*, 2014, **132**, 512.
40 M. Landmann, E. Rauls and W. G. Schmidt, *J. Phys.: Condens. Matter*, 2012, **24**, 195503.